The Dissertation Committee for Nicholas Penha Malaya
certifies that this is the approved version of the following dissertation:

Reducing Turbulence- and Transition-Driven Uncertainty in Aerothermodynamic Heating Predictions for Blunt-Bodied Reentry Vehicles

Committee:

Robert D. Moser, Supervisor

George Biros

Noel T. Clemens

Leszek F. Demkowicz

Todd A. Oliver

Robert van de Geijn

Reducing Turbulence- and Transition-Driven Uncertainty in Aerothermodynamic Heating Predictions for Blunt-Bodied Reentry Vehicles

by

Nicholas Penha Malaya, B.S.; M.S.E.

DISSERTATION

Presented to the Faculty of the Graduate School of

The University of Texas at Austin

in Partial Fulfillment

of the Requirements

for the Degree of

DOCTOR OF PHILOSOPHY

THE UNIVERSITY OF TEXAS AT AUSTIN

May 2016

To my wife, Emily.

Acknowledgments

Reducing Turbulence- and Transition-Driven Uncertainty in Aerothermodynamic Heating Predictions for Blunt-Bodied Reentry Vehicles

Nicholas Penha Malaya, Ph.D.
The University of Texas at Austin, 2016

Supervisor: Robert D. Moser

Much of the solar energy incident on the Earth's surface is absorbed into the ground, which in turn heats the air layer above the surface. This buoyant air layer contains considerable gravitational potential energy. The energy in this layer can drive the formation of columnar vortices ("Dust Devils") which arise naturally in the atmosphere. A new energy harvesting approach makes use of this phenomena by creating and anchoring the vortices artificially and extracting energy from them. In the research proposed here, we will explore the characteristics of these vortices through numerical simulation. Computational models of the turning vane system which generates the vortex and the turbine used to extract energy have been developed and are presented here. These models have been tested against available experimental measurements. Preliminary results from these studies are also presented, as well as initial details of the columnar vortex structure. In addition, we introduce the approach used to optimize the system configuration to maximize the power extraction. The objective of this work

is to explore a wide variety of configurations to assess the technological feasibility of the overall endeavor.

Table of Contents

List of Tables

List of Figures

Chapter 1

Introduction

1.1 Motivation

A vehicle reentering Earth's atmosphere requires a thermal protection system (TPS) to mitigate aerothermodynamic heating. Gauging reentry heat load is critical to mission success. Undersizing a TPS at best destroys expensive equipment and at worst causes loss of life. Oversizing a TPS increases vehicle weight and fuel costs and therefore reduces available payload. Decision makers need these heating predictions with quantified uncertainty so they may balance reliability requirements against cost constraints.

Turbulence and laminar-turbulent transition enter critically into this balance. Turbulence in the fluid boundary layer around a vehicle intensifies heating because turbulent mixing enhances momentum, energy, and chemical species transport to the TPS. Recent coupled multiphysics studies by Bauman et al. [8] and Stogner et al. [154] showed that ablative TPS predictions are highly sensitive to uncertainty in turbulence model calibration parameters. Further, while low-turbulence freestream conditions allow at least the stagnation point region within the flow to be laminar, prediction efforts often assume these boundary layers are fully turbulent. Both incorrectly applying turbulence models to laminar regions and neglecting the downstream laminar-turbulent

transition processes add markedly to heat load uncertainty. Transition models may be employed to relax this assumption by accounting for transitional flow. However, the extreme sensitivity of transition phenomena to the upstream environment (see, for example, Fedorov [43]) brings with those models another uncertainty penalty.

1.2 Objectives

This work aims to reduce turbulence- and transition-driven uncertainty in aerothermodynamic heating predictions for blunt-bodied reentry vehicles in two ways. The first way will reduce the uncertainty entering through the turbulence model calibration parameters. The second way will reduce the uncertainty arising from incorrectly treating laminar regions as fully turbulent.

First, we aim to use direct numerical simulation (DNS) of the compressible Navier–Stokes equations to generate high-quality supersonic boundary layer data for turbulence model calibration. DNS was selected because the technique produces data uncertainties limited only by the available computing resources. We have designed and implemented a new, well-verified Fourier/B-spline pseudospectral DNS code called Suzerain employing "slow growth," a spatiotemporal boundary layer homogenization approach by Topalian et al. [163, 165, 166], to efficiently generate turbulence statistics with accurately quantified uncertainties. The code is used to create a rich database of compressible turbulence statistics for use by the reentry community. In addition to the long-lived, public datasets we generate, our modern DNS code can serve others as a robust, extensible platform for computational turbulence research.

Second, we aim to detect which regions of an ablative thermal protection system on a blunt-bodied vehicle can sustain turbulence. Given the strength of the favorable pressure gradients found in these flows, it is reasonable to expect that a contiguous region extending some distance radially from the stagnation point simply cannot maintain turbulence. Rather than taking the classical transition modeling approach and seeking where laminar-turbulent transition occurs, this study instead aims to map where turbulence cannot survive. The spatiotemporal boundary layer DNS code is reused to parametrically explore pointwise flow conditions found within simulations like those of Bauman et al. [8]. Fully turbulent fields are initialized and evolved at local conditions taken from such simulations. We say the conditions cannot sustain turbulence if the field relaminarizes. By exploring this parameter space, we aim to discover where turbulence models might not be employed when engineering practitioners simulate these reentry flows.

1.3 Outline

This work is organized as follows:

Chapter 2 provides background on the uncertainties arising from applying turbulence models within reentry applications, how calibration data impacts these uncertainties, and evaluates potential sources for obtaining that data. It further discusses uncertainties arising from transition phenomena and proposes a concrete scenario for study based on the Orion MPCV.

Chapter 3 summarizes the mathematical models required to pursue the aims of

the thesis. Chapter 4 details the computational techniques used to apply these models while Chapter 5 describes their software implementation.

Chapter 6 presents new direct numerical simulations of spatiotemporally homogenized turbulent boundary layers with features similar to those found on the Orion MPCV thermal protection system. It investigates the character of the turbulence, presents Favre-averaged equation budgets, and communicates the information necessary to use the data for turbulence model calibration.

Chapter 7 detects turbulence-sustaining regions on the Orion MPCV using spatiotemporally homogenized boundary layers. The study methodology is discussed followed by a collection of results corresponding to locations on the MPCV thermal protection system.

Finally, Chapter 8 summarizes the conclusions of this thesis and presents recommendations for future work.

1.4 Contributions

This work has made the following contributions:

1. Creation of a well-verified, openly available pseudospectral code for the direct numerical simulation (DNS) of sub- through supersonic turbulent boundary layers using “slow growth” homogenization techniques.

2. Generation and characterization of metadata-rich DNS data, with well-quantified sampling uncertainty, for sub- and supersonic spatiotemporally homogenized tur-

bulent boundary layers on cold, transpiring walls and subject to strong favorable pressure gradients.

3. Design of a novel DNS experiment to determine where on a vehicle surface turbulence can be sustained without requiring the flight environment to be sufficiently well-understood that transition modeling can be reliably applied.

4. Application of this novel DNS experiment to conditions from the NASA Orion Multi-Purpose Crew Vehicle ablative thermal protection system during atmospheric reentry from the International Space Station.

Chapter 2

Background

This chapter provides the background material necessary to link the motivation from Section 1.1 with the numerical studies in Chapter 6 and Chapter 7. The first four sections cover state-of-the-art turbulence model prediction for blunt-bodied reentry vehicles and, in particular, the dearth of suitable model calibration data. In Section 2.5, homogenization approaches are then seen to remedy that shortcoming leading to the study in Chapter 6. Next, the shortcomings of transition prediction are described in Section 2.6 along with a novel idea for bounding transition-related uncertainty based on relaminarization arguments. Both empirical parameters and rigorous stability bounds are shown to be inadequate for applying this idea in Sections 2.6 and 2.7. However, homogenization is again applicable as discussed in Section 2.8 prompting the study in Chapter 7. Finally, to provide a concrete setting for both aforementioned studies, data from NASA Orion Multi-Purpose Crew Vehicle simulations is presented in Section 2.9

2.1 The Impact of Turbulence on Aerothermodynamic Heating Predictions

In 2006, Roy and Blottner [132] summarized state-of-the-art aerodynamic predictions in hypersonics:

> Accurate aerodynamic prediction is critical for the design and optimization of hypersonic vehicles. Turbulence modeling remains a major source of uncertainty in the computational prediction of aerodynamic forces and heating for these systems.... While some [one- and two-equation] turbulence models do provide reasonable predictions for the surface pressure, the predictions for surface heat flux are generally poor, and often in error by a factor of four or more....

In the same year, Wilcox [176, §5.7] made the more subdued comment that supersonic model predictions involving surface heat transfer "often show nontrivial discrepancies from measured values."

On a reentry vehicle, thermal protection material selection is controlled by predicted heat flux, surface pressure, and shear stress while material thickness is governed primarily by the total integrated heat load across a flight trajectory [178]. Potentially large errors in surface heat transfer predictions, like those delivered by current turbulence models, necessitate more conservative designs and can add significant vehicle mass penalties. Broad uncertainty bounds can often be as important as the nominal aeroheating value predicted from a designer or risk assessor's perspective [117].

As part of The University of Texas at Austin's Center for Predictive Engineer-

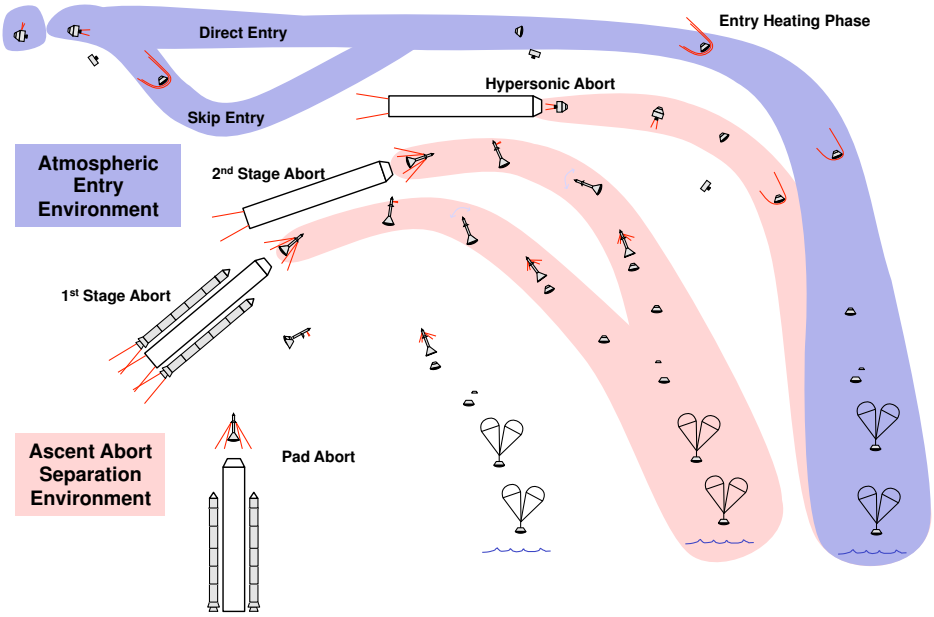

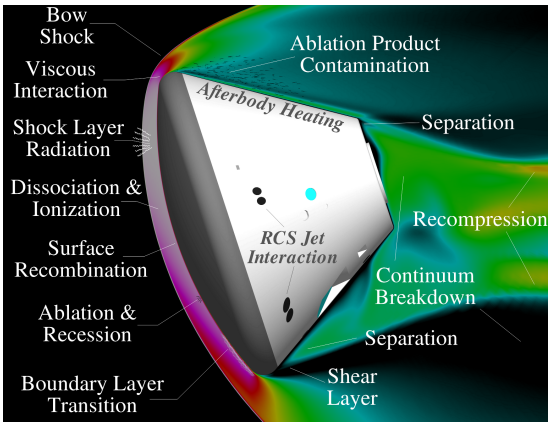

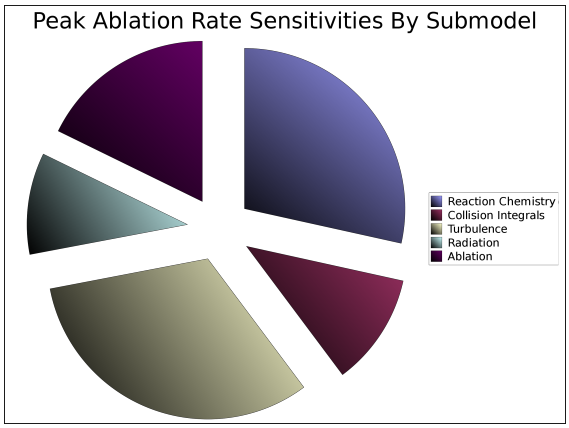

Figure 2.1: The Entry Heating Phase during atmospheric reentry is a complex multi-physics problem with uncertainties in system response predictions arising from many causes. In particular, aerothermodynamic heating and any associated ablative thermal protection system response predictions are highly sensitive to turbulence model parameters. Top and lower-left images courtesy of NASA. Lower right image reproduced from Stogner et al. [154].

ing and Computational Sciences'[1] larger investigation into verification, validation, and uncertainty quantification, Bauman et al. [8] and Stogner et al. [154] performed coupled multiphysics simulations of the blunt-bodied Orion Multi-Purpose Crew Vehicle (MPCV), then called the Crew Exploration Vehicle (CEV), undergoing peak heating during return from the International Space Station. The upper portion of Figure 2.1 shows this entry heating phase amongst the many other flight regimes in which the MPCV must operate while the lower left portion depicts the multi-physics nature of the reentry environment. The lower right portion of Figure 2.1 reproduces the finding by Bauman et al. and Stogner et al. that the surface heat flux and associated thermal protection system ablation rate showed more sensitivity to the uncertainties from turbulence models than to any other physics model they employed.

2.2 Data Requirements for Bayesian Calibration of Turbulence Models

Turbulence modeling is a rich discipline built on theoretical results derived from first principles, physical intuition obtained from precise measurements, and, by necessity, judicious curve fitting [24, 36, 124, 176]. All practically useful turbulence models contain imperfectly known free parameters which must be calibrated via some statistical inference procedure. For example, least squares approaches can be used to determine parameters by minimizing the discrepancy between model predictions and some relevant reference observations, also known as calibration data.

Recently, Bayesian techniques for turbulence model calibration have been in-

[1] `http://pecos.ices.utexas.edu/`

troduced by Cheung et al. [25] and expounded upon by Oliver and Moser [112, 113]. Following Bayesian philosophy, the turbulence model parameters, θ, are assigned a joint prior probability density function (PDF) characterizing prior knowledge about the parameters' uncertain, "true" values. During calibration, this prior PDF, $p_{\text{prior}}(\theta)$, is merged with a likelihood distribution depending on new data, d, to obtain a posterior PDF, $p_{\text{post}}(\theta|d)$, via Bayes' theorem:

$$p_{\text{post}}(\theta|d) \propto L(d|\theta)\, p_{\text{prior}}(\theta)\,. \tag{2.1}$$

The likelihood function, $L(d|\theta)$, gauges the probability that the model with parameters θ is consistent with the data d. In effect, the posterior PDF captures the updated state of model parameter knowledge obtained by incorporating the calibration data.

Measurement uncertainty in the calibration data is accounted for in the likelihood function. By Bayes' theorem, larger measurement uncertainties cause the calibration data to less strongly influence the posterior PDF which, in turn, causes less certain turbulence model predictions. While smaller uncertainties are therefore desirable, it is far more important that the calibration data have accurately quantified uncertainties. Indeed, inaccuracies poison the posterior PDF. For these reasons, we say calibration data is "high quality" if, firstly, it is accompanied by accurately quantified measurement uncertainties and, secondly, if those uncertainties are small.

Additionally, "high quality" calibration data must satisfy Settles and Dodson's long-established assessment criteria listed in Table 2.1. The preceding discussion motivates and sharpens their requirements regarding *well-defined error bounds*. Three of the other criteria are paraphrased briefly as they will be important in the sequel:

- *Realistic test conditions*. More application-like but comparatively rare data are preferred. For example, in the context of reentry vehicles with ablative heat shields, data collected from experiments with non-adiabatic walls are preferred.

- *Simplicity*. Experimental geometries must be sufficiently simple that they may be modeled without enormous difficulty.

- *Well-defined boundary conditions*. All incoming conditions, especially the state and "fluctuating character" of the incoming boundary layer, must be carefully documented.

Comprehensive criterion descriptions appear in Settles and Dodson [144].

Assuming a predictive model can be validated in a given context [104, 109, 110], it is the scarcity of high-quality calibration data that dominates predictive uncertainty. Because the present work is intended to reduce the uncertainty of aerothermodynamic heating predictions on blunt-bodied reentry vehicles, and because these predictions are sensitive to turbulence model parameters, we seek relevant high-quality turbulence model calibration data.

2.3 High-Quality Calibration Data from the Experimental Literature

We seek high-quality experimental data, as defined in Section 2.2, for supersonic turbulent boundary layers experiencing favorable pressure gradients that are attached to cold walls possessing either flat or convex geometries. Following earlier data compilations by Fernholz and Finley [45, 46] and Fernholz et al. [47], Settles

Table 2.1: While "...looking for those few experimental studies of unimpeachable quality..." in the super- and hypersonics literature, Settles and Dodson [143, 144, 145, 146] set forth these criteria for assessing the utility of data sets to the testing and validation of turbulence models.

Necessary criteria	Desirable criteria
1. Baseline applicability	1. Turbulent data
2. Simplicity	2. Realistic test conditions
3. Specific applicability	3. Non-intrusive instrumentation
4. Well-defined boundary conditions	4. Redundant measurements
5. Well-defined error bounds	5. Flow structure and physics
6. Consistency	
7. Adequate documentation	
8. Adequate spatial resolution	

and Dodson [144] surveyed the 1962–1993 literature to find experimental data from $\mathrm{Ma} \geq 3$ attached turbulent boundary layer flows in nonzero pressure gradients. Of the entire corpus then-indexed by the AIAA Aerospace Database, only nine experimental data sets satisfied their necessary criteria listed in Table 2.1. Of those nine, only the work of Lewis et al. [92] included a favorable pressure gradient. That study used adiabatic wall conditions,[2] only implicitly reported its error bounds [45, p. 7201-A-1], and provided no fluctuating quantity measurements. Settles and Dodson concluded that both additional nonintrusive fluctuating flow field measurements and data from pressure gradient flows having prescribed wall temperatures would be valuable.

Since 1993, experimentalists have generated extensive, nonintrusive fluctuating data from flows with a variety of pressure gradient conditions [e.g. 3, 12, 13, 38–40, 54, 55, 85, 95, 96]. Explicitly stated, well-characterized error bounds commonly accompany these more recent measurements. However, adiabatic wall conditions continue to overwhelmingly dominate the literature and experimental data from constant-temperature, cold wall flows remains comparatively quite rare. That is, Settles and Dodson's *realistic test conditions* criterion, discussed in Section 2.2, remains largely unfulfilled in the current literature. Regardless of the wall conditions, obtaining near-wall data also remains a challenge and limits the utility of experimental measurements for compressible turbulence model development.

In generally accepted frameworks for predictive simulation, high-quality data

[2] Subsequent favorable pressure gradient experiments by the same authors employed constant-temperature, cold walls [58]. Though extant, this data was not assessed by Settles and Dodson [144]

is unequivocally required for model validation [2, 4, 5].[3] The currently available experimental data sets pertinent to the scenario of interest are, at best, sufficient for turbulence model validation [132]. Calibration is fundamentally different from validation in that the data consumed need not be drawn from the system of interest or some approximate facsimile thereof — anything traceable that a practitioner deems informative to a particular model may be used, provided that the consequential model can be validated. To make the strongest possible statement, within the above frameworks, about a model's validity requires assessing it against data not used during calibration. For these reasons, the present work espouses the view that the scant, high-quality experimental data available should be reserved for validation alone.

2.4 High-Quality Calibration Data from the Computational Literature

Direct numerical simulation (DNS) is a high-fidelity computational technique in which the full spatiotemporal scales of turbulence are resolved numerically. When performed carefully, DNS accurately captures the dynamics of turbulent flows permitting unfettered measurement of experimentally inaccessible quantities. However, because of the need to resolve fine dissipative processes, DNS' computational expense grows like Re^4 where Re is an appropriate Reynolds number. This explosive scaling places high Reynolds number flow regimes out of reach of DNS for the foreseeable future.

[3] As defined by Moser et al. [104], "…validation [determines] whether a mathematical model is a sufficient representation of reality … for predicting specified [quantities of interest] to inform a specific decision."

Fortunately, turbulent boundary layers on blunt-bodied reentry vehicles often have Reynolds numbers low enough to be accessible by compressible DNS techniques on current high-performance computing platforms. Here, the Reynolds number based on the momentum thickness, Re_θ, is the pertinent one. Bauman et al. [8] found $\mathrm{Re}_\theta \approx 400$–$700$ in their heat shield simulations. For comparison, Komminaho and Skote [78] reported incompressible DNS results for that same Re_θ range in 2002. Though compressible DNS is markedly more expensive than its incompressible counterpart, computing hardware has improved by more than an order of magnitude in the interim.

Turbulent boundary layers are more challenging to simulate than streamwise-homogeneous channel flows because they evolve as they progress downstream. If the streamwise direction is treated with aperiodic numerics, some form of turbulent inflow condition is required. One common approach is tripping a laminar profile to cause the flow to transition inside the computational domain [180]. Another approach is providing an approximately realistic turbulent profile via generation [e.g. 97], some auxiliary computation, or by "recycling" rescaled turbulent profiles from elsewhere within the computation [147]. Employing highly efficient, streamwise-periodic numerics innately forces recycling. Any chosen technique brings with it complexity and the danger of introducing unintended and undesirable time- and length-scales through the streamwise boundary treatment.

In 2010, Schlatter and Örlü [137] assessed zero-pressure-gradient, incompressible, low-Re turbulent boundary layer simulations [48, 74, 75, 78, 135, 136, 147, 150, 179] with the goal of quantifying the variability of reported results. Schlatter and Örlü found "…surprisingly inconsistent predictions for quantities as basic as the friction co-

efficient, shape factor, and fluctuation maxima…" despite the fact that all authors used "reliable numerical methods with sufficiently high resolutions." They concluded that the discrepancies arose from differences in inflow Reynolds number and turbulence generation, the amount of settling length the flow was permitted before it was deemed to have reached its final turbulent state, and the selection of computational domain dimensions and boundary conditions. In short, computational shortcuts anticipated to be benign were demonstrably not so in subtle ways.

It is reasonable to expect that DNS data sets for compressible boundary layers, with their additional thermodynamic complexity and greater computational expense, possess inconsistencies of at least the same severity as their incompressible counterparts. The straightforward consequence is that using spatially evolving compressible boundary layer DNS as a high-quality calibration data source requires great care with respect to Settles and Dodson's criteria for *simplicity* and *well-defined boundary conditions* discussed in Section 2.2. Addressing these concerns in the context of a given data set certainly is possible but is sufficiently difficult[4] that finding a less complicated class of calibration data is worthwhile.

[4]Confirming that, for example, an inflow-tripping or inflow-rescaling procedure has not aphysically perturbed spatially evolving DNS results seemingly necessitates performing an auxiliary study checking that reported statistics, to reported uncertainties, are insensitive to the inflow treatment. Performing such studies incurs computational expense of same order as the original DNS.

2.5 Recent Developments in Homogenization of Turbulent Boundary Layers

To reduce computational expense and avoid the need for inflow boundary conditions, Spalart [150] pioneered the simulation of spatially homogenized boundary layers. In his approach, additional assumptions are introduced to homogenize the boundary layer in the streamwise direction thus permitting the use of periodic boundary conditions. Using 1988 computing hardware, Spalart simulated incompressible boundary layers at Re_θ up to 1410 which remain among the few widely accepted DNS-derived data sets in the zero-pressure-gradient turbulent boundary layer literature [64, 179]. Guarini [59] extended Spalart's work to spatially homogenized compressible boundary layers, again achieving considerable expense reduction. From the perspective of the current work, homogenization permits better adherence to Settles and Dodson's criteria for *simplicity* and *well-defined boundary conditions* because it removes the subtle inflow boundary condition.

Beyond introducing periodicity, the Spalart [150] and Guarini [59] spatial homogenizations add additional "slow growth" forcing terms to the residual of governing equations. These terms must be Reynolds-averaged and accounted for during the calibration of the one- and two-equation turbulence models typically used in super- and hypersonic applications. However, taking the Reynolds average of these spatial slow growth forcing terms causes new, unclosed turbulence correlations to appear which subsequently must be closed through a modeling ansatz beyond that required to develop the off-the-shelf turbulence models. This is undesirable.

Motivated by Rayleigh's problem, in 2011 Topalian et al. [163] sidestepped the

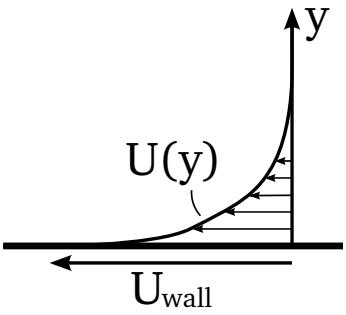

Figure 2.2: Rayleigh's problem.

appearance of these unclosed terms by instead homogenizing a temporally evolving boundary layer. This classical problem, depicted in Figure 2.2, concerns the behavior of a fluid in a semi-infinite domain bounded below by a no-slip wall. At time $t = 0$ the wall impulsively is started with some constant velocity. The resulting boundary layer grows upward as time progresses but is statistically homogeneous in the streamwise and spanwise directions.

The temporal homogenization approach, to recant from Topalian et al. [166] employing Spalart-like notation, begins by manipulating the evolution of a conserved flow quantity $\phi = \phi[x, y, z, t]$ governed by some nonlinear spatial operator N according to

$$\frac{\partial \phi}{\partial t} + N[\phi] = 0. \tag{2.2}$$

The quantity $\phi = \bar{\phi} + \phi'$ is decomposed into its mean and zero-mean fluctuating components, respectively. Defining A^{RMS} to be proportional to the root-mean-squared fluctuation ϕ^{RMS},

$$\phi = \bar{\phi} + A^{\mathrm{RMS}} \frac{\phi'}{A^{\mathrm{RMS}}} = \bar{\phi} + A^{\mathrm{RMS}} \phi'_p \tag{2.3}$$

where ϕ'_p now captures periodic fluctuating behavior. One introduces a fast time $t_f = t$ and a slow time $t_s = \epsilon t$ where $\epsilon \ll 1$ and assumes $\bar{\phi}$ and A^{RMS} vary only with y and t_s while ϕ'_p does not vary with t_s. This is intuitively sensible in Rayleigh's problem as $\bar{\phi}$ and A^{RMS} should depend on the slowly evolving boundary layer thickness and the distance from the wall but not on the field's instantaneous state. That is,

$$\phi[x, y, z, t] = \bar{\phi}[y, t_s] + A^{\text{RMS}}[y, t_s]\phi'_p[x, y, z, t_f] \tag{2.4}$$

which yields, after some manipulation,

$$\frac{\partial \phi}{\partial t_f} + N[\phi] = -\epsilon \frac{\partial \phi}{\partial t_s} = -\epsilon \frac{\partial \bar{\phi}}{\partial t_s} - \left(\frac{\epsilon}{\phi^{\text{RMS}}} \frac{\partial \phi^{\text{RMS}}}{\partial t_s} \right) \phi'. \tag{2.5}$$

As alluded to previously, taking the expectation of (2.5) does not produce derivatives of mean fast-fluctuating quantities with respect to slow time. Consequently, the data produced can be used directly for calibration of Reynolds-average turbulence models under the additional mild assumption that modeled quantities, like the turbulent kinetic energy, can also be decomposed analogously to (2.4). The final right hand side in (2.5) is the general form of such temporal slow growth forcing.

Additional work is necessary to completely determine that forcing and render it in a computable form. Topalian et al. [166] invoked tensor consistency and self-similarity arguments to permit DNS of a fixed slow time instant in a zero-pressure-gradient temporal boundary layer. This homogenization ultimately adds conserved-quantity forcing terms

$$\mathscr{S}_\rho = \mathscr{S}_{\rho,t}, \qquad \mathscr{S}_{\rho u_i} = \rho \mathscr{S}_{u_i,t} + u_i \mathscr{S}_{\rho,t}, \qquad \mathscr{S}_{\rho E} = \rho \mathscr{S}_{E,t} + E \mathscr{S}_{\rho,t} \tag{2.6a}$$

to the fast-time mass, momentum, and total energy equations, respectively. The associated specific-quantity forcing terms are

$$\mathscr{S}_{\rho,t} = y\ \mathrm{gr}_{t_0}(\Delta)\left(\frac{\rho}{\bar{\rho}}\frac{\partial\bar{\rho}}{\partial y}\right) \tag{2.6b}$$

$$\mathscr{S}_{u_i,t} = y\ \mathrm{gr}_{t_0}(\Delta)\left(\frac{\partial\tilde{u}_i}{\partial y} + \frac{u_i''}{\sqrt{\widetilde{u_k''u_k''}}}\frac{\partial\sqrt{\widetilde{u_k''u_k''}}}{\partial y}\right) \tag{2.6c}$$

$$\mathscr{S}_{E,t} = y\ \mathrm{gr}_{t_0}(\Delta)\left(\frac{\partial\tilde{E}}{\partial y} + \frac{E''}{\sqrt{\widetilde{E''E''}}}\frac{\partial\sqrt{\widetilde{E''E''}}}{\partial y}\right). \tag{2.6d}$$

Here, y is the wall-normal distance and E is the specific total energy. Tildes denote density-weighted, Favre averages and double primes denote Favre fluctuations. To close the model one must supply a temporal growth rate parameter, $\mathrm{gr}_{t_0}(\Delta)$, which controls the momentum thickness θ achieved at stationarity.

Recently, Topalian et al. augmented their temporal model (2.6) with spatial homogenization terms to model the fast evolution of a homogenized flow defect relative to some prescribed, spatially developing inviscid base flow [165]. With an appropriate inviscid base flow construction, they achieved favorable pressure-gradient-like conditions. The construction of this new "spatiotemporal" model is technical and has yet to be published— a self-contained summary appears in Section 3.3 while a full derivation is presented in Section A.3.

The homogenized boundary layers obtained by Spalart, Guarini, and Topalian et al. differ from their physically real, spatially evolving brethren and produce somewhat different turbulent statistics. For instance, clearly the former produce statistically stationary one-dimensional profiles while the latter produces a two-dimensional profile. Nevertheless, homogenized boundary layer DNS data is expected to beneficially

inform turbulence model calibration efforts because, relative to the current state of super- and hypersonic aerodynamic predictions discussed in Section 2.1, it adequately resembles truth data. In summary, the present work pursues homogenization because it provides a reproducible, cost-effective way to produce high-quality calibration data for turbulence models.

2.6 The Impact of Transition on Aerothermodynamic Heating Predictions

Provided the freestream impinging on a blunt-bodied reentry vehicle has low enough turbulence, the flow in some neighborhood of the stagnation point will be laminar because the mean flow velocity must approach zero there. As favorable pressure gradients and convex surfaces are well-known to stabilize flows [see, e.g., 3, 96, 162], the laminar region will extend radially outward some distance from the stagnation point. Discerning, with well-quantified uncertainty, when the flow becomes turbulent is difficult as laminar-to-turbulent transition processes are highly sensitive to many environmental details that defy robust characterization [43]. Indeed, even experimental data exhibits considerable intra-facility, observation-to-observation variability as shown in Figure 2.3. Contributing and compounding in-flight factors that must be weighed include freestream perturbation levels, magnification of perturbations as they pass through the bow shock, chemically reacting ablation products outgassing into the hot flow, and surface roughness due to ablator fibrosity and possibly spallation.

Engineering estimates of these factors, when inserted into state-of-the-art transition models, can incur too much uncertainty for engineering use as Hollis et al. [63]

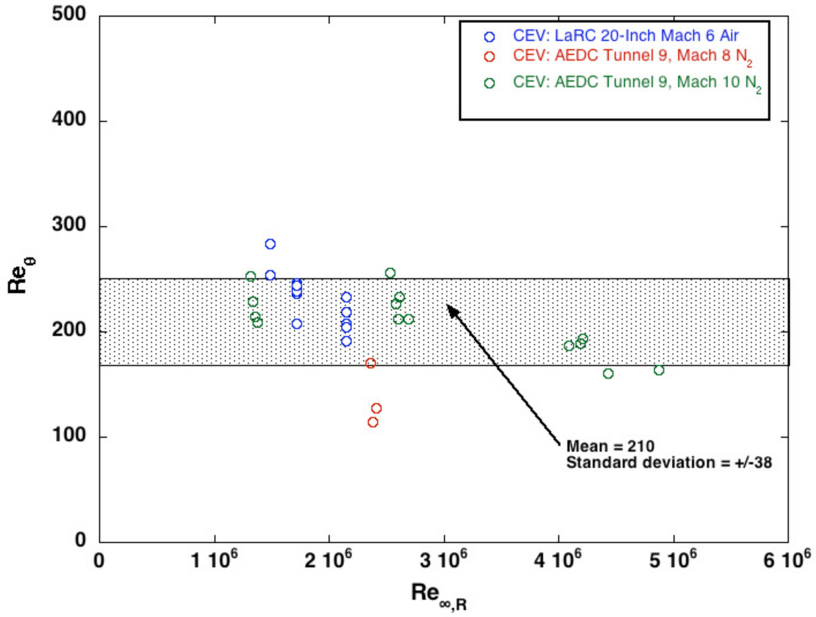

Figure 22. Transition onset values of Re_θ

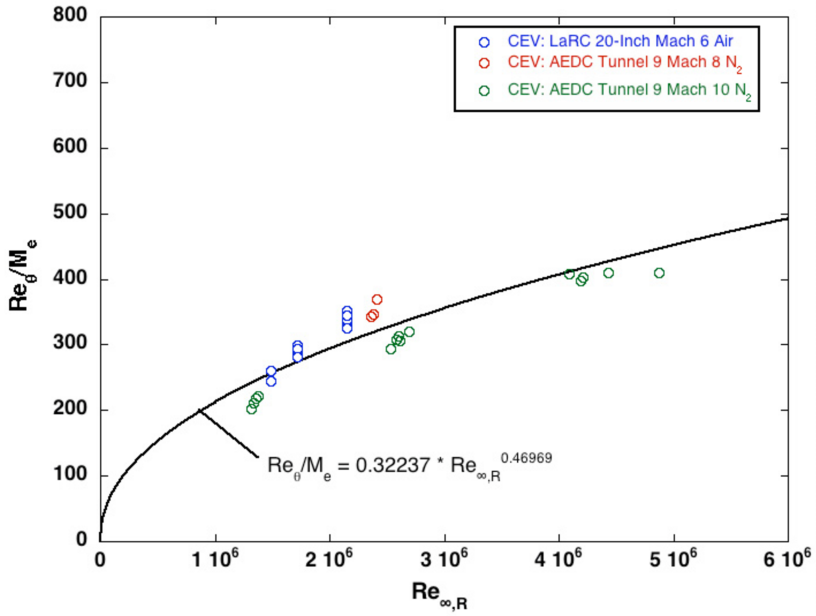

Figure 23. Transition onset values of Re_θ/M_e

Figure 2.3: Transition onset values of Re_θ (above) and $\mathrm{Re}_\theta/\mathrm{Ma}_e$ (below) reproduced from Hollis et al. [63]. Labels LaRC and AEDC denote the NASA Langley Research Center 20-Inch Mach 6 Tunnel and the Arnold Engineering Development Center Hypervelocity Wind Tunnel Number 9.

implied in 2008:

> "Because of the challenges associated with analysis of all the possible transition mechanisms, it is the defined policy of the [Orion MPCV] program to make a conservative assumption that the vehicle will experience turbulent flow throughout its trajectory."

However, using a fully turbulent assumption also impacts aerothermodynamic heating prediction uncertainty for two reasons. First, given the high probability of a laminar region near the stagnation point, the range of feasible predictions must encompass both globally turbulent and globally laminar behavior. The difference between these two behaviors in the context of the Orion MPCV is depicted in Figure 2.4. Second, again assuming a laminar region exists, all fully turbulent boundary layer calculations see incorrect upstream conditions.

Aerothermodynamic heating prediction uncertainty would be decreased if one could reliably use laminar predictions in demonstrably laminar regions and turbulent predictions everywhere else without incurring the unacceptably large penalty associated with transition models. Near-stagnation point laminar prediction bounds would be tighter and uncertainty in downstream turbulent predictions would improve as those calculations would subsume more physically correct upstream information.

One useful bound on the laminar region would be to assume that if local conditions can at all sustain turbulence, the flow is locally turbulent. This bound is reasonable because flight environments contain many perturbation sources— any one of which could individually cause transition. The bound is conservative because, when used

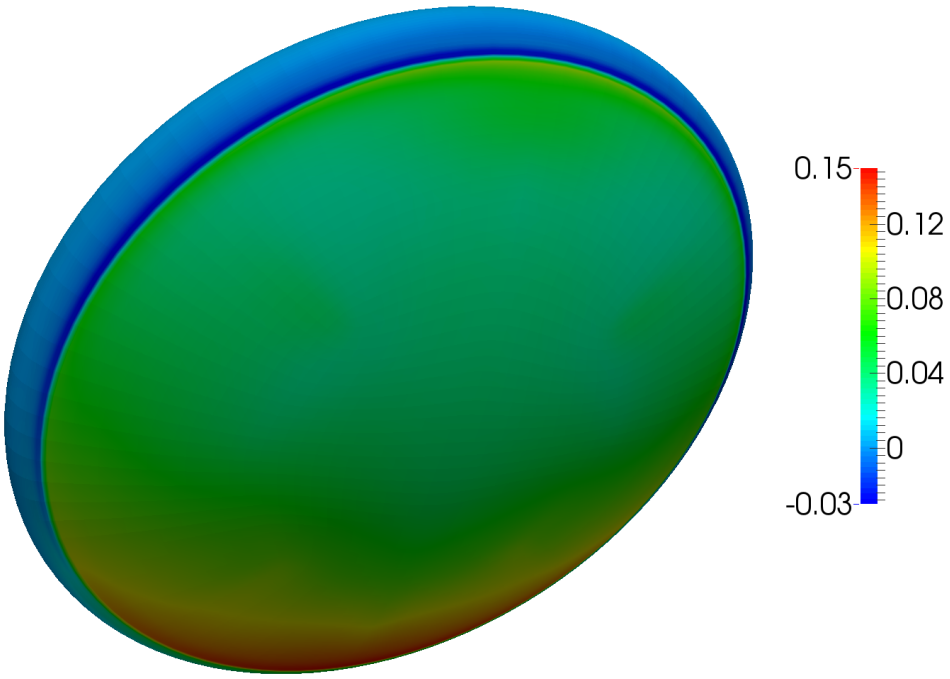

Figure 2.4: Normalized ablator recession rate difference between fully laminar and fully turbulent simulations, $(\dot{m}_{\text{turbulent}} - \dot{m}_{\text{laminar}}) / \max(\dot{m}_{\text{turbulent}})$, for Orion MPCV at peak heating conditions from International Space Station return trajectory. Data, which includes aerothermochemistry and ablation, courtesy of P. T. Bauman.

for prediction, turbulent heating is applied as far upstream as turbulence-enhanced momentum and energy transport to the heat shield can occur.

Rather than asking where small disturbances induce turbulence, as transition modeling does, the proposed bound determines where exceedingly large disturbances are damped, as relaminarization studies do [9, 11, 68, 69, 105–107, 139, 159]. Unfortunately, in their 2008 review of a wealth of experimental relaminarization data, Cal and Castillo [22] concluded, as had Sreenivasan [152] before them, that while nondimensional parameters [e.g. 86] could estimate when a flow might revert from

turbulent to a “quasi-laminar” state, such parameters were not predictive. Given the pragmatic value of finding a predictive bound, it is worthwhile to investigate analytic results regarding the stability of compressible fluids to large disturbances with the possibility that these might help rigorously characterize turbulence-sustaining behavior.

2.7 The Stability of Compressible Flows to Arbitrary Disturbances

The onset of turbulence in a transitional flow is triggered by the nonlinear growth of small disturbances in the flow field. The short-time analysis of the rate of growth of such disturbances is the realm of hydrodynamic linear stability theory. In incompressible viscous flows, this process is governed by the Orr–Sommerfeld equation. Linear stability theory extends to compressible, viscous fluids in unbounded domains [98] and can be used as a transition-prediction mechanism [127]. However, this theory is not useful for studying relaminarization because the discrepancies between a fully turbulent flow and a steady laminar flow are in no sense small.

As turbulence can be a self-sustaining process, it is reasonable to assume turbulent discrepancies from a laminar base flow are somehow pathologically large. Serrin [142] proved sufficient conditions for the nonlinear stability of an incompressible viscous fluid in a bounded region to arbitrarily large disturbances using the energy method. Suppose one has a base incompressible velocity field v obeying

$$\frac{\partial v}{\partial t} + \nabla \cdot v \otimes v = -\frac{1}{\rho}\nabla p + \nu \Delta v + f \qquad p, v \in \Omega, \tag{2.7a}$$

$$v = v_0 \qquad v \in \partial\Omega \tag{2.7b}$$

for some prescribed boundary value v_0 where both density ρ and kinematic viscosity ν are constant. The pressure p, obtainable from $\Delta p = -\rho \operatorname{tr}\left(\nabla v \nabla v^{\mathsf{T}}\right)$, instantaneously maintains v as solenoidal. Given another admissible v' one may form the perturbation $u = v' - v$ which evolves locally according to

$$\frac{\partial u}{\partial t} = \frac{\partial v'}{\partial t} - \frac{\partial v}{\partial t} \qquad u \in \Omega, \tag{2.8a}$$

$$u = 0 \qquad u \in \partial\Omega. \tag{2.8b}$$

Taking the scalar product of u with $\partial u/\partial t$, employing smoothness, using incompressibility, and simplifying yields the pointwise evolution of the perturbation energy $E = u^2/2$,

$$\frac{\partial E}{\partial t} = (u \cdot D \cdot u - \nu \nabla u : \nabla u) + \nabla \cdot \left(\frac{p - p'}{\rho} u + \nu \nabla E - E v' \right). \tag{2.9}$$

Here, $D = \frac{1}{2}\left(\nabla v + \nabla v^{\mathsf{T}}\right)$ represents the rate of strain tensor for the base flow. By the Reynolds transport theorem, the global perturbation energy may be written

$$\frac{\mathrm{d}}{\mathrm{d}t} \int_\Omega E = \int_\Omega \frac{\partial E}{\partial t} + \int_{\partial\Omega} E v \cdot \hat{n}. \tag{2.10}$$

Using the divergence theorem and that $u = 0 \implies E = 0$ on $\partial\Omega$, gives the Reynolds–Orr energy equation,

$$\frac{\mathrm{d}}{\mathrm{d}t} \int_\Omega E = \int_\Omega (u \cdot D \cdot u - \nu \nabla u : \nabla u). \tag{2.11}$$

Nondimensionalizing,

$$\frac{\mathrm{d}}{\mathrm{d}t} \int_\Omega E = \int_\Omega \left(u \cdot D \cdot u - \mathrm{Re}^{-1} \nabla u : \nabla u\right) \tag{2.12}$$

where $\mathrm{Re} = v_0 l_0 / \nu_0$ is the Reynolds number. The viscous term always promotes stability but its success in doing so depends on the relative magnitude of the interaction between the perturbations and the base flow rate of strain.

Serrin [142] observed that the base flow v is stable under arbitrary disturbances as $t \to \infty$ whenever the right hand side of (2.12) is strictly negative for arbitrary, nonvanishing vectors u. Notice any relevant hysteresis has been implicitly addressed. Using analytical estimates relying on the boundedness of Ω, Serrin characterized critical Reynolds numbers below which various bounded geometries with steady base flows must be stable to arbitrary disturbances. Joseph [71, 72] extended these results to incompressible flows with heat transfer while Dudis and Davis [34, 35] analyzed boundary layers achieving weaker results due to the unbounded nature of that particular domain. Davis and Kerczek [30] demonstrated those weaker results could be made equivalently strong provided

$$\lambda(t; D(t), \mathrm{Re}) = \max \frac{\int_\Omega \left(u \cdot D \cdot u - \mathrm{Re}^{-1} \nabla u : \nabla u \right)}{\int_\Omega E} \tag{2.13}$$

is well-defined. The maximum is taken over the space of sufficiently smooth, divergence-free vector functions satisfying the homogeneous boundary conditions and behaving appropriately in directions in which the domain is unbounded. In particular, the space must permit progressing from (2.9) to (2.12). Davis and Kerczek reformulated the maximization problem (2.13) using the equivalent Euler–Lagrange equations to numerically obtain critical Reynolds numbers below which oscillatory Stokes layers must be asymptotically stable. Estimates for exterior domains not relying on numerical solutions can be found in Galdi and Rionero [51], Maremonti [101].

In problems where thermodynamic properties vary, the identity analogous to (2.12) additionally must incorporate property perturbation energies. For example, Joseph chose $E = u^2 + \mathrm{Pr}\, T^2$ when studying buoyancy problems characterized by a

Prandtl number Pr in which temperature perturbations T were present. The predictive quality of the resulting estimates depends strongly on such choices and good selections are by no means obvious [52]. Galdi and Padula [53] set forth an abstract framework providing guidance on energy identity selection techniques producing promising estimates.

Working within this framework, Padula [116] cataloged extensive stability proofs for barotropic and polytropic compressible viscous fluids.[5] The latter class is therein proved asymptotically stable when bounded by rigid boundaries provided the initial temperature gradient is sufficiently small [116, theorem 2.4.20]. Padula conjectured that this proof may be extended to the boundary layer [116, page 207] similarly to how she obtained boundary layer results for isothermal fluids [116, §§2.4.1–2, §4].

Any such proof of the asymptotic stability of a compressible viscous boundary layer to arbitrary disturbances, whether or not it is extended from the work of Padula, must simultaneously address several issues. First, the space chosen must permit exact pointwise perturbation evolution equations like (2.9) to be converted to global statements like (2.12) despite the unbounded nature of the domain. Second, these global evolution statements for perturbation energies ρ^2, u^2, T^2, etc. must be combined into a single, appropriately weighted identity. Third, the evolution of that single identity must either be bounded using a host of analytical estimates or a maximization problem resembling (2.13) must be solved numerically. Finally, for the proof to be practically useful to those studying relaminarization, the provably stable region within

[5] An exemplary, earlier appearance of the barotropic results [115] is recommended as an introduction.

the parameter space consisting of Re, Pr, etc. must be reasonably sharp relative to the "true bounds" one could hypothetically observe in engineered systems like the Orion MPCV. Though no currently known asymptotic stability estimate applies to the present work, energy method concepts and, in particular, interpreting turbulence as a large, self-sustaining perturbation will be important to the discussion in Chapter 7.

2.8 Bounding Turbulence-Sustaining Regions via Homogenized Simulation

Absent practical, analytical methods for characterizing turbulence-sustaining regions at the experimentally inaccessible flight conditions of interest, simulation is a logical tool to exploit. Studying the relaminarization of spatially evolving boundary layers is subject to the issues raised in Section 2.4. However, the spatiotemporal homogenization approach by Topalian et al. [165], mentioned in Section 2.5, does permit numerically investigating this class of flows while avoiding reproducibility problems and excessive computational cost. The present work pursues this approach.

A homogenized relaminarization study takes as its input the steady flow field experienced by the vehicle's thermal protection system during peak heating from some reentry trajectory. This "full system" of interest should be computed with the maximum possible fidelity [77, 108, 177] in all respects save for assuming fully laminar conditions. Fully turbulent, homogenized flow fields are prepared at local conditions taken from those laminar full system computations. The local conditions are said to be unable to sustain turbulence if the field relaminarizes. The parameter space of local conditions is searched by traversing the two-dimensional surface of the full system simulation.

Starting from just upstream of the heat shield's edge, the relaminarization tests are repeated at local conditions taken closer and closer to the stagnation point until the edge of the turbulence-sustaining region is detected.

By using laminar full system conditions as "upstream" input, the present study aims to answer where on a mixed laminar-turbulent heat shield the local flow conditions can sustain turbulence. That is, this approach enjoys independence from the uncertainties associated with turbulence modeling. A different question is, can the entire thermal protection system surface be turbulent? That question could be addressed partially by taking as input the local conditions from assumed-turbulent computations of the full thermal protection system. However, such work would carry appreciably greater uncertainty because the required full system simulations would employ turbulence models.

Two issues merit immediate attention. First, the purely temporal forcing terms from (2.6) and their spatiotemporal brethren to be relayed in Section 3.3 are formally ill-defined in the laminar limit because both $\sqrt{\widetilde{u_k'' u_k''}}$ and $\sqrt{\widetilde{E'' E''}}$ must eventually vanish there. However, when subject to relaminarizing conditions, turbulent flows tend towards a "quasi-laminar" state [152] in which nontrivial streamwise fluctuations persist though turbulent production becomes nearly zero [22]. Second, the extent to which relaminarization processes in a homogenized boundary layer reflect those in a spatially evolving boundary layer is admittedly unknown. That said, for predicting the initial onset of relaminarization, the homogenized treatment is likely more conservative than the spatially evolving flow because disturbances cannot exit a homogenized simulation's periodic domain.

The concrete scenario investigated for its turbulence-sustaining region is taken from Orion MPCV thermal protection system simulations discussed in the following section. To keep the calculations tractable, in the current work aerothermochemistry is neglected and the ablative conditions are emulated by wall transpiration. Convex surface curvature, which has a stabilizing impact [13], is also neglected as it cannot be accommodated by the spatiotemporal homogenization. The parameter space of local conditions, to be detailed in Section 2.9, consists of the Reynolds number based on momentum thickness, the Mach number, the pressure gradient strength, the wall transpiration rate, and the coldness of the wall relative to the boundary layer edge.

2.9 Peak Heating Conditions on the Orion Multi-Purpose Crew Vehicle

The NASA Orion[6] Multi-Purpose Crew Vehicle (MPCV) concept was recommended by NASA's Exploration Systems Architecture Study in 2005 under the earlier Crew Exploration Vehicle (CEV) moniker [1, §5]. Configurations of this vehicle are intended to transport a crew of four-to-six during International Space Station, Lunar, and Mars mission scenarios. Its roughly 5-meter-diameter, Avcoat-based, ablative heat shield uses sacrificial epoxy novolac resin in a fiberglass honeycomb matrix to withstand temperatures of roughly 3,600 K [73] while limiting the thermal exposure of the protected components to only 450 K [1, §5.3.1.3.7]. Figure 2.5 provides a sense of scale for this heat shield while Figure 2.6 depicts one possible orientation relative to oncoming flow. An unmanned, heavily instrumented reentry as part of NASA's Exploration Flight Test-1 is currently planned to occur during December 2014 [118].

[6] `http://www.nasa.gov/orion/`

Figure 2.5: Scale comparison for the Orion MPCV TPS. Image courtesy of NASA.

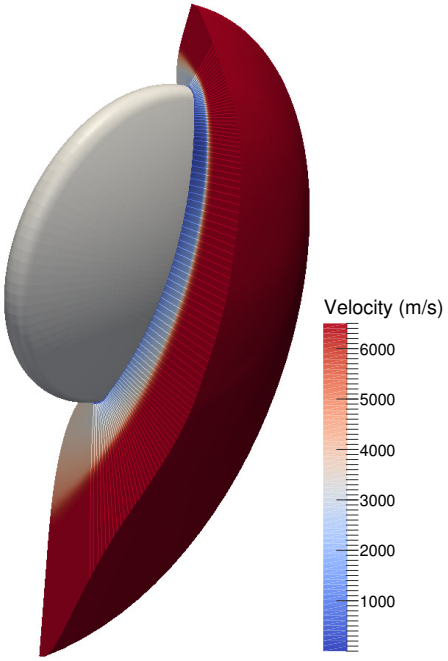

Figure 2.6: The velocity magnitude on the symmetry plane for a fully laminar Orion MPCV TPS simulation performed by P. T. Bauman.

Bauman et al. [8] performed coupled multiphysics simulations of the Orion MPCV geometry undergoing peak heating during return from the International Space Station at a 19° angle of attack. A fully turbulent assumption, implemented through use of the Baldwin–Lomax model, was applied over the entire thermal protection system (TPS) surface. Local turbulent boundary layer conditions, taken from the colored symmetry plane in Figure 2.6, appear in Table 2.2. This boundary layer data has several peculiar features. The wall is quite cold compared with the freestream ($T_e/T_w \approx 3.5$) causing large thermodynamic state ($\rho_e/\rho_w \approx 0.23$) and property changes ($\mu_e/\mu_w \approx 2.8$) across the layer. The shape factor ($\delta^*/\theta \approx 0.85$) has a small value only possible in flows with significant density variations. The magnitude of the negative-valued Clauser parameter β [26] indicates that a very strong favorable pressure gradient is present as magnitudes like 0.1 are considered strong [96, 148]. The momentum Reynolds numbers Re_θ are modest with the flow accelerating from the subsonic into the supersonic regime. The present work cannot precisely match these flow characteristics because aerothermochemistry is neglected. Holding the edge Mach number constant, Table 2.3 maps the data onto an ideal air equation of state as is appropriate for the governing equations to be presented in Section 3.1.

Bauman additionally performed fully laminar simulations of the same scenario using the FIN-S hypersonic flow solver [77]. Post-processing along the symmetry plane from Figure 2.6 produced the reduced data depicted in Figure 2.7. The horizontal axis measures the distance leeward from the stagnation point taken along the MPCV's curved heat shield. The local surface curvature is seen to be small and constant across a large portion of this symmetry plane. The stagnation condition, located at the abscissa

Table 2.2: Reacting boundary layer conditions at five representative locations within fully turbulent Orion MPCV TPS simulations by Bauman et al. [8]. Dimensional quantities use MKS units. Data reduction by O. Sahni and V. Topalian.

Location label	1	2	3	4	5
δ	6.95e-02	7.60e-02	8.71e-02	8.93e-02	9.19e-02
δ^*	7.70e-03	8.37e-03	1.02e-02	1.02e-02	1.04e-02
θ	9.49e-03	1.03e-02	1.16e-02	1.18e-02	1.20e-02
T_w	1665	1656	1646	1636	1634
T_e	5851	5772	5701	5647	5604
ρ_w	0.0148	0.0133	0.0123	0.0115	0.0109
ρ_e	0.0033	0.0031	0.0029	0.0027	0.0026
p_e	8507	7664	7066	6621	6317
$\left\vert\frac{dp}{d\xi}\right\vert_e$	2059	2089	2112	2171	2345
μ_w	5.83e-05	5.81e-05	5.79e-05	5.77e-05	5.76e-05
μ_e	1.64e-04	1.62e-04	1.60e-04	1.59e-04	1.58e-04
a_e	1987	1967	1949	1937	1928
τ_w	26.72	29.38	31.13	32.26	34.89
Ma_e	0.88	0.99	1.09	1.15	1.19
$\mathrm{Re}_\theta = \frac{\rho_e u_e \theta}{\mu_e}$	338	380	441	449	455
$\beta = \frac{\delta^*}{\tau_w}\left(\frac{\partial p}{\partial \xi}\right)_e$	-0.59	-0.60	-0.69	-0.68	-0.70

Table 2.3: Translation of selected data, holding Ma_e constant, from Table 2.2 to $\gamma = 1.4$ ideal air obeying Sutherland viscosity law. Reduction by O. Sahni and V. Topalian.

Location label	1	2	3	4	5
Ma_e	0.88	0.99	1.09	1.15	1.19
$\mathrm{Re}_\theta = \frac{\rho_e u_e \theta}{\mu_e}$	391	440	511	520	526
$\beta = \frac{\delta^*}{\tau_w}\left(\frac{\partial p}{\partial \xi}\right)_e$	-0.81	-0.81	-0.93	-0.92	-0.94

origin, is evident in the behavior of the momentum Reynolds number, Re_θ, and the edge Mach number, Ma_e. When measured by the outgassing velocity normalized by viscous units, v_w^+, the ablator becomes more active as one approaches the stagnation point. Strong thermodynamic property variations occur because the ablator maintains a cold surface relative to the freestream and because of active aerothermochemistry. The former effect appears in the ratio of the edge-to-wall temperature, T_e/T_w, and is the predominant driver between the edge-to-wall viscosity ratio, μ_e/μ_w, causing the difference between the two Re_θ curves. The lower curve, momentum Reynolds number based on edge viscosity, is what has been discussed thus far and what the current work predominantly uses. Notice that absent cold wall effects these Re_θ are well into the range where relaminarization is expected [150, §3.2]. Temperature differences in conjunction with chemical reactions cause wall-to-edge differences in the ratio of specific heats, γ, and in the Prandtl number, Pr.

The strength of the favorable pressure gradient from this fully laminar data has been quantified using a variety of parameters in Figure 2.8. The nondimensional quantities are the Clauser parameter β [26], Launder's acceleration parameter K [86], the Pohlhausen parameter K_s [122], similarity parameter Λ [22], parameter Λ_n [107], and a new invention $p^*_{e,\xi}$. The figure caption shows their definitions with ξ denoting the streamwise direction and e and w being edge and wall values, respectively. Here, δ^* is the displacement thickness, τ_w the wall shear stress, δ the boundary layer thickness, and ν the kinematic viscosity. Though physical truth would produce smooth curves in Figure 2.8, numerical artifacts are apparent despite care during the data reduction process. They arise because the grid refinement strategies used to produce the source

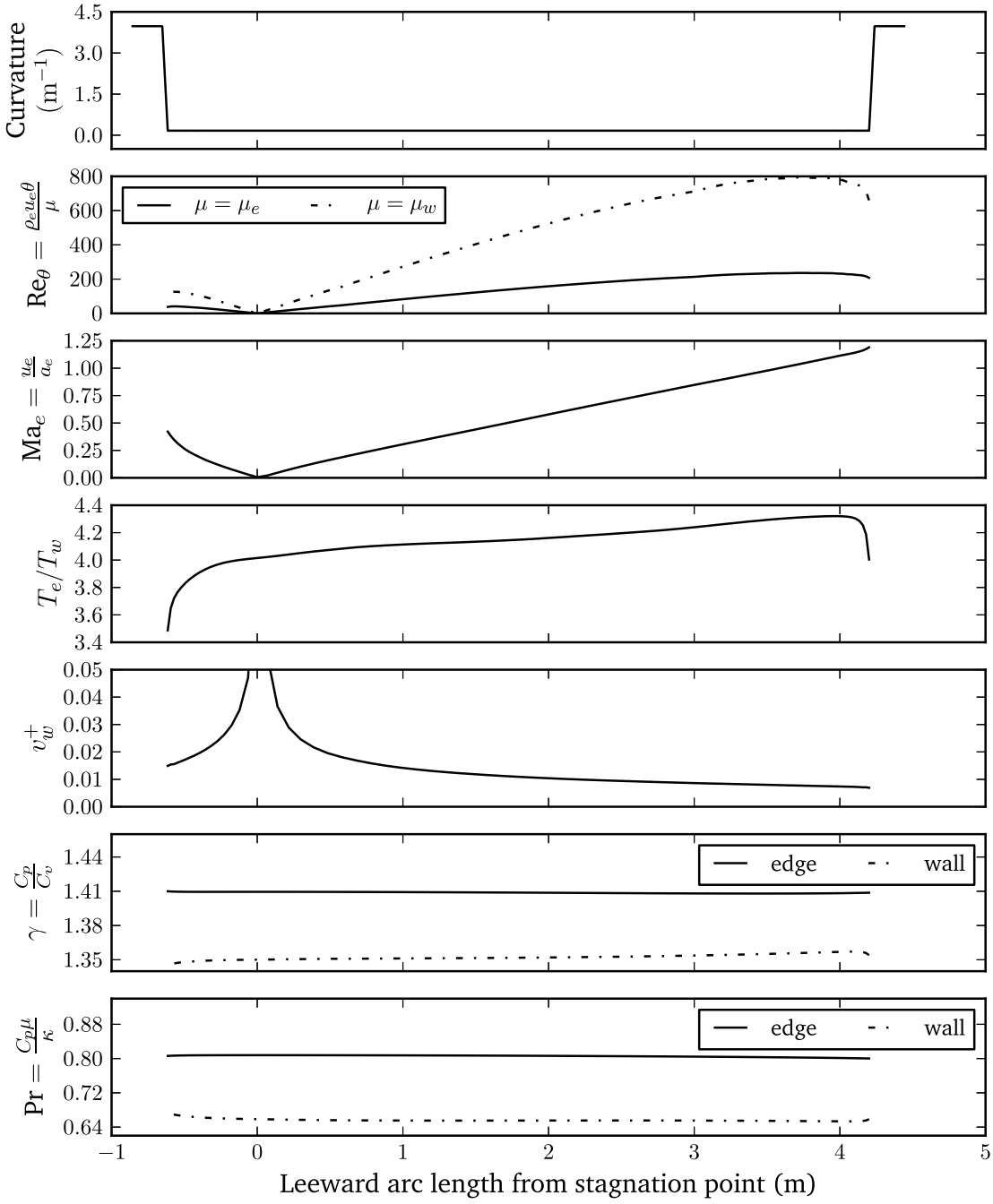

Figure 2.7: Reacting boundary layer conditions from the symmetry plane on a fully laminar Orion MPCV TPS simulation performed by P. T. Bauman.

data did not target these parameters. All quantities shown become problematic near the stagnation point. The curves for K_s and Λ are particularly noisy due to their dependence on functions of δ.

Choosing one pressure gradient parameter to match for a turbulence-sustaining study based on this Orion MPCV data is not entirely straightforward. Clearly K_s and Λ are not suitable based on their numerical issues. K shows no errant behavior but its definition uses the streamwise velocity derivative making it more of an acceleration parameter than a pressure gradient parameter. Quantities β and Λ_n depend on τ_w which cannot be matched *a priori* due to its dependence on turbulent behavior. Clauser's β is also problematic because δ^* behaves atypically in the flows of interest, as will be shown in Chapter 6.

These concerns motivated defining the new parameter

$$p^*_{e,\xi} = \frac{\delta}{\rho_e u_e^2}\frac{\partial p_e}{\partial \xi}. \tag{2.14}$$

It nondimensionalizes the pressure gradient magnitude using freestream kinetic energy, like K, but scaled using the boundary layer thickness δ to avoid difficulties associated with τ_w and δ^*. Figure 2.8 shows that this new parameter qualitatively captures the same trends as β, K, and Λ_n while being more robust numerically. Moreover, in Topalian et al.'s class of homogenization models the growth rate $\mathrm{gr}_{t_0}(\Delta)$ can be used to control δ independently of Re_θ. Hence, given some target thickness, one can design an inviscid base flow, as is done in Appendix C, in order to have a homogenized direct numerical simulation easily match $p^*_{e,\xi}$ *a priori*. Consequently, the present work uses parameter (2.14) for scenario-matching purposes and compares it against other measures of pressure gradient strength in Chapter 6.

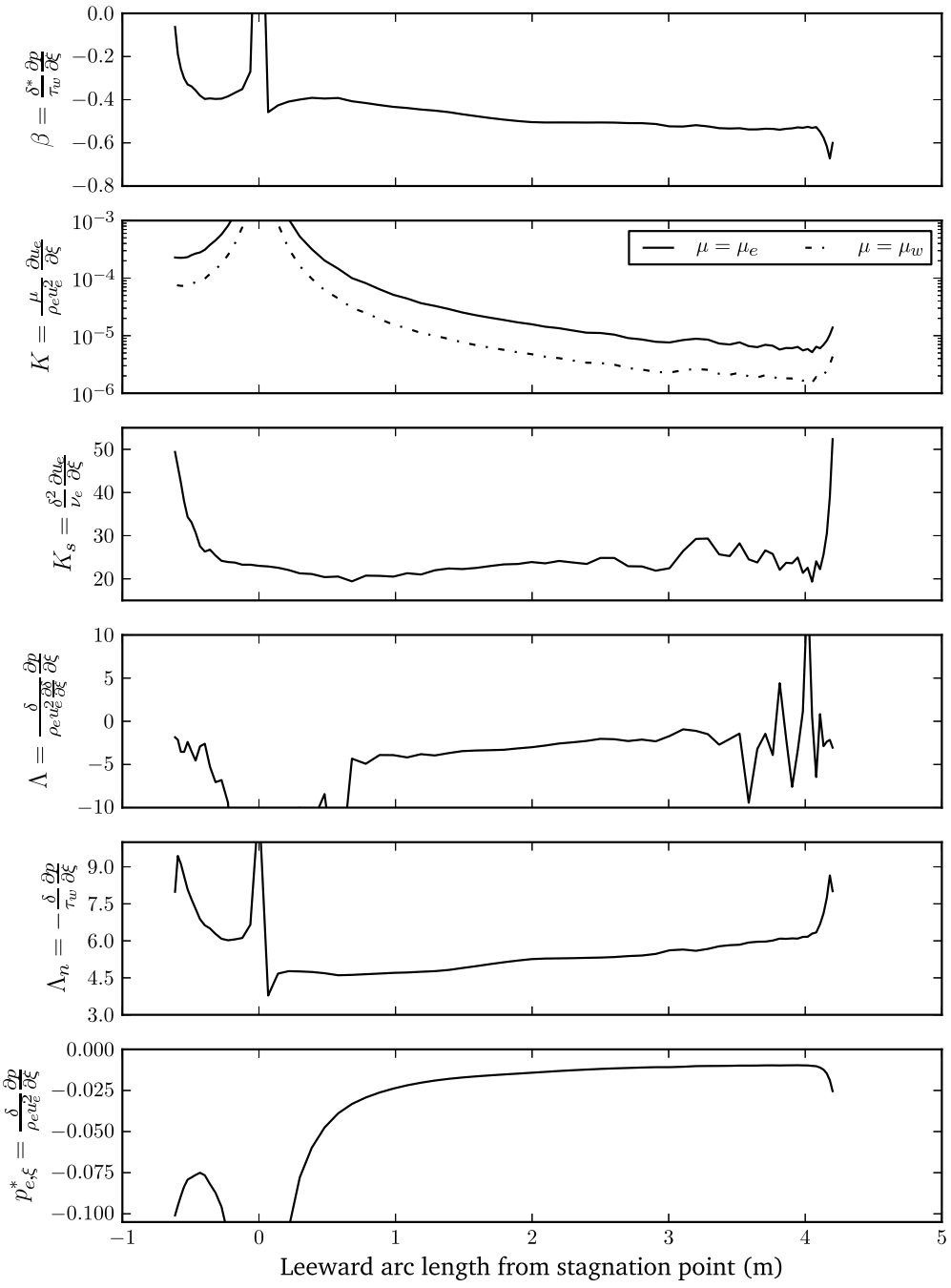

Figure 2.8: Pressure gradient conditions from the symmetry plane on a fully laminar Orion MPCV TPS simulation performed by P. T. Bauman.

Chapter 3

Mathematical Models

This chapter summarizes the nondimensional mathematical models used in the present work. First the governing Navier–Stokes are shown. Reynolds and Favre averaging is briefly defined followed by the form of the Favre-averaged Navier–Stokes equations used. Lastly, the spatiotemporal homogenization forcing terms due to [165] are presented. One can find the underlying derivations in Appendix A.

3.1 The Governing Navier–Stokes Equations

The flow physics are modeled using the unsteady, three-dimensional, compressible Navier–Stokes equations. These continuum equations arise from applying conservation of mass, momentum, and energy to a Newtonian, perfect gas. The model assumes that the first viscosity μ obeys a power law in temperature T, the other viscosity λ is a constant multiple of μ, heat conduction through the gas obeys Fourier's law, and momentum and thermal diffusivity are related by a constant Prandtl number. For simplicity, aerothermochemical effects are neglected.

The governing equations may be written in nondimensional form as

$$\frac{\partial}{\partial t}\rho = -\nabla\cdot\rho u + \mathscr{S}_\rho \tag{3.1a}$$

$$\frac{\partial}{\partial t}\rho u = -\nabla\cdot(u\otimes\rho u) - \frac{1}{\mathrm{Ma}^2}\nabla p + \frac{1}{\mathrm{Re}}\nabla\cdot\tau + f + \mathscr{S}_{\rho u} \tag{3.1b}$$

$$\begin{aligned}\frac{\partial}{\partial t}\rho E = &-\nabla\cdot\rho E u + \frac{1}{\mathrm{Re}\,\mathrm{Pr}\,(\gamma-1)}\nabla\cdot\mu\nabla T \\ &-\nabla\cdot pu + \frac{\mathrm{Ma}^2}{\mathrm{Re}}\nabla\cdot\tau u + \mathrm{Ma}^2 f\cdot u + q_b + \mathscr{S}_{\rho E}\end{aligned} \tag{3.1c}$$

along with the constitutive relationships

$$p = (\gamma-1)\left(\rho E - \frac{\mathrm{Ma}^2}{2}\rho u^2\right) \qquad T = \gamma\frac{p}{\rho} \qquad a = \sqrt{T} \qquad h = \frac{T}{\gamma-1} \tag{3.1d}$$

$$\mu = T^\beta \qquad \lambda = \left(\alpha - \frac{2}{3}\right)\mu \qquad \tau = \mu\left(\nabla u + \nabla u^{\mathsf{T}}\right) + \lambda\,(\nabla\cdot u)\,I \tag{3.1e}$$

where the nondimensional free parameters

$$\mathrm{Re} = \frac{\rho_0 u_0 l_0}{\mu_0} \qquad \mathrm{Ma} = \frac{u_0}{a_0} \qquad \mathrm{Pr} = \frac{\mu_0 C_p}{\kappa_0} \tag{3.1f}$$

are the Reynolds, Mach, and Prandtl numbers, respectively. Other free parameters include the ratio of specific heats γ and the viscosity power law exponent β. The von Kármán relationship for the Knudsen number becomes

$$\mathrm{Kn} = \frac{\mathrm{Ma}}{\mathrm{Re}}\sqrt{\frac{\gamma\pi}{2}} \tag{3.2}$$

where the present continuum assumptions are justified when $\mathrm{Kn} \ll 1$. The nondimensionalization requires some dimensional reference density ρ_0, length l_0, velocity u_0, and temperature T_0. Other references quantities are defined as follows:

$$t_0 = \frac{l_0}{u_0} \qquad a_0 = \sqrt{\gamma R T_0} \qquad p_0 = \rho_0 a_0^2 \qquad E_0, H_0, h_0 = a_0^2 \tag{3.3a}$$

$$\mu_0, \lambda_0 = \mu(T_0) \qquad \tau_0 = \frac{\mu_0 u_0}{l_0} \qquad f_0 = \frac{\rho_0 u_0}{t_0} \qquad q_0 = \frac{\rho_0 a_0^2}{t_0} \tag{3.3b}$$

$$\mathscr{S}_{\rho_0} = \frac{\rho_0}{t_0} \qquad \mathscr{S}_{\rho u_0} = \frac{\rho_0 u_0}{t_0} \qquad \mathscr{S}_{\rho E_0} = \frac{\rho_0 E_0}{t_0}. \tag{3.3c}$$

The terms f and q_b accommodate problem-specific momentum and total energy forcing. When employed, boundary layer homogenization is accomplished through slow growth terms $\mathscr{S}_\rho$, $\mathscr{S}_{\rho u}$, and $\mathscr{S}_{\rho E}$ which take forms similar to the right hand side of (2.5).

The bulk viscosity,

$$\mu_B = \lambda + \frac{2}{3}\mu, \tag{3.4}$$

and the deviatoric component of the strain rate tensor,

$$S = \varepsilon - \frac{1}{3}\operatorname{tr}(\varepsilon) I = \frac{1}{2}\left(\nabla u + \nabla u^{\mathsf{T}}\right) - \frac{1}{3}(\nabla \cdot u) I, \tag{3.5}$$

alternatively may be used to write τ as

$$\tau = 2\mu S + \mu_B (\nabla \cdot u) I. \tag{3.6}$$

The final free parameter α then controls the bulk viscosity according to

$$\mu_B = \alpha\mu. \tag{3.7}$$

Setting $\alpha = 0$ recovers Stokes' hypothesis. The kinematic and bulk kinematic viscosities

$$\nu = \frac{\mu}{\rho} \qquad \nu_B = \frac{\mu_B}{\rho} \tag{3.8}$$

will be used at times to simplify notation. This completes the description of the model which is said to be "closed" because knowing ρ, u, and E permits advancing that state in time.

3.2 The Favre-Averaged Navier–Stokes Equations

As turbulence is chaotic, reporting a statistical description of its behavior is essential. With only additional modest mathematical assumptions, the above instantaneous model may be manipulated to describe the evolution of mean quantities. Notationally, the expectation or "Reynolds average" of a generic flow variable q is written $\bar{q}$. The density-weighted expectation or "Favre average" is defined by

$$\tilde{q} = \overline{\rho q}/\bar{\rho}. \tag{3.9}$$

Fluctuations about the mean and the density-weighted mean are denoted

$$q' \equiv q - \bar{q}, \qquad\qquad q'' \equiv q - \tilde{q}, \tag{3.10}$$

respectively. Reynolds averaging commutes with differentiation under mild smoothness assumptions. Here the common convention that taking Favre fluctuations, $(\cdot)''$, has higher precedence than differentiation, $\nabla(\cdot)$, has been adopted. Additional background on these two averaging approaches can be found in Section A.2.1.

Assuming that all required expectations are finite and that Reynolds averaging commutes with differentiation whenever necessary, the model of Section 3.1 gives rise

to the unsteady Favre-averaged Navier–Stokes (FANS) equations:

$$\frac{\partial}{\partial t}\bar{\rho} = -\nabla\cdot\bar{\rho}\tilde{u} + \overline{\mathscr{S}_\rho} \tag{3.11a}$$

$$\frac{\partial}{\partial t}\bar{\rho}\tilde{u} = -\nabla\cdot(\tilde{u}\otimes\bar{\rho}\tilde{u}) - \frac{1}{\mathrm{Ma}^2}\nabla\bar{p} + \nabla\cdot\left(\frac{\bar{\tau}}{\mathrm{Re}} - \bar{\rho}\widetilde{u''\otimes u''}\right) + \bar{f} + \overline{\mathscr{S}_{\rho u}} \tag{3.11b}$$

$$\begin{aligned}\frac{\partial}{\partial t}\bar{\rho}\tilde{E} = &-\nabla\cdot\bar{\rho}\tilde{H}\tilde{u} + \mathrm{Ma}^2\nabla\cdot\left(\left(\frac{\bar{\tau}}{\mathrm{Re}} - \bar{\rho}\widetilde{u''\otimes u''}\right)\tilde{u} - \frac{1}{2}\bar{\rho}\widetilde{u''^2u''} + \frac{\overline{\tau u''}}{\mathrm{Re}}\right)\\ &+ \frac{1}{\gamma-1}\nabla\cdot\left(\frac{\bar{\mu}\widetilde{\nabla T} + \bar{\rho}\,\widetilde{\nu''(\nabla T)''}}{\mathrm{RePr}} - \bar{\rho}\widetilde{T''u''}\right)\\ &+ \mathrm{Ma}^2\left(\bar{f}\cdot\tilde{u} + \overline{f\cdot u''}\right) + \bar{q}_b + \overline{\mathscr{S}_{\rho E}}\end{aligned} \tag{3.11c}$$

$$\begin{aligned}\frac{\partial}{\partial t}\bar{\rho}k = &-\nabla\cdot\bar{\rho}k\tilde{u} - \bar{\rho}\widetilde{u''\otimes u''} : \nabla\tilde{u} - \frac{\bar{\rho}\epsilon}{\mathrm{Re}} + \nabla\cdot\left(-\frac{1}{2}\bar{\rho}\widetilde{u''^2u''} + \frac{\overline{\tau u''}}{\mathrm{Re}}\right)\\ &+ \frac{1}{\mathrm{Ma}^2}\left(\bar{p}\nabla\cdot\overline{u''} + \overline{p'\nabla\cdot u''} - \frac{1}{\gamma}\nabla\cdot\bar{\rho}\widetilde{T''u''}\right) + \overline{f\cdot u''} + \overline{\mathscr{S}_{\rho u}\cdot u''}.\end{aligned} \tag{3.11d}$$

The equations are augmented by the following nondimensional relationships:

$$\bar{p} = \frac{\bar{\rho}\tilde{T}}{\gamma} \qquad \bar{\rho}\,\widetilde{\nu} = \bar{\mu} = \overline{T^\beta} \qquad k = \frac{1}{2}\widetilde{u''^2} \qquad \bar{\rho}\epsilon = \overline{\tau : \nabla u''} \tag{3.11e}$$

$$\tilde{E} = \frac{\tilde{T}}{\gamma(\gamma-1)} + \mathrm{Ma}^2\left(\frac{1}{2}\tilde{u}^2 + k\right) \qquad \tilde{H} = \tilde{E} + \frac{\tilde{T}}{\gamma} \qquad \tilde{h} = \frac{\tilde{T}}{\gamma-1} \tag{3.11f}$$

$$\tilde{S} = \frac{1}{2}\left(\widetilde{\nabla u} + \widetilde{\nabla u}^{\mathsf{T}}\right) - \frac{1}{3}\left(\widetilde{\nabla\cdot u}\right)I \tag{3.11g}$$

$$\bar{\tau} = 2\bar{\mu}\tilde{S} + 2\bar{\rho}\,\widetilde{\nu''S''} + \alpha\bar{\mu}\widetilde{\nabla\cdot u}I + \alpha\bar{\rho}\,\widetilde{\nu''(\nabla\cdot u)''}I. \tag{3.11h}$$

Beyond references (3.3), this nondimensionalization additionally selects:

$$k_0 = u_0^2 \qquad\qquad \epsilon_0 = \frac{u_0^2}{t_0}. \tag{3.12}$$

Several correlations affect the evolution of mean quantities: the Reynolds stress, $-\bar{\rho}\widetilde{u''\otimes u''}$; the Reynolds heat flux, $\bar{\rho}\widetilde{h''u''} = \bar{\rho}\widetilde{T''u''}/(\gamma-1)$; turbulent production, $-\bar{\rho}\widetilde{u''\otimes u''} : \nabla\tilde{u}$; turbulent dissipation, $\bar{\rho}\epsilon/\mathrm{Re}$; turbulent transport, $-\frac{1}{2}\bar{\rho}\widetilde{u''^2u''}$; turbulent work, $\overline{\tau u''}/\mathrm{Re}$; and the two forcing-velocity correlations, $\overline{f\cdot u''}$ and $\overline{\mathscr{S}_{\rho u}\cdot u''}$. The Reynolds stress and heat flux augment the viscous stress and heat flux, respectively. The production term generates the turbulent kinetic energy density k from the interaction of fluctuations with mean gradients while the dissipation term destroys k. The turbulent transport and work terms represent transport of the k and viscous stress work due to turbulent velocity fluctuations, respectively. The commonly encountered pressure–velocity correlation, $\overline{p'u''}$, does not appear in the k equation because an exact ideal gas relationship for the turbulent mass flux discussed by Lele [91, p. 216],

$$\overline{u''} = \frac{\widetilde{T''u''}}{\tilde{T}} - \frac{\overline{p'u''}}{\bar{p}}, \tag{3.13}$$

has been used to eliminate it.

The FANS equations may be expressed equivalently using only Reynolds averaging and therefore are often called the compressible Reynolds-averaged Navier–Stokes (RANS) equations. Notice that no new constitutive assumptions have been employed to produce this FANS formulation— caveat integrability and smoothness requirements they are as exact a description of flow physics as the governing Navier–Stokes equations. Several common simplifications, none of which has been made above, along with the correlations they implicitly neglect are documented in Appendix A.2.2.

The FANS equations are "unclosed" because knowing $\bar{\rho}$, $\tilde{u}$, $\tilde{E}$, and k does not

permit advancing that state in time. Advancing a solution requires:

$$\bar{\rho} \qquad \tilde{u} \qquad \tilde{E} \qquad \bar{\mu} \qquad \bar{f} \qquad \bar{q}_b \qquad k \qquad \epsilon \qquad \overline{u''} \qquad \operatorname{sym}\left(\widetilde{\nabla u}\right)$$

$$\overline{f \cdot u''} \qquad \overline{\tau u''} \qquad \overline{p' \nabla \cdot u''} \qquad -\widetilde{u'' \otimes u''} \qquad -\frac{1}{2}\widetilde{u''^2 u''}$$

$$\widetilde{T'' u''} \qquad \widetilde{\nu'' S''} \qquad \widetilde{\nu'' (\nabla \cdot u)''} \qquad \widetilde{\nu'' (\nabla T)''}$$

$$\overline{\mathscr{S}_\rho} \qquad \overline{\mathscr{S}_{\rho u}} \qquad \overline{\mathscr{S}_{\rho E}} \qquad \overline{\mathscr{S}_{\rho u} \cdot u''}.$$

In many circumstances, the mean state is known *a priori* to be independent of time and of a lower spatial dimensionality than the instantaneous state.

Experimentally obtained estimates of the reduced set of these quantities required to "close" a particular problem are referred to as "statistics" in the turbulence community. For example, channel flows are characterized by statistics varying only in the wall-normal direction. Spatially evolving boundary layers possess statistics that vary in both the streamwise and wall-normal direction. Homogenization, as summarized in the following section, trades the boundary layer's streamwise statistical evolution for a dependence on a collection of auxiliary closure assumptions and modeling parameters.

3.3 Spatiotemporal Homogenization Permitting an Inviscid Base Flow

Topalian et al. [165] recently postulated a spatiotemporal homogenization formulation for simulating the fast evolution of a homogenized flow defect relative to

some prescribed, spatially developing inviscid base flow. This section states the forcing terms in sufficient detail to reproduce the simulation results in the present work. The construction of this spatiotemporal model appears in Section A.3 for completeness.

The nondimensional, conserved spatiotemporal forcing entering into (3.1) is

$$\mathscr{S}_\rho = \mathscr{S}_{\rho,xt}, \qquad \mathscr{S}_{\rho u_i} = \rho\,\mathscr{S}_{u_i,xt} + u_i \mathscr{S}_{\rho,xt}, \qquad \mathscr{S}_{\rho E} = \rho\,\mathscr{S}_{E,xt} + E\mathscr{S}_{\rho,xt} \tag{3.15a}$$

where, fixing a temporal growth rate $\mathrm{gr}_{t_0}(\Delta)$, the primitive constituents are:

$$\mathscr{S}_{\rho,xt} = \tilde{u}\,(\rho)_{x_0} + \rho\,(\tilde{u})_{x_0} \tag{3.15b}$$

$$\mathscr{S}_{u_i,xt} = \tilde{u}\,(\tilde{u}_i)_{x_0} + \frac{\delta_{ix}\,(\bar{p})_{x_0}}{\mathrm{Ma}^2\bar{\rho}} + u_i''\left[-\mathrm{gr}_{t_0}\left(A_u^A\right) + \frac{y\,\mathrm{gr}_{t_0}(\Delta)}{\sqrt{\widetilde{u_k''u_k''}}}\frac{\partial\sqrt{\widetilde{u_k''u_k''}}}{\partial y}\right] \tag{3.15c}$$

$$\mathscr{S}_{E,xt} = \tilde{u}\left(\tilde{E}\right)_{x_0} + \frac{\bar{p}}{\bar{\rho}}\,(\tilde{u})_{x_0} + \frac{\tilde{u}}{\bar{\rho}}\,(\bar{p})_{x_0} + E''\left[-\mathrm{gr}_{t_0}\left(A_E^A\right) + \frac{y\,\mathrm{gr}_{t_0}(\Delta)}{\sqrt{\widetilde{E''E''}}}\frac{\partial\sqrt{\widetilde{E''E''}}}{\partial y}\right]. \tag{3.15d}$$

These terms are considerably more complex than their temporal predecessors (2.6). Subscripts t_0 and x_0 indicate forcing arising from temporal or spatial homogenization, respectively. The former terms are gathered inside brackets in (3.15). Topalian et al. modeled the latter terms as

$$(\rho)_{x_0} = \frac{\rho}{\bar{\rho}}\left(-\frac{\partial\rho_I}{\partial x_0} - \bar{\rho}_D\,\mathrm{gr}_{x_0}\left(\bar{\rho}_D^A\right) + y\,\mathrm{gr}_{x_0}(\Delta)\,\frac{\partial\bar{\rho}_D}{\partial y}\right) \tag{3.16a}$$

$$(\tilde{u}_i)_{x_0} = -\frac{\partial u_{i,I}}{\partial x_0} - \tilde{u}_{i,D}\,\mathrm{gr}_{x_0}\left(\tilde{u}_{i,D}^A\right) + y\,\mathrm{gr}_{x_0}(\Delta)\,\frac{\partial\tilde{u}_{i,D}}{\partial y} \tag{3.16b}$$

$$(\bar{p})_{x_0} = -\frac{\partial p_I}{\partial x_0} - \bar{p}_D\,\mathrm{gr}_{x_0}\left(\bar{p}_D^A\right) + y\,\mathrm{gr}_{x_0}(\Delta)\,\frac{\partial\bar{p}_D}{\partial y} \tag{3.16c}$$

$$\left(\tilde{E}\right)_{x_0} = -\frac{\partial E_I}{\partial x_0} - \tilde{E}_D\,\mathrm{gr}_{x_0}\left(\tilde{E}_D^A\right) + y\,\mathrm{gr}_{x_0}(\Delta)\,\frac{\partial\tilde{E}_D}{\partial y} \tag{3.16d}$$

which must be computed against a base flow satisfying the steady Euler equations. That is, in conjunction with the instantaneous Favre-averaged state, pointwise inviscid

data

$$\begin{matrix} \rho_I(y) & \rho u_I(y) & \rho v_I(y) & \rho E_I(y) & p_I(y) \\ \frac{\partial}{\partial y}\rho_I(y) & \frac{\partial}{\partial y}\rho u_I(y) & \frac{\partial}{\partial y}\rho v_I(y) & \frac{\partial}{\partial y}\rho E_I(y) & \frac{\partial}{\partial y}p_I(y) \\ \frac{\partial}{\partial x}\rho_I(y) & \frac{\partial}{\partial x}\rho u_I(y) & \frac{\partial}{\partial x}\rho v_I(y) & \frac{\partial}{\partial x}\rho E_I(y) & \frac{\partial}{\partial x}p_I(y) \end{matrix} \tag{3.17}$$

must be specified to define the mean primitive viscous flow defects

$$\bar{\rho}_D = \bar{\rho} - \rho_I \qquad \tilde{u}_{i,D} = \tilde{u}_i - u_{i,I} \qquad \tilde{E}_D = \tilde{E} - E_I \qquad \bar{p}_D = \bar{p} - p_I \tag{3.18}$$

entering into (3.16). Nonzero streamwise derivatives in the inviscid base flow data, for example p_I entering into (3.16c), are what permit the model to impose pressure-gradient-like conditions while retaining streamwise periodicity in the fast time solution. A semi-analytical procedure to generate the base flow data (3.17) necessary for the present work is the subject of Appendix C.

The two parameters

$$\mathrm{gr}_{t_0}(\Delta) = \left(-\frac{\epsilon}{\Delta}\frac{\partial \Delta}{\partial t_s}\right)\bigg|_{t_s=t_0} \qquad \mathrm{gr}_{x_0}(\Delta) = \left(-\frac{\epsilon}{\Delta}\frac{\partial \Delta}{\partial x_s}\right)\bigg|_{x_s=x_0} \tag{3.19}$$

represent the growth rate of a characteristic length scale Δ at some fixed slow time t_0 or some fixed slow location x_0 for small homogenization parameter ϵ. In practice, $\mathrm{gr}_{t_0}(\Delta)$ is a constant supplied to target some desired boundary layer thickness with ϵ indirectly fixed. The inviscid base flow streamwise velocity controls the second parameter per

$$\mathrm{gr}_{x_0}(\Delta) = \frac{\mathrm{gr}_{t_0}(\Delta)}{u_{I,w}} \tag{3.20}$$

where the subscript w denotes wall data taken from $y = 0$. The wall reference is chosen as no freestream limit exists for flows experiencing nonzero pressure gradients.

Expressions (3.16) include constants governing the growth rates for the amplitude of the mean flow defect, denoted $\mathrm{gr}_{x_0}\left(q_D^A\right)$ for $q \in \left\{\bar{\rho}, \tilde{u}, \tilde{v}, \tilde{w}, \tilde{E}, \bar{p}\right\}$. In scenarios with an isothermal wall, known boundary state in conjunction with the inviscid base flow (3.17) informs these quantities. By definition,

$$\mathrm{gr}_{x_0}\left(q_D^A\right) = \frac{1}{q_D^A}\frac{\partial q_D^A}{\partial x_s}\bigg|_{x_s=x_0} = \frac{1}{q_w - q_{I,w}}\left(\frac{\partial q_w}{\partial x_s} - \frac{\partial q_{I,w}}{\partial x_s}\right)\bigg|_{x_s=x_0}. \tag{3.21}$$

For convenience, $(\partial q/\partial x_s)|_{x_s=x_0}$ is henceforth abbreviated as $\partial q/\partial x_s$. From (3.1d), uniform wall temperature T_w, and the isobaric assumption $\partial \bar{p}/\partial_y \approx 0$,

$$\bar{\rho}_w = \frac{\gamma \bar{p}_w}{T_w} \approx \frac{\gamma p_{I,w}}{T_w}. \tag{3.22}$$

Taking the slow spatial derivative under these assumptions,

$$\frac{\partial \bar{\rho}_w}{\partial x_s} \approx \frac{\gamma}{\bar{T}_w}\frac{\partial p_{I,w}}{\partial x_s}. \tag{3.23}$$

Therefore,

$$\mathrm{gr}_{x_0}(\bar{\rho}_D) \approx \frac{1}{\frac{\gamma p_{I,w}}{T_w} - \rho_{I,w}}\left(\frac{\gamma}{T_w}\frac{\partial p_{I,w}}{\partial x_s} - \frac{\partial \rho_{I,w}}{\partial x_s}\right) = \frac{T_w \frac{\partial \rho_{I,w}}{\partial x_s} - \gamma \frac{\partial p_{I,w}}{\partial x_s}}{T_w \rho_{I,w} - \gamma p_{I,w}}. \tag{3.24}$$

Consider the wall-normal momentum growth rate at a no-slip wall,

$$\mathrm{gr}_{x_0}\left(\overline{\rho v}_D^A\right) = \frac{\frac{\partial}{\partial x_s}\rho v_{I,w}}{\rho v_{I,w}}. \tag{3.25}$$

Any nonzero wall blowing velocity v_w has been neglected because mimicking (3.24),

$$\begin{aligned}\mathrm{gr}_{\substack{x_0 \\ \text{rejected}}}\left(\overline{\rho v}_D^A\right) &\approx \frac{1}{\rho v_{I,w} - \frac{\gamma p_{I,w}}{T_w} v_w}\left(\frac{\partial}{\partial x_s}\rho v_{I,w} - \frac{\gamma v_w}{T_w}\frac{\partial}{\partial x_s} p_{I,w}\right) \\ &= \frac{T_w \frac{\partial}{\partial x_s}\rho v_{I,w} - \gamma v_w \frac{\partial}{\partial x_s} p_{I,w}}{T_w \rho v_{I,w} - \gamma v_w p_{I,w}},\end{aligned} \tag{3.26}$$

behaves oddly on two accounts. First, from it one recovers (3.24) whenever the base flow is designed with transpiration as then both $v_{I,w} = v_w \neq 0$ and $\frac{\partial v_{I,w}}{\partial x_s} = 0$ hold. Second, whenever $v_{I,w} = 0$ its limiting $v_w \to 0$ behavior is broken in the sense that one recovers $\left(\frac{\partial p_{I,w}}{\partial x_s}\right)/p_{I,w}$ for any $v_w \neq 0$ but not when $v_w = 0$. Consequently, the velocity growth rates also ignore blowing and are:

$$\mathrm{gr}_{x_0}\left(\tilde{u}_D^A\right) = \frac{1}{u_{I,w}}\frac{\partial u_{I,w}}{\partial x_s} \qquad \mathrm{gr}_{x_0}\left(\tilde{v}_D^A\right) = \frac{1}{v_{I,w}}\frac{\partial v_{I,w}}{\partial x_s} \qquad \mathrm{gr}_{x_0}\left(\tilde{w}_D^A\right) = \frac{1}{w_{I,w}}\frac{\partial w_{I,w}}{\partial x_s}. \tag{3.27}$$

The specific energy mean defect growth rate is

$$\mathrm{gr}_{x_0}\left(\tilde{E}_D^A\right) = \frac{\frac{\partial E_{I,w}}{\partial x_s}}{E_{I,w} - E_w} \tag{3.28}$$

where wall blowing is now neither problematic nor neglected so (3.1d) fixes

$$E_w = \frac{T_w}{\gamma(\gamma-1)} + \frac{\mathrm{Ma}^2}{2}v_w^2. \tag{3.29}$$

Finally, whenever growth rates are uninformed or ill-defined according to these arguments, they are taken to be zero. Therefore,

$$\mathrm{gr}_{x_0}\left(\tilde{p}_D^A\right) = 0, \qquad \mathrm{gr}_{t_0}\left(A_u^A\right) = 0, \qquad \mathrm{gr}_{t_0}\left(A_E^A\right) = 0. \tag{3.30}$$

Other cases necessitating this final clause include the thermodynamic growth rates when $\left|1 - T_w/T_{I,w}\right| < 1\%$ and the wall-normal and spanwise velocity rates when the base flow at the wall is trivial in those directions.

Chapter 4

Computational Techniques

This chapter reviews the computational techniques used to solve the governing equations presented in the previous chapter for the geometries of interest.

4.1 Numerical Discretization

The target geometries are channels and flat plates with coordinates as depicted in Figure 4.1. The former geometry requires nearly a proper subset of the capabilities necessary to solve the latter and is used for validation purposes in Chapter 5. The flat plate geometry is the subject of Chapters 6 and 7. The streamwise and spanwise directions are formally infinite which is emulated using periodicity in these directions in conjunction with a sufficiently large domain.

A mixed Fourier–Galerkin/B-spline collocation spatial discretization is com-

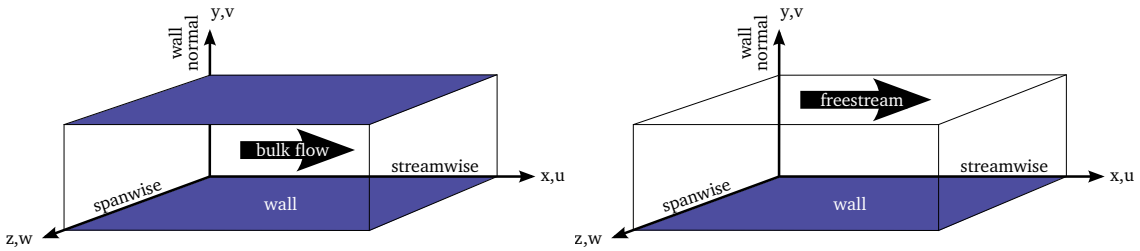

Figure 4.1: The channel (left) and flat plate (right) geometries.

bined with a low-storage, semi-implicit third-order Runge–Kutta scheme. The spatial discretization yields excellent spectral resolution [82], has long been proven for supersonic, spatially homogenized boundary layer simulations [60], and provides a natural, scalable parallel domain decomposition on high-performance computing environments. The temporal discretization, used repeatedly at large scale [e.g. 65] since its introduction [151], mitigates the potentially severe acoustic and diffusive stability limits present in our problems of interest. Nondimensional density ρ, momentum $m = \rho u$, and total energy $e = \rho E$ were used as state variables.

4.1.1 Fourier/B-Spline Spatial Discretization

Mimicking the governing equations in Section 3.1, consider the abstract continuous system

$$\frac{\partial u}{\partial t} = \mathscr{L}u + \mathscr{N}(u) \tag{4.1}$$

on the spatial domain $\left[-\frac{L_x}{2}, \frac{L_x}{2}\right] \times [0, L_y] \times \left[-\frac{L_z}{2}, \frac{L_z}{2}\right]$. The operators $\mathscr{L}$ and $\mathscr{N}$ are linear and nonlinear, respectively. To discretize this system, introduce its finite dimensional analog

$$\frac{\partial u^h}{\partial t} = \mathscr{L}u^h + \mathscr{N}\left(u^h\right) + R^h \tag{4.2}$$

where the continuous field $u = u(x, y, z, t)$ has been replaced by the discrete field $u^h = u^h(x, y, z, t)$ with $N_x \times N_y \times N_z$ degrees of freedom, and R^h is the discretization error. Fourier expansions are selected for the periodic x and z directions while a B-

spline expansion is adopted for the aperiodic y direction. That is,

$$\begin{aligned} u^h(x,y,z,t) &= \sum_{l=0}^{N_y-1} \sum_{m=-\frac{N_x}{2}}^{\frac{N_x}{2}-1} \sum_{n=-\frac{N_z}{2}}^{\frac{N_z}{2}-1} \hat{u}_{lmn}(t) B_l(y)\, e^{\mathrm{i}\frac{2\pi m}{L_x}x} e^{\mathrm{i}\frac{2\pi n}{L_z}z} \\ &= \sum_l \sum_m \sum_n \hat{u}_{lmn}(t) B_l(y)\, e^{\mathrm{i}k_m x} e^{\mathrm{i}k_n z} \end{aligned} \tag{4.3}$$

where $k_m = 2\pi m/L_x$, $k_n = 2\pi n/L_z$, and $B_l(y)$ are a B-spline basis for some order and knot selection.

Applying the method of weighted residuals, a mixed Galerkin/collocation approach (often called a "pseudospectral" technique) is chosen that employs the L_2 inner product and test "functions" like $\delta(y-y_{l'})e^{\mathrm{i}k_{m'}x}e^{\mathrm{i}k_{n'}z}$ where l', m', and n' range over the same values as l, m, and n, respectively. The fixed collocation points $y_{l'}$ depend on the B-spline basis details. Three orthogonality results are

$$\int_0^{L_y} \varphi(y)\,\delta(y-y_{l'})\,dy = \varphi(y_{l'}) \tag{4.4a}$$

$$\int_{-\frac{L_x}{2}}^{\frac{L_x}{2}} e^{\mathrm{i}k_m x} e^{-\mathrm{i}k_{m'}x}\,dx = L_x \delta_{mm'} \tag{4.4b}$$

$$\int_{-\frac{L_z}{2}}^{\frac{L_z}{2}} e^{\mathrm{i}k_n z} e^{-\mathrm{i}k_{n'}z}\,dz = L_z \delta_{nn'} \tag{4.4c}$$

where the inner product's conjugate operation is accounted for by introducing a negative sign into the latter two exponentials. The weighted residual is forced to be zero in the sense that

$$\int_0^{L_y} \int_{-\frac{L_x}{2}}^{\frac{L_x}{2}} \int_{-\frac{L_z}{2}}^{\frac{L_z}{2}} R^h(x,y,z)\,\delta(y-y_{l'}) e^{-\mathrm{i}k_{m'}x} e^{-\mathrm{i}k_{n'}z}\,dz\,dx\,dy = 0 \tag{4.5}$$

holds for all l', m', and n'. Inserting (4.3) into (4.2), testing with the test functions,

applying (4.5), and simplifying

$$
\begin{aligned}
&L_x L_z \sum_l B_l(y_{l'}) \frac{\partial}{\partial t} \hat{u}_{lmn}(t) \\
&\qquad = L_x L_z \mathscr{L} \left(\sum_l B_l(y_{l'}) \hat{u}_{lmn}(t) \right) \\
&\qquad + \int_{-\frac{L_x}{2}}^{\frac{L_x}{2}} \int_{-\frac{L_z}{2}}^{\frac{L_z}{2}} \mathscr{N} \left(\sum_m \sum_n \left(\sum_l B_l(y_{l'}) \hat{u}_{lmn}(t) \right) e^{\mathrm{i} k_m x} e^{\mathrm{i} k_n z} \right) \left(e^{-\mathrm{i} k_{m'} x} e^{-\mathrm{i} k_{n'} z} \right) dz\, dx.
\end{aligned}
\tag{4.6}
$$

Approximating the two integrals by discrete sums and dividing by L_x and L_z,

$$
\begin{aligned}
&\sum_l B_l(y_{l'}) \frac{\partial}{\partial t} \hat{u}_{lmn}(t) \\
&\quad \approx \mathscr{L} \left(\sum_l B_l(y_{l'}) \hat{u}_{lmn}(t) \right) \\
&\quad + \frac{1}{N_x N_z} \sum_{m'} \sum_{n'} \mathscr{N} \left(\sum_m \sum_n \left(\sum_l B_l(y_{l'}) \hat{u}_{lmn}(t) \right) e^{\mathrm{i} k_m x_{m'}} e^{\mathrm{i} k_n z_{n'}} \right) \left(e^{-\mathrm{i} k_{m'} x_m} e^{-\mathrm{i} k_{n'} z_n} \right)
\end{aligned}
\tag{4.7}
$$

where $x_{m'} = L_x m'/N_x$ and $z_{n'} = L_z n'/N_z$. The quadrature error in this approximation can be controlled by increasing the number of quadrature points [15]. Here $3N_x/2$ and $3N_z/2$ quadrature points were used in x and z, which eliminates quadrature error when $\mathscr{N}$ is quadratic [23]. This approach has been found to reduce quadrature error to acceptable levels for the compressible Navier–Stokes equations [21].

Result (4.7) represents $N_x \times N_z$ time-dependent systems containing N_y equations coupled in the x and z directions only through discrete Fourier transforms and the requirements of the $\mathscr{L}$ and $\mathscr{N}$ operators. Its left hand side has a time-independent mass matrix arising from the B-spline basis and collocation point choices. The mass matrix is retained on the same side as the time derivative in anticipation of the time

discretization scheme. The constant factor $(N_x N_z)^{-1}$ also will be accommodated during time advance.

4.1.2 Semi-Implicit, Low-Storage Temporal Discretization

Time is advanced via the low-storage, semi-implicit scheme from Spalart, Moser, and Rogers [151, Appendix A] extended following Yang [181]. The "SMR91" scheme advances the system

$$Mu_t = Lu + \chi N(u,t) \tag{4.8}$$

from $u(t)$ to $u(t+\Delta t)$. Here L and N are a linear and nonlinear operator, respectively, distinct from but related to the preceding section's $\mathscr{L}$ and $\mathscr{N}$. Both operators take the state to an isomorphic, non-state representation from which the state can be recovered by the action of the linear "mass matrix" M. The constant χ permits scaling $\mathscr{N}$ during time advance; it will later be used to apply the factor $(N_x N_z)^{-1}$ from (4.7). The scheme treats $\chi M^{-1} N$ with third-order accuracy and $M^{-1}L$ with second-order accuracy.

Each substep $i \in \{1,2,3\}$ possesses the form

$$\begin{aligned}(M - \Delta t \beta_i L) u^{i+1} = (M + \Delta t \alpha_i L) u^i \\ + \Delta t \gamma_i \chi N\left(u^i, t_n + \eta_i \Delta t\right) \\ + \Delta t \zeta_{i-1} \chi N\left(u^{i-1}, t_n + \eta_{i-1} \Delta t\right)\end{aligned} \tag{4.9}$$

and uses the following substep-specific coefficients:

$$\alpha_1, \alpha_2, \alpha_3 = \left\{\frac{29}{96}, -\frac{3}{40}, \frac{1}{6}\right\} \quad \beta_1, \beta_2, \beta_3 = \left\{\frac{37}{160}, \frac{5}{24}, \frac{1}{6}\right\} \quad \gamma_1, \gamma_2, \gamma_3 = \left\{\frac{8}{15}, \frac{5}{12}, \frac{3}{4}\right\}$$

$$\zeta_0, \zeta_1, \zeta_2 = \left\{0, -\frac{17}{60}, -\frac{5}{12}\right\} \qquad \eta_0, \eta_1, \eta_2, \eta_3 = \left\{0, 0, \frac{8}{15}, \frac{2}{3}\right\}.$$

As shown, L is time-independent throughout each interval $[t, t + \Delta t)$ but N is permitted to vary in time.

The scheme (4.9) requires implementations of $u \mapsto N(u)$, $u \mapsto (M + \varphi L)u$, and $u \mapsto (M + \varphi L)^{-1} u$ for a given M and some arbitrary scalar φ. To require only two storage locations a and b, the $N(u)$ and $(M + \varphi L)^{-1}$ implementations must operate in-place while $(M + \varphi L)$ must operate out-of-place. Two issues bear attention. First, the step size Δt needs to be dynamically computable based on a stability criterion accessible only during the first nonlinear operator application. Second, memory usage can be reduced by applying N against only one storage location, say b, so that only one location requires auxiliary padding for quadrature. Taken together, $(M + \varphi L)$ also must support in-place application and therefore storage a and b should support a swap operation, $a \longleftrightarrow b$.

In conclusion, time is advanced by one full step per Algorithm 1. Using (4.9) to advance state $\hat{u}_{lmn}(t)$ per (4.7) finally unites the spatial and temporal operator notion used in this and the preceding subsection:

$$Mu\big|_{mn} = \sum_l B_l(y_{l'})\, \hat{u}_{lmn} \tag{4.10a}$$

$$Lu|_{mn} = \mathscr{L}\left(\sum_l B_l(y_{l'})\, \hat{u}_{lmn}\right) \tag{4.10b}$$

$$N(u)|_{mn} = \underbrace{\frac{1}{N_x N_z}}_{\chi} \sum_{m'} \sum_{n'} \mathscr{N}\left(\sum_m \sum_n \left(\sum_l B_l(y_{l'})\, \hat{u}_{lmn}\right) e^{\mathrm{i}k_m x_{m'}} e^{\mathrm{i}k_n z_{n'}}\right) \left(e^{-\mathrm{i}k_{m'} x_m} e^{-\mathrm{i}k_{n'} z_n}\right). \tag{4.10c}$$

Algorithm 1 Perform the three-step, low-storage time advance described in §4.1.2

Require: Storage $a = u(t_n) = u^0$; storage b content undefined
  $b \leftarrow a$
  $b \leftarrow N(b, t_n)$
  Compute Δt from $a = u^0$ and $b = N\left(u^0, t_n\right)$
  $a \leftarrow (M + \Delta t \alpha_1 L)\, a$
  $a \leftarrow \Delta t \gamma_1 \chi\, b + a$
  $a \leftarrow (M - \Delta t \beta_1 L)^{-1}\, a$
Ensure: Storage $a = u^1$; storage $b = N\left(u^0, t_n\right)$
  $b \leftarrow (M + \Delta t \alpha_2 L)\, a + \Delta t \zeta_1 \chi\, b$
  $a \leftrightarrow b$
  $b \leftarrow N(b, t_n + \eta_2 \Delta t)$
  $a \leftarrow \Delta t \gamma_2 \chi\, b + a$
  $a \leftarrow (M - \Delta t \beta_2 L)^{-1}\, a$
Ensure: Storage $a = u^2$; storage $b = N\left(u^1, t_n + \eta_2 \Delta t\right)$
  $b \leftarrow (M + \Delta t \alpha_3 L)\, a + \Delta t \zeta_2 \chi\, b$
  $a \leftrightarrow b$
  $b \leftarrow N(b, t_n + \eta_3 \Delta t)$
  $a \leftarrow \Delta t \gamma_3 \chi\, b + a$
  $a \leftarrow (M - \Delta t \beta_3 L)^{-1}\, a$
Ensure: Storage $a = u(t + \Delta t) = u^3$; storage $b = N\left(u^2, t_n + \eta_3 \Delta t\right)$

Time advancement occurs in "coefficient" or "wave" space but nonlinear terms must be computed at "collocation points" or in "physical" space. The parallel communication and on-node computation cost required to convert state data from wave space to physical space or vice versa can be high. Consequently, many of the following numerical choices were made to maximize both the amount of simulation time advanced per Runge–Kutta step and to maintain as much numerical resolution as possible.

4.1.3 Discrete B-Spline Operators

Discrete operators for differentiation in the wall-normal direction map B-spline coefficients to derivatives at wall-normal collocation points. That is,

$$D^{(j)}u\Big|_{mn} = \sum_{l} B_l^{(j)}(y_{l'})\,\hat{u}_{lmn} \tag{4.11}$$

where the banded matrix $D^{(j)}$ is wavenumber independent. $D^{(0)}$ is the "mass matrix"

$$M = D^{(0)}. \tag{4.12}$$

Similar to, but different from, the approaches discussed by Kwok et al. [82, §2.1.3], the present work uses the Greville abscissae, also called the Marsden–Schoenberg points, as its collocation points [10, 70]. Selecting these abscissae automatically avoids the near-wall stability problems empirically circumvented by Kwok et al. [82, §4.4]. Boundary treatments for B-spline collocation operators use the property that the j^{th} derivative of the function at the first (last) collocation point depends only on the first (last) $j+1$ B-spline coefficients.

For some uniform B-spline order k and wall-normal number of degrees of freedom N_y, $N_y - k + 2$ breakpoint locations must be specified. Here $k = 4$ denotes

a piecewise cubic basis. For the channel geometry, a two-sided hyperbolic tangent function [172] stretches these breakpoints via $f_2 : [0,1] \to [0,1]$:

$$f_2(y) = \frac{1}{2}\left(1 + \frac{\tanh\left((y-1/2)\,\delta\right)}{\tanh\left(\delta/2\right)}\right). \tag{4.13}$$

For the flat plate, a one-sided hyperbolic tangent stretching function [172] is applied per $f_1 : [0,1] \to [0,1]$:

$$f_1(y) = 1 + \frac{\tanh\left((y-1)\,\delta\right)}{\tanh\left(\delta\right)}. \tag{4.14}$$

Here $\delta \geq 0$ is an adjustable stretching parameter where setting $\delta = 0$ recovers uniform spacing. Values like $1 \leq \delta \leq 3$ are used in practice. After mapping uniform points on $[0,1]$ to stretched points on $[0,1]$ using f_2 or f_1, a further affine transformation is then used to map the breakpoints onto $\left[0, L_y\right]$. These breakpoint locations on $\left[0, L_y\right]$ fix the collocation points and consequently the collocation-based discrete operators $D^{(j)}$ through the definition of the Greville abscissae applied for order k.

Unlike Fourier-based derivatives, with B-splines applying $D^{(1)}D^{(1)}$ gives a result that differs significantly from applying $D^{(2)}$ because repeated first differentiation severely abates high frequency modes [82, Figures 2–3]. Second derivatives enter (3.1) only through terms $\nabla \cdot \tau$, $\nabla \cdot \tau u$, and $\nabla \cdot \mu \nabla T$. These first and second derivative applications are computed wholly separately to discretely obtain the most physically consistent dissipation of high-frequency content at a given spatial resolution. This decision comes with additional implementation complexity, see Table 4.1, but this choice eliminated any need to add aphysical discrete filtering which is often used to prevent the catastrophic buildup of spurious numerical noise.

Table 4.1: Communications overhead inherent to computing quantities without repeated first differentiation. Overhead measured relative to transforming a single scalar field from wave space to physical space. A check (✓) indicates that a quantity is required to compute terms in the leftmost column. A bullet (•) indicates the quantity is required but it can be computed from other required quantities. Total costs for each term are summarized in the rightmost column.

	1	3	1	6	3	1	6	9	3	3	1	3	1	
	ρ	$\nabla\rho$	$\Delta\rho$	$\nabla\nabla\rho$	m	$\nabla\cdot m$	$\mathrm{sym}(\nabla m)$	∇m	Δm	$\nabla\nabla\cdot m$	e	∇e	Δe	
$\nabla\cdot\frac{m}{\rho}$	✓	✓			✓	✓								8
$\nabla\frac{m}{\rho}$	✓	✓			✓			✓						16
$\mathrm{sym}\left(\nabla\frac{m}{\rho}\right)$	✓	✓			✓		✓							13
$\Delta\frac{m}{\rho}$	✓	✓	✓		✓			✓	✓					20
$\nabla\nabla\cdot\frac{m}{\rho}$	✓	✓		✓	✓	•		✓		✓				25
p, T, μ, λ	✓				✓						✓			5
∇p, ∇T, $\nabla\mu$, $\nabla\lambda$	✓	✓			✓			✓			✓	✓		20
Δp	✓	✓	✓		✓			✓	✓				✓	21
ΔT	✓	✓	✓		✓			✓	✓		✓	✓	✓	25
τ	✓	✓			✓	•	✓				✓			14
$\mathrm{sym}\left(\nabla\frac{m}{\rho}\right)\nabla\mu$	✓	✓			✓		•	✓			✓	✓		20
$\mu\Delta\frac{m}{\rho}$	✓	✓	✓		✓			✓	✓		✓			21
$(\mu+\lambda)\nabla\nabla\cdot\frac{m}{\rho}$	✓	✓		✓	✓	•		✓		✓	✓			26
$\left(\nabla\cdot\frac{m}{\rho}\right)\nabla\lambda$	✓	✓			✓	•		✓			✓	✓		20
$\nabla\cdot\tau$	✓	✓	•	✓	✓	•	•	✓	✓	✓	✓	✓		32
$\frac{m}{\rho}\cdot(\nabla\cdot\tau)$	✓	✓	•	✓	✓	•	•	✓	✓	✓	✓	✓		32
$\mathrm{tr}\left(\tau^{\mathsf{T}}\nabla\frac{m}{\rho}\right)$	✓	✓			✓	•	•	✓			✓			20
$\nabla\cdot\tau\frac{m}{\rho}$	✓	✓	•	✓	✓	•	•	✓	✓	✓	✓	✓		32
$\nabla\mu\cdot\nabla T$	✓	✓			✓			✓			✓	✓		20
$\mu\Delta T$	✓	✓	✓		✓			✓	✓		✓	✓	✓	25
$\nabla\cdot\mu\nabla T$	✓	✓	✓		✓			✓	✓		✓	✓	✓	25

4.1.4 Time Step Stability Criteria

The step size Δt used in the SMR91 scheme is limited by both a convective and a diffusive stability criterion. The time step is taken to be the largest stable time step possible according to both restrictions. As both criteria are approximate, the resulting Δt is further multiplied by a safety factor less than one. Safety factors 0.70–0.77 are often used [151, 171]. Efforts to improve stability estimates for a given discretization are worthwhile because even small increases in time step size can translate into appreciable compute savings over the course of a long simulation.

4.1.4.1 Convective Stability Limit from Scalar Analysis

The convective criterion uses the maximum imaginary eigenvalue magnitude from the Euler equations as a surrogate for the more complicated Navier–Stokes system. Both Kwok [81, Equation 2.39] and Guarini [59, Equations 4.20–21] derived the stability result

$$\Delta t \leq \frac{\left|\lambda_I \Delta t\right|_{\max}}{\left(|u_x| + a\right)\lambda_x^{(1)} + \left(\left|u_y\right| + a\right)\lambda_y^{(1)} + \left(|u_z| + a\right)\lambda_z^{(1)}} \tag{4.15}$$

where a is the local acoustic velocity, u_x denotes the velocity in the x direction, $\lambda_x^{(1)}$ represents the maximum imaginary eigenvalue magnitude of the first derivative operator in the x direction, etc. In the two Fourier directions these eigenvalues are exactly known:

$$\lambda_x^{(1)} = \frac{\pi N_x}{L_x} = \frac{\pi}{\Delta x}, \qquad \lambda_z^{(1)} = \frac{\pi N_z}{L_z} = \frac{\pi}{\Delta z}. \tag{4.16}$$

For the B-spline operator $M^{-1}D^{(1)}$ which maps function coefficients to first derivative coefficients, one may similarly estimate

$$\lambda_y^{(1)} = \frac{\pi}{C^{(1)}\Delta y} \tag{4.17}$$

where the definition of Δy and $C^{(1)}$ are for now deferred. Analogously to the Fourier case, for a periodic, uniform B-spline basis, $C^{(1)}$ would be one. The maximum pure imaginary eigenvalue magnitude, $|\lambda_I \Delta t|_{\max}$, is a feature of the chosen time-stepping method. For the SMR91 scheme,

$$|\lambda_I \Delta t|_{\max} = \sqrt{3}. \tag{4.18}$$

For nondimensional formulations in which an explicit Mach number, $\mathrm{Ma} = u_0/a_0$ appears, one must provide the velocities and the sound speed both nondimensionalized using u_0. Expressions like $|u| + a/\mathrm{Ma}$ are appropriate for this context, as can be seen by finding the eigenvalues of the Euler equations in such a nondimensionalization. Using an A-stable scheme, like the implicit portion of SMR91, to compute acoustic terms effectively sets the sound speed to zero when computing this convective criterion.

Returning to Equation (4.17), both Guarini and Kwok used the breakpoint separation for Δy and set $C^{(1)} = 1$. When Venugopal used a nearly identical convective criterion to (4.15), he found using $C^{(1)} = 1$ to be overly conservative for aperiodic $D^{(1)}$ built from nonuniform breakpoints. Venugopal [171, §3.2] presented a linearized analysis taking into account the inhomogeneous nature of his wall-normal direction. He determined that the wall-normal imaginary eigenvalue magnitude dropped by nearly

an order of magnitude after taking into account the inhomogeneity. He concluded that, taking Δy to be the breakpoint separation, $C^{(1)} = 4$ was feasible [171, Equation 3.29]. The present choice of Δy and $C^{(1)}$ is discussed after the diffusive stability limit.

4.1.4.2 Diffusive Stability Limit from Scalar Analysis

The diffusive criterion uses the maximum real eigenvalue magnitude from a model diffusion equation as a surrogate for the more complicated Navier–Stokes system. Both Kwok [81, Equation 2.40] and Guarini [59, Equations 4.29–30] derived the stability result

$$\Delta t \leq \frac{|\lambda_R \Delta t|_{\max}}{\max\left(\left|\frac{\gamma(\nu-\nu_0)}{\mathrm{RePr}}\right|, \left|\frac{\nu-\nu_0}{\mathrm{Re}}\right|, \left|\frac{\nu_B-\nu_{B0}}{\mathrm{Re}}\right|\right)\left(\lambda_x^{(2)} + \lambda_y^{(2)} + \lambda_z^{(2)}\right)} \tag{4.19}$$

where a bulk kinematic viscosity has been added to their results. As in the convective criterion, in the Fourier direction these eigenvalues are exactly known and we introduce $C^{(2)}$ in the wall-normal B-spline direction:

$$\lambda_x^{(2)} = \left(\frac{\pi N_x}{L_x}\right)^2 = \frac{\pi^2}{\Delta x^2}, \quad \lambda_y^{(2)} = \left(\frac{\pi}{C^{(2)}\Delta y}\right)^2, \quad \lambda_z^{(2)} = \left(\frac{\pi N_z}{L_z}\right)^2 = \frac{\pi^2}{\Delta z^2}. \tag{4.20}$$

Here $M^{-1}D^{(2)}$ is the B-spline operator of interest, which maps function coefficients to second derivative coefficients. Again, the definition of Δy and $C^{(2)}$ are for now deferred. The maximum pure real eigenvalue magnitude, $|\lambda_R \Delta t|_{\max}$, is a feature of the chosen time-stepping method. For the SMR91 scheme,

$$|\lambda_R \Delta t|_{\max} \approx 2.512. \tag{4.21}$$

Using an A-stable scheme, like the implicit portion of SMR91, to compute linearized viscous terms allows subtracting the linearization reference kinematic viscosities ν_0 and

ν_{B0} when computing this diffusive criterion. The absolute values within the maximum operations account for the possibility that $\nu < \nu_0$.

Returning to Equation (4.20), both Guarini and Kwok used the breakpoint separation for Δy and set $C^{(2)} = 1$. Venugopal used a nearly identical diffusive criterion [171, Equation 3.15]. His analysis determined that the diffusive stability criterion was not overly conservative for an aperiodic B-spline discretization. The present choices for Δy and $C^{(2)}$ are discussed next.

4.1.4.3 Empirical Limits for Inhomogeneous B-Spline Operators

Employing stability estimates (4.15) and (4.19) requires information about the wall-normal discrete operator eigenvalue magnitudes. By Equations (4.17) and (4.20) this is equivalent to estimating both $C^{(1)}$ and $C^{(2)}$. Per Section 4.1.3, our operators are a function of three parameters: the piecewise polynomial order k where $k = 4$ indicates piecewise cubic B-splines, the hyperbolic tangent stretching parameter $\delta \geq 0$, and the wall-normal number of degrees of freedom $N_y \geq k$.

Using numerically obtained eigenvalue magnitudes $\lambda^{(1)} = \lambda_y^{(1)}\left(k, \delta, N_y\right)$ and $\lambda^{(2)} = \lambda_y^{(2)}\left(k, \delta, N_y\right)$ from a large collection of discrete operators, exact $C^{(1)}$ and $C^{(2)}$ values were computed. The results are shown in Figure 4.2. The minimum grid spacing Δy was measured using either adjacent breakpoints or adjacent collocation points to permit a comparison. Considering only breakpoint-based results for $k = 8$, one can see how Venugopal [171] probably chose $C^{(1)} = 4$ and $C^{(2)} = 1$ as discussed in Section 4.1.4.1 and Section 4.1.4.2. However, it is striking just how nonuniversal those choices are. Evidently, neither a breakpoint-based nor a collocation point-based Δy

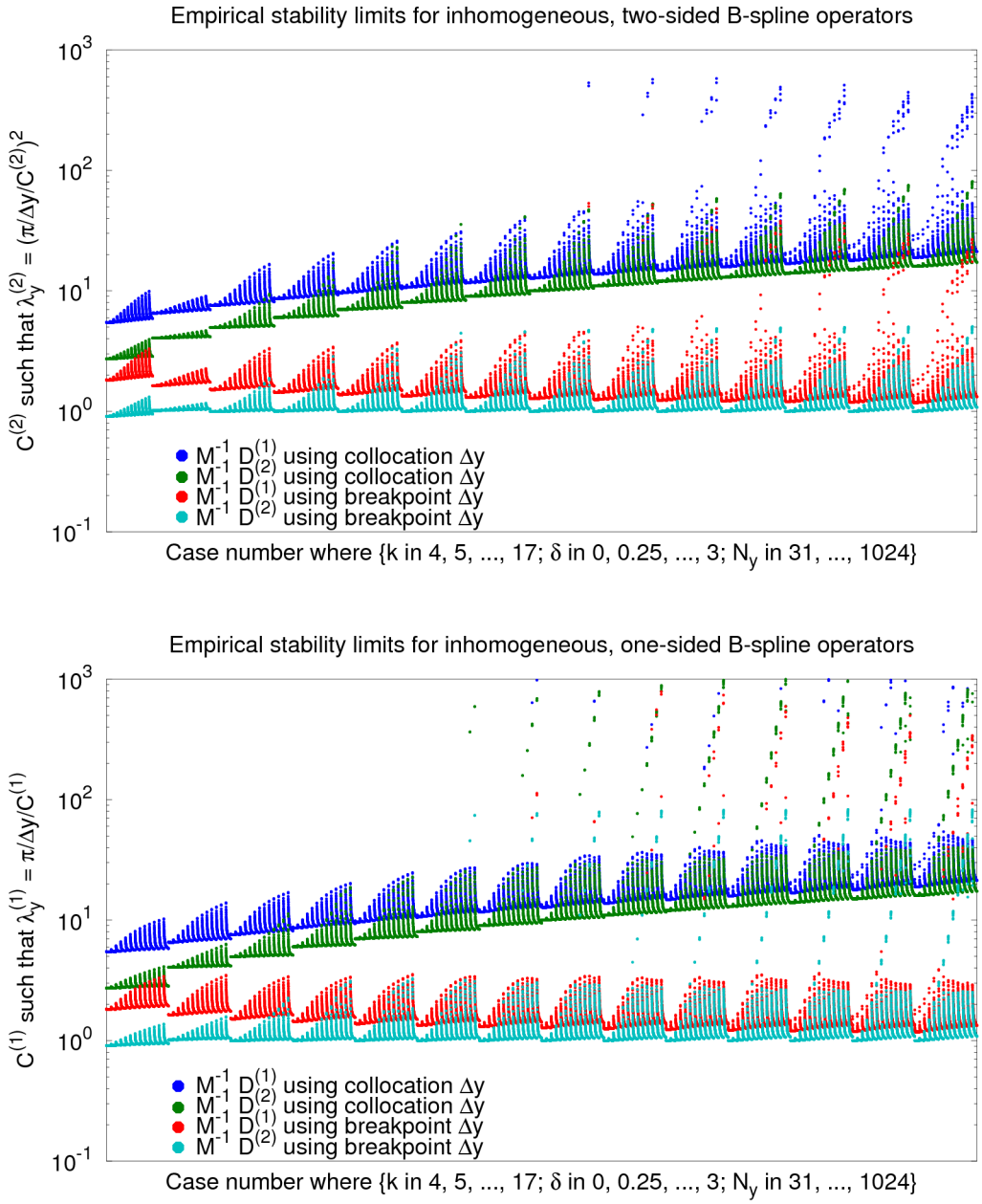

Figure 4.2: Exact values of $C^{(1)}$ and $C^{(2)}$ computed per Equations (4.17) and (4.20) for roughly 32,500 combinations of k, δ, and N_y. Above, two-sided stretching was performed on breakpoints per (4.13). Below, one-sided stretching was performed per (4.14). In both figures, the leftmost four "triangles" correspond to $k = 4$ while δ was varied slowly and N_y varied quickly. Moving rightward, the next "triangles" are for $k = 5$, then $k = 6$, etc.

inherently captures the maximum eigenvalue magnitudes as k, δ, and N_y vary— some nonlinear combination of the complete set of grid parameters is necessary.

Hereafter, unlike Guarini, Kwok, and Venugopal, we take Δy to be the spacing between adjacent collocation points. Performing Levenberg–Marquardt nonlinear regression against the vast majority of the empirical data in Figure 4.2 shows good agreement with curve fits like the following

$$C^{(i)}_{\text{approx}}\left(k,\delta,N_y\right) \approx ak + b\hat{\delta} + \frac{c}{\sqrt{k}} + k^{d+e\hat{\delta}}\left(1+\left(\frac{fk}{N_y-k+1}\right)^{gk+h\hat{\delta}}\right), \tag{4.22a}$$

$$\hat{\delta} = (1+\delta)^i \tanh\delta. \tag{4.22b}$$

The data from "nearly spectral" discrete operators, defined as when $N_y \leq 5k$, proved difficult to fit and was omitted. Such cases look like outliers in Figure 4.2 and are not operationally important as the present work does not use a spectral wall-normal basis. When using two-sided stretching per (4.13), one collection of constants a–i permits fitting the retained $C^{(1)}$ observations for $k = 5$ through 11 to within relative errors of [-2.55%, 1.76%]. Another collection permits fitting retained $C^{(2)}$ observations to within [-11.3%, 17.1%]. While those results are encouraging for the generality of the chosen functional forms, they are less than satisfactory for production use. More precise, k-specific, coefficients for two-sided stretching appear in Table 4.2 and Table 4.4 while coefficients for one-sided stretching appear in Table 4.3 and Table 4.5.

Unfortunately, using either $C^{(1)}_{\text{approx}}$ or $C^{(2)}_{\text{approx}}$ directly proved to be overly aggressive as measured using a collection of contrived test problems known *a priori* to be either convectively or diffusively limited. Scaling these by a single safety factor

was problematic as no unique value allowed pushing up against both criteria simultaneously. Against the same test problems, however, using approximations like the square root of $C^{(i)}_{\text{approx}}$ did permit using a uniform safety factor across a variety of test conditions.

In summary, the present work takes nearly the square root of a conservative estimate of $C^{(i)}_{\text{approx}}$. That is,

$$C^{(1)} = \left(\frac{C^{(1)}_{\text{approx}}}{1 - (\text{negative relative error percentage})/100} \right)^{33/64} \tag{4.23}$$

$$C^{(2)} = \left(\frac{C^{(2)}_{\text{approx}}}{1 - (\text{negative relative error percentage})/100} \right)^{27/64} \tag{4.24}$$

where the fit-specific, negative-valued lower error bounds appear in the rightmost column of the coefficient tables. Adjusting to the empirical fits' lower bounds gives slightly more conservative $\lambda^{(i)}_y$ estimates. These values of $C^{(i)}$ are plugged into Equations (4.17) and (4.20) with those results feeding into Equations (4.15) and (4.19). These estimates were designed for use with safety factors like 0.72 whenever $N_y > 5k$, which will be revisited in Section 5.3.

Table 4.2: B-spline order-specific curve fits for estimating $C^{(1)}_{\text{approx}}$ via Equation (4.22a) when Δy is the minimum distance between *collocation points* from breakpoints stretched according to f_2 defined in (4.13).

k	a	b	c	d	e	f	g	h	i	relative error
5–11	$\frac{5054}{4549}$	$-\frac{3953}{12175}$	$\frac{4321}{5893}$	$-\frac{5839}{8805}$	$\frac{3121}{7385}$	$\frac{235081}{5659}$	$\frac{399}{13421}$	$\frac{2795}{8687}$	$\frac{3548}{7037}$	-2.55 – 1.76%
4	$\frac{8753}{6138}$	$\frac{184}{3513}$	$-\frac{3868}{6327}$	$-\frac{22756}{5215}$	$\frac{19435}{28258}$	$\frac{152882005}{9731}$	$\frac{1605}{12298}$	$\frac{814}{5783}$	$\frac{7755}{19621}$	-1.52 – 0.46%
5	$-\frac{182723}{7970}$	$\frac{121}{6080}$	$-\frac{7061095}{23119}$	$\frac{115483}{33477}$	$\frac{1}{5560}$	$\frac{197}{3683}$	$\frac{761}{2741}$	$-\frac{2307}{6251}$	$\frac{1845}{5548}$	-1.12 – 0.53%
6	$\frac{8193}{7183}$	$\frac{74}{7487}$	$\frac{10787}{6960}$	$-\frac{12529}{6209}$	$\frac{3196}{4771}$	$\frac{4441318}{12819}$	$\frac{932}{12135}$	$\frac{3915}{17923}$	$\frac{870}{2123}$	-1.39 – 1.14%
7	$\frac{9063}{5683}$	$\frac{291}{6739}$	$-\frac{26786}{3839}$	$-\frac{2757}{1352}$	$\frac{2959}{4613}$	$\frac{2666741}{4919}$	$\frac{507}{6947}$	$\frac{498}{2627}$	$\frac{3572}{8791}$	-1.50 – 1.12%
8	$\frac{20956}{18111}$	$\frac{73}{3043}$	$\frac{3316}{4207}$	$-\frac{17945}{10877}$	$\frac{6659}{11166}$	$\frac{2564433}{9169}$	$\frac{658}{10813}$	$\frac{2725}{12594}$	$\frac{1181}{2847}$	-1.48 – 1.18%
9	$\frac{4351}{3996}$	$\frac{204}{4093}$	$\frac{13726}{5957}$	$-\frac{19388}{12047}$	$\frac{10397}{18003}$	$\frac{1200048}{3823}$	$\frac{246}{4289}$	$\frac{1395}{6839}$	$\frac{4244}{10183}$	-1.54 – 1.09%
10	$\frac{3174}{3221}$	$\frac{340}{4047}$	$\frac{435835}{78898}$	$-\frac{24457}{14830}$	$\frac{3057}{5416}$	$\frac{5464428}{12505}$	$\frac{166}{3013}$	$\frac{679}{3691}$	$\frac{2669}{6422}$	-1.59 – 1.11%
11	$\frac{6141}{6356}$	$\frac{513}{5051}$	$\frac{35557}{5371}$	$-\frac{5359}{3384}$	$\frac{6824}{12279}$	$\frac{3628675}{8504}$	$\frac{1012}{19681}$	$\frac{363}{2008}$	$\frac{1873}{4520}$	-1.56 – 0.94%
12	$\frac{9953}{8604}$	$\frac{521}{4751}$	$-\frac{2623}{3140}$	$-\frac{12011}{8190}$	$\frac{9067}{16522}$	$\frac{1947584}{5723}$	$\frac{141}{2959}$	$\frac{1231}{6652}$	$\frac{8479}{20445}$	-1.58 – 1.12%
13	$\frac{6428}{6247}$	$\frac{28}{239}$	$\frac{28437}{6178}$	$-\frac{13912}{10071}$	$\frac{2717}{5125}$	$\frac{3512083}{11082}$	$\frac{542}{12275}$	$\frac{701}{3776}$	$\frac{7291}{17441}$	-1.58 – 1.08%
14	$\frac{18221}{17050}$	$\frac{573}{3767}$	$\frac{37351}{13944}$	$-\frac{12384}{8881}$	$\frac{2238}{4193}$	$\frac{3701821}{10597}$	$\frac{231}{5389}$	$\frac{2953}{16836}$	$\frac{3950}{9507}$	-1.59 – 1.10%
15	$\frac{9251}{9369}$	$\frac{1001}{5400}$	$\frac{1033331}{141480}$	$-\frac{13367}{9358}$	$\frac{7583}{14554}$	$\frac{2662722}{5819}$	$\frac{392}{9519}$	$\frac{555}{3394}$	$\frac{2181}{5234}$	-1.56 – 1.01%
16	$\frac{8003}{8200}$	$\frac{2503}{12108}$	$\frac{263686}{31457}$	$-\frac{5713}{4107}$	$\frac{4803}{9290}$	$\frac{8189082}{18419}$	$\frac{93}{2371}$	$\frac{1663}{10299}$	$\frac{2945}{7073}$	-1.56 – 1.08%
17	$\frac{10594}{8835}$	$\frac{2615}{11361}$	$-\frac{38602}{5641}$	$-\frac{3464}{2537}$	$\frac{3372}{6575}$	$\frac{4481119}{10024}$	$\frac{355}{9469}$	$\frac{811}{5107}$	$\frac{1129}{2714}$	-1.53 – 0.97%

Table 4.3: B-spline order-specific curve fits for estimating $C^{(1)}_{\text{approx}}$ via Equation (4.22a) when Δy is the minimum distance between *collocation points* from breakpoints stretched according to f_1 defined in (4.14).

k	a	b	c	d	e	f	g	h	i	relative error
5–11	$\frac{12101}{11060}$	$-\frac{16426}{49749}$	$\frac{4524}{12157}$	$-\frac{4083}{8722}$	$\frac{4648}{11133}$	$\frac{645696}{14887}$	$\frac{117}{4057}$	$\frac{3436}{8883}$	$\frac{2329}{6500}$	-2.80 – 2.67%
4	$\frac{4129}{3316}$	$\frac{1052}{13345}$	$\frac{5769}{7262}$	$-\frac{29140}{6539}$	$\frac{3051}{5753}$	$\frac{271951060}{6969}$	$\frac{3691}{26472}$	$\frac{458}{3255}$	$\frac{3944}{13269}$	-2.65 – 1.39%
5	$\frac{3747}{2863}$	$\frac{722}{6223}$	$-\frac{3064}{13069}$	$-\frac{43215}{13954}$	$\frac{4867}{8717}$	$\frac{54938146}{12669}$	$\frac{607}{5225}$	$\frac{863}{5306}$	$\frac{1663}{5196}$	-2.73 – 1.43%
6	$\frac{793}{577}$	$\frac{2234}{16675}$	$-\frac{12137}{6441}$	$-\frac{19450}{5421}$	$\frac{8944}{17333}$	$\frac{201430625}{6661}$	$\frac{799}{7654}$	$\frac{1290}{9821}$	$\frac{974}{3283}$	-3.00 – 1.48%
7	$\frac{10401}{9794}$	$\frac{1356}{8845}$	$\frac{30469}{10756}$	$-\frac{11151}{3473}$	$\frac{3321}{7345}$	$\frac{1029376385}{36246}$	$\frac{377}{4242}$	$\frac{1838}{13631}$	$\frac{2446}{8123}$	-2.88 – 1.50%
8	$\frac{13867}{11300}$	$\frac{1847}{10004}$	$-\frac{899}{1084}$	$-\frac{24247}{8311}$	$\frac{2025}{4691}$	$\frac{208465759}{9898}$	$\frac{1195}{15107}$	$\frac{131}{957}$	$\frac{3041}{9933}$	-2.90 – 1.47%
9	$\frac{11292}{11417}$	$\frac{2667}{12475}$	$\frac{71783}{14593}$	$-\frac{23753}{8884}$	$\frac{15279}{38327}$	$\frac{170388497}{10015}$	$\frac{913}{12919}$	$\frac{2803}{19841}$	$\frac{16957}{54130}$	-2.87 – 1.41%
10	$\frac{4941}{9610}$	$\frac{830}{3611}$	$\frac{279834}{13813}$	$-\frac{4892}{2245}$	$\frac{1823}{4351}$	$\frac{11323441}{2063}$	$\frac{366}{5827}$	$\frac{1918}{12879}$	$\frac{2981}{9362}$	-2.83 – 1.42%
11	$\frac{12725}{12639}$	$\frac{1233}{4685}$	$\frac{29103}{5882}$	$-\frac{17641}{7391}$	$\frac{812}{2251}$	$\frac{93817310}{6013}$	$\frac{575}{9852}$	$\frac{1238}{8665}$	$\frac{2801}{8822}$	-2.79 – 1.32%
12	$\frac{5215}{5156}$	$\frac{1009}{3470}$	$\frac{77977}{15613}$	$-\frac{29719}{12774}$	$\frac{3890}{10879}$	$\frac{75236231}{4566}$	$\frac{579}{10655}$	$\frac{3977}{28471}$	$\frac{2948}{9301}$	-2.86 – 1.36%
13	$\frac{16753}{16972}$	$\frac{794}{2485}$	$\frac{100717}{15948}$	$-\frac{34434}{15637}$	$\frac{2493}{7441}$	$\frac{61372987}{4090}$	$\frac{479}{9560}$	$\frac{451}{3156}$	$\frac{1286}{3991}$	-2.82 – 1.34%
14	$\frac{9761}{9871}$	$\frac{1461}{4217}$	$\frac{281}{43}$	$-\frac{33703}{15770}$	$\frac{6378}{19271}$	$\frac{170777218}{11389}$	$\frac{543}{11569}$	$\frac{1880}{13293}$	$\frac{4685}{14541}$	-2.82 – 1.33%
15	$\frac{7329}{7286}$	$\frac{2281}{6042}$	$\frac{48733}{8398}$	$-\frac{8421}{4222}$	$\frac{1839}{6014}$	$\frac{87107021}{7039}$	$\frac{1578}{36371}$	$\frac{1153}{7805}$	$\frac{1189}{3613}$	-2.72 – 1.29%
16	$\frac{7733}{8163}$	$\frac{3533}{8665}$	$\frac{121822}{12527}$	$-\frac{6932}{3573}$	$\frac{2407}{8036}$	$\frac{57224710}{4651}$	$\frac{286}{6989}$	$\frac{377}{2558}$	$\frac{4584}{13895}$	-2.72 – 1.29%
17	$\frac{10349}{9079}$	$\frac{4121}{9390}$	$-\frac{49628}{15233}$	$-\frac{16811}{8933}$	$\frac{1143}{3880}$	$\frac{103494425}{8753}$	$\frac{1589}{41049}$	$\frac{817}{5544}$	$\frac{2196}{6637}$	-2.66 – 1.24%

Table 4.4: B-spline order-specific curve fits for estimating $C^{(2)}_{\text{approx}}$ via Equation (4.22a) when Δy is the minimum distance between *collocation points* from breakpoints stretched according to f_2 defined in (4.13).

k	a	b	c	d	e	f	g	h	i	relative error
5–11	$\frac{5958}{6049}$	$\frac{334}{5909}$	$-\frac{14563}{5926}$	$-\frac{35330}{11929}$	$\frac{1554}{3265}$	$\frac{4042664}{8379}$	$\frac{887}{9011}$	$\frac{2243}{13757}$	$\frac{1066}{1585}$	-11.30 – 17.11%
4	$-\frac{132683}{8121}$	$-\frac{8}{7617}$	$-\frac{1156372}{9759}$	$\frac{78080}{22333}$	$\frac{2}{10139}$	$\frac{83}{5144}$	$\frac{911}{2744}$	$-\frac{4791}{13862}$	$\frac{1479}{4412}$	-1.86 – 1.81 %
5	$-\frac{96752}{19419}$	$\frac{27}{10108}$	$-\frac{360604}{4723}$	$\frac{24551}{9533}$	$\frac{1}{5309}$	$\frac{277}{4330}$	$\frac{13424}{46671}$	$-\frac{3888}{10265}$	$\frac{1289}{3770}$	-0.50 – 0.32 %
6	$\frac{2635}{8541}$	$-\frac{299}{15112}$	$\frac{174058}{24237}$	$-\frac{17342}{13001}$	$\frac{2894}{10471}$	$\frac{291982}{9057}$	$\frac{68}{17203}$	$\frac{5579}{13080}$	$\frac{6911}{9355}$	-1.51 – 2.62 %
7	$\frac{7358}{11623}$	$-\frac{120}{6169}$	$\frac{82091}{23515}$	$-\frac{10147}{9621}$	$\frac{2735}{11778}$	$\frac{212175}{7154}$	$\frac{10}{6231}$	$\frac{10354}{24479}$	$\frac{2416}{3043}$	-1.70 – 3.97 %
8	$\frac{4751}{5346}$	$\frac{2143}{18802}$	$-\frac{46259}{19493}$	$-\frac{4506}{9193}$	$\frac{4}{6951}$	$\frac{49249}{1482}$	$-\frac{24}{8359}$	$\frac{959}{3662}$	$\frac{9327}{7114}$	-4.50 – 6.86 %
9	$\frac{17841}{19519}$	$\frac{553}{8538}$	$-\frac{20719}{8083}$	$-\frac{3783}{7057}$	$\frac{856}{10529}$	$\frac{121124}{5101}$	$-\frac{115}{30303}$	$\frac{2467}{7116}$	$\frac{4707}{4139}$	-3.68 – 7.17 %
10	$\frac{20122}{5145}$	$-\frac{5}{6272}$	$-\frac{1003532}{10415}$	$-\frac{11287}{15030}$	$\frac{3429}{17696}$	$\frac{258125}{9817}$	$\frac{7}{7694}$	$\frac{4286}{9151}$	$\frac{8126}{9217}$	-5.97 – 8.01 %
11	$\frac{32624}{11799}$	$\frac{23}{3905}$	$-\frac{466211}{6855}$	$-\frac{14065}{10992}$	$\frac{4693}{11010}$	$\frac{335615}{7641}$	$\frac{187}{7994}$	$\frac{4512}{8461}$	$\frac{1469}{2419}$	-6.09 – 6.61 %
12	$\frac{21510}{19531}$	$\frac{407}{3029}$	$-\frac{40991}{5317}$	$-\frac{34333}{13993}$	$\frac{7253}{9181}$	$\frac{1291629}{5929}$	$\frac{217}{3456}$	$\frac{2659}{8092}$	$\frac{4103}{9334}$	-6.88 – 6.21 %
13	$\frac{3889}{5285}$	$\frac{2389}{15117}$	$\frac{52947}{6029}$	$-\frac{17456}{5339}$	$\frac{4061}{4625}$	$\frac{11135709}{8452}$	$\frac{488}{7087}$	$\frac{1474}{6209}$	$\frac{383}{987}$	-6.88 – 5.89 %
14	$\frac{13010}{10487}$	$\frac{1375}{10628}$	$-\frac{201367}{12385}$	$-\frac{24232}{6743}$	$\frac{11512}{10801}$	$\frac{6297203}{2487}$	$\frac{428}{6171}$	$\frac{648}{3823}$	$\frac{4064}{11831}$	-6.54 – 5.79 %
15	$\frac{25912}{21893}$	$\frac{1831}{16699}$	$-\frac{58570}{4063}$	$-\frac{14377}{4017}$	$\frac{18889}{18281}$	$\frac{16561349}{4390}$	$\frac{272}{4179}$	$\frac{367}{2451}$	$\frac{919}{2686}$	-6.57 – 5.36 %
16	$\frac{3826}{5191}$	$\frac{800}{13057}$	$\frac{213790}{16397}$	$-\frac{16873}{4447}$	$\frac{10559}{9248}$	$\frac{84802177}{11958}$	$\frac{607}{9491}$	$\frac{1313}{14052}$	$\frac{2667}{8263}$	-6.11 – 5.04 %
17	$\frac{6127}{6960}$	$-\frac{163}{9791}$	$\frac{22545}{4961}$	$-\frac{115738}{31923}$	$\frac{10232}{10879}$	$\frac{167869433}{10467}$	$\frac{439}{8114}$	$\frac{10720}{81537}$	$\frac{3302}{10275}$	-5.35 – 4.96 %

Table 4.5: B-spline order-specific curve fits for estimating $C^{(2)}_{\text{approx}}$ via Equation (4.22a) when Δy is the minimum distance between *collocation points* from breakpoints stretched according to f_1 defined in (4.14).

k	a	b	c	d	e	f	g	h	i	relative error
5–11	$\frac{10951}{10966}$	$\frac{692}{17487}$	$-\frac{58794}{21577}$	$-\frac{12439}{4860}$	$\frac{1536}{1951}$	$\frac{1826729}{9846}$	$\frac{854}{8115}$	$\frac{1731}{7739}$	$\frac{2360}{5791}$	-23.87 – 19.78%
4	$-\frac{37181}{3006}$	$-\frac{35}{19004}$	$-\frac{1709799}{12403}$	$\frac{11429}{3303}$	$\frac{1}{4633}$	$\frac{207}{9529}$	$\frac{8025}{25267}$	$-\frac{1792}{5289}$	$\frac{1579}{6332}$	-2.73 – 2.66 %
5	$\frac{6843}{7364}$	$-\frac{113}{5126}$	$-\frac{19508}{11693}$	$-\frac{15410}{9853}$	$\frac{2215}{5596}$	$\frac{199827}{5060}$	$\frac{117}{5482}$	$\frac{3886}{7977}$	$\frac{3618}{7763}$	-0.63 – 1.38 %
6	$\frac{1309}{1894}$	$\frac{472}{6839}$	$\frac{10796}{10079}$	$-\frac{13268}{14331}$	$\frac{1942}{14501}$	$\frac{169657}{5987}$	$\frac{2}{3287}$	$\frac{1786}{3447}$	$\frac{9664}{13071}$	-3.14 – 5.22 %
7	$\frac{62991}{64619}$	$\frac{10271}{61625}$	$-\frac{146725}{39021}$	$-\frac{6349}{10362}$	$\frac{23}{3440}$	$\frac{26371}{794}$	$-\frac{17}{10006}$	$\frac{798}{1681}$	$\frac{13080}{14621}$	-4.53 – 9.31 %
8	$\frac{5701}{6404}$	$\frac{543}{10115}$	$-\frac{15926}{10845}$	$-\frac{9214}{11799}$	$\frac{1960}{8807}$	$\frac{759503}{31646}$	$\frac{9}{4685}$	$\frac{3636}{5393}$	$\frac{5996}{8919}$	-5.10 – 7.39 %
9	$\frac{57103}{12153}$	$\frac{349}{6313}$	$-\frac{292899}{2840}$	$-\frac{15197}{10802}$	$\frac{3317}{6840}$	$\frac{6115361}{140104}$	$\frac{431}{8216}$	$\frac{7073}{12325}$	$\frac{10286}{21381}$	-6.57 – 7.12 %
10	$\frac{4753}{6483}$	$\frac{215}{1719}$	$\frac{32327}{6251}$	$-\frac{8563}{4452}$	$\frac{1981}{2831}$	$\frac{1180287}{14438}$	$\frac{599}{7682}$	$\frac{1695}{4003}$	$\frac{3259}{8267}$	-8.44 – 6.56 %
11	$\frac{3058}{4871}$	$\frac{2994}{14713}$	$\frac{34703}{3382}$	$-\frac{15557}{4053}$	$\frac{6541}{5144}$	$\frac{5024384}{5503}$	$\frac{2720}{22829}$	$\frac{961}{20910}$	$\frac{2347}{7629}$	-6.87 – 7.13 %
12	$\frac{12242}{10351}$	$\frac{785}{5066}$	$-\frac{108847}{9907}$	$-\frac{38407}{8945}$	$\frac{8189}{5423}$	$\frac{54739986}{21557}$	$\frac{1903}{16894}$	$-\frac{381}{7330}$	$\frac{6661}{24933}$	-7.21 – 7.11 %
13	$\frac{24826}{20307}$	$\frac{4749}{40912}$	$-\frac{170233}{12219}$	$-\frac{4785}{1084}$	$\frac{16494}{11557}$	$\frac{720241352}{105099}$	$\frac{2930}{29579}$	$-\frac{807}{19174}$	$\frac{2725}{10439}$	-7.16 – 6.65 %
14	$\frac{13245}{12827}$	$\frac{163}{5022}$	$-\frac{25753}{4855}$	$-\frac{176237}{37876}$	$\frac{21379}{17208}$	$\frac{315490949}{7639}$	$\frac{4100}{49413}$	$\frac{2}{4983}$	$\frac{1942}{7671}$	-6.65 – 6.31 %
15	$\frac{5358}{5287}$	$-\frac{142}{11949}$	$-\frac{16365}{3631}$	$-\frac{173358}{39355}$	$\frac{10908}{10097}$	$\frac{529204799}{8657}$	$\frac{119}{1628}$	$\frac{216}{7747}$	$\frac{1637}{6397}$	-6.47 – 5.75 %
16	$\frac{8995}{9151}$	$-\frac{367}{3056}$	$-\frac{13906}{5041}$	$-\frac{40441}{10087}$	$\frac{4335}{4703}$	$\frac{366898466}{4633}$	$\frac{324}{5153}$	$\frac{440}{8139}$	$\frac{1633}{6441}$	-5.99 – 5.43 %
17	$\frac{19825}{20211}$	$-\frac{3148}{12971}$	$-\frac{7791}{2918}$	$-\frac{27739}{8000}$	$\frac{4651}{6107}$	$\frac{516527143}{8065}$	$\frac{321}{5962}$	$\frac{1049}{12527}$	$\frac{1391}{5436}$	-5.04 – 5.04 %

4.1.5 Implicitly Treated Linearized Terms

Within the confines of (4.9), any implicit terms must be expressed as a linear operator acting only on conserved density ρ, momentum $m = \rho u$, and total energy $e = \rho E$. Precious little of the spatial Navier–Stokes operator from Section 3.1 is linear in this sense— we must carve it up [21].

The goal is to separate relevant terms into an explicitly treated nonlinear portion plus a linear contribution satisfying these implicit operator restrictions. A hypothetical example is

$$\begin{aligned} \rho^{-1}\Delta m = &\left(\rho^{-1} - \left\{\rho^{-1}\right\}_0\right)\Delta m \\ &+ \left\{\rho^{-1}\right\}_0 \Delta m \end{aligned} \tag{4.25}$$

where $\left\{\rho^{-1}\right\}_0$ denotes the term ρ^{-1} evaluated at some reference state. The example sets a useful convention wherein the final line(s) of each expansion contains the linearized, implicit-ready portion. An explicit-only operator is recovered whenever reference values are taken to be zero.

The spatial discretization chosen in Section 4.1.1 does not permit linearization reference quantities to vary in the x or z directions because doing so would spoil the orthogonality conditions permitting decoupled, wavenumber-by-wavenumber implicit solves in (4.10). Either a one-dimensional, y-varying profile or a constant reference value is possible. A constant reference value, which should be chosen from the wall as grid spacing is smallest there, would have smaller runtime overhead but would provide smaller time step gains. The present work employs the former, a one-dimensional reference state profile across the wall-normal direction, as it was expected to permit

larger stable time steps when nontrivial thermodynamic property differences occur in the inhomogeneous direction.

Implicit operator implementation details become more complicated when "off diagonal" state derivatives are treated implicitly. By "off diagonal" we mean derivatives of conserved state appearing in equations other than their own. For example, the term $\nabla \cdot m$ in (3.1a) or derivatives of the wall-normal momentum appearing in the streamwise portion of (3.1b). In contrast, an "on diagonal" example is the divergence of total energy appearing within (3.1c). Handling off-diagonal terms implicitly is better from the perspective of taking the largest possible time step while maintaining stability at fixed communication cost but it incurs both an associated programming and runtime overhead.

The implicit treatment of the linearized viscous terms begins by expanding three mixed-order, nonlinear contributions to (3.1) and using the symmetry of τ:

$$\nabla \cdot \tau = 2\,\mathrm{sym}\left(\nabla \frac{m}{\rho}\right)\nabla\mu + \mu\Delta\frac{m}{\rho} + (\mu+\lambda)\nabla\nabla\cdot\frac{m}{\rho} + \left(\nabla\cdot\frac{m}{\rho}\right)\nabla\lambda \tag{4.26}$$

$$\nabla\cdot\tau\frac{m}{\rho} = \frac{m}{\rho}\cdot(\nabla\cdot\tau) + \mathrm{tr}\left(\tau^{\mathsf{T}}\nabla\frac{m}{\rho}\right) \tag{4.27}$$

$$\nabla\cdot\mu\nabla T = \nabla\mu\cdot\nabla T + \mu\Delta T. \tag{4.28}$$

Only the second-order terms where a linear operator acts on conserved state,

$$\mu\Delta\frac{m}{\rho} \qquad (\mu+\lambda)\nabla\nabla\cdot\frac{m}{\rho} \qquad \frac{m}{\rho}\cdot\mu\Delta\frac{m}{\rho} \qquad \frac{m}{\rho}\cdot(\mu+\lambda)\nabla\nabla\cdot\frac{m}{\rho} \qquad \mu\Delta T,$$

are linearized. That is, their derivatives are expanded using the chain rule until they can be expressed as operations on ρ, m, or e. Any nonlinear coefficient scaling a second-order term is linearized about a reference quantity like (4.25) to produce implicit-ready

results. To provide two concrete examples, the leftmost candidate generates

$$\begin{aligned}\mu\Delta\frac{m}{\rho} &= 2\mu\rho^{-2}\left[\rho^{-1}m\left(\nabla\rho\right)^2-\left(\nabla m\right)\nabla\rho\right]\\ &\quad+\left(\mu\rho^{-1}-\left\{\mu\rho^{-1}\right\}_0\right)\Delta m-\left(\mu\rho^{-2}m-\left\{\mu\rho^{-2}m\right\}_0\right)\Delta\rho\\ &\quad+\left\{\mu\rho^{-1}\right\}_0\Delta m-\left\{\mu\rho^{-2}m\right\}_0\Delta\rho\end{aligned}\tag{4.29}$$

while the rightmost one produces a monstrosity due to the nonlinear constitutive relations,

$$\begin{aligned}\mu\Delta T =&-2\gamma\mu\rho^{-2}\nabla\rho\cdot\left(\nabla p-\rho^{-1}p\nabla\rho\right)\\ &-\gamma\left(\gamma-1\right)\mathrm{Ma}^2\mu\rho^{-2}\left[\mathrm{tr}\left(\nabla m^{\mathsf{T}}\nabla m\right)-\rho^{-1}\left[2\nabla m^{\mathsf{T}}m\cdot\nabla\rho-\rho^{-1}m^2\left(\nabla\rho\right)^2\right]\right]\\ &+\gamma\left(\gamma-1\right)\left(\mu\rho^{-1}-\left\{\mu\rho^{-1}\right\}_0\right)\Delta e-\gamma\left(\gamma-1\right)\mathrm{Ma}^2\left(\mu\rho^{-2}m-\left\{\mu\rho^{-2}m\right\}_0\right)\cdot\Delta m\\ &+\gamma\left(\mu\rho^{-2}\left(\left(\gamma-1\right)e-2p\right)-\left\{\mu\rho^{-2}\left(\left(\gamma-1\right)e-2p\right)\right\}_0\right)\Delta\rho\\ &+\gamma\left(\gamma-1\right)\left\{\mu\rho^{-1}\right\}_0\Delta e-\gamma\left(\gamma-1\right)\mathrm{Ma}^2\left\{\mu\rho^{-2}m\right\}_0\cdot\Delta m\\ &+\gamma\left\{\mu\rho^{-2}\left(\left(\gamma-1\right)e-2p\right)\right\}_0\Delta\rho.\end{aligned}\tag{4.30}$$

The implicit treatment of acoustics focuses on first-order, pressure-like terms in the momentum and energy equations. These terms give rise to the acoustic characteristics traveling at speeds $u\pm a$ in the inviscid limit of the hyperbolic Euler equations. They are fundamentally an off-diagonal phenomenon requiring off-diagonal implicit treatment. The pressure gradient term in (3.1b) yields

$$\begin{aligned}\nabla p =&\left(\gamma-1\right)\mathrm{Ma}^2\left(\frac{1}{2}\left(m^2\rho^{-2}-\left\{m^2\rho^{-2}\right\}_0\right)\nabla\rho-\nabla m^{\mathsf{T}}\left(\rho^{-1}m-\left\{\rho^{-1}m\right\}_0\right)\right)\\ &+\left(\gamma-1\right)\nabla e+\frac{\gamma-1}{2}\mathrm{Ma}^2\left\{m^2\rho^{-2}\right\}_0\nabla\rho-\left(\gamma-1\right)\mathrm{Ma}^2\nabla m^{\mathsf{T}}\left\{\rho^{-1}m\right\}_0.\end{aligned}\tag{4.31}$$

The total energy convection and pressure work contributions, $\nabla \cdot (e+p)\frac{m}{\rho}$, in (3.1c) are likewise manipulated.

Once the complete off-diagonal linearized acoustic terms are computed implicitly, the incremental cost to similarly treat the convective term from Equation (3.1b) is small. The linearization is

$$\begin{aligned}\nabla \cdot \left(\frac{m}{\rho} \otimes m\right) = &(\nabla m + I \nabla \cdot m)\left(\rho^{-1} m - \left\{\rho^{-1} m\right\}_0\right) \\ &- \left(\rho^{-1} m \otimes \rho^{-1} m - \left\{\rho^{-1} m \otimes \rho^{-1} m\right\}_0\right) \nabla \rho \\ &+ (\nabla m + I \nabla \cdot m)\left\{\rho^{-1} m\right\}_0 - \left\{\rho^{-1} m \otimes \rho^{-1} m\right\}_0 \nabla \rho . \end{aligned} \tag{4.32}$$

Implicitly treating mean convection in all equations replaces u_x, u_y, and u_z in criterion (4.15) with $|u_x - u_{x0}|$, $\left|u_y - u_{y0}\right|$, and $|u_z - u_{z0}|$, similar to the appearance of $\nu - \nu_0$ in (4.19). While such large time steps should not be taken in time-accurate simulations because the temporal discretization error would adversely impact turbulent dynamics, these time steps can greatly accelerate time-inaccurate simulations advancing across uninteresting transients in flows with sufficiently low Re. For example, changing Re, Pr, or Ma often causes a lengthy transient in the total energy in the domain. Time-inaccurate simulation may be used until this total energy is again stationary. Of course, time-accurate calculations must then be performed until the turbulent dynamics become stationary prior to collecting statistics.

In summary, this work treats implicitly all terms identified as candidates in the preceding discussion. In the full context of (3.1), the complete implicit-ready linearized

operator is

$$\frac{\partial \rho}{\partial t} = \quad -\nabla \cdot m \tag{4.33a}$$

$$\begin{aligned}\frac{\partial m}{\partial t} = \ldots &+ \overleftrightarrow{c^{u\otimes u}}\nabla\rho - (\nabla m + I\nabla\cdot m)\,\overrightarrow{c^{u}} - \frac{\gamma-1}{2}c^{u^2}\nabla\rho \\ &+ (\gamma-1)\,\nabla m^{\mathsf{T}}\overrightarrow{c^{u}} - \frac{\gamma-1}{\mathrm{Ma}^2}\nabla e \\ &- \mathrm{Re}^{-1}\overrightarrow{c^{\nu u}}\Delta\rho - \mathrm{Re}^{-1}\left(\alpha+\frac{1}{3}\right)(\nabla\nabla\rho)\,\overrightarrow{c^{\nu u}} \\ &+ \mathrm{Re}^{-1}c^{\nu}\Delta m + \mathrm{Re}^{-1}\left(\alpha+\frac{1}{3}\right)c^{\nu}\nabla\nabla\cdot m + \ldots\end{aligned} \tag{4.33b}$$

$$\begin{aligned}\frac{\partial e}{\partial t} = \ldots &- \overrightarrow{c^{e}_{\nabla\rho}}\cdot\vec{\nabla}\rho - c^{e}_{\nabla\cdot m}\nabla\cdot m - \gamma\overrightarrow{c^{u}}\cdot\nabla e + \frac{\gamma}{\mathrm{RePr}\,(\gamma-1)}c^{e}_{\Delta\rho}\Delta\rho \\ &- \frac{\gamma\mathrm{Ma}^2}{\mathrm{RePr}}\overrightarrow{c^{\nu u}}\cdot\Delta m + \frac{\gamma}{\mathrm{RePr}}c^{\nu}\Delta e \\ &+ \frac{\mathrm{Ma}^2}{\mathrm{Re}}\left(-c^{\nu u^2}\Delta\rho - \left(\alpha+\frac{1}{3}\right)\mathrm{tr}\left(\nabla\nabla\rho^{\mathsf{T}}\overleftrightarrow{c^{\nu u\otimes u}}\right)\right) \\ &+ \frac{\mathrm{Ma}^2}{\mathrm{Re}}\left(+\overrightarrow{c^{\nu u}}\cdot\Delta m + \left(\alpha+\frac{1}{3}\right)\overrightarrow{c^{\nu u}}\cdot\nabla\nabla\cdot m\right) + \ldots\end{aligned} \tag{4.33c}$$

where some reference values have physically motivated superscripts

$$\overrightarrow{c^{u}} = \left\{\rho^{-1}m\right\}_0 = \begin{pmatrix} c^{u_x} \\ c^{u_y} \\ c^{u_z}\end{pmatrix} \qquad\qquad c^{u^2} = \left\{m^2\rho^{-2}\right\}_0$$

$$c^{\nu} = \left\{\rho^{-1}\mu\right\}_0 \qquad \overrightarrow{c^{\nu u}} = \left\{\rho^{-2}\mu m\right\}_0 = \begin{pmatrix} c^{\nu u_x} \\ c^{\nu u_y} \\ c^{\nu u_z}\end{pmatrix} \qquad c^{\nu u^2} = \left\{\rho^{-3}\mu m^2\right\}_0$$

$$\overleftrightarrow{c^{u\otimes u}} = \left\{\rho^{-1}m\otimes\rho^{-1}m\right\}_0 = \begin{pmatrix} c^{u_xu_x} & c^{u_xu_y} & c^{u_xu_z} \\ c^{u_xu_y} & c^{u_yu_y} & c^{u_yu_z} \\ c^{u_xu_z} & c^{u_yu_z} & c^{u_zu_z}\end{pmatrix}$$

$$\overleftrightarrow{c^{\nu u\otimes u}} = \left\{\rho^{-3}\mu m\otimes m\right\}_0 = \begin{pmatrix} c^{\nu u_xu_x} & c^{\nu u_xu_y} & c^{\nu u_xu_z} \\ c^{\nu u_xu_y} & c^{\nu u_yu_y} & c^{\nu u_yu_z} \\ c^{\nu u_xu_z} & c^{\nu u_yu_z} & c^{\nu u_zu_z}\end{pmatrix}$$

while the remaining reference values

$$\overrightarrow{c^{e}_{\nabla\rho}} = \left\{m\rho^{-2}\left((\gamma-2)\,e-2p\right)\right\}_0 = \begin{pmatrix} c^{e_x}_{\nabla\rho} \\ c^{e_y}_{\nabla\rho} \\ c^{e_z}_{\nabla\rho} \end{pmatrix}$$

$$c^{e}_{\nabla\cdot m} = \left\{\rho^{-1}\left(e+p\right)\right\}_0 \qquad\qquad c^{e}_{\Delta\rho} = \left\{\mu\rho^{-2}\left((\gamma-1)\,e-2p\right)\right\}_0$$

have superscripts indicating the relevant equation and subscripts indicating the associated term. An investigation of the effectiveness of this linearized operator at mitigating convective and diffusive restrictions on stable time sizes is delayed until Section 5.4.

4.1.6 Implementation of the Discrete Linear Operator

Following Algorithm 1 in light of (4.7), operator $M+\varphi L$ must be implemented for arbitrary φ, k_m, and k_n. L is the discrete form of the linear terms summarized in the previous section. Notice for any reference value $c^{\bullet}$ left-multiplying by the diagonal matrix

$$C^{\bullet} = \begin{bmatrix} c^{\bullet}|_{y=0} & & 0 \\ & \ddots & \\ 0 & & c^{\bullet}|_{y=L} \end{bmatrix} \tag{4.34}$$

scales linear operators in a way that accommodates wall-normal variations in reference quantities. For example, applying $C^{\nu}D^{(2)}$ rather than $D^{(2)}$ scales the result at collocation point $y=y_l$ by $c^{\nu}|_{y=y_l}$.

Switching to a blocked matrix representation employing five scalar conserved state fields, the complete, implicit-ready discrete operator $M+\varphi L$ is shown in Figure 4.3. The representation chosen highlights how the full operator is built from discrete operators applied to individual state fields. For simulations with no mean velocity

in the spanwise direction, the reference coefficient matrices C^{u_z} and $C^{\nu u_z}$ may be taken as zero to reduce the required linear algebra. If desired, the density equation and density terms in the other equations may be treated fully explicitly to reduce operator assembly and factorization overhead. Previous work by Guarini [59] did not treat density implicitly. Implicit density treatment reduces by one the number of scalar fields that must be converted from physical space to wave space during each substep in problems, like channel flows, with relatively simple forcing. Finally, implicitly handling only the wall-normal directions may be accomplished by setting k_m and k_n to zero. Doing so results in a wavenumber independent operator requiring factorization only once per Runge–Kutta substep.

The discretized implicit operator $M + \varphi L$ depicted in Figure 4.3 is a blocked square matrix with banded submatrices (BSMBSM). Matrix A is a "BSMBSM" when

$$A = \begin{pmatrix} B^{0,0} & \cdots & B^{0,S-1} \\ \vdots & \ddots & \vdots \\ B^{S-1,0} & \cdots & B^{S-1,S-1} \end{pmatrix}$$

where every $B^{i,j}$ is an `n` by `n` banded submatrix containing `kl` subdiagonals and `ku` superdiagonals. The convention is henceforth adopted that that lowercase fixed-width identifiers indicate submatrix details while uppercase ones indicate global details for A. The structure of a BSMBSM is defined completely by the parameters `S`, `n`, `kl`, and `ku`. The number of rows and columns is $\mathtt{N} = \mathtt{S}\,\mathtt{n}$.

Applying A from individually contiguous, banded submatrices $B_{i,j}$ is both convenient and efficient. For example, banded matrix accumulation operations and boundary condition imposition are simple in such a storage format. However, using individually contiguous, banded submatrices is highly inefficient for solving linear equations.

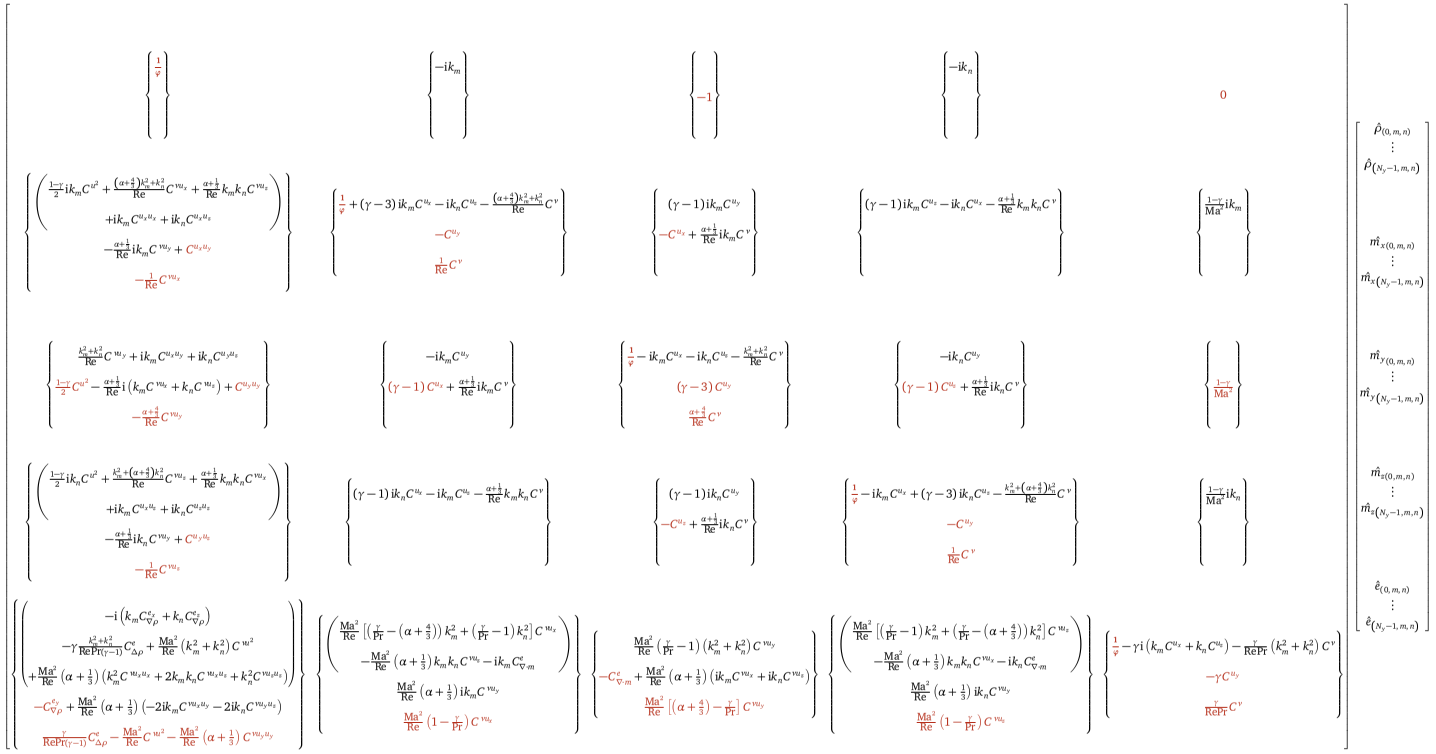

Figure 4.3: The complete discrete operator $M + \varphi L$ used for implicit time advance is depicted. Notice the leftmost scalar factor φ. The $3N_y \times N_y$ blocked vectors surrounded by curly braces are to be "dotted" against the blocked vector $\begin{bmatrix} M & D^{(1)} & D^{(2)} \end{bmatrix}^{\mathsf{T}}$ to form $N_y \times N_y$ subblocks. Each of M, $D^{(1)}$, and $D^{(2)}$ is a $N_y \times N_y$ banded matrix. Reference quantities like C^{ν} are $N_y \times N_y$ diagonal matrices. The complex-valued, wavenumber-dependent operator takes wall-normal B-spline coefficients to B-spline collocation point values. A real-valued, wavenumber-independent operator is the degenerate case obtained by setting $k_m = k_n = 0$; the nonzero terms in this special circumstance are colored.

With appropriate renumbering of A, solving linear equations can be done efficiently. The zero-indexed permutation vector

$$q(i) = (i \bmod S)\, n + \lfloor i/S \rfloor$$

may always be used to convert a BSMBSM into a globally banded $\mathtt{N}$ by $\mathtt{N}$ matrix with minimum bandwidth. More concretely, the permutation matrix P uniquely defined by vector q causes PAP^{T} to have $\mathtt{KL} = \mathtt{S}\,(\mathtt{kl}+1)-1$ subdiagonals and $\mathtt{KU} = \mathtt{S}\,(\mathtt{ku}+1)-1$ superdiagonals summing to overall bandwidth $\mathtt{KL}+1+\mathtt{KU} = \mathtt{S}\,(\mathtt{kl}+\mathtt{ku}+2)-1$. The reverse permutation vector has a simple closed form

$$q^{-1}(i) = (i \bmod n)\, S + \lfloor i/n \rfloor.$$

With $A_{i,j}$ in hand, the banded renumbering can be formed using the relationships

$$A|_{i,j} = PAP^{\mathsf{T}}\Big|_{q^{-1}(i),q^{-1}(j)}, \qquad PAP^{\mathsf{T}}\Big|_{i,j} = A|_{q(i),q(j)}. \tag{4.35}$$

This renumbering is factorizable in order

$$\mathtt{N}\,(\mathtt{KL}+1+\mathtt{KU})^2 = \mathtt{S}\,\mathtt{n}\,(\mathtt{S}\,(\mathtt{kl}+\mathtt{ku}+2)-1)^2 \tag{4.36}$$

floating point operations to find $LU = PAP^{\mathsf{T}}$. Schulz et al. [140] showed that modern many-core architectures excel at performing many such conveniently parallel factorizations. The linear equation $AX = B$, which is equivalent to $LUPX = PB$, then has the solution

$$X = A^{-1}B = P^{\mathsf{T}}\,(LU)^{-1}\,PB$$

where inversion has been used as a notational convenience representing triangular back substitution.

The efficiency of this BSMBSM linear solution procedure, including whether it makes the wavenumber-dependent or wavenumber-independent variant of Figure 4.3 more advantageous, will be quantified in Section 5.4.

4.2 Boundary Conditions

This section discusses the required continuous boundary conditions for the problems of interest and how they are mapped into a discrete form.

4.2.1 Isothermal Walls with and without Transpiration

An isothermal boundary requires specifying a constant temperature T_{w}. Both no-slip and transpiring walls are of interest. The former possess constant wall velocities $u_{\mathrm{w}} = v_{\mathrm{w}} = w_{\mathrm{w}} = 0$ while the later permit nonzero-but-constant velocities. A transpiring wall condition is achieved by setting $v_{\mathrm{w}} \neq 0$. One thermodynamic quantity must be allowed to vary for such boundary conditions to be well-posed [123]. Allowing ρ to vary is simplest given the present use of density, momentum, and total energy to represent system state. Using $\partial_t u = \partial_t v = \partial_t w = 0$, smoothness, and the constitutive assumptions yields four scalar constraints relating the evolution of momentum and

total energy to the evolution of density:

$$\partial_t (\rho u)_\mathrm{w} = u_\mathrm{w} \partial_t \rho_\mathrm{w} + \rho_\mathrm{w} \partial_t u_\mathrm{w} = u_\mathrm{w} \partial_t \rho_\mathrm{w} \tag{4.37a}$$

$$\partial_t (\rho v)_\mathrm{w} = v_\mathrm{w} \partial_t \rho_\mathrm{w} + \rho_\mathrm{w} \partial_t v_\mathrm{w} = v_\mathrm{w} \partial_t \rho_\mathrm{w} \tag{4.37b}$$

$$\partial_t (\rho u)_\mathrm{w} = u_\mathrm{w} \partial_t \rho_\mathrm{w} + \rho_\mathrm{w} \partial_t u_\mathrm{w} = u_\mathrm{w} \partial_t \rho_\mathrm{w} \tag{4.37c}$$

$$\begin{aligned} \partial_t (\rho E)_\mathrm{w} &= E_\mathrm{w} \partial_t \rho_\mathrm{w} + \rho_\mathrm{w} \partial_t E_\mathrm{w} = E_\mathrm{w} \partial_t \rho_\mathrm{w} \\ &= \left(\frac{T_\mathrm{w}}{\gamma(\gamma-1)} + \frac{\mathrm{Ma}^2}{2} \left(u_\mathrm{w}^2 + v_\mathrm{w}^2 + w_\mathrm{w}^2 \right) \right) \partial_t \rho . \end{aligned} \tag{4.37d}$$

The above evolution conditions are strongly enforced by modifying the first and/or last several rows of the linear implicit operator, shown in Figure 4.3, using the way B-spline basis support limits the number of nonzero coefficients at the wall, as discussed in Section 4.1.3

4.2.2 Nonreflecting Freestream Boundary Conditions

When simulating problems on semi-infinite domains, such as flat plates, nonreflecting freestream boundary conditions are necessary. Without these, acoustic waves generated by the flow cannot leave the domain. The trapped acoustics then accumulate causing an aphysical partition of energy and corrupting the simulated statistics.

Following Engquist and Majda [42], Giles [56, 57] developed localized, approximate two-dimensional, unsteady nonreflecting boundary conditions for the Euler equations. Giles' boundary conditions are adopted over the "locally one-dimensional inviscid" relations of Poinsot and Lele [123] because other codes with similar numerics have successfully employed Giles' conditions for our problems of interest. While Rowley and Colonius [130] present higher order techniques expected to perform better than

Giles' approach, what they describe is considerably more complex to implement. Saxer and Giles [134] extended the technique to three dimensions for transonic axial flow turbomachinery computations. Guarini [59] summarizes the Cartesian extension of Giles' approach to three spatial dimensions without reproducing the associated analysis. Medida [102] lucidly catalogs the intermediate results necessary in three dimensions. Baum et al. [7] provides useful test cases as well as examples of correct boundary condition behavior.

4.2.2.1 The Abstract Approach

Giles' approach is now reviewed following Guarini's presentation with the goal of setting notation suitable for presenting and manipulating Medida's results for nonreflecting x boundaries in three-dimensional, Cartesian coordinates. For complete details, especially motivations and proofs, the work of Giles, Medida, and Guarini should be consulted in that respective order.

For the state vector

$$U = \{\rho, u, v, w, p\} \tag{4.38a}$$

the Euler equations, using the ideal gas equation of state

$$\rho a^2 = \gamma p, \tag{4.38b}$$

can be written as follows:

$$\frac{\partial}{\partial t}U + A\frac{\partial}{\partial x}U + B\frac{\partial}{\partial y}U + C\frac{\partial}{\partial z}U = 0 \tag{4.38c}$$

$$A=\begin{bmatrix} u & \rho & 0 & 0 & 0 \\ 0 & u & 0 & 0 & \frac{1}{\rho} \\ 0 & 0 & u & 0 & 0 \\ 0 & 0 & 0 & u & 0 \\ 0 & \gamma p & 0 & 0 & u \end{bmatrix} \quad B=\begin{bmatrix} v & 0 & \rho & 0 & 0 \\ 0 & v & 0 & 0 & 0 \\ 0 & 0 & v & 0 & \frac{1}{\rho} \\ 0 & 0 & 0 & v & 0 \\ 0 & 0 & \gamma p & 0 & v \end{bmatrix} \quad C=\begin{bmatrix} w & 0 & 0 & \rho & 0 \\ 0 & w & 0 & 0 & 0 \\ 0 & 0 & w & 0 & 0 \\ 0 & 0 & 0 & w & \frac{1}{\rho} \\ 0 & 0 & 0 & \gamma p & w \end{bmatrix}. \tag{4.38d}$$

This system of equations identically describes the behavior of an analogous U^* whenever all of

$$U^*=\left\{\frac{\rho}{\rho_0},\frac{u}{u_0},\frac{v}{u_0},\frac{w}{u_0},\frac{p}{\rho_0 u_0^2}\right\} \qquad t_0=\frac{l_0}{u_0} \qquad a_0=u_0 \tag{4.39}$$

hold. Therefore, all dimensional results obtained for U remain unchanged in the setting of U^*.

Consider perturbations

$$\delta U=\{\delta\rho,\delta u,\delta v,\delta w,\delta p\}$$

taken about some steady, uniform reference state $\bar{U}$ so that

$$U=\bar{U}+\delta U.$$

The short-time perturbation evolution is governed by the linearized Euler equations

$$\frac{\partial}{\partial t}\delta U+\bar{A}\frac{\partial}{\partial x}\delta U+\bar{B}\frac{\partial}{\partial y}\delta U+\bar{C}\frac{\partial}{\partial z}\delta U=0 \tag{4.40}$$

where matrices $\bar{A}$, $\bar{B}$, and $\bar{C}$ are evaluated at $\bar{U}$. This linearized system satisfies the prerequisites for Giles' analysis. Assuming a solution of the form

$$\delta U=e^{\mathrm{i}\left(k_x x+k_y y+k_z z-\omega t\right)}\delta\hat{U}^R \tag{4.41}$$

and substituting into the linearized equations produces

$$\mathrm{i}\left(-\omega I + k_x\bar{A} + k_y\bar{B} + k_z\bar{C}\right)\delta\hat{U}^R = 0 \tag{4.42}$$

which has nontrivial solutions only if the dispersion relation

$$\det\left(-\omega I + k_x\bar{A} + k_y\bar{B} + k_z\bar{C}\right) = 0 \tag{4.43}$$

holds. Defining $\lambda_x = k_x/\omega$, $\lambda_y = k_y/\omega$, and λ_z/ω, the dispersion relation can be equivalently expressed as

$$\det\left(-I + \lambda_x\bar{A} + \lambda_y\bar{B} + \lambda_z\bar{C}\right) = 0. \tag{4.44}$$

Assuming $\bar{A}$ is invertible and applying $-\left(\mathrm{i}\omega\bar{A}\right)^{-1}$ to Equation (4.42), one finds

$$\left(\bar{A}^{-1} - \lambda_x I - \lambda_y\bar{A}^{-1}\bar{B} - \lambda_z\bar{A}^{-1}\bar{C}\right)\delta\hat{U}^R = 0. \tag{4.45}$$

This is an eigenvalue problem in λ_x where $\delta\hat{U}^R$ is the eigenvector and a solution to the right null space problem. The signs of the associated eigenvalues, determined using the magnitude of $\bar{u}$ relative to $\bar{a}$, are required to determine how many characteristics are entering or exiting through the boundary. The left null space problem,

$$V^L\left(\bar{A}^{-1} - \lambda_x I - \lambda_y\bar{A}^{-1}\bar{B} - \lambda_z\bar{A}^{-1}\bar{C}\right) = 0, \tag{4.46}$$

naturally gives rise to the associated left null vector V^L.

Giles, following Engquist and Majda, used several orthogonality properties to build the exact, nonreflecting boundary conditions

$$V_n^L\delta U = 0 \tag{4.47}$$

for each $V_n^L = V^L\left(k_{x_n}\right)$ corresponding to either incoming or outgoing waves. This exact condition is approximated using a Taylor series in λ_y and λ_z for reasons of computational tractability. Truncating the series is equivalent to assuming waves have a small angle of incidence to the boundary. To first order,

$$V_n^L\Big|_{\lambda_y,\lambda_z=0}\delta U + \lambda_y \left.\frac{dV_n^L}{d\lambda_y}\right|_{\lambda_y,\lambda_z=0}\delta U + \lambda_z \left.\frac{dV_n^L}{d\lambda_z}\right|_{\lambda_y,\lambda_z=0}\delta U \approx 0. \tag{4.48}$$

As noted by Engquist and Majda [42] and later expounded upon by Trefethen and Halpern [167], only particular higher-order series truncations of this form lead to well-posedness. Moreover, the straightforward application of even this first order approximation requires either ad hoc [56, 102] or systematic [130] modification to produce well-behaved inflow constraints. Multiplying by $-\mathrm{i}\omega$, Fourier transforming in both time and space, and using that $\bar{U}$ and therefore V_n^L are both steady and uniform yields

$$\frac{\partial}{\partial t}V^L\delta U \approx \frac{dV^L}{d\lambda_y}\frac{\partial}{\partial y}\delta U + \frac{dV^L}{d\lambda_z}\frac{\partial}{\partial z}\delta U \tag{4.49}$$

where the $\lambda_y, \lambda_z = 0$ and subscript n are now suppressed. Inserting $V^{L^{-1}}V^L$,

$$\frac{\partial}{\partial t}V^L\delta U \approx \frac{dV^L}{d\lambda_y}V^{L^{-1}}\frac{\partial}{\partial y}V^L\delta U + \frac{dV^L}{d\lambda_z}V^{L^{-1}}\frac{\partial}{\partial z}V^L\delta U. \tag{4.50}$$

Defining characteristic variables using the action of V^L,

$$\delta C = V^L\delta U, \tag{4.51}$$

allows writing a more compact form

$$\frac{\partial}{\partial t}\delta C \approx B^G\frac{\partial}{\partial y}\delta C + C^G\frac{\partial}{\partial z}\delta C \tag{4.52}$$

employing the notation

$$B^G = \frac{dV^L}{d\lambda_y} V^{L^{-1}} \qquad\qquad C^G = \frac{dV^L}{d\lambda_z} V^{L^{-1}} \tag{4.53}$$

where the superscript G is meant to suggest "Giles".

Condition (4.52) intermingles the constraints for inflow and outflow conditions. Only the incoming characteristics should be evolved. Which waves are incoming may be determined by comparing the magnitude of $\bar{u}$ relative to $\bar{a}$. Care must be taken to account for the choices made in representing V^L and to correctly treat left versus right boundaries. Notationally, it will later be convenient to have a projection

$$P^G : \delta C \to \delta C \tag{4.54}$$

such that

$$P^G \frac{\partial}{\partial t} \delta C \approx P^G B^G \frac{\partial}{\partial y} \delta C + P^G C^G \frac{\partial}{\partial z} \delta C \tag{4.55}$$

imposes conditions on only incoming characteristics. In contrast, applying

$$I - P^G : \delta C \to \delta C \tag{4.56}$$

recovers the outgoing characteristics not constrained by the boundary condition For some $\bar{U}$ possessing an agreed upon relationship between $\bar{u}$ and $\bar{a}$, specifying V^L, P^G, B^G, and C^G concretely states a Giles-like nonreflecting x boundary condition for the Euler equations.

4.2.2.2 Subsonic Inflow and Outflow Conditions

In Section 5.8 of his thesis, Medida presents two such concrete nonreflecting boundary condition specifications for subsonic inflows and outflows where $0 < \bar{u} <$

$\bar{a}$. Medida's Equations (5.78) and (5.79) specify the transformations to and from characteristic variables:

$$V^L = \begin{bmatrix} -\bar{a}^2 & 0 & 0 & 0 & 1 \\ 0 & 0 & \bar{\rho}\bar{a} & 0 & 0 \\ 0 & 0 & 0 & \bar{\rho}\bar{a} & 0 \\ 0 & \bar{\rho}\bar{a} & 0 & 0 & 1 \\ 0 & -\bar{\rho}\bar{a} & 0 & 0 & 1 \end{bmatrix} \quad V^{L-1} = \begin{bmatrix} -\frac{1}{\bar{a}^2} & 0 & 0 & \frac{1}{2\bar{a}^2} & \frac{1}{2\bar{a}^2} \\ 0 & 0 & 0 & \frac{1}{2\bar{\rho}\bar{a}} & -\frac{1}{2\bar{\rho}\bar{a}} \\ 0 & \frac{1}{\bar{\rho}\bar{a}} & 0 & 0 & 0 \\ 0 & 0 & \frac{1}{\bar{\rho}\bar{a}} & 0 & 0 \\ 0 & 0 & 0 & \frac{1}{2} & \frac{1}{2} \end{bmatrix}. \quad (4.57)$$

For this V^L, the characteristics δC travel at speeds $[\bar{u}, \bar{u}, \bar{u}, \bar{u}+\bar{a}, \bar{u}-\bar{a}]$. Direct computation shows

$$\det V^L = -2\bar{\rho}^3\bar{a}^5$$

and so V^L is always nonsingular for a realizable reference state. Using the outward normal n with value -1 or 1 at a left or right boundary, respectively,

$$P^G = \left(n \begin{bmatrix} \bar{u} & 0 & 0 & 0 & 0 \\ 0 & \bar{u} & 0 & 0 & 0 \\ 0 & 0 & \bar{u} & 0 & 0 \\ 0 & 0 & 0 & \bar{u}+\bar{a} & 0 \\ 0 & 0 & 0 & 0 & \bar{u}-\bar{a} \end{bmatrix} < 0 \right) \quad (4.58)$$

specifies the appropriate projection operator if comparisons are deemed to indicate 1 if true and 0 if false. Medida's Equations (5.82) and (5.83) provide conditions for which reflection coefficients were not reported:

$$B^G = \begin{bmatrix} 0 & 0 & 0 & 0 & 0 \\ 0 & \bar{v} & 0 & \frac{\bar{a}+\bar{u}}{2} & \frac{\bar{a}-\bar{u}}{2} \\ 0 & 0 & \bar{v} & 0 & 0 \\ 0 & m_- & 0 & \bar{v} & 0 \\ 0 & m_+ & 0 & 0 & \bar{v} \end{bmatrix} \quad C^G = \begin{bmatrix} 0 & 0 & 0 & 0 & 0 \\ 0 & \bar{w} & 0 & 0 & 0 \\ 0 & 0 & \bar{w} & \frac{\bar{a}+\bar{u}}{2} & \frac{\bar{a}-\bar{u}}{2} \\ 0 & 0 & m_- & \bar{w} & 0 \\ 0 & 0 & m_+ & 0 & \bar{w} \end{bmatrix} \quad (4.59a)$$

$$m_- = \begin{cases} \frac{\bar{a}-\bar{u}}{2} & \text{if } n\bar{u} < 0 \\ \bar{u} & \text{otherwise} \end{cases} \qquad m_+ = \begin{cases} \frac{\bar{a}+\bar{u}}{2} & \text{if } n\bar{u} < 0 \\ \bar{u} & \text{otherwise} \end{cases}. \tag{4.59b}$$

The constants m_- and m_+ arise from the modifications Giles chose, which both Medida and Guarini reproduced, to obtain well-posed inflow conditions. The form of these constants follows from Medida's Equation (5.84) and is similar to Guarini's Equation (4.86).

We assume, but have not verified, reflection analysis like that presented in Giles [56, §3.7.4] extends to Medida's (4.59). At the inflow, an outgoing pressure wave would then produce no reflected entropy or vorticity waves and would generate a fourth-order pressure reflection. At the outflow, an outgoing entropy or vorticity wave would then produce no reflection while an outgoing pressure wave would generate a second order reflection.

4.2.2.3 Application to the Present Equations

In Section 4.3 of his thesis, Guarini [59] proved the linear structure of the Euler equations admits a straightforward translation of Giles' boundary conditions to another set of state variables V with steady, uniform reference state $\bar{V}$ and therefore perturbations

$$\delta V = V - \bar{V}. \tag{4.60}$$

The corresponding coordinate transformation Jacobian matrix is

$$S = \frac{\partial U}{\partial V}.$$

In this new setting, Guarini rewrote the exact nonreflecting conditions (4.47) as

$$\left(V^L S\right) \delta V = 0 \tag{4.61}$$

which causes the approximate condition (4.49) to become

$$V^L S \frac{\partial}{\partial t} \delta V \approx \frac{dV^L}{d\lambda_y} S \frac{\partial}{\partial y} \delta V + \frac{dV^L}{d\lambda_z} S \frac{\partial}{\partial z} \delta V. \tag{4.62}$$

Using notation from the compact representation (4.55),

$$P^G V^L S \frac{\partial}{\partial t} \delta V \approx P^G B^G V^L S \frac{\partial}{\partial y} \delta V + P^G C^G V^L S \frac{\partial}{\partial z} \delta V \tag{4.63}$$

is the simplest form for applying Medida's x boundary condition matrices to alternative state variables.

The particular coordinate transformation required maps the nondimensional primitive state U^* satisfying requirements (4.39) to the conserved state V^* nondimensionalized per Section 3.1:

$$V^* = \left\{ \frac{\rho}{\rho_0}, \frac{\rho u}{\rho_0 u_0}, \frac{\rho v}{\rho_0 u_0}, \frac{\rho w}{\rho_0 u_0}, \frac{\rho E}{\rho_0 a_0^2} \right\} = \{\rho^*, \rho^* u^*, \rho^* v^*, \rho^* w^*, \rho^* E^*\} \tag{4.64a}$$

$$a^* = \frac{a}{a_0} \qquad \mathrm{Ma} = \frac{u_0}{a_0} \qquad t_0 = \frac{l_0}{u_0}. \tag{4.64b}$$

Observing several relationships between U^* and V^* with care to distinguish between u_0 and a_0:

$$\frac{\rho}{\rho_0} = \rho^* \qquad \frac{u}{u_0} = \frac{\frac{\rho u}{\rho_0 u_0}}{\frac{\rho}{\rho_0}} = \frac{\rho^* u^*}{\rho^*} \qquad \frac{v}{u_0} = \frac{\rho^* v^*}{\rho^*} \qquad \frac{w}{u_0} = \frac{\rho^* w^*}{\rho^*} \tag{4.65}$$

$$\begin{aligned}\frac{p}{\rho_0 u_0^2} &= \frac{\gamma-1}{\rho_0 u_0^2}\rho E + \frac{1-\gamma}{2\rho_0 u_0^2 \rho}\left((\rho u)^2+(\rho v)^2+(\rho w)^2\right) \\ &= \frac{\gamma-1}{\mathrm{Ma}^2}\rho^* E^* + \frac{1-\gamma}{2\rho^*}\left((\rho^* u^*)^2+(\rho^* v^*)^2+(\rho^* w^*)^2\right). \end{aligned} \tag{4.66}$$

aids computing the Jacobian matrix evaluated at some $\bar{V}^*$,

$$S = \begin{bmatrix} 1 & 0 & 0 & 0 & 0 \\ -\frac{\bar{u}^*}{\bar{\rho}^*} & \frac{1}{\bar{\rho}^*} & 0 & 0 & 0 \\ -\frac{\bar{v}^*}{\bar{\rho}^*} & 0 & \frac{1}{\bar{\rho}^*} & 0 & 0 \\ -\frac{\bar{w}^*}{\bar{\rho}^*} & 0 & 0 & \frac{1}{\bar{\rho}^*} & 0 \\ \frac{\gamma-1}{2}\left(\bar{u}^{*2}+\bar{v}^{*2}+\bar{w}^{*2}\right) & (1-\gamma)\bar{u}^* & (1-\gamma)\bar{v}^* & (1-\gamma)\bar{w}^* & \frac{\gamma-1}{\mathrm{Ma}^2} \end{bmatrix}. \tag{4.67}$$

As expected, the transformation is nonsingular for realizable fields because

$$\det S = \frac{\gamma-1}{\mathrm{Ma}^2 \bar{\rho}^{*3}}.$$

The inverse is

$$S^{-1} = \begin{bmatrix} 1 & 0 & 0 & 0 & 0 \\ \bar{u}^* & \bar{\rho}^* & 0 & 0 & 0 \\ \bar{v}^* & 0 & \bar{\rho}^* & 0 & 0 \\ \bar{w}^* & 0 & 0 & \bar{\rho}^* & 0 \\ \frac{\mathrm{Ma}^2}{2}\left(\bar{u}^{*2}+\bar{v}^{*2}+\bar{w}^{*2}\right) & \mathrm{Ma}^2\bar{\rho}^*\bar{u}^* & \mathrm{Ma}^2\bar{\rho}^*\bar{v}^* & \mathrm{Ma}^2\bar{\rho}^*\bar{w}^* & \frac{\mathrm{Ma}^2}{\gamma-1} \end{bmatrix}. \tag{4.68}$$

Medida's matrices V^L, B^G, and C^G derived for U remain valid for nondimensional U^* possessing sound speed a/u_0. When reusing these matrices for V^* every sound speed must be scaled by $1/\mathrm{Ma}$ because

$$\frac{\bar{a}}{u_0} = \frac{a_0 \bar{a}^*}{u_0} = \frac{\bar{a}^*}{\mathrm{Ma}}.$$

The correctness of this intuitive find-and-replace operation has been verified using *Mathematica*® to reproduce Medida's results in this particular nondimensional context.

Thus far nonreflecting x boundary conditions in physical space have been presented. The present work requires rotating these results to handle nonreflecting y boundaries per Figure 4.1 followed by transforming the constraints into coefficient space. Defining

$$x' = z \qquad y' = x \qquad z' = y$$

induces the relationships:

$$\begin{aligned} u &= v' & v &= w' & w &= u' \\ \frac{\partial}{\partial x} &= \frac{\partial}{\partial y'} & \frac{\partial}{\partial y} &= \frac{\partial}{\partial z'} & \frac{\partial}{\partial z} &= \frac{\partial}{\partial x'}. \end{aligned}$$

The perturbed state vector entries may be reordered more conventionally by defining R^Y and $\delta V'$ per

$$\delta V = \begin{bmatrix} \delta\rho \\ \delta\rho u \\ \delta\rho v \\ \delta\rho w \\ \delta\rho E \end{bmatrix} = \begin{bmatrix} \delta\rho \\ \delta\rho v' \\ \delta\rho w' \\ \delta\rho u' \\ \delta\rho E \end{bmatrix} = R^Y \delta V' = \begin{bmatrix} 1 & 0 & 0 & 0 & 0 \\ 0 & 0 & 1 & 0 & 0 \\ 0 & 0 & 0 & 1 & 0 \\ 0 & 1 & 0 & 0 & 0 \\ 0 & 0 & 0 & 0 & 1 \end{bmatrix} \begin{bmatrix} \delta\rho \\ \delta\rho u' \\ \delta\rho v' \\ \delta\rho w' \\ \delta\rho E \end{bmatrix}. \tag{4.69}$$

Substituting these details into Equation (4.63) produces the desired nonreflecting y boundary condition,

$$\begin{aligned} \left[P^G V^L S\right]\Big|_{\bar{u}=\bar{v}',\bar{v}=\bar{w}',\bar{w}=\bar{u}'} R^Y \frac{\partial}{\partial t}\delta V' \approx\ & \left[P^G C^G V^L S\right]\Big|_{\bar{u}=\bar{v}',\bar{v}=\bar{w}',\bar{w}=\bar{u}'} R^Y \frac{\partial}{\partial x'}\delta V' \\ & + \left[P^G B^G V^L S\right]\Big|_{\bar{u}=\bar{v}',\bar{v}=\bar{w}',\bar{w}=\bar{u}'} R^Y \frac{\partial}{\partial z'}\delta V'. \end{aligned} \tag{4.70}$$

Suppressing the primes and the matrix evaluation details,

$$\left[P^G V^L S\right] R^Y \frac{\partial}{\partial t}\delta V \approx \left[P^G C^G V^L S\right] R^Y \frac{\partial}{\partial x}\delta V + \left[P^G B^G V^L S\right] R^Y \frac{\partial}{\partial z}\delta V. \tag{4.71}$$

Replacing δV by $V - \bar{V}$ per (4.60) and recalling that by assumption $\frac{\partial}{\partial t}\bar{V} = \frac{\partial}{\partial x}\bar{V} = \frac{\partial}{\partial z}\bar{V} = 0$,

$$\left[P^G V^L S\right] R^Y \frac{\partial}{\partial t} V \approx \left[P^G C^G V^L S\right] R^Y \frac{\partial}{\partial x} V + \left[P^G B^G V^L S\right] R^Y \frac{\partial}{\partial z} V. \tag{4.72}$$

Transforming to Fourier space gives a linear condition almost suitable for implicit advance per Section 4.1.2,

$$\left[P^G V^L S\right] R^Y \frac{\partial}{\partial t} \hat{V} \approx -\mathrm{i}k_x \left[P^G C^G V^L S\right] R^Y \hat{V} - \mathrm{i}k_z \left[P^G B^G V^L S\right] R^Y \hat{V}. \tag{4.73}$$

Notice that when $k_x = k_z = 0$ the relevant mean characteristics are held constant in time. The previous evolution equation is a pointwise condition suitable when $\hat{V}$ contains pointwise state (for example, collocation point values). When another representation is chosen for state, one should use

$$\left[P^G V^L S\right] R^Y M \frac{\partial}{\partial t} \hat{V} \approx -\mathrm{i}k_x \left[P^G C^G V^L S\right] R^Y M \hat{V} - \mathrm{i}k_z \left[P^G B^G V^L S\right] R^Y M \hat{V} \tag{4.74}$$

where time-invariant M maps state to non-state. However, the distinction is somewhat blurred for B-spline boundary collocation points and boundary coefficients because the boundary value for a B-spline basis expansion is nothing but the boundary coefficient.

While Equation (4.74) constrains incoming characteristics, it does not evolve the remainder of the solution in accordance with the interior of the simulation domain. Returning to the time discretization, Equation (4.8) evolves coefficients $\hat{V}$ per

$$M \frac{\partial}{\partial t} \hat{V} = L\hat{V} + \chi N(\hat{V}) \tag{4.75}$$

where both L and N map state (i.e. coefficients) to a non-state representation (i.e. collocation point values) and M state to non-state. At the nonreflecting y boundary,

projecting the evolution into characteristic space yields

$$\left[V^L S\right] R^Y M \frac{\partial}{\partial t}\hat{V} = \left[V^L S\right] R^Y \left(L\hat{V} + \chi N(\hat{V})\right). \tag{4.76}$$

Updating only the unconstrained characteristics using the previously defined P^G,

$$\left[I - P^G\right]\left[V^L S\right] R^Y M \frac{\partial}{\partial t}\hat{V} = \left[I - P^G\right]\left[V^L S\right] R^Y \left(L\hat{V} + \chi N(\hat{V})\right). \tag{4.77}$$

Adding Equation (4.74) and collecting like terms,

$$\begin{aligned}\left[V^L S\right] R^Y M \frac{\partial}{\partial t}\hat{V} \approx{}& \left[I - P^G\right]\left[V^L S\right] R^Y \left(L\hat{V} + \chi N(\hat{V})\right) \\ &- \left(\mathrm{i}k_x \left[P^G C^G\right] + \mathrm{i}k_z \left[P^G B^G\right]\right)\left[V^L S\right] R^Y M\hat{V}.\end{aligned} \tag{4.78}$$

Moving the nonsingular characteristic projection to the right hand side,

$$\begin{aligned}M \frac{\partial}{\partial t}\hat{V} \approx{}& R^{Y-1}\left[V^L S\right]^{-1}\left[I - P^G\right]\left[V^L S\right] R^Y \left(L\hat{V} + \chi N(\hat{V})\right) \\ &- R^{Y-1}\left[V^L S\right]^{-1}\left(\mathrm{i}k_x \left[P^G C^G\right] + \mathrm{i}k_z \left[P^G B^G\right]\right)\left[V^L S\right] R^Y M\hat{V},\end{aligned} \tag{4.79}$$

a boundary evolution equation matching the form (4.75) is recovered. Auxiliary definitions could improve the result's brevity but they obfuscate the physics.

4.2.2.4 Enforcement in the Explicit or Implicit Operator

Two different nonreflecting boundary enforcement approaches were desired. The first approach imposed the above conditions through the nonlinear, explicit operator for software implementation debugging purposes. The second approach applied the conditions through the linear implicit operator for production use. In the latter case, implicit treatment of the derivatives in the nonreflecting condition is warranted

whenever the streamwise and spanwise directions are handled linearly implicitly per Section 4.1.5. Otherwise acoustics traveling in those grid directions limit stable time step choices thus defeating the implementation efforts from Section 4.1.6.

Rearranging (4.79) for the first case, one obtains

$$M\frac{\partial}{\partial t}\hat{V} \approx \overbrace{R^{Y^{-1}}\left[V^L S\right]^{-1}\left[I-P^G\right]\left[V^L S\right]R^Y L}^{L_E^G}\hat{V} + \chi\underbrace{R^{Y^{-1}}\left[V^L S\right]^{-1}\begin{pmatrix}\chi^{-1}\left(-\mathrm{i}k_x\left[P^G C^G\right]-\mathrm{i}k_z\left[P^G B^G\right]\right)\left[V^L S\right]R^Y M\hat{V}\\ +\left[I-P^G\right]\left[V^L S\right]R^Y N(\hat{V})\end{pmatrix}}_{N_E^G(\hat{V})}. \tag{4.80}$$

Evidently, Giles' conditions can be fit into the framework in Section 4.1.2 by modifying the action of any existing global operators L and N to obtain the boundary-specific L_I^G and N_I^G behavior described by Equation (4.80). The required C^G-, B^G-, and P^G-related matrices may be computed only once for this $\bar{V}$ and then cached for repeated use. Conveniently, $N_E^G\left(\hat{V}\right)$ can be obtained from $N\left(\hat{V}\right)$ using only information available in Fourier space assuming that reference state $\bar{V}$ has already been gathered.

Reshuffling (4.79) for the second case, one can cast the boundary condition primarily as a modification of the linear operator L:

$$M\frac{\partial}{\partial t}\hat{V} \approx \overbrace{R^{Y^{-1}}\left[V^L S\right]^{-1}\begin{pmatrix}\left(-\mathrm{i}k_x\left[P^G C^G\right]-\mathrm{i}k_z\left[P^G B^G\right]\right)\left[V^L S\right]R^Y M\\ +\left[I-P^G\right]\left[V^L S\right]R^Y L\end{pmatrix}}^{L_I^G}\hat{V} + \chi\underbrace{R^{Y^{-1}}\left[V^L S\right]^{-1}\left[I-P^G\right]\left[V^L S\right]R^Y N(\hat{V})}_{N_I^G(\hat{V})}. \tag{4.81}$$

$N_I^G(\hat{V})$ can be found from a straightforward, wavenumber-independent linear transformation of $N(\hat{V})$. Accumulating product $\left(M+\varphi L_I^G\right)\hat{V}$ out-of-place in an L-agnostic

way can be done by first accumulating $(M+\varphi L)\hat{V}$ and subsequently adjusting the boundary action:

$$\begin{aligned}\left(M+\varphi L_I^G\right)-(M+\varphi L)\Big|_{\text{boundary}} = &-\mathrm{i}\varphi k_x R^{Y^{-1}}\left[V^L S\right]^{-1}\left[P^G C^G\right]\left[V^L S\right]R^Y M\\ &-\ \mathrm{i}\varphi k_z R^{Y^{-1}}\left[V^L S\right]^{-1}\left[P^G B^G\right]\left[V^L S\right]R^Y M\\ &-\ \varphi\ R^{Y^{-1}}\left[V^L S\right]^{-1}\left[P^G\ \right]\left[V^L S\right]R^Y\ L. \end{aligned} \tag{4.82}$$

To illustrate L-agnostic $\left(M+\varphi L_I^G\right)$ assembly, suppose the state coefficients at the non-reflecting boundary are interleaved at the bottom of vector $\hat{V}$ per (4.35). Then one can partition (4.82) as

$$\begin{aligned}M+\varphi L_I^G = &\underbrace{\begin{bmatrix}M_{00} & M_{01}\\ 0 & M_{11}\end{bmatrix}+\varphi\begin{bmatrix}L_0\\ L_1\end{bmatrix}}_{M+\varphi L}\\ &-\varphi\begin{bmatrix}0 & 0\\ 0 & C\end{bmatrix}\underbrace{\begin{bmatrix}L_0\\ L_1\end{bmatrix}}_{L}+\varphi\begin{bmatrix}0 & 0\\ 0 & -\mathrm{i}k_xA-\mathrm{i}k_zB\end{bmatrix}\underbrace{\begin{bmatrix}M_{00} & M_{01}\\ 0 & M_{11}\end{bmatrix}}_{M}\end{aligned} \tag{4.83}$$

using rectangular M_{01}, L_0 and L_1. Here, the $[P^G C^G]$-, $[P^G B^G]$-, and $[P^G]$-dependent Giles dense matrix products mapping collocation points to collocation points have been abbreviated to A, B, and C, respectively. As $M_{11}=I$ holds for collocation-based B-spline operators,

$$\begin{aligned}M+\varphi L_I^G &= \begin{bmatrix}M_{00} & M_{01}\\ 0 & I\end{bmatrix}+\varphi\begin{bmatrix}I & 0\\ 0 & I-C\end{bmatrix}\begin{bmatrix}L_0\\ L_1\end{bmatrix}+\varphi\begin{bmatrix}0 & 0\\ 0 & -\mathrm{i}k_xA-\mathrm{i}k_zB\end{bmatrix}\\ &= \begin{bmatrix}I & 0\\ 0 & I-C\end{bmatrix}(M+\varphi L)+\begin{bmatrix}0 & 0\\ 0 & C-\mathrm{i}\varphi k_xA-\mathrm{i}\varphi k_zB\end{bmatrix}.\end{aligned} \tag{4.84}$$

The above form can be straightforwardly used in software routines for banded operator application and assembly.

When only the wall-normal direction is treated implicitly, simplifying Figure 4.3 to its wavenumber-independent form, the wavenumber-dependent terms above may be collected into the explicit operator producing a hybrid between (4.80) and (4.81). In that circumstance, the operator modification (4.84) remains intact with the k_x and k_z terms simply omitted. Surprisingly, splitting this higher order boundary treatment between the implicit linear and explicit nonlinear operators empirically behaved, over long simulation times, in an ill-posed manner on problems for which the implementations of both (4.80) and (4.81) remained stable. Caveat human error being responsible for this unexpected observation, it is conjectured that splitting the boundary treatment introduces sufficient numerical noise that the well-posedness modifications in (4.59) somehow break down.[1] Regardless of the root cause, the lower order treatment (4.81) always taking $k_x = k_z = 0$ is applied when only the wall-normal direction is handled implicitly.

4.2.2.5 Impact of Homogenization and Viscosity

Testing has shown inviscid, nonreflecting subsonic inflow and outflow conditions, as formulated above, to behave as expected. The impact homogenization and viscous effects have on the application of these boundary conditions is now considered.

Temporal slow growth models add homogenization forcing (2.6) to the gov-

[1] A coding error was certainly possible but believed to be unlikely because the relevant code execution paths are wholly shared with the fully implicit and fully explicit treatments. The conjecture is based solely on the effort Rowley and Colonius [130] dedicate to the subtleness of such well-posedness corrections.

erning equations. These terms have the form

$$-y\,\mathrm{gr}_{t_0}(\Delta)\,\frac{\partial}{\partial y}\rho q = \mathrm{gr}_{t_0}(\Delta)\,\rho q - \frac{\partial}{\partial y}\left(y\,\mathrm{gr}_{t_0}(\Delta)\,\rho q\right) \tag{4.85}$$

for each scalar q with $\mathrm{gr}_{t_0}(\Delta)$ being constant. As just demonstrated, such terms may be split into a reaction term and a conserved flux. Relative to the Euler equations, this additional conserved flux modifies the inviscid eigensystem to make the wall-normal eigenvalues $\bar{v}$ and $\bar{v} \pm \bar{a}$ become $\bar{v} - y\,\mathrm{gr}_{t_0}(\Delta)$ and $(\bar{v} \pm \bar{a}) - y\,\mathrm{gr}_{t_0}(\Delta)$. Consequently, only subsonic inflow conditions are necessary to simulate temporally homogenized boundary layers as $-y\,\mathrm{gr}_{t_0}(\Delta)$ typically dominates $\bar{v}$ at the $y = L_y$ boundary given a reasonable wall-normal domain extent. Identical wall-normal modifications empirically were found to be adequate when employing the spatiotemporal formulation from Section 3.3.

Poinsot and Lele [123] suggest two additional viscous conditions be supplied when Euler-derived conditions are applied to the Navier–Stokes equations. These involve disabling viscous stress and heat flux terms at the boundary.[2] While testing has shown viscous subsonic inflows to be stable without this further treatment, viscous subsonic outflows were not. The simplest way to enforce all of Poinsot and Lele's recommendations is to make the entire $X - Z$ computational plane at the nonreflecting boundary be inviscid. At $y = L_y$ the nonlinear pointwise computations use $1/\mathrm{Re} = 0$ and the viscous linearization references from Section 4.1.5 (c^{ν}, $\overrightarrow{c^{\nu u}}$, etc.) are set to zero.

[2] Interestingly, though he applied their two shear conditions, Guarini [59] either did not enforce or did not report enforcing Poinsot and Lele's recommended heat flux condition.

4.3 Accounting for Uncertainty in Computed Statistics

Providing uncertainty estimates in reported results is essential whenever experimentally or numerically obtained flow statistics are taken as truth data. Assuming the absence of coding errors, the application of adequate numerical resolution to a well-posed problem, and the correct determination of stationary conditions in an ergodic simulation, uncertainties in DNS can arise from two sources. First, approximately solving the continuous Navier–Stokes equations with a computer introduces discretization errors. Second, sampling flow quantities over a finite duration introduces finite sampling errors. Oliver et al. [114] set forth Bayesian Richardson extrapolation as a means to disentangle these two sources of error when finite sampling uncertainty could be quantified. That work confirmed for some quantities of interest the notion that well-resolved DNS discretization errors are small relative to DNS sampling errors. Therefore, in this dissertation, finite sampling errors will be reported while discretization error is neglected.

Calculation of finite sampling errors in a statistically stationary DNS is complicated by the fact that the samples possess an *a priori* unknown temporal autocorrelation structure. As any well-defined numerical experiment must cause the autocorrelation to ultimately decay to zero, many authors downsample instantaneous measurements until the retained samples are independent. However, increasing the number of independent samples is computationally expensive in DNS.

As part of the present work, an automated technique using information-theoretic autoregressive model estimation [14, 17–19, 125, 126, 173] in conjunction with effective sample sizes [168] to extract more information from a fixed amount of auto-

correlated data was developed. The method was benchmarked, found favorable, and published in Oliver et al. [114]. An open source, header-only C++ reference implementation is available.[3] Convenient wrappers for GNU Octave [37] and Python [33] were also provided to facilitate adoption by the DNS community. This autoregressive technique will be used to estimate finite sampling errors for the Reynolds-averaged quantities reported in Chapters 5–7.

Uncertainty propagation into derived quantities computed from directly sampled data (and its associated finite sampling uncertainty estimates) is performed using Taylor series methods [29, 79]. To recall, consider one observation $\vec{d}$ of some deterministic truth $\vec{x}$ obscured by bias error $\vec{\beta}$ as well as measurement error $\vec{\epsilon}$. That is,

$$\vec{d} = \vec{x} - \vec{\beta} - \vec{\epsilon} \tag{4.86}$$

Assume $\vec{\beta}$ is relatively small and independent of $\vec{\epsilon}$. Assume also that $\vec{\epsilon} \sim \mathcal{N}(\vec{0}, \Sigma)$ for some known or estimable covariance matrix Σ containing scalar components σ_{ij}. The variances on the diagonal of Σ are produced from finite sampling error estimates computed by the autoregressive technique. To ensure Σ is positive definite, off-diagonal covariances are estimated by scaling empirical correlation coefficients by the two associated diagonal entries.

Given some physically relevant functional $f = f(\vec{x})$, computing the quantities $\mathbb{E}[f(\vec{x})]$ and $\operatorname{var} f(\vec{x})$ is of interest. Expanding f about $\vec{d}$ up to k^{th} order and evaluating

[3] `http://rhysu.github.com/ar/`

at the unknown truth $\vec{x}$,

$$f(\vec{x}) \approx \sum_{|\alpha| \leq k} \left(\vec{x} - \vec{d}\right)^{\alpha} \frac{\left(D^{\alpha} f\right)\left(\vec{d}\right)}{\alpha!}. \tag{4.87}$$

Choosing $k = 2$, expanding the above multi-index, and using the definition of $\vec{d}$,

$$\begin{aligned} f\left(\vec{x}\right) &\approx f\left(\vec{d}\right) + \sum_i \left(x_i - d_i\right) \partial_{x_i} f\left(\vec{d}\right) + \frac{1}{2} \sum_{i,j} \left(x_i - d_i\right)\left(x_j - d_j\right) \left(\partial_{x_i} \partial_{x_j} f\right)\left(\vec{d}\right) \\ &= f\left(\vec{d}\right) + \sum_i \left(\beta_i + \epsilon_i\right) \left(\partial_{x_i} f\right)\left(\vec{d}\right) + \frac{1}{2} \sum_{i,j} \left(\beta_i + \epsilon_i\right)\left(\beta_j + \epsilon_j\right) \left(\partial_{x_i} \partial_{x_j} f\right)\left(\vec{d}\right). \end{aligned} \tag{4.88}$$

Taking the expectation, assuming $\mathbb{E}[\beta_i]\left(\partial_{x_i} f\right)\left(\vec{d}\right)$ is negligible, and dropping terms containing $\mathbb{E}\left[\beta_i \beta_j\right]$ yields the second-order result

$$\begin{aligned} \mathbb{E}[f\left(\vec{x}\right)] &\approx f\left(\vec{d}\right) + \frac{1}{2} \sum_{i,j} \sigma_{ij} \left(\partial_{x_i} \partial_{x_j} f\right)\left(\vec{d}\right) \\ &\approx f\left(\vec{d}\right) + \frac{1}{2} \sum_i \sigma_{ii} \left(\partial_{x_i} \partial_{x_i} f\right)\left(\vec{d}\right) + \sum_{i<j} \sigma_{ij} \left(\partial_{x_i} \partial_{x_j} f\right)\left(\vec{d}\right). \end{aligned} \tag{4.89}$$

The $k = 2$ result (4.89) is the lowest-order approximation that corrects for Σ. Revisiting expansion (4.88) but now retaining only up to the $k = 1$ terms,

$$f\left(\vec{x}\right) \approx f\left(\vec{d}\right) + \sum_i \left(\beta_i + \epsilon_i\right) \left(\partial_{x_i} f\right)\left(\vec{d}\right). \tag{4.90}$$

Squaring and expanding products of sums,

$$\begin{aligned} f^2\left(\vec{x}\right) \approx f^2\left(\vec{d}\right) &+ \sum_i \beta_i^2 \left(\partial_{x_i} f\right)^2\left(\vec{d}\right) + 2 \sum_{i<j} \beta_i \beta_j \left(\partial_{x_i} f\right)\left(\vec{d}\right)\left(\partial_{x_j} f\right)\left(\vec{d}\right) \\ &+ \sum_i \epsilon_i^2 \left(\partial_{x_i} f\right)^2\left(\vec{d}\right) + 2 \sum_{i<j} \epsilon_i \epsilon_j \left(\partial_{x_i} f\right)\left(\vec{d}\right)\left(\partial_{x_j} f\right)\left(\vec{d}\right) \\ &+ 2 f\left(\vec{d}\right) \sum_i \left(\beta_i + \epsilon_i\right) \left(\partial_{x_i} f\right)\left(\vec{d}\right) + 2 \sum_{i,j} \beta_i \epsilon_j \left(\partial_{x_i} f\right)\left(\vec{d}\right)\left(\partial_{x_j} f\right)\left(\vec{d}\right). \end{aligned} \tag{4.91}$$

Averaging and again neglecting $\mathbb{E}[\beta_i]\left(\partial_{x_i} f\right)\left(\vec{d}\right)$ and terms involving $\mathbb{E}\left[\beta_i \beta_j\right]$ gives

$$\mathbb{E}\left[f^2(\vec{x})\right] \approx f^2\left(\vec{d}\right) + \sum_i \sigma_{ii}\left(\partial_{x_i} f\right)^2\left(\vec{d}\right) + 2\sum_{i<j} \sigma_{ij}\left(\partial_{x_i} f\right)\left(\vec{d}\right)\left(\partial_{x_j} f\right)\left(\vec{d}\right). \quad (4.92)$$

Subtracting the square of the expectation of (4.90), neglecting the same quantities, from $\mathbb{E}\left[f^2(\vec{x})\right]$ one arrives at the first-order result

$$\operatorname{var} f(\vec{x}) \approx \sum_i \sigma_{ii}\left(\partial_{x_i} f\right)^2\left(\vec{d}\right) + 2\sum_{i<j} \sigma_{ij}\left(\partial_{x_i} f\right)\left(\vec{d}\right)\left(\partial_{x_j} f\right)\left(\vec{d}\right). \quad (4.93)$$

As expected, having neglected bias error contributions, the approximation (4.93) to $\operatorname{var} f(\vec{x})$ is controlled wholly by the functional form of f as well as the measurement error covariances σ_{ij}.

While these general uncertainty propagation formulas are simple, their application is tedious and error prone. A small application employing the open source, Python-based symbolic toolkit SymPy [158] was created to automate deriving these expressions. That application is packaged with the software to be discussed in the next chapter.

Chapter 5

Software Implementation

The computational techniques from Chapter 4 were implemented within a new spectral simulation framework called Suzerain.[1] Performing direct numerical simulations for perfect gases modeled per Chapter 3 was the motivating first application for the framework. The coevolving framework and application logic, along with supporting-but-independent subcomponents, was written primarily in C99/C++03 over the course of six years. Altogether they measure in excess of 100K lines of code. The source code[2] and development process[3] are both available openly to encourage reuse, reproducibility, and collaboration.

The software was developed to be demonstrably correct, to be decomposable and extensible, and to serve others as a long-lived computational tool. Indeed, a second Suzerain-based application targeting chemically reacting flows was designed and built by Victor Topalian, Todd A. Oliver, Nicholas Malaya, and Robert D. Moser during the past two years to produce the simulations reported in Topalian et al. [164, 165, 166]. Independent software subcomponents created during this dissertation have been em-

[1] The name was chosen to suggest that applications built using Suzerain would be granted internal autonomy but would have their external affairs fairly rigidly controlled— in software industry parlance, the framework aspires to be a domain-specific application container.

[2] `http://github.com/RhysU/suzerain`

[3] `http://red.ices.utexas.edu/projects/suzerain`

ployed by Lee and Moser [88], Lee et al. [89, 90], Malaya et al. [100], and Oliver et al. [114].

This chapter first covers the design and verification of the software in the context of the first, nondimensional perfect gas application. “Suzerain” will be used to refer to only that framework/application combination without ambiguity as no further discussion of the second, reacting application by Topalian et al. appears in this document. Next, the combination is validated against supersonic channel results by Coleman et al. [27] and Huang et al. [67] yielding important conclusions with respect to the B-spline stability estimates from Section 4.1.4.3. Performance and scalability are then assessed, including the effectiveness of the implicit treatment described in Section 4.1.5. All in all, Suzerain is well-suited to perform the simulation campaigns that are the subjects of the following two chapters.

5.1 Design

The high-level design of Suzerain is depicted in Figure 5.1. Best-of-breed third party libraries were used when it was advantageous to do so. Computing one Runge–Kutta substep per (4.9) transforms state from wave space to physical space and transforms residuals back using P3DFFT [121]. These parallel transposes, depicted in Figure 5.2, provide the natural domain decomposition which arises from the Fourier/B-spline spatial discretization (4.7). The communication and computation characteristics of those operations are crucial for scalability.

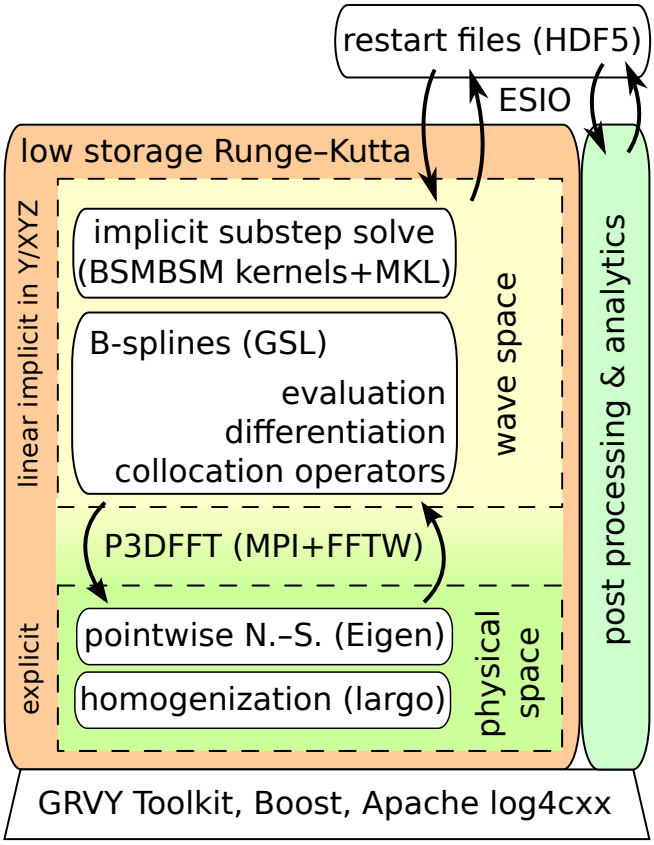

Figure 5.1: Architecture for the spectral simulation framework Suzerain

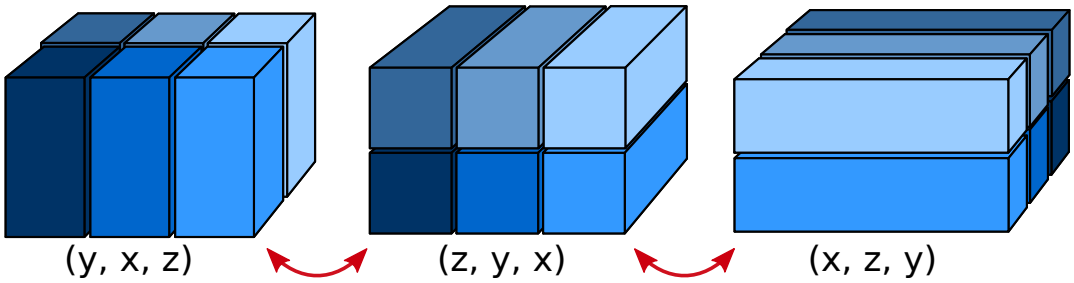

Figure 5.2: A pencil decomposition maps $O(N^2)$ data to $O(N^3)$ MPI ranks using two `MPI_Alltoall`-like global communication phases depicted with red arrows. Each color represents the data owned by a single rank in each configuration.

B-spline operators were formed using the GNU Scientific Library (GSL) [37].[4] The banded implicit solves in Algorithm 1 required custom compute kernels to assemble rescaled B-spline operators into large-bandwidth, complex-valued BSMBSMs per Section 4.1.6. Factorization and back-substitution are provided by the Intel® Math Kernel Library (MKL).[5] Custom banded matrix-vector product kernels were prepared because compiler-unrolled loops are appreciably faster than general-purpose MKL routines at small bandwidths [89].[6] In physical space, pointwise Navier–Stokes-related computations used Eigen [61] to simplify expressing complicated expansions like (4.31) and to facilitate accessing vectorized intrinsics for performance. When applied, the slow growth forcing discussed in Sections 2.5 and 3.3 is accomplished using largo, a standalone Fortran 90/C99 library developed by Victor Topalian which is distributed with Suzerain.

The GRVY Toolkit [119] was used for continuous performance monitoring while extensions atop Apache log4cxx [160] provided rich, MPI-aware logging of both application lifecycle events as well as the temporal evolution of statistical quantities of interest.[7] Input and output of HDF5-based [161] data files was performed using

[4] The author is a committer for the GSL project.

[5] By default, implicit solves employ a robust, LAPACK-like driver. The user may also choose the vanilla `GBTRF/GBTRS` pair for speed, the more expensive `GBSVX` driver to monitor operator conditioning, or a custom banded driver routine inspired by Langou et al. [84]'s `DGESIRSV` permitting mixed precision operation and/or exploiting approximate factorizations. While this last option provided verifiably correct results, reusing the (k_n, k_m)-dependent operator (see Figure 4.3) factorization along with iterative refinement to avoid nearby (k_n', k_m') factorizations was not found to be superior to invoking `GBTRF` for every (k_n, k_m) on the problems considered in this document.

[6] Note the matrix-vector product bandwidths are significantly smaller than that factorization problem bandwidths as discussed in Section 4.1.6.

[7] The author is a committer for both the GRVY Toolkit and Apache log4cxx projects.

the ESIO library [120], written as part of the current work and also openly available.[8] Operational considerations like automated batch job output management and reactive tear down in the event of job time expiration or queue-system-related interruption were implemented to permit long simulations to run virtually unattended.

Absent from Figure 5.1 are the pervasive computational science toolkits PETSc [6] and Trilinos [62]. During Suzerain's early design they were investigated but six years ago it was unclear how to fit the techniques from Chapter 4 into them. Three years ago, having learned more, it became apparent that doing so was possible. However, at that time, the basic features either toolkit would have provided had already been long ago implemented within Suzerain making porting a considerable effort without immediately obvious benefits. No port occurred.

In hindsight, not adopting a common toolkit into Suzerain's design was suboptimal. Gaining access to off-the-shelf, adaptive temporal schemes would have permitted taking full advantage of the increased stability provided by the wavenumber-dependent, linearly implicit operator implementation in the streamwise and spanwise directions without concerns as to whether or not doing so adversely impacts accurately capturing turbulent dynamics (see page 74 and, below, Section 5.3). It certainly would have largely rendered the work behind Section 4.1.4.3 unnecessary as classical CFL stability estimates would yield conservative initial guesses from which an adaptive scheme could ramp up the time step to a maximally efficient value given well-quantified accuracy requirements. If found prohibitively expensive for production calculations, adap-

[8] `http://github.com/RhysU/ESIO`

tive schemes could be applied during simulation “spin-up” followed by nonadaptive time advance using spin-up-informed time step choices. Reactive stability restrictions arising from spatiotemporal forcing would have been seamlessly handled rather than requiring the step size safety factors listed in Chapter 6. Finally, and most importantly, skeletally incorporating a ubiquitous toolkit could increase the likelihood and speed of future Suzerain adoption by PETSc- or Trilinos-savvy developers thus facilitating collaboration and providing better research returns for the time invested in the code.

5.2 Testing and Verification

Automated testing and code verification are essential as Suzerain is used to produce data for model calibration. Unit tests ensure lower level routines behave as expected while a collection of higher-level tests verify their proper integration. MPI-parallel system tests check first for correct operation and second, wherever applicable, for agreement with serial computations. Serial/parallel consistency tests include the full application lifecycle involving loading restart state, advancing time, computing statistics, and storing state back to disk. Gold solutions, which are known-correct results calculated by earlier code revisions, permit detecting when changes like implementing optimizations or switching compiler versions unintentionally influence results. The full test suite was run daily on a Buildbot continuous integration server [174] against both the GNU and Intel® compilers. At present, automated line and function coverage exceeds 80%.

To verify that Suzerain correctly implemented Equations (3.1), the method of manufactured solutions (MMS) was employed. The MMS adds to the governing

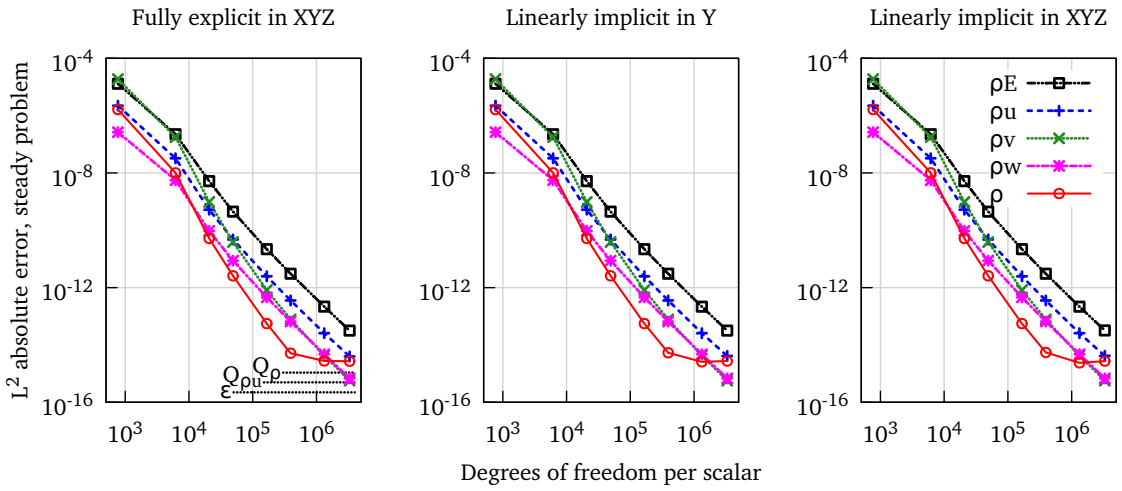

Figure 5.3: Convergence behavior against a steady problem solved using each available Navier–Stokes operator implementation. The wall-normal resolution — piecewise-septic B-splines atop uniform breakpoints with 12, 24, 36, 48, 72, 96, 144, and 192 collocation points — governs the asymptotic order. The three sample estimate (5.1) finds $k_0 > 7.34$ across $h = 48$, $h/s = 72$, and $h/t = 96$ for all scalars. Labels Q_ρ and $Q_{\rho u}$ indicate measured pointwise error in the floating point computations implementing manufactured forcing [170]. Beyond 96 collocation points that forcing error reduces empirical convergence rates. For reference, label ϵ marks machine epsilon.

equations new source terms such that the exact – manufactured – solution is known *a priori* [99, 129, 153]. New manufactured solutions were created to fully test all terms in compressible Navier–Stokes formulations like the present one [170]. The particular solution instantiation appropriate for the current nondimensionalization is recorded in Appendix B.

After the manufactured solution was constructed, three-sample observed order of accuracy studies were conducted [128, 131]. Assuming an approximation $A(h)$ shows an h-dependent truncation error compared to an exact value A, *viz.* $A - A(h) = a_0 h^{k_0} + a_1 h^{k_1} + \cdots$, gives rise to the classical Richardson extrapolation procedure. Ne-

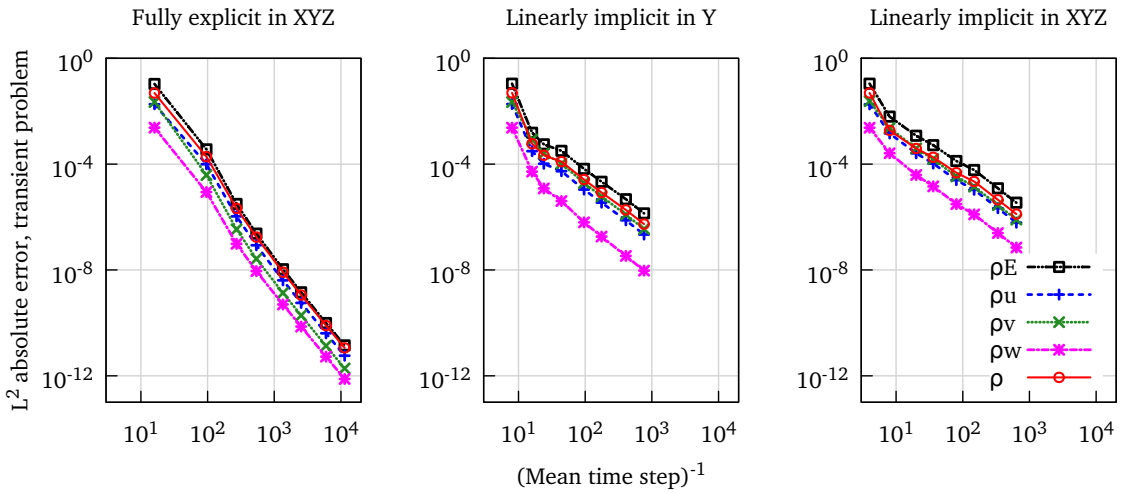

Figure 5.4: Convergence behavior against a transient problem over 0.25 time units solved using each available Navier–Stokes operator implementation. The same spatial resolutions from Figure 5.3 were reused to force temporal refinement to be driven by stability concerns per Section 4.1.4. When fully explicit (left), stable time steps are small enough that pre-asymptotic, almost-spatial orders are recovered ($k_0 > 6.45$). Wall-normal implicitness (center) exhibits $k_0 > 3.6$ for $N_y \geq 48$ while advancing linearly implicitly in three directions (right) shows $k_0 > 2.1$ for $N_y > 72$. Notice significant differences in step sizes occurring across the three implementations.

glecting $O(h^{k_1})$ contributions, one can estimate the leading error order k_0 by numerically solving

$$A = \frac{t^{k_0} A\left(\frac{h}{t}\right) - A(h)}{t^{k_0} - 1} + O(h^{k_1}) = \frac{s^{k_0} A\left(\frac{h}{s}\right) - A(h)}{s^{k_0} - 1} + O(h^{k_1}) \tag{5.1}$$

given three approximations $A(h)$, $A(h/s)$, and $A(h/t)$ to A. The L^2 norm of the absolute error in each scalar field was selected here. On steady problems, the wall-normal B-spline discretization error generally dominates that arising from the spectral streamwise and spanwise Fourier basis truncation as displayed in Figure 5.3. On transient problems, the linearly implicit temporal treatment can reduce the asymptotic conver-

gence rate to as low as second order as demonstrated in Figure 5.4.

Two important code features were not verified via manufactured solutions. Both features are, of course, believed to be formulated and implemented correctly but that belief is not based upon Figures 5.3 or 5.4. The first feature was the nonreflecting boundary treatment discussed in Section 4.2.2. The related matrix-manipulating logic (4.84) was exercised by automated tests. A variety of two- and three-dimensional test problems, like the one depicted in Figure 5.5, were used to assess proper boundary condition enforcement within the larger temporal advancement scheme per (4.80) and (4.81). The second feature was the data exchange between the main solver in Suzerain and the pointwise homogenized forcing computations coded in Topalian's largo library. The homogenization-agnostic data hand off between largo and Suzerain was subjected to intensive code review followed by capturing results in gold solution files to defend against regression. Topalian provided automated, pointwise verification of the computations inside largo.

5.3 Validation on Isothermal Channel Problems

To validate Suzerain, including its uncertainty and post-processing capabilities, a collection of sub- through supersonic, low Reynolds number isothermal channels was simulated [169]. The collection followed computations by Coleman et al. [27] which were further investigated by Huang et al. [67] to permit direct comparison with their results. A wide range of Mach numbers was simulated to permit investigating, later in this chapter, the efficiency of the linear-implicit treatment documented in Section 4.1.5. The data is openly archived as described in Appendix D.

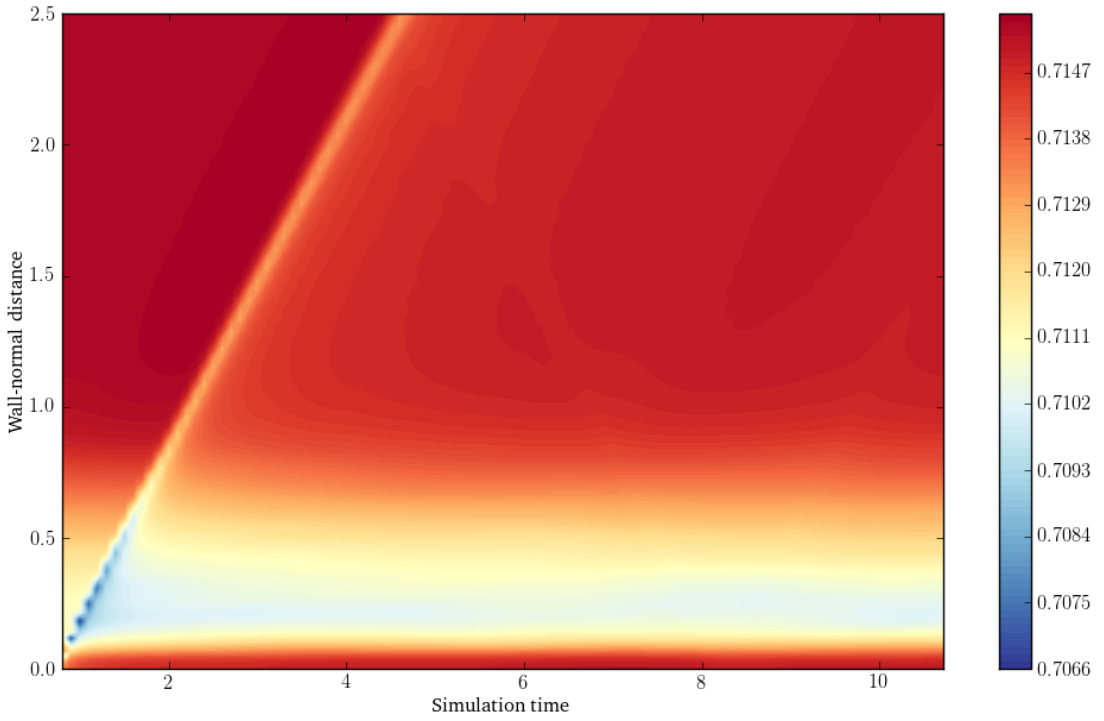

Figure 5.5: The temporal evolution of mean pressure across the streamwise and spanwise directions as a function of wall-normal distance is depicted during a nonreflecting boundary condition test. At $t = 0$ the wall temperature is instantaneously dropped causing a pressure pulse to travel towards the upper boundary which it exits before $t = 5$. An acceptable reflection is seen traveling back towards the wall which it reaches around $t = 8$. The effectiveness of the approximately nonreflecting boundary can be contrasted with the subsequent pressure reflection from the isothermal wall which is faint but visible at $y = 5/4$ when $t = 10$.

In channel flows a fluid is driven between two flat plates separated by a fixed distance as shown in Figure 4.1. The incompressible [31, 32, 65, 66, 76, 147] and compressible [27, 49, 50, 67, 87, 93, 103, 141] versions of this problem are well-studied. Half the plate separation distance is taken as reference length l_0 so that nondimensionally $L_y = 2$. No slip, isothermal conditions are enforced at the upper and lower boundaries. Unlike the classical plane Poiseuille flow in which a constant pressure gradient drives the fluid, in Coleman-like channels the bulk streamwise momentum, $\int \rho u \, \mathrm{d}y$, is constrained using a spatially uniform, time-varying body force f. The instantaneous bulk density is similarly fixed. In contrast, the total energy is not constrained so that the problem becomes energetically stationary only when the mean work done by f is balanced by the average heat transfer through the walls. To simplify comparison, the grid resolutions and domain size closely follow Coleman et al. [27] who found them to be adequate. The domain is small relative to more recent channels appearing in the literature.

The channels simulated, including resolution details and various quantities of interest, are reported in Table 5.1. In the table, wall and centerline quantities have subscripts w and c. Superscript + denotes normalization by the viscous length scale $\delta_\nu = \mu_w/\rho_w/u_\tau$ or the friction velocity $u_\tau = \sqrt{\tau_w/\rho_w}$ where the wall shear stress $\tau_w = \left(\mu \partial_y u\right)_w$. The friction Reynolds number Re_τ and friction Mach number Ma_τ are given by y_c/δ_ν and u_τ/a_w. Superscript $*$ marks scaling by semi-local units using either $u_\tau^* = \sqrt{\tau_w/\rho}$ or $\delta_\nu^* = \nu/u_\tau^*$ [67, 103]. The nondimensional heat flux is denoted by B_q [16]. The column "flow throughs" conveys the time over which the data ensemble was collected, divided by the time required for the bulk flow to traverse the streamwise

Table 5.1: Isothermal channel simulations performed with Suzerain v0.1.6.34-r45407. For all cases, $\overline{\rho} = 1$, $\overline{\rho u} = 1$, $T_w = 1$, $\mathrm{Pr} = \mu C_p/\kappa = 0.7$, $\alpha = 0$ for $\mu_B = \alpha\mu$, $\mu/\mu_0 = (T/T_0)^\beta$, and $\gamma = C_p/C_v = 1.4$. Extents were $L_x = 4\pi$, $L_y = 2$, $L_z = 4\pi/3$ employing $N_x = 192$ and $N_z = 168$ Fourier modes and a piecewise-septic B-spline basis with N_y collocation points stretched per the hyperbolic tangent parameter "tanh" following (4.13). By definition, $\mathrm{Re} = \overline{\rho u}\left(L_y/2\right)/\mu_w$, $\mathrm{Ma} = \bar{u}/a_w$. Simulations by Kim, Moin, and Moser [76] and Coleman, Kim, and Moser [27] are shown for comparison.

Case	Re	Ma	β	N_y	tanh	Re_τ	Δx^+	y_1^+	y_{10}^+	Δz^+	Flow throughs
c03k01	3000	0.1	2/3	128	2.25	191	12.5	0.22	11.9	5.0	15.6
c03k05	3000	0.5	2/3	128	2.25	194	12.7	0.22	12.1	5.1	15.7
c03k15	3000	1.5	2/3	128	2.25	222	14.6	0.26	13.8	5.8	11.9
c03k30	3000	3.0	2/3	128	2.25	297	19.4	0.34	18.5	7.8	15.5
c05k01	5000	0.1	2/3	144	2.50	298	19.5	0.26	14.2	7.8	11.1
c05k05	5000	0.5	2/3	144	2.50	303	19.8	0.26	14.4	7.9	11.6
c05k15	5000	1.5	2/3	144	2.50	349	22.8	0.31	16.6	9.1	13.2
c05k30	5000	3.0	2/3	144	2.50	480	31.4	0.42	22.8	12.6	12.9
KMM87	2800	0	0	129		180	12	0.05	5.4	7	12.4
CKM95a	3000	1.5	0.7	119		222	17	0.1	8	10	≥ 11.9
CKM95b	4880	3.0	0.7	119		451	39	0.2	17	24	≥ 11.9

Case	Ma_c	Ma_τ	Re_c	y_c^*	$-\mathrm{B}_q$	ρ_w	ρ_c	T_c	μ_c
c03k01	0.116	0.006	3481	190	0.0003	1.002	0.9999	1.002	1.001
c03k05	0.570	0.031	3387	185	0.0062	1.040	0.9973	1.043	1.028
c03k15	1.497	0.081	2772	151	0.0496	1.365	0.9780	1.391	1.246
c03k30	2.240	0.119	1765	94	0.1486	2.494	0.9278	2.666	1.923
c05k01	0.115	0.006	5752	297	0.0002	1.002	0.9999	1.002	1.001
c05k05	0.566	0.029	5606	288	0.0058	1.041	0.9979	1.042	1.028
c05k15	1.477	0.077	4585	238	0.0464	1.366	0.9835	1.385	1.242
c05k30	2.202	0.116	2974	157	0.1436	2.486	0.9500	2.598	1.890
KMM87	0	0	3300	180	0	1	1	1	1
CKM95a	1.502	0.082	2760	151	0.049	1.355	0.980	1.378	1.252
CKM95b	2.225	0.116	2872	150	0.137	2.388	0.952	2.490	1.894

extent of the domain. Linearly implicit operators were used in all three directions.

A direct comparison between the present results and those by Coleman et al. [27] can be made from the $\mathrm{Re} = 3000$, $\mathrm{Ma} = 1.5$ cases c03k15 and CKM95a, which are highlighted in Table 5.1. Aside from differences in the numerics,[9] in the upper half of the table the only appreciable parameter differences between these two cases are the wall normal resolution (Δy^+_{10} of 13.8 vs 8) and the viscosity power law exponent (β of 2/3 versus 0.7). One-dimensional Fourier spectra at $y \approx 0.04$ and $y \approx 1$ (not shown) compare favorably indicating the former difference is benign. The latter difference was deliberate as it produces data mildly more appropriate for high temperature environments as demonstrated by Figure A.1. In the lower half of the table, discrepancies between these two particular simulations range from 0.43% (Re_c) to 1.3% (Ma_τ). Minor disagreement is expected per the noted parameter differences but additional root causes are further explored below. Though nominally possible, another comparison between rows c05k30 and CKM95b is not valid as the c05k30 hyperbolic tangent stretching parameter was too small causing insufficient near-wall resolution as assessed by spectra (not shown).

Based on techniques from Section 4.3, mean primitive quantity and Favre-averaged Reynolds stress profiles along with pointwise uncertainty estimates appear for simulation c03k15 in Figure 5.6. The autoregressive technique by Oliver et al. [114] was used to estimate pointwise sampling error at each wall-normal collocation point based on 383 instantaneous averages over the two Fourier directions. In the

[9] Coleman et al. used a Fourier-Legendre spatial discretization and a third-order, four-substep temporal scheme by Buell [21].

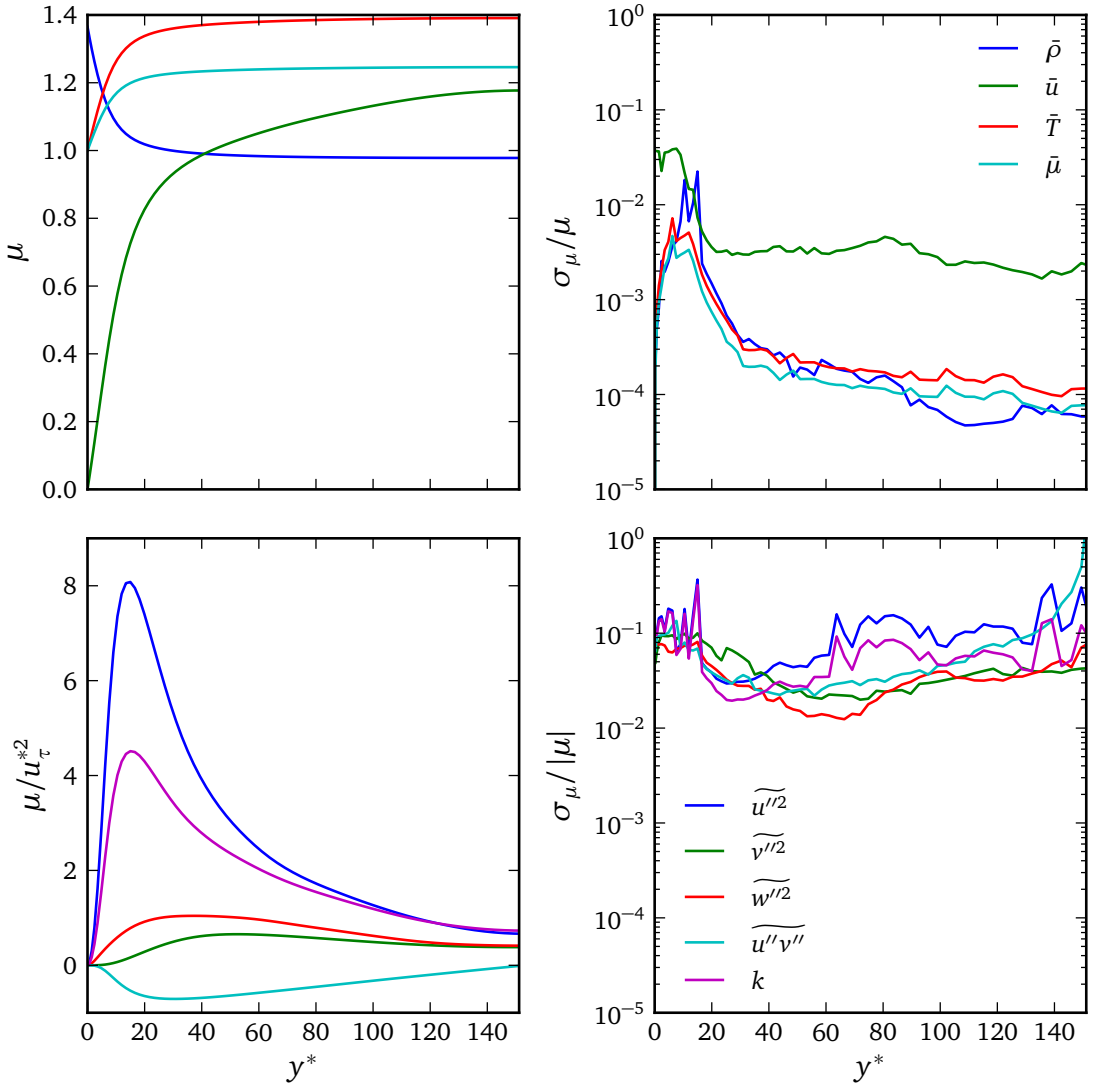

Figure 5.6: Reynolds-averaged primitive profiles (upper left) and Favre-averaged Reynolds stresses scaled by semi-local units [67] (lower left) with estimated standard errors as a fraction of mean (upper right, lower right) from simulation c03k15.

upper right of the figure, uncertainties normalized by mean velocity $\bar{u}$, temperature $\bar{T}$, and viscosity $\bar{\mu}$ are higher near the wall due to both turbulent fluctuations and the fact that the mean values take minima there. The largest normalized uncertainties in mean density $\bar{\rho}$ are slightly offset from the other peaks because the mean value increases as one approaches the wall. Uncertainty in $\bar{u}$ is appreciably larger than that for the thermodynamic quantities consistent with their relative root-mean-squared magnitudes [27, Figures 10 and 18]. We were unable to locate a published uncertainty estimate by Coleman or his collaborators for the CKM95a simulation data against which to compare. Uncertainty in near-wall $\bar{u}$ and centerline $\bar{u}$ are roughly 6 and 1.5 times larger, respectively, than analogous incompressible results from Oliver et al. [114] when both are scaled by the inverse root of the number of flow throughs in the ensemble. This difference will be addressed in more detail below.

In the lower right of the figure, sampling errors have been propagated into the derived, Favre-averaged quantities via the Taylor series method (4.93). Uncertainty in the density-weighted Reynolds stresses is approximately an order of magnitude higher than was found for quantities like $\bar{u}$. The stresses are partially less certain because their calculation takes as input higher order moments which are inherently less well-known given a finite sampling window. A second factor contributing to uncertainty in the stresses is that the definition of $\widetilde{u_i'' u_j''}$ involves scaling by $\bar{\rho}^{-1}$ which magnifies uncertainty when applying the Taylor expansion (4.93).

A third factor contributing to relatively higher uncertainties in the Reynolds stress was an operational error. It was discovered because the *a posteriori* uncertainty estimates showed larger-than-anticipated asymmetries about the channel centerline

though mean values did not. Given the solver verification results in Figure 5.3 and Figure 5.4, an error in the implementation of the post-processing logic initially was suspected but no symmetry-breaking issues were uncovered there. On careful review, all new simulations in Table 5.1 showed evidence of infrequent, mild near-wall temporal instability though they used the empirical B-spline operator stability estimates with the safety factor of 0.72. The problem was diagnosed from temporal traces of the instantaneous global minimum of the streamwise momentum— a simulation monitoring feature not yet implemented when the empirical stability estimates were created. Channel flows exhibit small, pointwise-negative velocities near the wall and it is exactly these locations where linear-implicitness about the instantaneous mean state, as described in Section 4.1.5, is most subject to stability problems when time steps are too large. Implicit treatment in only the wall-normal direction also showed, under review, the same symptom indicating that the operator stability estimates from Section 4.1.4.3 were too aggressive for the safety factor 0.72.

Marginal temporal instability was manifest in asymmetric uncertainty estimates because independent, short-duration instability events occurred infrequently enough near each wall that over O(10) flow throughs in a small domain their impact was not distributed evenly between the upper and lower halves of the channel. As a consequence of this mistake, figures in the present section do not merge the upper and lower portions of the channel as is commonly done. Not merging data across the centerline accounts for a factor of 1.5 increase in $\bar{u}$ uncertainty relative to aforementioned scaled results by Oliver et al. [114]. The remaining threefold increase in near-wall $\bar{u}$ uncertainty relative to their work is at least partially due to these infrequent events. That

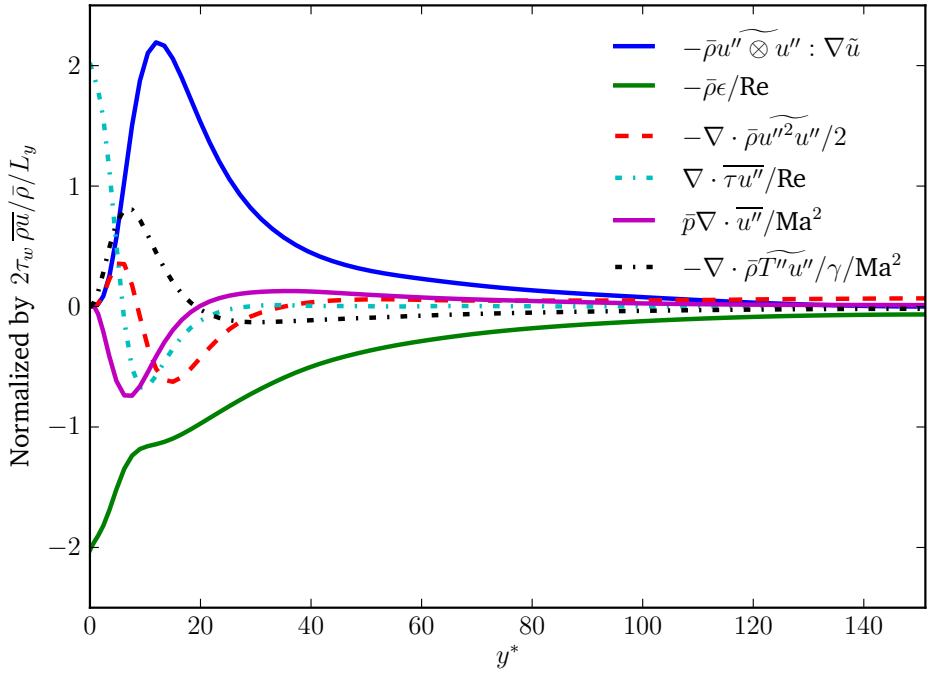

Figure 5.7: Budgets for the turbulent kinetic energy (3.11d) for channel simulation c03k15 normalized as by Huang et al. [67, figure 16a]. Omitted terms relative to (3.11d) are a factor of 25 times smaller than maximum production. [60].

said, it is also partially attributed to the growth in root-mean-squared u fluctuations as the Mach number increases. The same time step size mistake certainly contributes to the disagreement between cases c03k15 and CKM95a found in Table 5.1 and the jaggedness of the near-wall uncertainty curves in the upper right of Figure 5.6.

Term-by-term budgets for the turbulent kinetic energy (3.11d) in Figure 5.7 support the conclusion that time discretization errors are appreciable in simulation c03k15. Qualitatively, all terms show expected trends. However, relative to Huang et al. [67, Figure 16a], approximately 5% too much turbulent dissipation, $\bar{\rho}\epsilon/\mathrm{Re}$, is

present at the wall along with a counterbalancing increase in turbulent work. Coleman and Sandberg [28] linked increased dissipation with temporal inaccuracy when Runge–Kutta schemes are used. Other terms are similarly affected. For example, peak production $-\bar{\rho}\widetilde{u'' \otimes u''} : \nabla \tilde{u}$ is roughly 10% lower than Huang et al. reported. However, Suzerain's post-processing logic and the overall budget balance are sound because the pointwise turbulent kinetic energy equation residual, is appropriately small.

5.4 Performance and Scalability

This section first discusses the efficiency of three available Navier–Stokes operator implementations, briefly compares Suzerain's performance against a highly tuned incompressible channel code, and lastly examines Suzerain's scalability on production homogenized boundary layer simulations. All performance measurements were made on the Lonestar4 supercomputer at the Texas Advanced Computing Center (TACC) as it will be the resource used for production simulations in subsequent chapters. Each compute node on Lonestar contains 2 hex-core Intel® Xeon® 5680 3.33 GHz processors and 24 GB of DDR3-1333 MHz memory. Every core was used as a separate MPI rank as Suzerain presently is not OpenMP-enabled. Compute nodes are interconnected in a fat-tree topology using Mellanox® InfiniBand™ switches running at quad data rates of 40 Gbits/second. Compilation was performed with version 11.1 20101201 of the Intel® compilers at optimization level 3 with host-specific extensions enabled.

The efficiency of the fully explicit, linearly implicit in the wall-normal direction, and linearly implicit in three directions operators were benchmarked and are reported in Table 5.2. Efficiency was measured as the amount of wall time required to advance

Table 5.2: Normalized wall time to advance simulation one nondimensional time unit using each of the available Navier–Stokes operator implementations. Cases, defined in Table 5.1, were executed with Suzerain v0.1.6.34-r45407 using 12 nodes of Lonestar4.

Case	Linearly implicit XYZ	Linearly implicit Wall-normal	Fully explicit
c03k01	1.0	11.0	49.5
c03k05	1.0	2.9	10.3
c03k15	1.0	1.3	3.7
c03k30	1.0	1.4	2.0
c05k01	1.0	8.7	48.7
c05k05	1.0	2.5	10.4
c05k15	1.0	1.7	4.4
c05k30	1.0	1.3	2.3

one nondimensional time unit because that physics-oriented metric directly translates into the expense of acquiring converged turbulence statistics. Another metric, wall time per time step, will be presented later alongside scalability results. Centerline Mach numbers across the eight cases considered vary by nearly a factor of twenty. This broad range permits assessing efficiency for widely varying acoustic-versus-convective restrictions as well as significant differences in thermodynamic property fluctuation magnitudes.

On the eight cases examined, linear implicitness in three directions produced time to solution speedups of 1.3–11x relative to treating only the wall-normal direction implicitly. The speedup improved as the Mach number decreased because the more implicit operator mitigates streamwise and spanwise acoustic stability concerns that would otherwise dominate at those conditions. The measurable speedup in higher speed channels is perhaps counterintuitive as the more implicit implementation re-

quires matrix assembly and factorization for every (k_m, k_n) wavenumber pair while the second fastest does not. Though factorization has a much higher asymptotic complexity than assembly, at this resolution the former takes only twice the wall time of the latter. Factorization of the assembled matrices, here possessing bandwidth 69, has a favorable memory access pattern in contrast with the assembly kernels and consequently performs comparatively well despite the larger number of floating point operations it requires.

The above conclusions are what prompted selecting implicitness in three directions for the isothermal channel simulations discussed in the prior section. Note that though less aggressive time step safety factors than 0.72 were in that section concluded to be required, safety factor reductions impact both available implicit treatments fairly equitably and therefore do not grossly upset their relative efficiencies. Some simulations performed as part of the next two chapters will use only wall-normal implicitness because they were not limited by streamwise or spanwise stability thus making wavenumber-dependent linear algebra detrimental to time-to-solution efficiency. In summary, having both types of implicitness available in Suzerain as equally viable options permits the code to effectively address the wide range of flow conditions studied.

To assess the performance of Suzerain as a direct numerical simulation framework, we compared it against the highly optimized channel code PoongBack [89, 90], written by Myoungkyu Lee. PoongBack is a comparatively monolithic Fortran code for solving the incompressible Navier–Stokes equations. Like Suzerain, PoongBack uses a Fourier–Galerkin/B-spline collocation spatial representation in conjunction with a

three-stage, low-storage semi-implicit advance. The Kim et al. [76] Navier–Stokes formulation advances two scalar state variables in time requiring three wave-to-physical parallel Fourier transforms and five physical-to-wave transforms per time step. Every (k_m, k_n) wavenumber pair requires multiple linear solves but the operators do not couple multiple equations and require relatively uncomplicated matrix assembly to form. Unlike Suzerain, PoongBack uses wholly custom linear algebra routines, wholly custom, quadrature-aware parallel Fourier transforms built atop FFTW 3.3's MPI capabilities, and hybrid MPI/OpenMP parallelism. The comparison is apt because many of Lee's improvements could be adopted by Suzerain if performance improvements are required for future work.

Mimicking the resolution from our simulation c03k01, Lee performed an $\mathrm{Re}_\tau = 180$ simulation on 12 nodes of Lonestar4 using 6 OpenMP threads per processor. PoongBack took 0.1299 seconds to complete one Runge–Kutta step. The timing of high-level tasks from our c03k01 case were collected and then scaled by the frequency with which they are required to advance the Kim et al. [76] formulation. For example, the wall time P3DFFT required to transform 30+ scalar fields from wave space to physical space was scaled to reflect PoongBack only needing to perform that task for three fields. Physical space nonlinear product costs were scaled by the ratio of the number of scalar equations involved, a conservative choice because the incompressible system of equations is considerably less complex than the compressible one. Scaling for linear algebra tasks, including matrix-vector products, matrix assembly, back substitution, and factorization, reflected both the relative number of tasks performed during one substep as well as relative code-to-code operation costs arising from differences in equation coupling. For

example, factorization costs were scaled by $6/5^3$ as, per wavenumber pair, PoongBack performs six single-equation factorizations while Suzerain performs one monolithic factorization with a leading-order, S-dependent cubic complexity (4.36).

After rescaling, each hypothetical Suzerain time step solving the incompressible Kim et al. formulation required 0.629 seconds representing a 4.8x slowdown relative to PoongBack. About 30% of the hypothetical wall time per time step would be spent on parallel transposes with the vast majority of the remainder consumed by banded algebraic operations. Less conservative estimates of the nonlinear product costs incurred in physical space bring the hypothetical slowdown as low as 4×. The hypothetical slowdown is larger than hoped but reasonable— Lee took in excess of a year to produce PoongBack with much of that time spent crafting and tuning formulation-specific banded algebraic logic to which he attributes an overall speedup of 2× (personal communication).

Suzerain's strong scalability as well as timings for the three available Navier–Stokes operator implementations are shown in Figure 5.8. The problem size studied, which could run on as few as 24 MPI ranks, corresponds to the production grid to appear in Chapter 6. The state is only 168 million real-valued degrees of freedom (1.3 GB) but each full Runge–Kutta step required P3DFFT to transmit and fast Fourier transform 69 GB of information. Scalability from 24 to 48 ranks was not good but from 48 to 384 ranks operator-specific parallel efficiencies exceeded 93.3%. Within this sweet spot, advancing linear implicitly in one or three directions took 107–110% or 152–155% of the wall time of a fully explicit time step, respectively.

At 768 and 1536 ranks, job-to-job measurements of the wall seconds per time

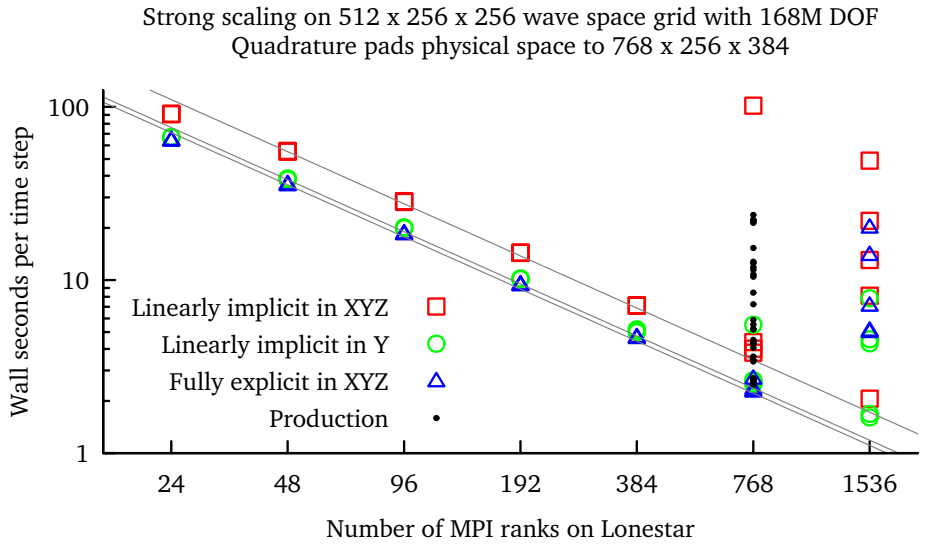

Figure 5.8: Strong scalability on a homogenized boundary layer scenario. At least three samples are present for each rank count and Navier–Stokes operator implementation. Workload is well-balanced at all rank counts. Grey lines indicate perfect parallel efficiency based upon 48-rank performance. Production timings, here implicit in only the wall-normal direction, included the overhead of writing statistics and checkpoint files.

step became highly variable. We attribute the behavior either to such batch jobs often executing on compute nodes separated widely on Lonestar4's fat-tree interconnect or to some other intermittent network issue. Though some variability was always present at these rank counts, atop an unchanged Suzerain binary it became dramatically worse after a Lonestar4 system maintenance on 27 May 2014. The better jobs measured after that date exhibited coefficients of variation between 2–4% for the time it took P3DFFT to transform a single scalar field while the worse jobs exceeded 500%. P3DFFT scalability problems on Lonestar4 at 768 and 1536 ranks was also observed by Lee et al. [89] though they encountered nothing so severe. Despite these issues and due to time-to-solution considerations, production simulations were executed on 768 ranks

because, when provided with a favorable network fragment, job efficiency moving from 384 to 768 ranks could approach 100%. Figure 5.8 includes laggard production jobs that, when detected, were manually stopped to conserve compute resources.

Chapter 6

Characteristics of the Homogenized Boundary Layers at Atmospheric Reentry-like Conditions

To reduce turbulence-driven uncertainty in aerothermodynamic heating predictions for blunt-bodied reentry vehicles, new direct numerical simulations of spatiotemporally homogenized boundary layers were performed to address the need for high-quality turbulence model calibration data identified in Chapter 2. In this chapter, the characteristics of these new homogenized boundary layer simulations are examined. The chapter additionally provides enough information so that a prediction-oriented practitioner may assess this new data's merit towards inclusion in some calibration process. The simulations will be described and analyzed, which includes simulation details (Section 6.1), notes on the observed integral boundary layer thicknesses (Section 6.2), turbulence statistics (Section 6.3), and Favre-averaged equation budgets (Section 6.4).

For a more in-depth investigation of the homogenization see Topalian et al. [165]. Also note that homogenization-related forcing terms from that reference must be incorporated when calibrating a turbulence model using the present results. The terms are not, however, required for subsequent use of a calibrated model.

6.1 Simulation Details

Two cold-wall boundary layers were simulated at conditions representative of flow over the Orion MPCV thermal protection system at peak heating during vehicle reentry from the International Space Station. Additional background on the reentry conditions can be found in Section 2.9. The two scenarios of interest were constructed by taking conditions found 3.199 meters and 4.134 meters leeward of the stagnation point in Figures 2.7 and 2.8 and then increasing the momentum Reynolds numbers Re_θ to match similar flow speeds in Table 2.3 as measured by the edge Mach numbers Ma_e. That is, the scenarios combined Re_θ and Ma_e from fully turbulent conditions with fully laminar edge-to-wall temperature ratios T_e/T_w, wall blowing velocities v_w^+, and pressure gradient strengths $p_{e,\xi}^*$. Relative to drawing from only the fully turbulent conditions in Tables 2.2 and 2.3, these hybrid conditions produced larger T_e/T_w and somewhat milder favorable pressure gradients. The choice of these conditions was motivated by the work to be presented in Chapter 7. Though the resulting hybrid scenarios strictly speaking appear nowhere in the fully turbulent simulations by Bauman et al. [8] or Stogner et al. [154], the two scenarios meet Settles and Dodson [143]'s *realistic test conditions* criterion, discussed in Section 2.2, and are therefore suitable for turbulence model calibration targeting this predictive context.

One direct numerical simulation was performed at each scenario of interest. The coordinate system is depicted in Figure 4.1. Tables 6.1–6.4 document the two scenarios, for reproducibility distinguishing between code input parameters and *a posteriori* observations. These tables will be discussed in more detail below. The calculations used the Navier–Stokes formulation from Section 3.1 equipped with the "slow growth"

Table 6.1: Homogenized boundary layer simulations performed by Suzerain v0.1.6.34-r45407 intended for turbulence model calibration. For all cases, $\mathrm{Pr} = \mu C_p/\kappa = 0.7$, $\alpha = 0$ in $\mu_B = \alpha\mu$, $\beta = 2/3$ in $\mu/\mu_0 = (T/T_0)^\beta$, and $\gamma = C_p/C_v = 1.4$. Extents were $L_x/l_0 = 10$, $L_y/l_0 = 2.5$, $L_z/l_0 = 3$ employing a piecewise-quintic B-spline basis with N_y collocation points stretched per the hyperbolic tangent parameter "tanh" following (4.14). Grid spacings are normalized by $\delta_\nu = \mu_w/\rho_w/u_\tau$ where $u_\tau = \sqrt{\tau_w/\rho_w}$ and $\tau_w = \left(\mu\partial_y u\right)_w$. The distance between the isothermal wall and the first and tenth collocation point is written y_1^+ and y_{10}^+, respectively.

	Code inputs										
Case	Re	Ma	N_x	N_y	N_z	tanh	Δx^+	y_1^+	y_{10}^+	Δz^+	Turnovers
t3.199	2400	0.8985	512	256	256	2.25	13.9	0.14	6.1	8.4	6.4
t4.134	3250	1.1522	512	256	256	2.35	19.0	0.17	7.2	11.4	6.9

Table 6.2: Input parameters and resulting homogenized boundary layer conditions. Re_{99} and Ma_{99} computed from conditions at δ_{99}. To properly account for a nonuniform base flow, Re_θ is defined per (6.8). Wall blowing velocity $v_w^+ = v_w/u_\tau$.

	Code inputs								
Case	$\mathrm{gr}_{t_0}(\Delta)$	T_w/T_0	v_w/u_0	δ_{99}/l_0	Re_{99}	Re_θ	Ma_{99}	T_{99}/T_w	v_w^+
t3.199	0.0135	0.2346	2.30e−4	1.001	2468	382	0.9041	4.128	8.52e−3
t4.134	0.0200	0.2333	1.90e−4	1.002	3346	531	1.1523	4.201	7.18e−3

Table 6.3: Pressure gradient strengths for the simulated boundary layers. The inviscid base flow was constructed per Appendix C using inputs $\delta/l_0 = 1$, γ, $\mathrm{Ma}_e = \mathrm{Ma}$ from Table 6.1 and $p^*_{e,\xi}$. Observations of $p^*_{99,\xi}$, Launder's acceleration parameter K [86], the Pohlhausen parameter K_s, and parameter Λ_n [107] are shown evaluated as defined in Figure 2.8 taking δ_{99} to be the boundary layer edge.

	Code input					
Case	$p^*_{e,\xi}$	$p^*_{99,\xi}$	$K, \mu = \mu_{99}$	$K, \mu = \mu_w$	K_s	Λ_n
t3.199	−0.010 19	−0.010 25	4.176e−6	1.623e−6	25.44	3.345
t4.134	−0.012 34	−0.012 33	3.734e−6	1.434e−6	41.81	4.113

Table 6.4: Edge versus wall conditions in the simulated boundary layers. Friction quantities $\mathrm{Re}_\tau = \delta_{99}/\delta_\nu$, $\mathrm{Ma}_\tau = u_\tau/a_w = u_\tau/\sqrt{T_w}$, and $c_f = 2\tau_w/\left(\rho_{99}u_{99}^2\right)$. Nondimensional heat flux $B_q = -\mu_w\left(\partial_y T\right)_w/\left(\mathrm{Pr}\,\rho_w u_\tau T_w\right)$ [16] and local Nusselt number $\mathrm{Nu}_{99} = \delta_{99}\left(\partial_y T\right)_w/\left(T_{99}-T_w\right)$.

Case	ρ_{99}/ρ_w	μ_{99}/μ_w	ν_{99}/ν_w	Re_τ	Ma_τ	c_f	$-B_q$	Nu_{99}
t3.199	0.2427	2.573	− 3.003	714	0.05008	6.128e−3	0.09765	15.59
t4.134	0.2383	2.603	30.95	976	0.06311	5.994e−3	0.1018	21.74

spatiotemporal homogenization of Section 3.3. Favorable pressure gradients were obtained by supplying an inviscid base flow, constructed as described in Appendix C, to the spatiotemporal model. The continuous equations were discretized following Chapter 4 and implemented in Suzerain as described by Chapter 5. Simulation data has been archived per Appendix D.

Table 6.1 reports the target Re and Ma based on boundary layer edge conditions for each simulation, along with the domain sizes and numerical resolutions used. The nondimensional formulation in conjunction with the inviscid base flow design procedure *a priori* causes ρ_{99}/ρ_0, u_{99}/u_0, δ_{99}/l_0, and T_{99}/T_0 to all be approximately one so that code inputs $\mathrm{Re} \approx \rho_{99}u_{99}\delta_{99}/\mu_{99}$ and $\mathrm{Ma} \approx u_{99}/a_{99}$. The slow growth parameter $\mathrm{gr}_{t_0}(\Delta)$ was tuned to obtain $\delta_{99}/l_0 \approx 1$ as an operational convenience. As a result, for either scenario and for any length L it holds that $L/l_0 \approx L/\delta_{99}$ to within 0.2%. The streamwise domain extent normalized by the boundary layer thickness was taken 25% larger than the value of eight employed by Guarini et al. [60] because they reported their choice was mildly too small. The spanwise extent approximately matches that used by Spalart [150]. Grid resolution in the streamwise and spanwise directions is similar to the cold-wall channel simulations by Coleman et al. [27] listed in Table 5.1.

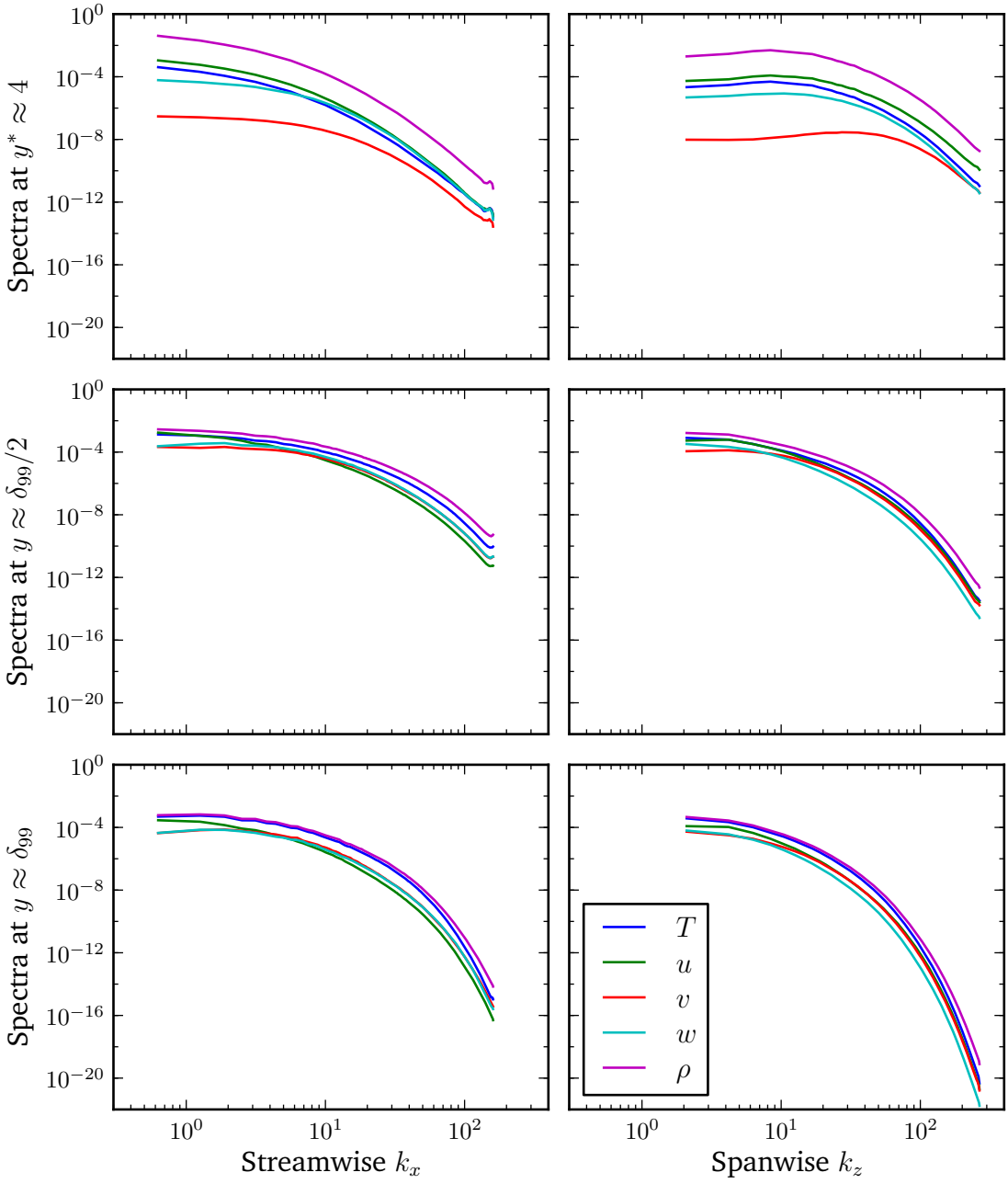

Figure 6.1: One-dimensional, unnormalized Fourier energy spectra for case t3.199.

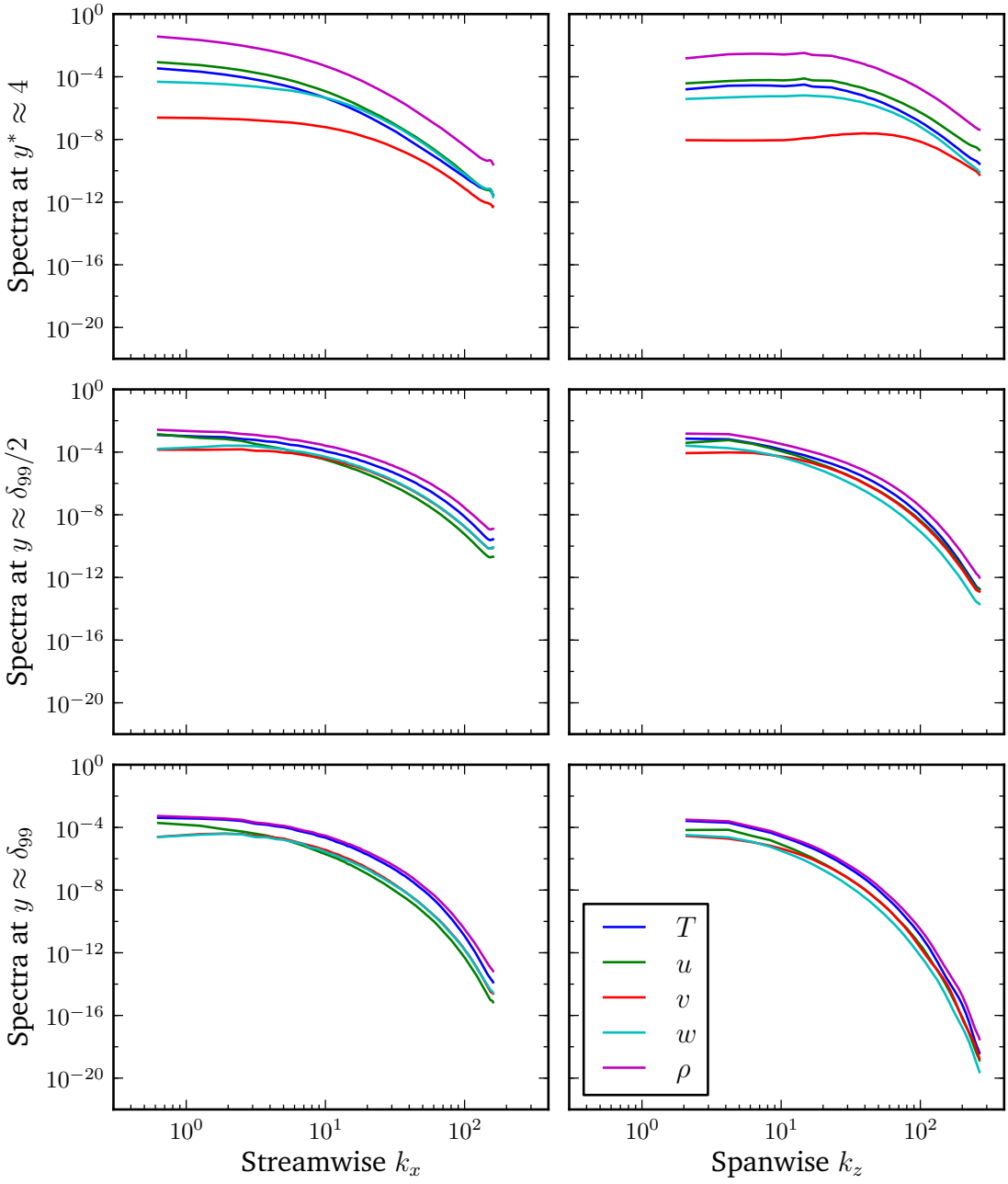

Figure 6.2: One-dimensional, unnormalized Fourier energy spectra for case t4.134.

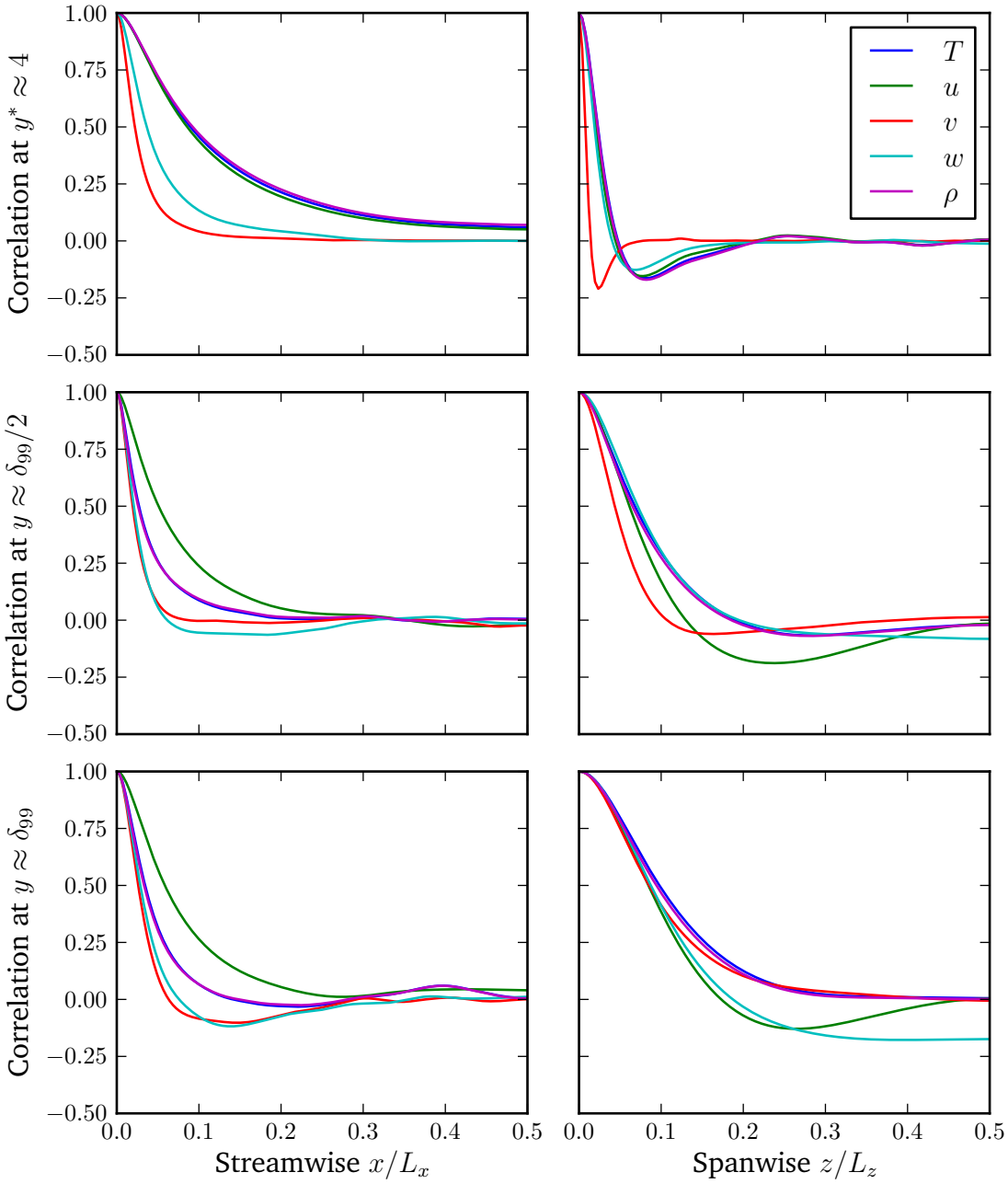

Figure 6.3: Two-point correlations for simulation t3.199.

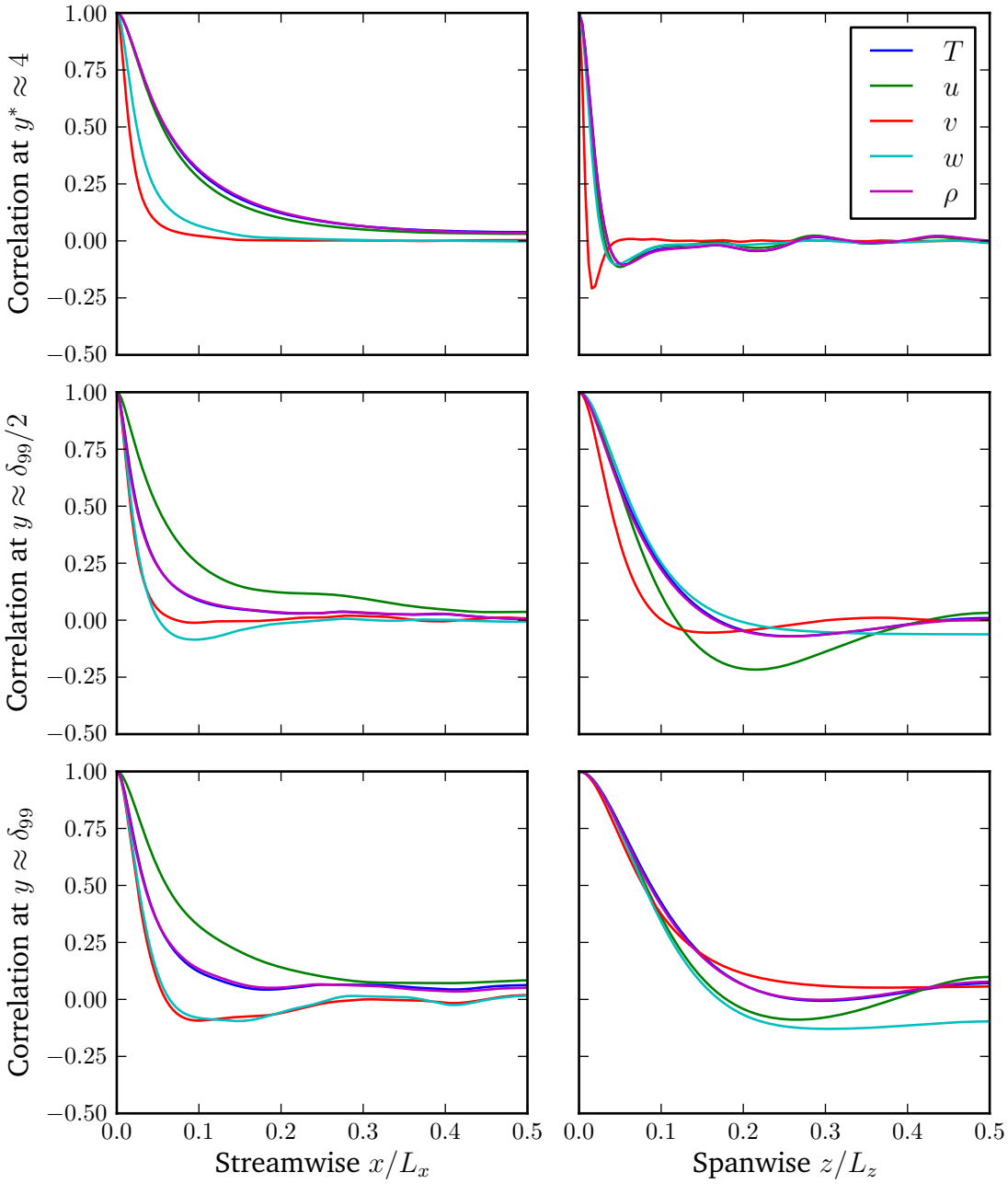

Figure 6.4: Two-point correlations for simulation t4.134.

The one-dimensional Fourier spectra, shown for primitive variables in Figures 6.1 and 6.2, indicate that the present simulations are better resolved in the periodic directions than those of Coleman et al.. The streamwise spectra at $y^* = y\sqrt{\tau_w/\rho}/\nu \approx 4$ demonstrate that L_x was slightly smaller than required to eliminate artifacts from the periodic boundary conditions. This is corroborated by the two-point correlations in Figures 6.3 and 6.4 which show T, u, and ρ not decorrelating fully at $x/L_x = 0.5$. However, the streamwise correlations exhibit less coherence than those of Coleman et al. and Guarini et al. and, like those authors, we anticipate finite domain effects to have little impact on the results presented here. Aside from the spanwise velocity w, spanwise coherence far from the wall is smaller than Guarini et al. reported and is found acceptable. The increase in w correlation as y increases, also observed by Victor Topalian (personal communication), is thought to be a benign artifact of the homogenization. Given the quality of the spectra, evidently L_z could have been larger without incurring extra computational expense and without adversely decreasing spanwise resolution.

In the wall-normal direction for case t3.199, collocation point $y^+_{15} \approx 10.4$, 178 points were inside δ_{99}, and $\Delta y^+|_{y=\delta_{99}} \approx 10.7$. For case t4.134, $y^+_{13} \approx 10.1$, 180 points were inside δ_{99}, and $\Delta y^+|_{y=\delta_{99}} \approx 15.0$. To account for the considerable density and temperature gradients arising from holding wall temperatures fixed, the wall-normal grid spacings are more appropriately assessed when scaled by semi-local units [67, 103] which use either $u^*_\tau = \sqrt{\tau_w/\rho}$ or $\delta^*_\nu = \nu/u^*_\tau$. For simulation t3.199, collocation point $y^*_{27} \approx 10.1$ and $\Delta y^*|_{y=\delta_{99}} \approx 1.6$. For case t4.134, $y^*_{24} \approx 10.3$ and $\Delta y^*|_{y=\delta_{99}} \approx 2.2$.

Both simulations used linear implicit time discretization only for operators involving derivatives in the wall-normal direction and, given the lessons learned in Section 5.3 regarding the aggressiveness of the eigenvalue estimates from Section 4.1.4.3, time step safety factors of 0.35 were selected. As measured by time-to-solution, linear implicitness in three directions was equally but no more performant than the wall-normal-only variant. The latter was chosen as it used smaller time steps and therefore was expected to better resolve flow dynamics. The column "turnovers" conveys the time over which the statistical ensemble was collected divided by δ_{99}/u_τ. The ensemble for cases t3.199 and t4.134 includes 764 and 837 instantaneous planar averages over x and z which were collected *in situ* from the simulations. Uncertainties were estimated from the temporal trace of these equispaced samples following procedures outlined in Section 4.3.

Table 6.2 documents the fixed temporal slow growth rates $\mathrm{gr}_{t_0}(\Delta)$, the isothermal wall temperatures, and the wall blowing rates. It shows that the homogenization held $\delta_{99} \approx 1$ and that the desired Re_{99} and Ma_{99} conditions were produced. The remaining columns confirm that simulations t3.199 and t4.134 indeed correspond to their namesake locations in Figures 2.7 and 2.8 save for possessing Re_θ representative of those found in in Table 2.3.

Table 6.3 characterizes the favorable pressure gradients found in the two simulations in a variety of ways. The desired inviscid pressure gradient parameter $p^*_{e,\xi}$, defined in (2.14), is listed alongside the observed result at δ_{99} labeled $p^*_{99,\xi}$. The inviscid base flow design procedure from Appendix C produced the target pressure gradient strength to within 0.6%. Comparing the tabulated values against Figure 2.8, the sim-

ulated values of Launder's acceleration parameter K are between the bands shown calculated from fully laminar Orion MPCV computations. Simulation t3.199 shows reasonable agreement with the expected Pohlhausen parameter K_s from the same figure while simulation t4.134 is more than 50% too large. However, the K_s values computed from the MPCV source data are suspect as they possess appreciable numerical artifacts. Both simulations produced Λ_n values roughly a factor of two less than the MPCV data but the discrepancy is not surprising as the wall shear τ_w entering into Λ_n was not specified *a priori*. We consider the inviscid base design procedure to be successful because it closely reproduced the desired condition on $p^*_{99,\xi}$ while yielding pressure gradients not too dissimilar from the MPCV data when quantified using other metrics.

Table 6.4 conveys several quantities of interest from the simulations. As expected, the prescribed wall temperatures T_w/T_0 produce larger densities and lower viscosities near the wall. Despite its wall-normal velocity at the edge being positive, simulation t4.134 uses subsonic inflow boundary conditions because of how the homogenization causes inputs L_y and $\mathrm{gr}_{t_0}(\Delta)$ to modify the wall-normal inviscid characteristics as discussed in Section 4.2.2.5. On account of wall injection, friction Reynolds number Re_τ is higher and skin friction c_f is lower than might be expected based upon Re_θ and Ma_{99} [149, 155]. To ease comparing surface heating predictions against the present results, the nondimensional heat flux B_q and the Nusselt number Nu_{99} are also tabulated.

6.2 A Note on Integral Thicknesses and the Clauser Parameter

The omissions of the displacement thickness δ^*, the momentum thickness θ, and the Clauser parameter β [26] from the above tables merit explanation. That explanation requires revisiting the classical definitions of the two thicknesses to properly account for the presence of the nonuniform inviscid base flows which were used to enforce nonzero pressure gradients. Along the way, the two related integral thickness Reynolds numbers accommodating nonuniform base flows will be derived.

As explained in, for example, Kundu et al. [80, §9.2] the displacement thickness δ^* is the distance by which the wall would have to be displaced upward in a hypothetical frictionless flow to maintain the same mass flux as that in the viscous flow. That is, δ^* is the length satisfying

$$\int_0^\infty \rho u_{\text{viscid}}(y)\,\mathrm{d}y = \int_{\delta^*}^\infty \rho u_{\text{inviscid}}(y)\,\mathrm{d}y. \tag{6.1}$$

Formally the upper limit may be replaced by any sufficiently large, finite value because $\rho u_{\text{viscid}} \to \rho u_{\text{inviscid}}$ as $y \to \infty$. Assuming our domains are large enough,

$$\int_0^{L_y} \rho u_{\text{viscid}}(y)\,\mathrm{d}y = \int_{\delta^*}^{L_y} \rho u_{\text{inviscid}}(y)\,\mathrm{d}y. \tag{6.2}$$

One can obtain a simplification often taken as a definition [138, Equation 10.95],

$$\delta^* = \int_0^{L_y} 1 - \frac{\rho u_{\text{viscid}}(y)}{\rho_e u_e}\,\mathrm{d}y, \tag{6.3}$$

for the special case of a uniform inviscid flow where $\rho u_{\text{inviscid}}(y) = \rho_e u_e$. Multiplying by $\rho_e u_e/\mu_e$, recognizing the displacement Reynolds number Re_{δ^*}, and formally converting

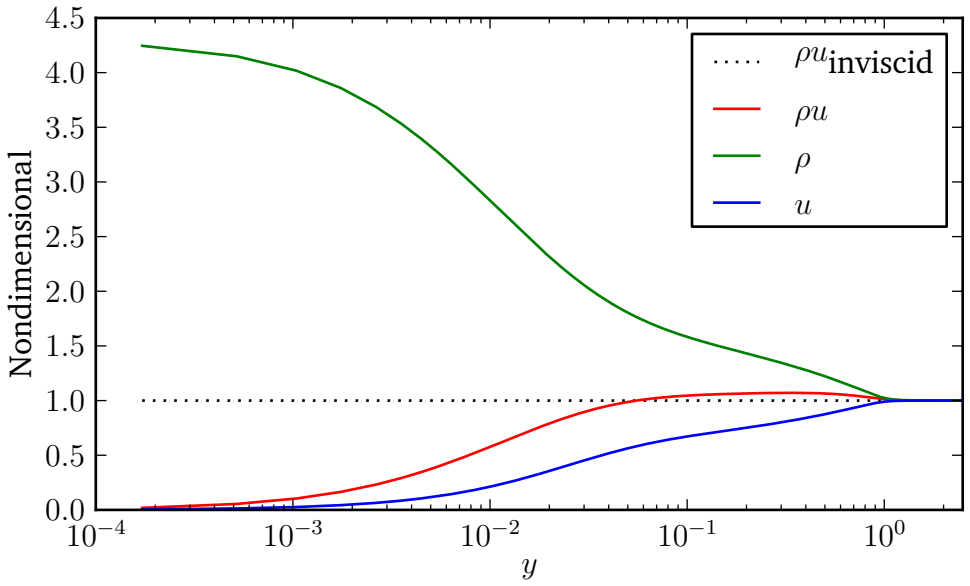

Figure 6.5: The inviscid base flow and viscous flow profiles for simulation t4.134

back to the nonuniform inviscid base flow,

$$\begin{aligned}
\mathrm{Re}_{\delta^*} = \frac{\rho_e u_e \delta^*}{\mu_e} &= \frac{\rho_e u_e}{\mu_e} \int_0^{L_y} 1 - \frac{\rho u_{\text{viscid}}(y)}{\rho_e u_e} \, \mathrm{d}y, \\
&= \mu_e^{-1} \int_0^{L_y} \rho_e u_e - \rho u_{\text{viscid}}(y) \, \mathrm{d}y, \\
&\approx \mu_e^{-1} \int_0^{L_y} \rho u_{\text{inviscid}}(y) - \rho u_{\text{viscid}}(y) \, \mathrm{d}y. \qquad (6.4)
\end{aligned}$$

A constant viscosity, here chosen to be μ_e, should scale the above integral when defining Re_{δ^*}. There is no sensible way to incorporate dimensions of inverse viscosity into its integrand's left term thus permitting $\mu^{-1}(y)$ to multiply the right term.

Mean profiles from simulation t4.134 pictured in Figure 6.5 are the impetus for recalling the general displacement thickness balance (6.2) as well as its simplification (6.3). Progressing from the cold wall at $y = 0$ to the boundary layer edge at $y = \delta_{99} \approx 1$, the streamwise velocity increases, the density drops considerably, and

the momentum in the viscous flow exceeds that of the inviscid base flow. Evaluating integral (6.3) taking $\rho_e u_e$ from δ_{99} produces $\delta^*/l_0 = -0.03923$. Interpreting this negative δ^* through the usual displacement effect intuition, for simulation t4.134 introducing the cold plate into the inviscid profile increases the mass flow rate because it significantly increases the near-wall density. Negative δ^* are reported for exotic flows but seem uncommon [e.g. 20, 44]. The flow, however, need not be exotic. The zero-pressure-gradient boundary layer forming on a sufficiently cold, flat plate in laminar air will exhibit a negative displacement thickness (Truman E. Ellis, personal communication). Evaluating the right hand integrand for the more correct balance (6.2) behaves unusually— the shape of the inviscid base flow when $y < 0$ does not influence the viscous solution on $y \in \left[0, L_y\right]$ but it impacts δ^*. For this reason, a generalization of (6.3),

$$\delta^* = \int_0^{L_y} 1 - \frac{\rho u_{\text{viscid}}(y)}{\rho u_{\text{inviscid}}(y)} \, \mathrm{d}y, \tag{6.5}$$

is selected as a definition and evaluating it shows $\delta^* = -0.03918$ in simulation t4.134. Therefore, Re_{δ^*} must be negative and indeed evaluating (6.4) finds $\mathrm{Re}_{\delta^*} = -129$. The Clauser parameter $\beta = \frac{\delta^*}{\tau_w}\frac{\partial p}{\partial x} = 0.1608$ is positive in this favorable pressure gradient flow, contrary to expectations [e.g. 13], because of negative displacement effects. Simulation t3.199 also exhibits the actual momentum exceeding the inviscid profile momentum (not shown) but possesses $\delta^*/l_0 = 0.006429$, $\mathrm{Re}_{\delta^*} = 15.8$, and $\beta = -0.02148$; β in no way communicates the strength of the pressure gradient as many authors term 0.1 a strong magnitude [96, 148].

Negative displacement effects are not evident in the reacting, fully turbulent Orion MPCV data from Table 2.2 ($\delta^*/\delta \approx 0.113$) nor do they appear in the fully

laminar results depicted in Figure 2.8 ($\beta < 0$ leeward of the stagnation point). These effects might not occur because of the higher edge Prandtl numbers in those reacting simulations (see Pr_e in Figure 2.7) because as the Prandtl number increases it causes the thermal boundary layer to grow more slowly relative to the momentum boundary layer.

The momentum thickness θ quantifies the momentum defect relative to the inviscid flow after removing displacement effects. That is, θ is the length satisfying

$$\int_0^{L_y} \rho u^2{}_{\text{viscid}}(y)\,\mathrm{d}y = \int_\theta^{L_y} \rho u^2{}_{\text{inviscid}}(y)\,\mathrm{d}y - \int_0^{\delta^*} \rho u^2{}_{\text{inviscid}}(y)\,\mathrm{d}y \tag{6.6}$$

given fixed δ^* where again the upper limit has been truncated to the domain extent. The commonly seen degenerate form of the above balance, often taken as a definition when $\rho u_{\text{inviscid}}(y) = \rho_e u_e$, is recovered as follows:[1]

$$\begin{aligned}
\int_0^{L_y} \rho u^2{}_{\text{viscid}}(y)\,\mathrm{d}y &= \rho_e u_e^2 \left(L_y - \theta\right) - \rho_e u_e^2 \delta^* \\
\rho_e u_e^2 \theta &= \rho_e u_e^2 L_y - \int_0^{L_y} \rho u^2{}_{\text{viscid}}(y)\,\mathrm{d}y - u_e \left[\rho_e u_e \delta^*\right] \\
&= \int_0^{L_y} \rho_e u_e^2 - \rho u^2{}_{\text{viscid}}(y)\,\mathrm{d}y - u_e \left[\int_0^{L_y} \rho_e u_e - \rho u_{\text{viscid}}(y)\,\mathrm{d}y\right] \\
\theta &= \int_0^{L_y} \left(1 - \frac{\rho u^2{}_{\text{viscid}}(y)}{\rho_e u_e^2}\right) \mathrm{d}y - \int_0^{L_y} \left(1 - \frac{\rho u_{\text{viscid}}(y)}{\rho_e u_e}\right) \mathrm{d}y \\
&= \int_0^{L_y} \frac{\rho u_{\text{viscid}}(y)}{\rho_e u_e} \left(1 - \frac{u_{\text{viscid}}(y)}{u_e}\right) \mathrm{d}y.
\end{aligned} \tag{6.7}$$

Unlike the analogous (6.3), only nonnegative values are possible. Multiplying by

[1] Smits and Dussauge [149, page 214] and Liepmann and Roshko [94, page 324] present result (6.7). Schlichting and Gersten [138, Equation 10.95] made an error in their definition for θ.

$\rho_e u_e/\mu_e$ and formally converting back to the nonuniform base flow,

$$\begin{aligned}\mathrm{Re}_\theta = \frac{\rho_e u_e \theta}{\mu_e} &= \frac{\rho_e u_e}{\mu_e}\int_0^{L_y} \frac{\rho u_{\text{viscid}}(y)}{\rho_e u_e}\left(1-\frac{u_{\text{viscid}}(y)}{u_e}\right)\mathrm{d}y \\ &= \mu_e^{-1}\int_0^{L_y} \rho u_{\text{viscid}}(y)\left(1-\frac{u_{\text{viscid}}(y)}{u_e}\right)\mathrm{d}y \\ &\approx \mu_e^{-1}\int_0^{L_y} \rho u_{\text{viscid}}(y)\left(1-\frac{u_{\text{viscid}}(y)}{u_{\text{inviscid}}(y)}\right)\mathrm{d}y. \end{aligned} \tag{6.8}$$

Here, $\mu(y)$ could have been incorporated into the integrand, but it was not for consistency with (6.4).

Defining θ via the general balance (6.6) is problematic when negative displacement effects are present because, for consistency, that approach should use δ^* from (6.2). For this reason, generalizing (6.7) the present work uses

$$\theta = \int_0^{L_y} \frac{\rho u_{\text{viscid}}(y)}{\rho u_{\text{inviscid}}(y)}\left(1-\frac{u_{\text{viscid}}(y)}{u_{\text{inviscid}}(y)}\right)\mathrm{d}y \tag{6.9}$$

and finds $\theta = 0.1557$ and $\theta = 0.1611$ for simulations t3.199 and t4.134, respectively. The generalization makes little difference— assuming the base flow was constant and directly evaluating (6.7) from inviscid values at $y = \delta_{99}$ changes only the final reported digit in each result. Computed either way, the two spatiotemporal simulations have momentum thicknesses larger than the reacting, fully turbulent Orion MPCV data from Table 2.2 ($\theta/\delta \approx 0.134$). The present simulation shape factors $H = \delta^*/\theta$ of 0.04129 and −0.2432 are well below standard turbulent boundary layer values and contrast strongly with the fully turbulent MPCV result of $H \approx 0.847$ acquired with the aid of a Baldwin–Lomax model. Momentum Reynolds numbers computed according to (6.8) appeared in Table 6.2.

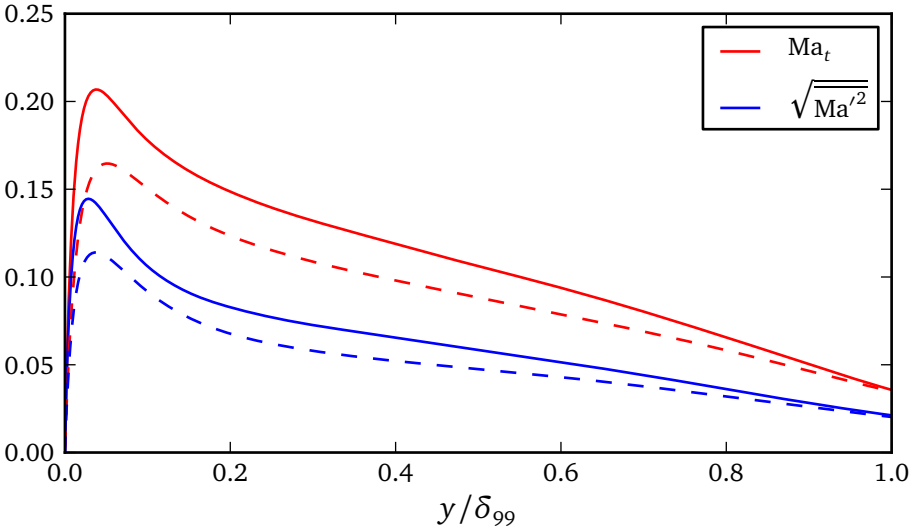

Figure 6.6: Turbulent Mach number $\mathrm{Ma}_t = \sqrt{2k}/\bar{a}$ and root-mean-squared local Mach number for simulations t3.199 (dashed) and t4.134 (solid).

6.3 Turbulence Statistics

This section reviews a collection of turbulent statistics for the present simulations. Comparisons to other work are included but are limited because, as evidenced by their shape factors, these two cold-wall spatiotemporally homogenized flows differ considerably from canonical boundary layers.

Figure 6.6 reports the turbulent Mach number Ma_t and root-mean-squared Mach number fluctuations. Turbulence in both simulations should only be weakly affected by compressibility effects because Ma_t is well below 0.3 [149]. Local shocklets are not expected and so the smoothness assumptions inherent to the numerical approach from Chapter 4 are valid. Consistent with Guarini et al. [60], the peak Ma_t is slightly offset from the root-mean-square profile because the former includes con-

tributions from all three velocity components while the latter uses only streamwise information. On this plot, and on the remainder of the plots in this section using abscissa y/δ_{99}, simulation t4.134 shows sharper near-wall gradients because its Re_θ is larger than simulation t3.199. Peak magnitudes for simulation t4.134 match a $\mathrm{Ma}_e = 1.2$ and $\mathrm{Re}_\theta = 420$ simulation by Topalian et al. [166] employing temporal homogenization (2.6) and also targeting Orion MPCV cold, blowing wall conditions. The introduction of spatial homogenization terms within the model seems to have no impact on these curves.

Though compressibility is weak, Figure 6.7 shows that for these large T_{99}/T_w ratios variable density effects are strongest near the wall and they continue throughout the boundary layer. This is consistent with $\mathrm{Pr} = 0.7 < 1$ and the earlier discussion of very small or negative displacement effects. Figure 6.8 shows an inner scaling plot appropriate for compressible boundary layers [24]. In a logarithmic inner region, one anticipates $\sqrt{\frac{\bar{\rho}}{\rho_w}}\frac{\partial \bar{u}^+}{\partial y^+} = \frac{1}{\kappa y^+}$ which does not appear because of the modest Re_θ in these simulations. A von Kármán constant κ of 0.40 predicts the tangent where a logarithmic region would be expected at higher Re_θ. In accordance with these two plots, semi-local units primarily will be used in the remainder of the chapter.

Figures 6.9 and 6.10 show nondimensional mean profiles and Reynolds stresses with the latter in semi-local units. The horizontal axes in the upper and lower images in the figures align so that one can visually translate from y^* to y/δ_{99}. Based on techniques from Section 4.3, uncertainties in the mean profiles are presented in the upper right of each figure. Qualitatively the uncertainty profiles are similar between the two simulations though t3.199 shows somewhat higher near-wall and mid-layer

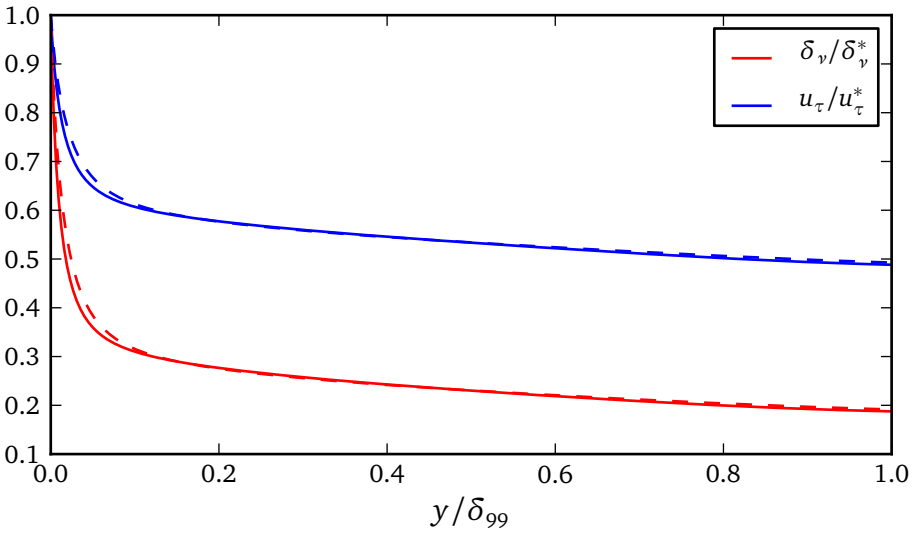

Figure 6.7: Comparison of viscous length and velocity scales using wall and semi-local units [67] in simulations t3.199 (dashed) and t4.134 (solid).

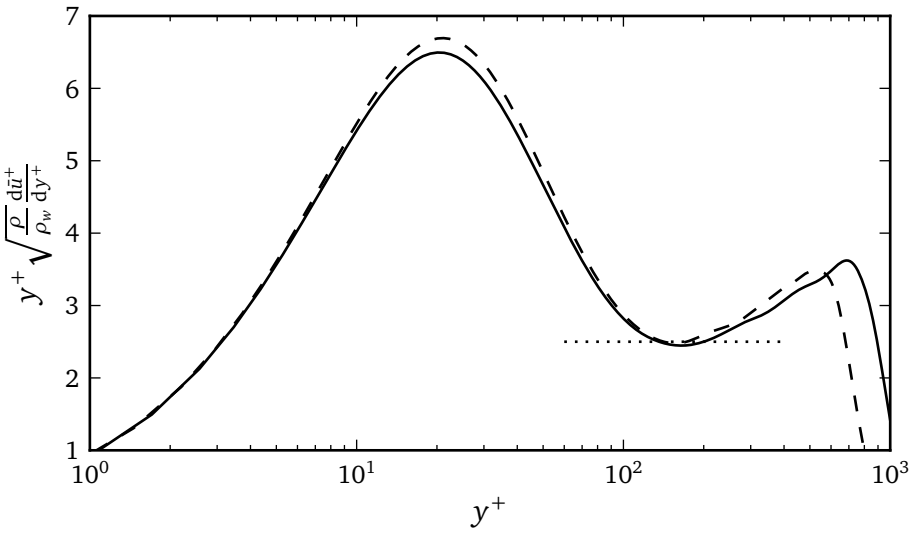

Figure 6.8: Examination of inner scaling in simulations t3.199 (dashed) and t4.134 (solid). For reference, the horizontal line shows $1/\kappa$ for $\kappa = 0.40$.

values and downward trends are more pronounced as $y/\delta_{99} \to 1$ in t4.134. The peak uncertainties are modestly higher in the higher Re_θ case. Importantly, the time step safety factor used in these simulations did not produce the near-wall jaggedness that was visible in Figure 5.6 and so the temporal resolution is not suspect. Turning to the lower half of the figure, the lower Ma_{99} t3.199 shows a slightly larger maximum $\widetilde{u''^2}$. Maximum values are higher than those found by Guarini et al. [60, Figure 6] and Coleman et al. [27, Figure 18] which is consistent with wall blowing [155]. Uncertainties in the fluctuating quantities grow as the edge of the boundary layer is approached but that is attributed to the normalization by the small mean value found there.

Similar uncertainty estimates for over 225 Reynolds averaged scalar quantities and their wall-normal derivatives were generated from *in situ* instantaneous averages taken over the streamwise and spanwise directions. They are not presented in this document but are available for calibration or modeling purposes per Appendix D.

Figure 6.11 displays root-mean-square vorticity fluctuations near the wall normalized in wall units following Guarini et al. [60]. Semi-local units also caused the curves to collapse for $y^+ \lessapprox 15$ in simulations t3.199 and t4.134 but they were less effective far from the wall (not shown). Neither scaling removed the offset between the two simulations appearing in the streamwise vorticity. The spanwise maximum at the wall matches that shown in Guarini et al. [60], reproduced in Figure 6.12. The streamwise wall value is half what they reported. Qualitatively, the shapes have fewer curvature changes for $y^+ < 20$, the near-wall local minimum in the streamwise data is more shallow, and no localized peak appears in the wall-normal fluctuations. These changes suggest the present simulations have atypical streamwise vortex structures,

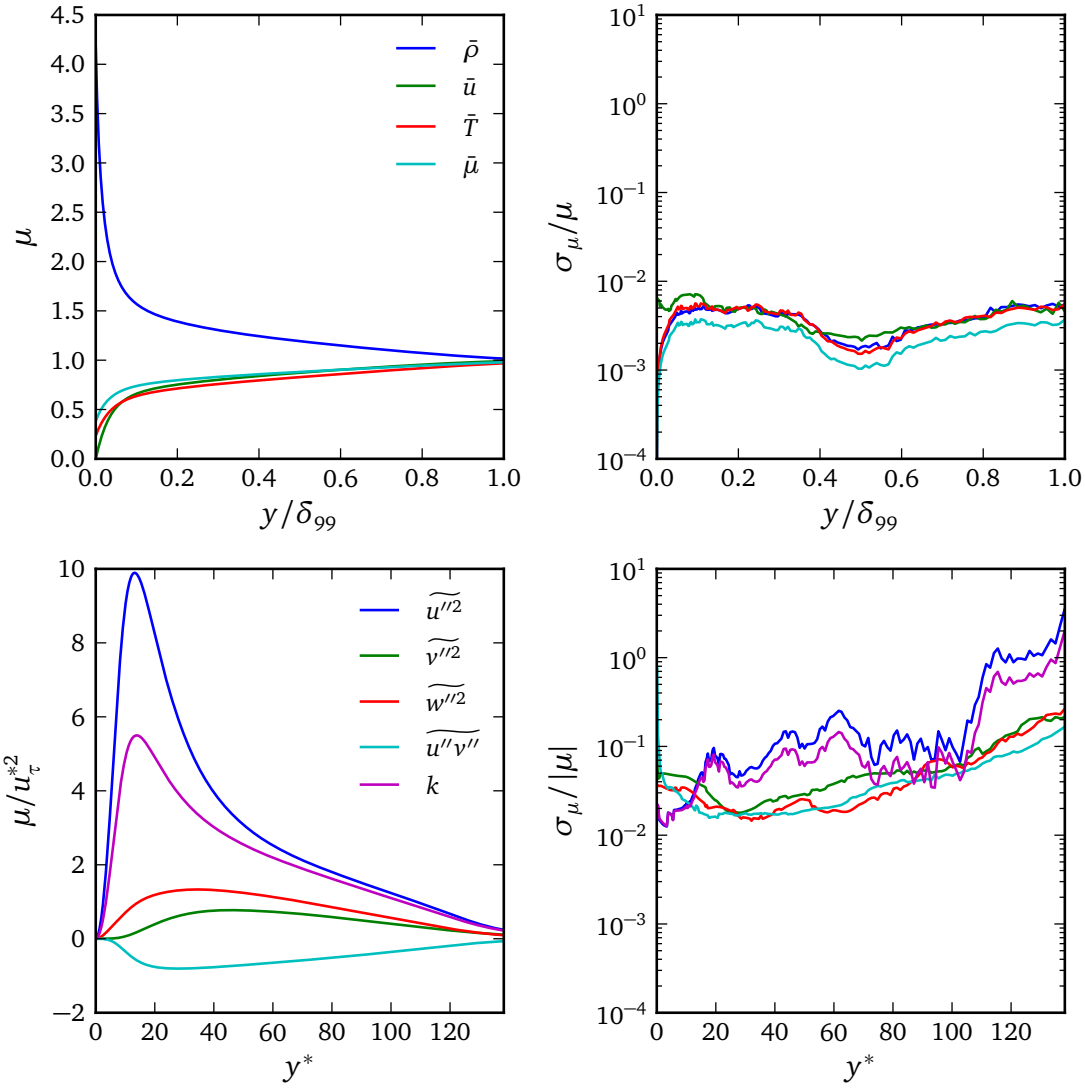

Figure 6.9: Reynolds-averaged primitive profiles (upper left) and Favre-averaged Reynolds stresses (lower left) with estimated standard errors as a fraction of mean (upper right, lower right) for simulation t3.199.

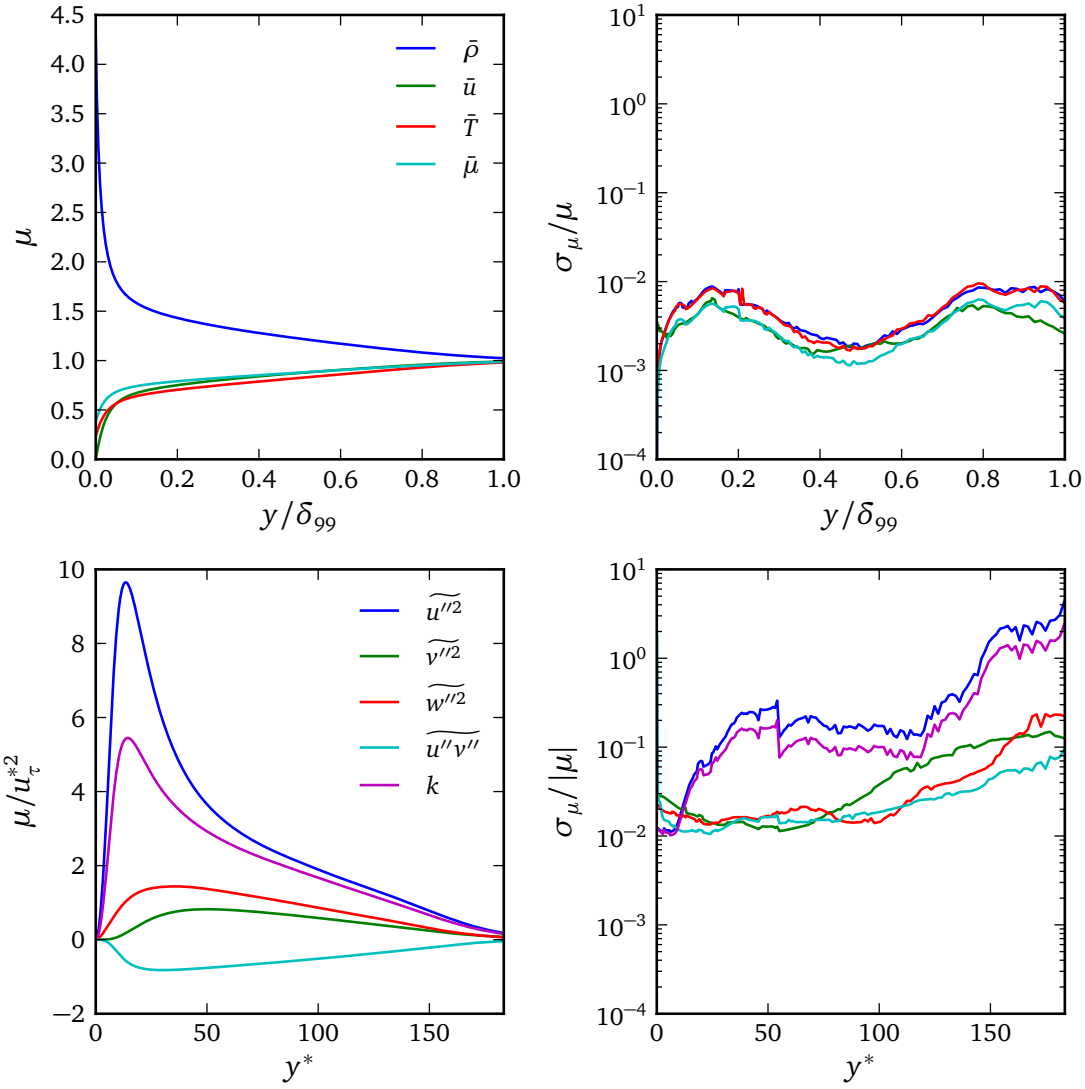

Figure 6.10: Reynolds-averaged primitive profiles (upper left) and Favre-averaged Reynolds stresses (lower left) with estimated standard errors as a fraction of mean (upper right, lower right) for simulation t4.134.

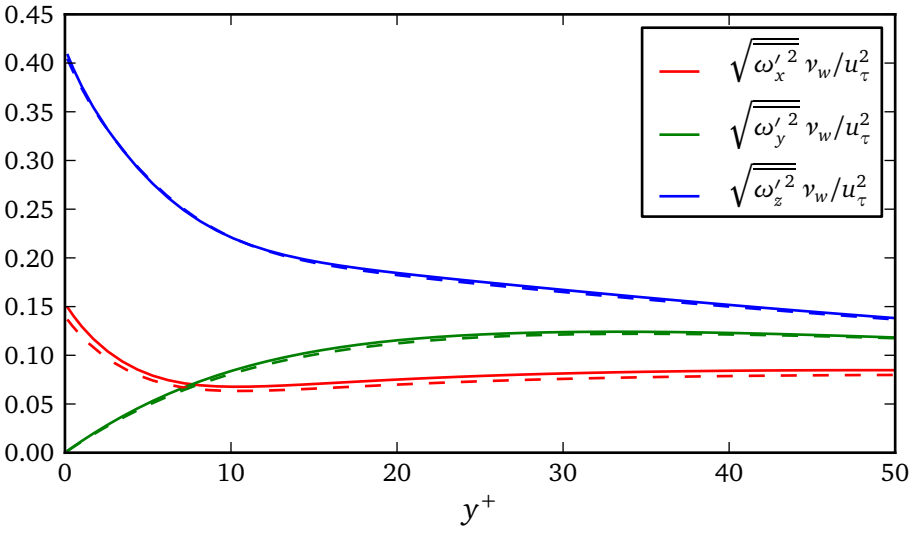

Figure 6.11: Root-mean-squared vorticity fluctuations normalized in wall units for simulations t3.199 (dashed) and t4.134 (solid).

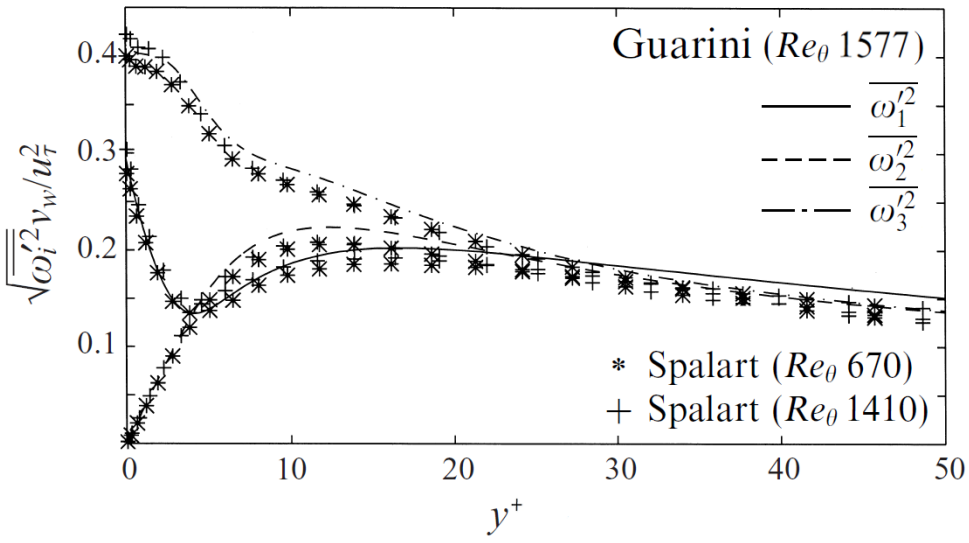

Figure 6.12: Root-mean-squared vorticity fluctuations from a Ma = 2.5, adiabatic-wall spatially homogenized boundary layer by Guarini et al. and incompressible results by Spalart [150]. Reproduced from Guarini et al. [60].

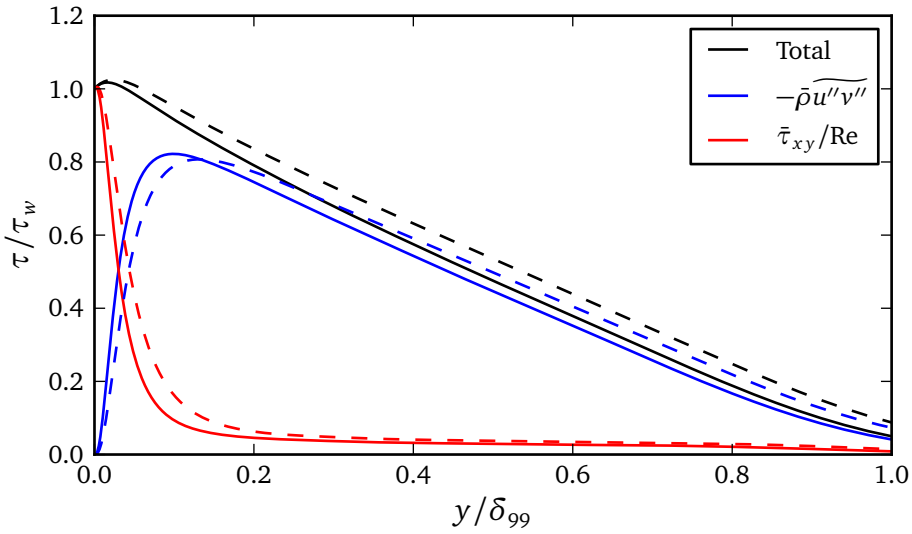

Figure 6.13: Total shear stress contributions normalized in wall units for simulations t3.199 (dashed) and t4.134 (solid).

perhaps as a consequence of wall blowing but the spatiotemporal homogenization may also play a role.

Figure 6.13 contains the total stress contributions for the streamwise momentum equation. The near-wall maxima are due to wall injection [155] with simulation t3.199 being slightly higher because of its 18% larger v_w^+. Topalian et al. [166], using temporal homogenization (2.6) in a zero-pressure-gradient simulation at $\mathrm{Ma}_e = 1.2$ and $\mathrm{Re}_\theta = 420$, observed a blowing-related total stress maximum of roughly 1.2 for a v_w^+ roughly 2.6x that used in simulation t4.134. In contrast, t4.134 has maximum 1.0175. The reduced maxima, relative to what might be expected if one scaled using only the blowing velocity, are believed to be a consequence of the pressure gradient.

Figure 6.14 reports the turbulent Prandtl number Pr_t The data shows perhaps

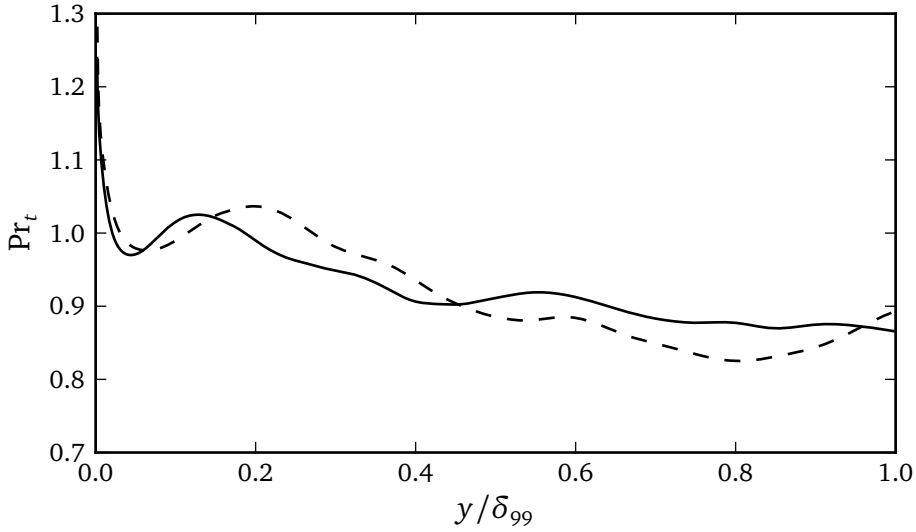

Figure 6.14: Turbulent Prandtl number $\mathrm{Pr}_t = \frac{\widetilde{u''v''}\partial_y\tilde{T}}{\widetilde{T''v''}\partial_y\tilde{u}}$ for simulations t3.199 (dashed) and t4.134 (solid).

unsettling waviness but similar fluctuations were observed by Guarini et al. [60, Figure 14]. However, away from the wall the present $\mathrm{Pr}_t > 0.8$ differs from their 0.7 result.

Figure 6.15 contrasts root-mean-squared thermodynamic property fluctuations between the two simulations. Simulation t3.199 unexpectedly has larger maxima than 4.134 for all quantities save pressure. Most striking about these fluctuation magnitudes is that, unlike t3.199, in t4.134 the pressure and density curves do not decay as fully outside the boundary layer. A fundamental difference between the inviscid base flow designs is one cause for this behavioral change. Simulation t3.199 is subsonic and therefore a favorable pressure gradient is achieved, per Appendix C, with a converging radial nozzle. Supersonic simulation t4.134 uses a diverging radial nozzle.

The mean wall-normal velocity $\bar{v}$ for these cases is shown in Figure 6.16. The

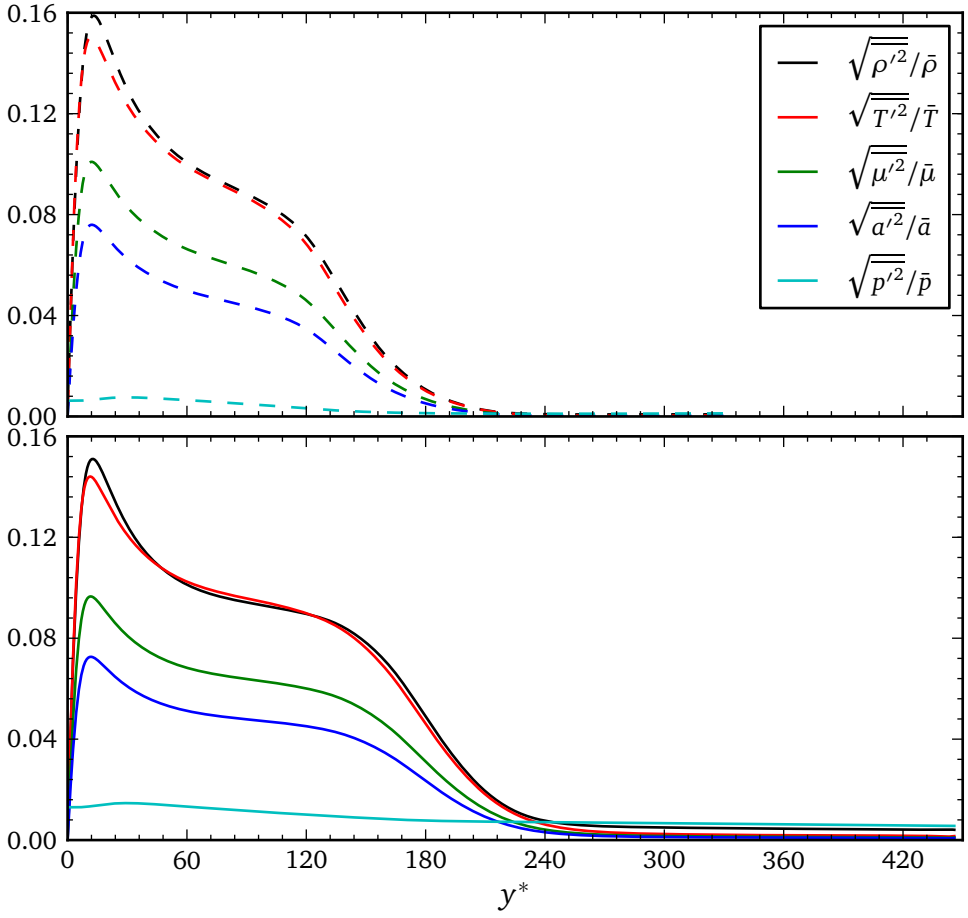

Figure 6.15: Root-mean-squared thermodynamic property fluctuations normalized by local means for simulations t3.199 (above, dashed) and t4.134 (below, solid).

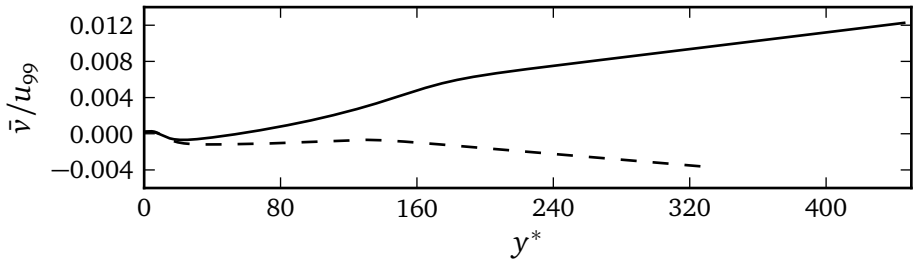

Figure 6.16: Mean wall-normal velocity normalized by the streamwise edge velocity for simulations t3.199 (dashed) and t4.134 (solid).

positive $\bar{v}$ at the wall quickly turns negative in both simulations. For t3.199 it stays negative thereafter causing $\overline{\rho v}$ to become negative by $y/\delta_{99} \approx 0.9$ (not shown). In t4.134, $\bar{v}$ changes sign before $y^* = 80$ and proceeds to increase throughout the upper portions of the domain with an appreciable curvature change at the edge of the boundary layer. At $y = L_y$ the wall-normal velocity is more than 1% of u_{99} and $\overline{\rho v}$ is everywhere positive (not shown).

A second potential cause for this lack of decay is the spatiotemporal homogenization, possibly in conjunction with the numerical isothermal wall and/or nonreflecting freestream boundary treatments. It was noticed and subsequently confirmed by Topalian that, unlike the temporal homogenization (2.6), the spatiotemporal homogenization causes small point-to-point oscillations to appear in the second derivative of pressure near both the lower and upper boundaries (not shown). This behavior can be reproduced by time-stepping a stationary one-dimensional laminar solution even in zero-pressure-gradient cases for which the inviscid base flow terms are inactive. Transferring such a solution to progressively finer grids will cause the pressure oscillations to eventually pollute other quantities and the numerical solution to diverge. Notably, only supersonic problems seem to be so affected. Setting the modeled defect growth rates (see Section 3.3) to be zero delays but does not prevent the divergence. The issue is not believed to be related to the implicit treatment as time-stepping with fully explicit operators also shows the same issue. However, at wall-normal resolutions like that used for case t4.134 the precursor pressure oscillations remain small and are not thought to spoil that simulations' results. Still, they suggest that, while suitable for calibration purposes and gross behavioral investigations like those pursued in the next chapter,

the spatiotemporal homogenization and accompanying numerics in their current form may not be appropriate for some studies of fundamental physics in supersonic flows.

6.4 Favre-Averaged Equation Budgets

The spatiotemporal homogenization by Topalian et al. [165] is sufficiently new that term-by-term contributions to the averaged governing equations, often called budgets, have not appeared in the literature. This section presents such budgets, per the Favre-averaged Navier–Stokes formulation documented in Section 3.2, to help quantify the impact of this slow growth forcing on mean flow profiles. Simulations t3.199 and t4.134 are particularly interesting for this purpose because they fully exercise the novel inviscid base flow capabilities of the homogenization. In addition to characterizing the impact of the homogenization, this data provides detailed information about the dynamics of complex boundary layers.

To begin, Figure 6.17 shows the budget for the Favre-averaged density (3.11a). Though somewhat mundane, its presentation serves three purposes. First, it exhibits several choices made throughout the remainder of this section. Subsonic simulation t3.199 appears on the upper half of the image with supersonic case t4.134 below. Both halves use identical ordinate ranges to communicate term-by-term budgets normalized by wall units. Semi-local abscissa are chosen so that the two cases collapse permitting comparisons of extrema locations between the upper and lower halves of the figure. The reader may find Figures 6.9 and 6.10 helpful if converting locations from y^* to y/δ_{99} is desired. A logarithmic scale was selected so that near-wall, edge, and freestream behaviors of the slow growth formulation can be assessed with one plot.

Second, Figure 6.17 demonstrates several qualitative differences between the sub- and supersonic behavior of the spatiotemporal formulation equipped with a favorable pressure gradient inviscid base flow. The subsonic case shows slow forcing, $\mathscr{S}_\rho$, changing sign inside the boundary layer while the supersonic forcing does not. The boundary layer edge is quite apparent in the figure and $\mathscr{S}_\rho$ changes curvature dramatically in its vicinity. Third, supporting comments in the last section that the supersonic case is somewhat ill-behaved at the freestream boundary, a kink appears only in the lower plot near $y = L_y$.

Figures 6.18 and 6.19 show budgets for the two nontrivial scalar components of the Favre-averaged momentum (3.11b). Figure 6.18 demonstrates that $\mathscr{S}_{\rho u}$ behaves similarly to $\mathscr{S}_\rho$ with regard to sub- versus supersonic conditions. At $y^* \approx 10$ simulation t4.134 shows a mildly more pronounced slow growth forcing peak and again slight boundary condition artifacts at the freestream. Slow growth makes an appreciable contribution to the streamwise momentum balance near the wall. Turning to wall-normal momentum in Figure 6.19, the homogenization is not active and the subsonic and supersonic cases are quite similar.

Figure 6.20 breaks apart the Favre-averaged total energy (3.11c). Aside from anticipated Mach number-related differences in viscous heating, the two simulations appear similar for $y^* < 40$. Above that cutoff, slow growth and convection are much more active in the supersonic case as a consequence of trends already shown in Figure 6.16.

Finally, the turbulent kinetic energy (3.11d) appears for simulation t3.199 in Figure 6.21 and for t4.134 in Figure 6.22. The upper half of each figure shows

terms that strongly impact turbulent kinetic energy ρk. The lower halves contain fine details that the upper plotting scale would not permit visualizing. The pressure dilatation and Reynolds heat flux appear almost perfectly juxtaposed against one another because (3.13) was used to eliminate the unclosed correlation $\overline{p'u''}$ from formulation (3.11d). The two terms are also summed in the lower half. As compared against a peak production of roughly 0.25 reported by Schlatter et al. [136] for a spatially evolving zero-pressure-gradient case at $\mathrm{Re}_\theta = 670$, the present peak production is unexpectedly small given that wall injection tends to energize turbulence [155]. Importantly, Figures 6.21 and 6.22 demonstrate that the Topalian et al. [165] spatiotemporal homogenization leaves the near-wall ρk budget largely unaffected. The direct slow forcing contribution $\overline{\mathscr{S}_{\rho u} \cdot u''}$ is of the same order of magnitude as the pressure terms for the present Mach numbers.

That last finding supports the expectation that a turbulence model calibrated to accurately reproduce data from simulations t3.199 and t4.134 would be suitable for use in predicting spatially evolving boundary layers with similar characteristics. Confirming this expectation by calibrating and validating turbulence models is outside the scope of the current work.

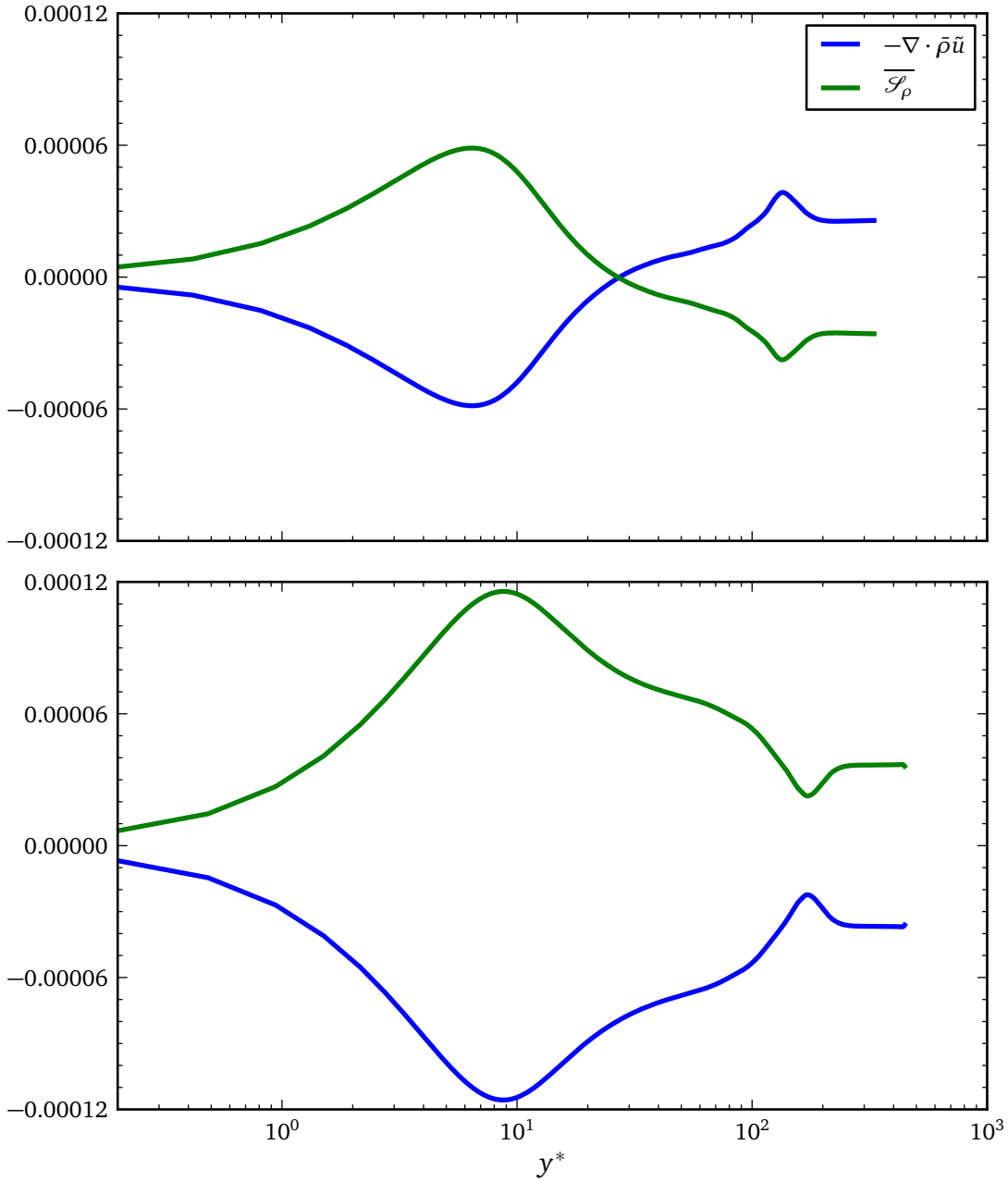

Figure 6.17: Budget for the Favre-averaged density (3.11a) in simulations t3.199 (above) and t4.134 (below) normalized by $\rho_w u_\tau^2/\nu_w$.

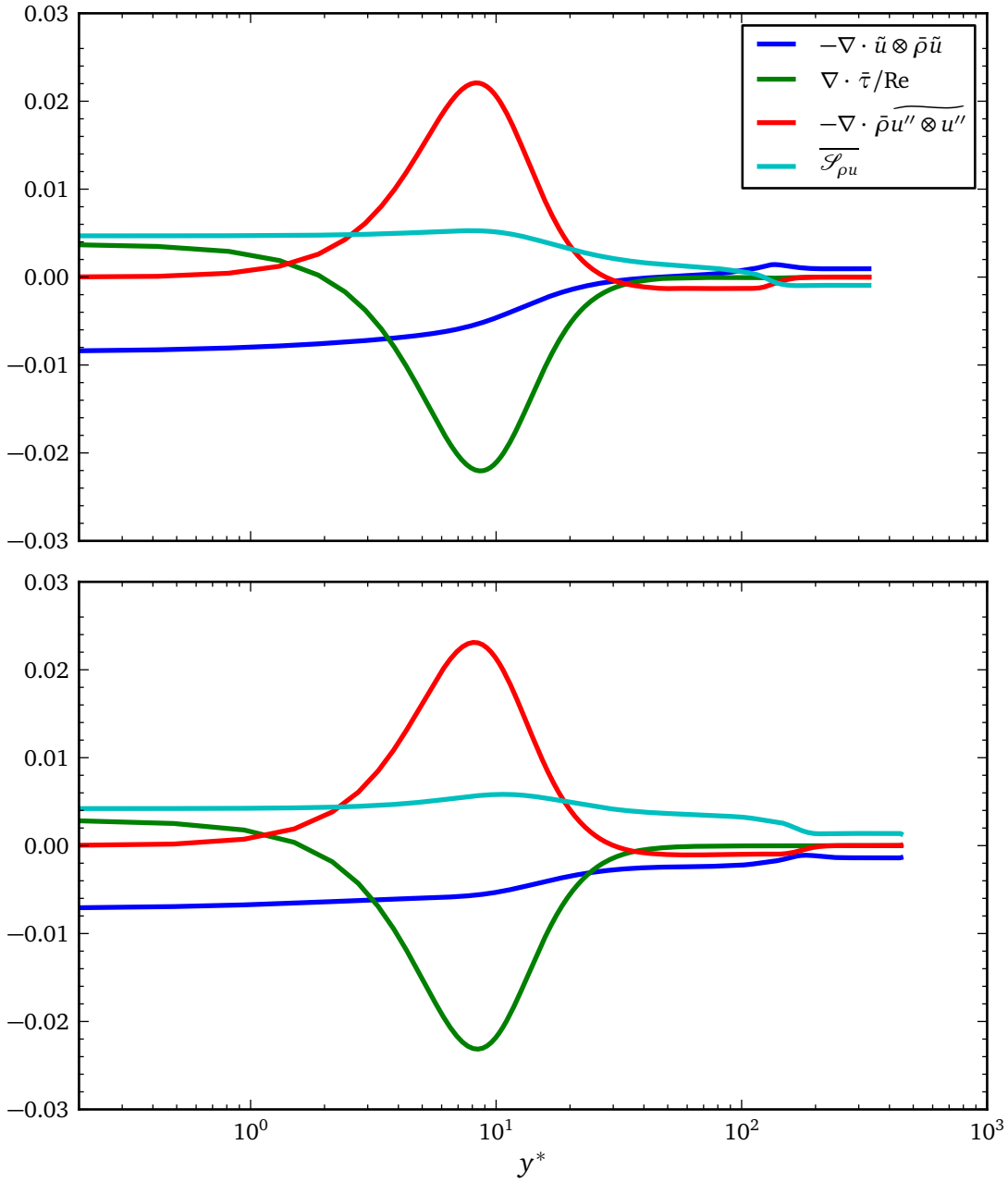

Figure 6.18: Budget for the Favre-averaged streamwise momentum (3.11b) in simulations t3.199 (above) and t4.134 (below) normalized by $\rho_w u_\tau^3/\nu_w$.

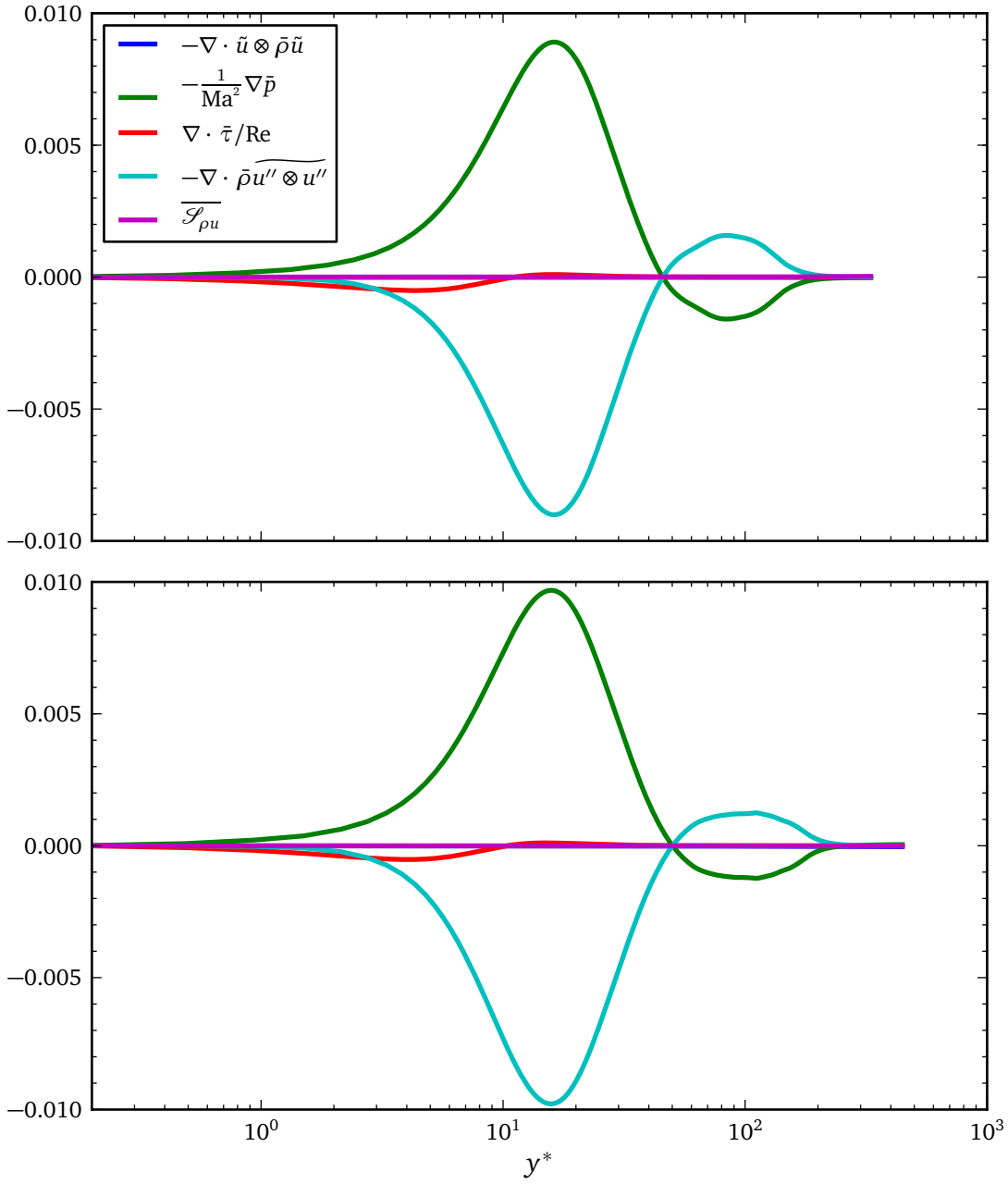

Figure 6.19: Budget for the Favre-averaged wall-normal momentum (3.11b) in simulations t3.199 (above) and t4.134 (below) normalized by $\rho_w u_\tau^3/\nu_w$.

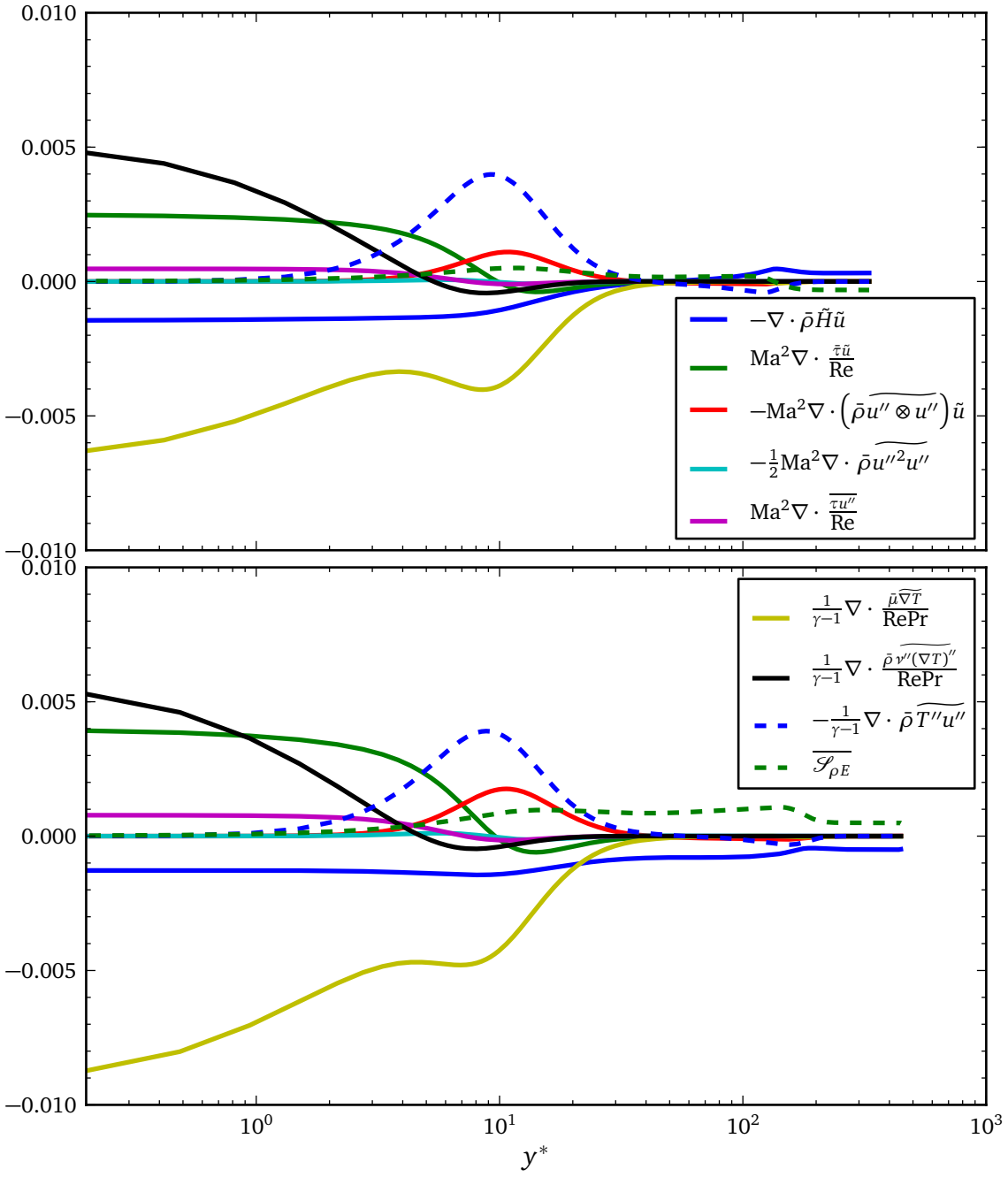

Figure 6.20: Budget for the Favre-averaged total energy (3.11c) in simulations t3.199 (above) and t4.134 (below) normalized by $\rho_w a_w^2 u_\tau^2/\nu_w$.

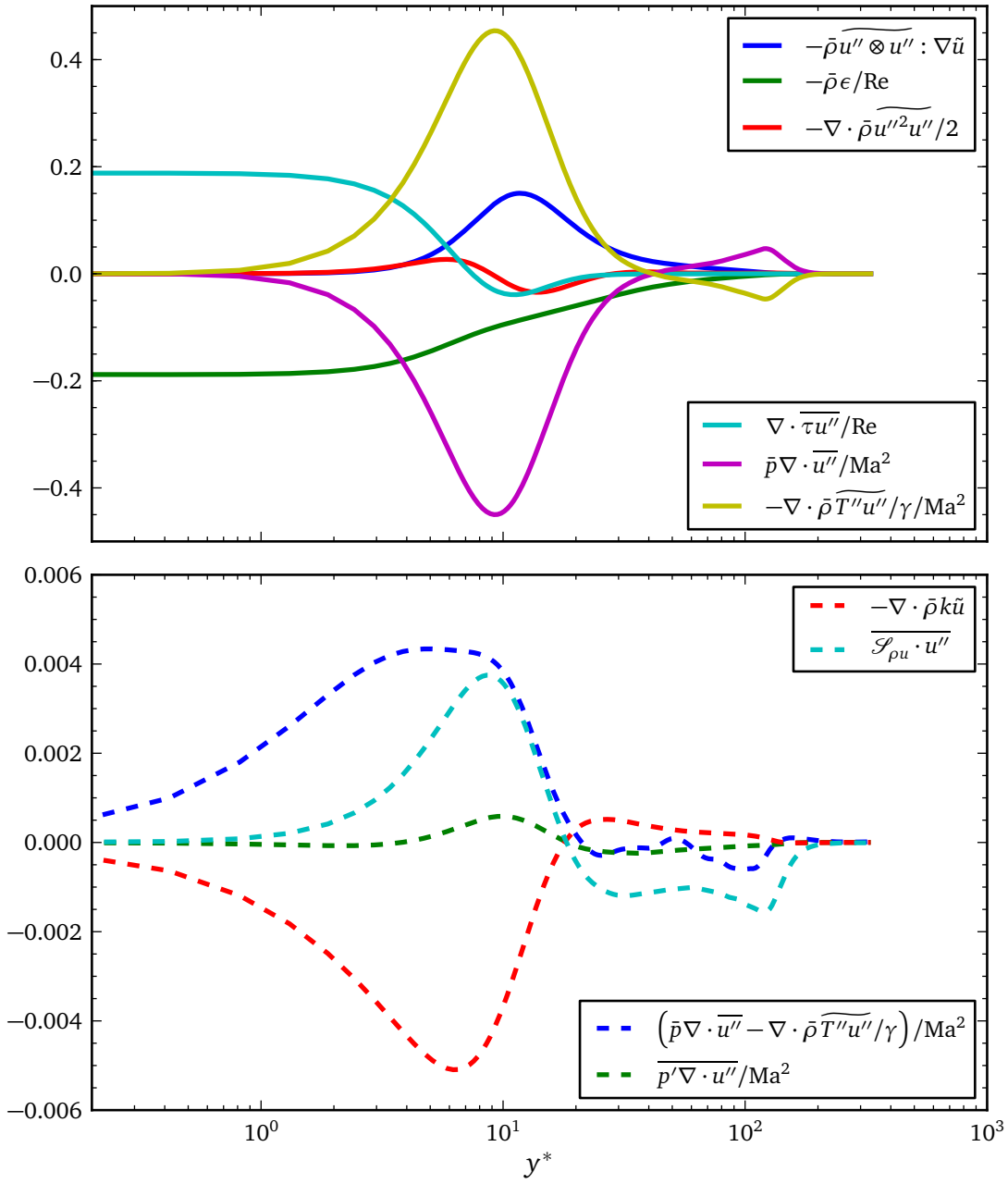

Figure 6.21: Budget for the turbulent kinetic energy (3.11d) in simulation t3.199 normalized by $\rho_w u_\tau^4/\nu_w$. More significant terms appear in the upper half of the figure while less significant contributions appear in the lower half. Two nearly symmetric thermodynamic terms above have their sum duplicated below.

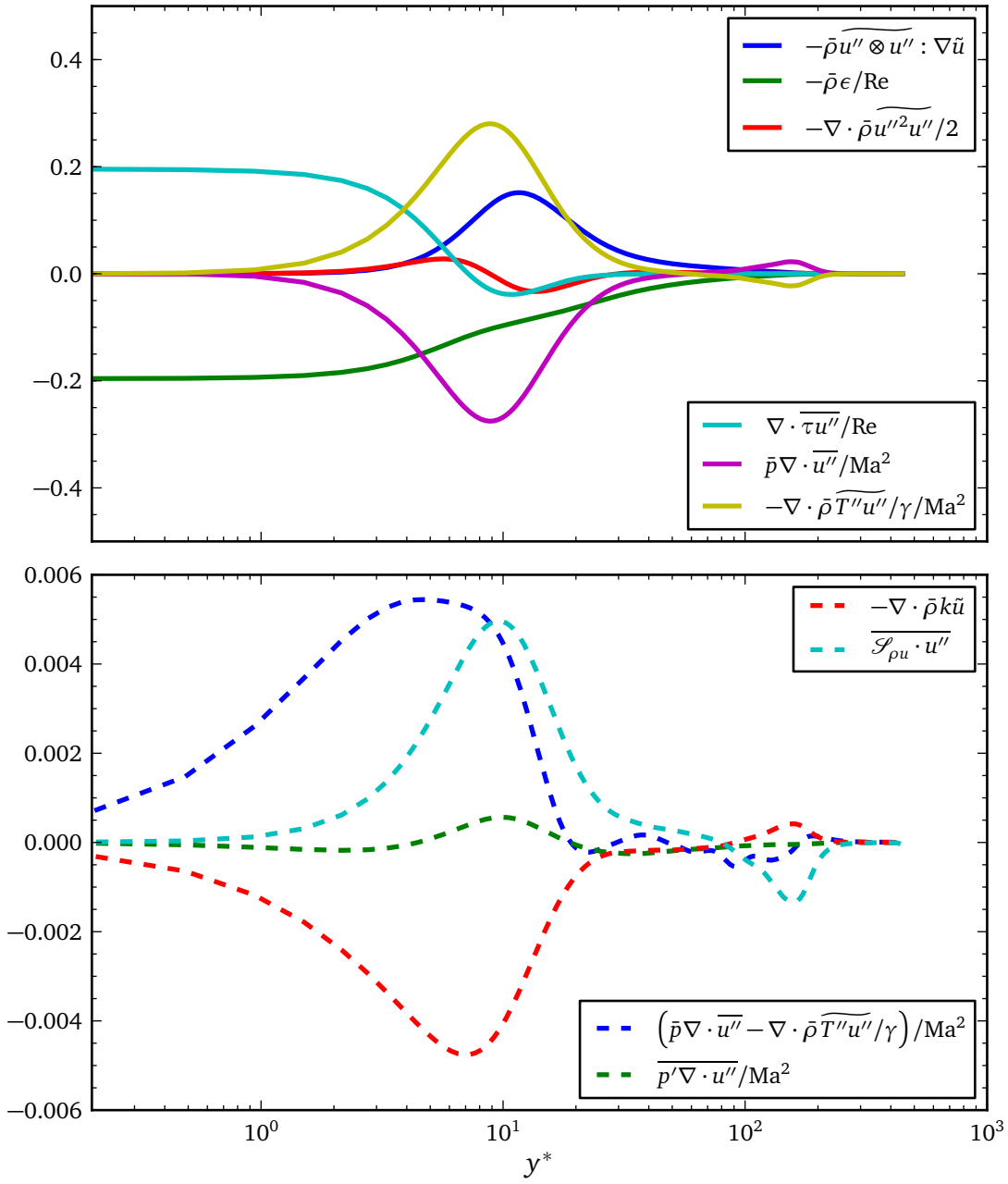

Figure 6.22: Budget for the turbulent kinetic energy (3.11d) in simulation t4.134 normalized by $\rho_w u_\tau^4/\nu_w$. More significant terms appear in the upper half of the figure while less significant contributions appear in the lower half. Two nearly symmetric thermodynamic terms above have their sum duplicated below.

Chapter 7

Detecting Turbulence-Sustaining Regions on Blunt-Bodied Reentry Vehicles

To reduce transition-driven uncertainty in aerothermodynamic heating predictions, spatiotemporally homogenized direct numerical simulation (DNS) was used to bound the turbulence-sustaining region on a blunt-bodied reentry vehicle. This chapter applies the ideas set forth in Section 2.8 to investigate which regions on the NASA Orion MPCV thermal protection system cannot sustain turbulence during the peak heating phase of return from the International Space Station. That particular reentry scenario, described in Section 2.9, was selected because of the availability of simulation data by Bauman et al. and because of the upcoming NASA Exploration Flight Test-1 [118]. Though that test will more closely resemble the Orion MPCV returning from Earth's moon rather than the International Space Station, it is nevertheless expected to produce experimental flight data against which our simulation-based predictions might later be compared. The method is described in Section 7.1. Results and discussion follow in Sections 7.2 and 7.3.

7.1 Method

The method is broken into three sequential phases. First, local conditions on the Orion MPCV heat shield surface during a fully laminar reentry are quantified to identify the search space over which the turbulence-sustaining study will proceed. Second, spatiotemporal DNS are prepared at local conditions representative of the heat shield edge with the goal of sustaining at least one statistically stationary turbulent simulation. Third, starting from a stationary simulation, the parameters are adjusted to incrementally reflect conditions found increasingly closer to the Orion MPCV stagnation point which are less likely to sustain turbulence. If at this stage the flow relaminarizes, or at least enters a demonstrably "quasi-laminar" state [152], the turbulence-sustaining region boundary has been detected. These three phases are elaborated in the remainder of this section.

In the first phase, an assumed laminar flow field over the Orion MPCV thermal protection system was obtained from a simulation by P. T. Bauman [8, 77]. The laminar solution captured the bow shock on the vehicle, accommodated the resulting high temperature aerothermochemistry, included the curved MPCV geometry as the flow passed over the thermal protection system, and incorporated a chemically reacting ablator actively maintaining a cold wall despite the incoming enthalpy flux. This solution was post-processed to extract local boundary layer quantities of interest along the thermal protection system symmetry plane, pictured in Figure 2.6, producing the results already shown in Figures 2.7 and 2.8. Those quantities are the Reynolds number based on momentum thickness Re_θ, the edge Mach number Ma_e, the favorable pressure gradient strength as measured by the parameter $p^*_{e,\xi}$ (2.14), the wall blowing

velocity normalized by the friction velocity $v_w^+ = v_w/u_\tau$, the coldness of the wall relative to the boundary layer edge T_e/T_w, the Prandtl number Pr, and the ratio of specific heats $\gamma = C_p/C_v$. Out of the many possible pressure gradient parameters that the study could target, $p^*_{e,\xi}$ was chosen motivated by the needs of the inviscid base flow design process of Appendix C in conjunction with that procedures' successful application in Chapter 6.

At each location on the thermal protection system surface the above quantities collectively characterize the subset of the peak heating boundary layer physics that can be captured by the governing equations from Section 3.1. Mapping Bauman's complex, multiphysics solution onto this comparatively simple Navier–Stokes formulation crudely approximates high temperature reacting air by a perfect gas. Further, variations in the Prandtl number and ratio of specific heats are neglected and replaced by constant air values Pr $= 0.7$ and $\gamma = 1.4$. A power law viscosity was assumed with exponent $\beta = 2/3$ based on fitting high temperature air data as shown in Figure A.1. At the end of the phase, the entire reentry scenario had been reduced to a single mapping of the distance leeward from the vehicle's stagnation point to the five nondimensional local conditions: Re_θ, Ma_e, T_e/T_w, v_w^+, and $p^*_{e,\xi}$.

In the second phase, the direct numerical simulation code Suzerain was used to prepare spatiotemporally homogenized flow fields at several "locations" from the reentry-specific mapping described above. Only one location at the heat shield edge was required to proceed to the third phase. However, as multiple independent locations easily could be made ready simultaneously, four locations roughly quadrisecting the search space were prepared.

Table 7.1: Selected reacting boundary layer conditions from the symmetry plane on a fully laminar Orion MPCV thermal protection system simulation depicted more fully in Figures 2.7 and 2.8. Column "Location" indicates the number of meters leeward of the stagnation point where the conditions are found.

Location	Re_θ	Ma_e	T_e/T_w	v_w^+	$p^*_{e,\xi}$
4.134 m	223	1.152	4.285	0.007178	−0.012 35
3.199 m	225	0.8986	4.262	0.008387	−0.010 19
2.299 m	177	0.6597	4.182	0.009765	−0.012 69
1.389 m	114	0.4112	4.129	0.01225	−0.017 93

Table 7.2: Suzerain v0.1.6.34-r45407 input parameters found to approximately match local boundary layer conditions at locations in Table 7.1. For all cases, $\mathrm{Pr} = \mu C_p/\kappa = 0.7$, $\alpha = 0$ in $\mu_B = \alpha\mu$, $\beta = 2/3$ in $\mu/\mu_0 = (T/T_0)^\beta$, and $\gamma = C_p/C_v = 1.4$. Extents were $L_x/l_0 = 10$, $L_y/l_0 = 2.5$, $L_z/l_0 = 3$ employing a piecewise-quintic B-spline basis with $N_y = 192$ collocation points. Column "Advance" reports which linear implicit operator and time step safety factor governed time advance. Refer to Tables 6.1 through 6.3 for other column definitions.

Location	Re	Ma	tanh	$\mathrm{gr}_{t_0}(\Delta)$	T_w/T_0	v_w/u_0	$p^*_{e,\xi}$	Advance	
4.134 m	1535	1.152	2.2	0.02175	0.2333	1.99e−4	−0.012 34	Y	0.35
3.199 m	1475	0.8985	2.2	0.016	0.2346	2.20e−4	−0.010 19	XYZ	0.2
2.299 m	1100	0.6598	2.0	0.01	0.2391	2.68e−4	−0.012 69	XYZ	0.2
1.389 m	800	0.4113	2.0	0.0035	0.2422	3.68e−4	−0.017 93	XYZ	0.175

Table 7.1 documents the four selected locations. Locations 3.199 m and 4.134 m correspond to $\mathrm{Re}_\theta = 223$ and 225 variants of the scenario conditions found in Chapter 6 simulations t3.199 and t4.134, respectively. Both of these locations were expected to sustain turbulence based on the Spalart [150, §3.2] finding that his constant viscosity, homogenized sink flow simulations quickly relaminarized below $\mathrm{Re}_\theta = 330$ because 3.199 m and 4.134 m have appreciably higher momentum Reynolds numbers when evaluated using wall viscosity (Figure 2.7). Having cases at subsonic and supersonic conditions was done to hedge against the possibility of either the spatiotemporal homogenization or the inviscid base flow design procedure becoming numerically problematic if the third phase of this study dictated iteratively adjusting a simulation across $\mathrm{Ma}_e = 1$.[1] Either location 2.299 m or 1.389 m was hypothesized to relaminarize.

At each of those four locations the MPCV-derived data in Table 7.1 furnished fixed values for only the Suzerain code input parameters $\mathrm{Ma} \approx u_{99}/a_{99}$, T_w/T_0, and $p^*_{e,\xi}$. As doing so had proved successful for Chapter 6, boundary layer thickness $\delta_{99}/l_0 = 1$ was chosen as a target to be achieved indirectly by adjusting the slow growth rate $\mathrm{gr}_{t_0}(\Delta)$. When that condition is met, the nondimensional formulation in conjunction with the inviscid base flow design procedure *a priori* causes ρ_{99}/ρ_0, u_{99}/u_0, and T_{99}/T_0 to all be nearly one. Appropriate values for the remaining code inputs $\mathrm{Re} \approx \rho_{99} u_{99} \delta_{99}/\mu_{99}$, $\mathrm{gr}_{t_0}(\Delta)$, and v_w/v_0 had to be discovered. An elegant way to discover suitable settings would be to invert for the appropriate values using a spatiotem-

[1] Concern about the spatiotemporal homogenization in supersonic circumstances arose based on observations reported at the end of Section 6.3. Concerns about the base flow procedure stemmed from the design procedure of Appendix C.6 driving the nozzle radius R to large values as Ma_e approaches one from either direction.

porally equipped turbulence model implementation properly calibrated for the current context. A less elegant way would be to iteratively seek values with such a tool in lieu of the more complicated inversion procedure. The inelegant way used in this study was to perform exploratory simulations to manually acquire the needed values by iteratively adjusting code input parameters until the desired stationary behavior was obtained. Table 7.2 reports those parameters. To conserve compute resources, these computations used coarse streamwise and spanwise resolution (for example, $\Delta x^+ \approx 30$) but production wall-normal bases with y_1^+ and y_{10}^+ comparable or better than those in Table 6.1. Final tests to ensure the parameters appearing in Table 7.2 were robust on near-production grids (for example, $\Delta x^+ \leq 25$ and $\Delta z^+ \leq 15$) yielded unexpected results which will be conveyed in Section 7.2.1.

For the third phase, the code input parameters shown in Table 7.2 were used to adjust a fully turbulent field so it matched the target conditions derived from MPCV data. A known-good turbulence field was required to ensure that the relaminarization study was seeded with a reasonable approximation of boundary layer physics. Moreover, turbulent conditions are a "large perturbation" with respect to a relaminarized flow per the energy method ideas discussed in Section 2.7. That adjustment process is simpler if the initial field already resembles the target flow conditions. Simulations t3.199 and t4.134 from Chapter 6 were designed to serve exactly that purpose. They differed from Table 7.1 locations 3.199 m and 4.134 m only in their Re_θ magnitudes. Results starting from these initial conditions will appear in Section 7.2.2.

Though the collapse of turbulent fluctuations and relaminarization can be a quick process in spatially evolving boundary layers subjected to pressure gradi-

ents [105] and spatially homogenized boundary layers [150, §3.2], it was uncertain if that would also be true for the Topalian et al. [165] spatiotemporal homogenization or if this slow growth formulation would bring about an extended "quasi-laminar" state [107, 152] that would prove difficult to identify. An extended relaminarization process would retard our ability to incrementally move to locations nearer the stagnation point because it would force us to simulate each station for a longer duration to ensure we did not accidentally pass over the critical location. For this reason, an *in situ* capability to assess the strength of the turbulence by monitoring the temporal trace of relevant quantities was added to Suzerain. Following findings by Cal and Castillo [22], the code was augmented to frequently output maxima values and locations for absolute values of Reynolds-averaged and Favre-averaged stress tensor components. Output of the wall-normal location and value of the peak streamwise- and spanwise-averaged production term as well as its integrated magnitude was also added. These monitors permitted early identification of relaminarization precursors.

An insufficiently large computational domain and inadequate spatial resolution tend to cause turbulent fluctuations to persist. The former introduces artificially long correlation lengths and the latter does not permit turbulent kinetic energy to be dissipated properly. Either effect would likely cause the study to incorrectly detect the turbulence-sustaining region. Plans were laid to repeat the final stages of the detection process with a larger domain and improved resolution.

7.2 Results

Two distinct sets of results are presented. The first set of results, found in Section 7.2.1, conveys the unexpected behavior observed when coarse, fluctuation-sustaining exploratory simulations were refined to production resolutions. The second set of results, appearing in Section 7.2.2, investigates relaminarization using fully turbulent fields from Chapter 6 so that the initial conditions represent boundary layers like those found on the Orion MPCV.

7.2.1 Results from Refining Coarse Exploratory Simulations

All four coarse simulations performed to discover inputs for Table 7.2 relaminarized when refined to $\Delta x^+ \leq 25$ and $\Delta z^+ \leq 15$. The relaminarization events were not cleanly captured— initially they were thought to be merely undesirable drift relative to target conditions which prompted us to adjust code inputs partway through each event. After appreciating what had occurred, the process was repeated but, unlike before, without any adjustments to code inputs once the simulations were underway.

Figure 7.1 on page 174 shows the temporal evolution of the supersonic coarse location 4.134 m simulation immediately after refinement. The earliest time shown is when the field was refined to $\Delta x^+ \approx 18.7$ and $\Delta z^+ \approx 11.2$ ($N_x = 256$ and $N_z = 128$) while holding the wall-normal basis constant. As the projection onto a larger Fourier basis is an exact operation, the refinement does not perturb the flow but it does permit the solution to populate higher wavenumbers and thereby gain additional dissipative capability. The upper six subplots in Figure 7.1 show the desired location-specific conditions as a horizontal dashed line and the actual simulation evolution in blue

curves. The mean flow in the freestream approximately traverses the streamwise extent of the domain once every 10 time units because because $u_{99}/u_0 \approx 1$ and $L_x/l_0 = 10$. For example, Re_θ starts out slightly too high, grows slowly until just before nondimensional time index 120, and then gradually drops. Proceeding down the subplots, the edge Mach number is seen to be very close to target while the temperature ratio is low. Wall blowing v_w^+, the pressure gradient parameter $p^*_{e,\xi}$, and the boundary layer thickness all match the desired values.

The lower three subplots in Figure 7.1 show turbulence diagnostics. The uppermost of the three is the instantaneous mean turbulent production $-\bar{\rho}\widetilde{u'' \otimes u''} : \nabla\tilde{u}$ averaged across all spatial directions. It is nondimensionalized by edge state similarly to Re and Ma defined earlier. Production begins to drop around time 100. The next subplot down is the pointwise maximum absolute values of each component of the Favre-averaged stress tensor. To permit visualizing both early- and late-time behavior, the logarithm of the absolute values are plotted. The data is clipped below 10^{-8} which only obscures low magnitude information at late times ($t > 240$). After $t > 120$ the fluctuation magnitudes slowly drop because of the extra dissipation available due to the increased spatial resolution. As Cal and Castillo [22] reported, the vv and uv curves decay sharply after the integrated production tails off at $t = 180$. The final curve is the skin friction factor which decays to a nearly constant value by $t > 300$. Basing δ_{99} and u_τ determinations on the initial boundary layer character, it took roughly 4.2 eddy turnovers[2] from the start of the study until relaminarization precursors appear and another 1.8 turnovers to reach $t = 180$ where the flow clearly is relaminarizing.

[2]Computed from $(t_f - t_i)u_\tau/\delta_{99}$.

Figure 7.2 shows the temporal evolution of the coarse location 3.199 m simulation immediately after refinement to $\Delta x^+ \approx 18.0$ and $\Delta z^+ \approx 10.8$ ($N_x = 256$ and $N_z = 128$). The Re_θ dips below target, the T_e/T_w is again low, but the other indirectly controlled parameters in the upper six subplots oscillate about the desired values. Turning to the lower turbulence diagnostics, the integrated production is quite variable and shows intermittent periods of decreased production. The maximum density-weighted stress tensor components show several relaminarization precursor signatures with the most pronounced at $t = 400$, $t = 800$, and $t = 1100$. These are also seen in the integrated production and skin friction traces. At each of those times, however, the fluctuations again kick up and the flow briefly appears turbulent from these plots. The dwell time between them is 10.2 and 8.7 eddy turnovers which is longer than the O(6.5) turnover statistical ensembles gathered in Chapter 6. These three diagnostic subplots show evidence of a characteristic frequency which may be related to the time scale of the structural interactions responsible for reinvigorating the fluctuations after each window of decay. From initialization until relaminarization, 36.3 eddy turnovers passed.

Figure 7.3 shows the evolution of the coarse location 2.299 m simulation after refinement to $\Delta x^+ \approx 14.1$ and $\Delta z^+ \approx 8.5$ ($N_x = 256$ and $N_z = 128$). The flow does not relaminarize over the 23.2 turnovers shown though short lulls appear in the production during which the stress tensor component magnitudes smooth out due to dissipation and the skin friction decreases. Glancing at the top portion of the figure, however, reveals that wall blowing is too weak and the favorable pressure gradient too strong on account of the growth rate parameter not achieving $\delta_{99} \approx 1$.

Figure 7.4 rectifies the target condition mismatch by proceeding with the new input parameters documented in the figure caption. Those new parameters took three attempts to discover. The T_e/T_w target is still too low and the wall blowing just slightly too high, but overall the disagreement with all target conditions, in particular the pressure gradient, was remedied. The production, stress tensor components, and skin friction continue to show intermittency but location 2.299 m sustained turbulence for another 23.4 turnovers. It was unclear whether or not the intermittency would continue indefinitely or if, eventually, 2.299 m would abruptly collapse as did 3.199 m in Figure 7.2.

Either way, the behavior at 2.199 m appears stationary enough to merit characterizing the flow. Based on an ensemble over the data appearing in Figure 7.4, one-dimensional Fourier spectra were computed and are presented in Figure 7.6. Comparing against Figure 6.1, the spectra appear reasonable demonstrating that the resolution is adequate. Turning to the two-point correlations, shown in Figure 7.5, the appearance of appreciable autocorrelation at length scales on the order of the approximately $10\delta_{99} \times 2.5\delta_{99} \times 3\delta_{99}$ domain extent indicates the finite domain size chosen strongly influences this simulation. Long correlations of this sort are not characteristic of fully developed turbulence, see Figure 6.3, suggesting the flow structures are transitional or marginally turbulent in nature. Due to these considerable numerical artifacts, the refinement-generated flow targeting 2.299 m conditions that is shown in Figures 7.3 and 7.4 does not merit further study as an approximation of a turbulent boundary layer. However, this boundary-layer-like flow is interesting as an example of a self-sustaining, pathologically large perturbation per ideas discussed in Section 2.7.

Continuing onward with Figure 7.7, location 1.389 m evolution is pictured after refinement to $\Delta x^+ \approx 11.7$ and $\Delta z^+ \approx 7.0$ ($N_x = 256$ and $N_z = 128$). The simulation relaminarizes in under 3.6 turnovers. The lack of a longer "turbulent dwell" before relaminarization is thought due to the 1.389 m conditions being unable to sustain turbulence, rather than an artifact of the initial field because the long dwell times at 3.199 m and 2.299 m were initialized in a similar manner.

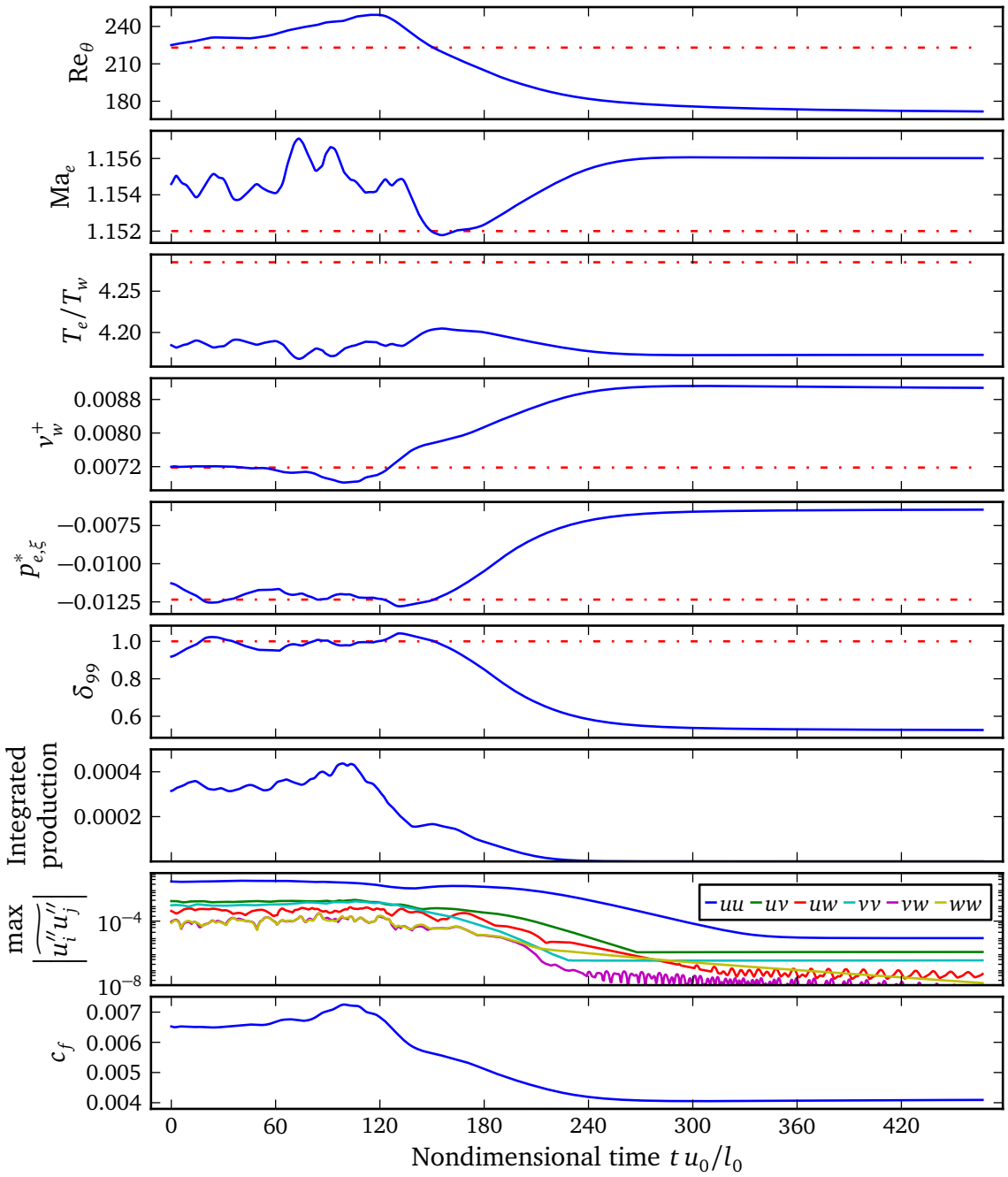

Figure 7.1: Refinement of exploratory simulation at location 4.134 m. Dashes mark target conditions.

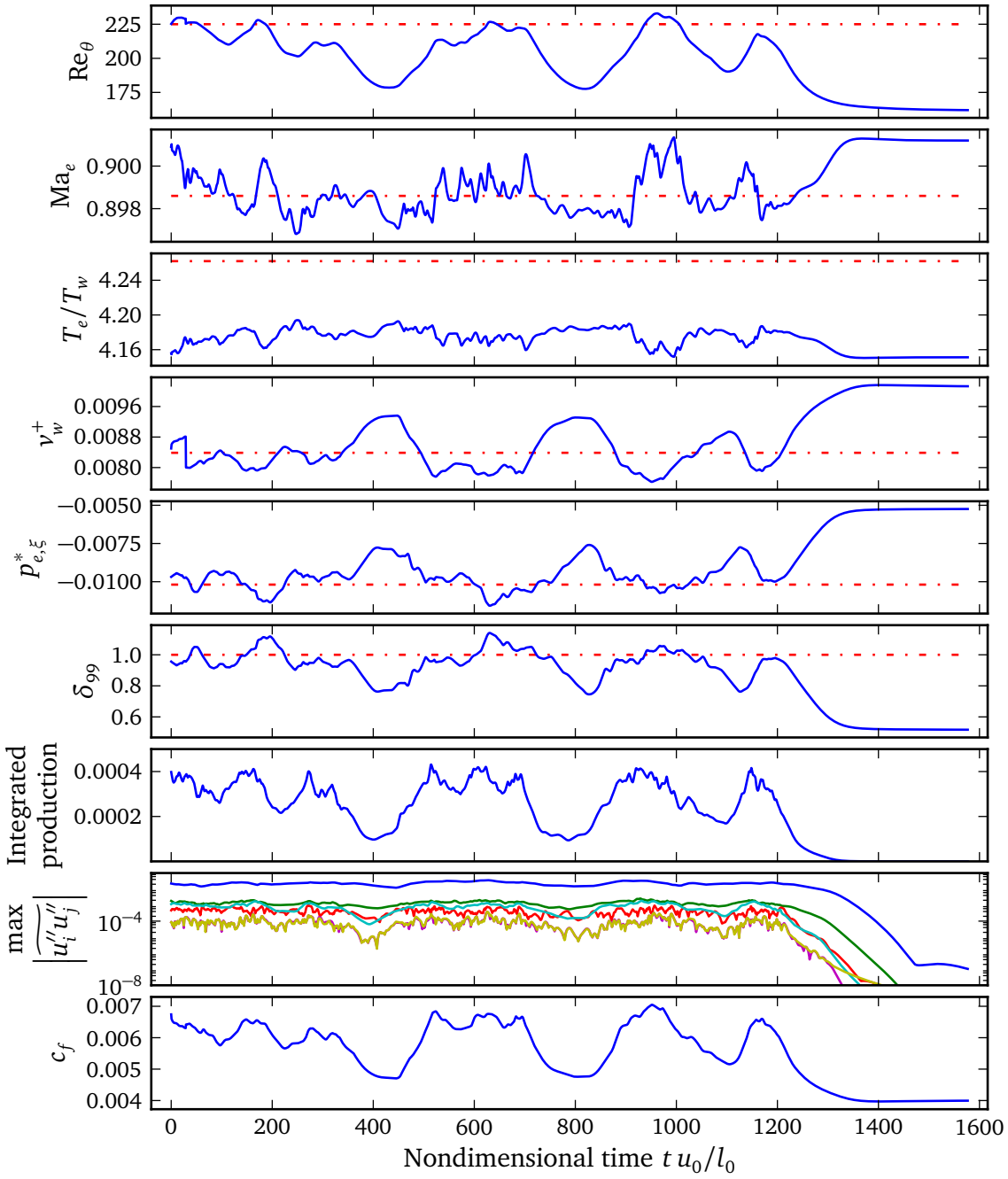

Figure 7.2: Refinement of exploratory simulation for location 3.199 m.

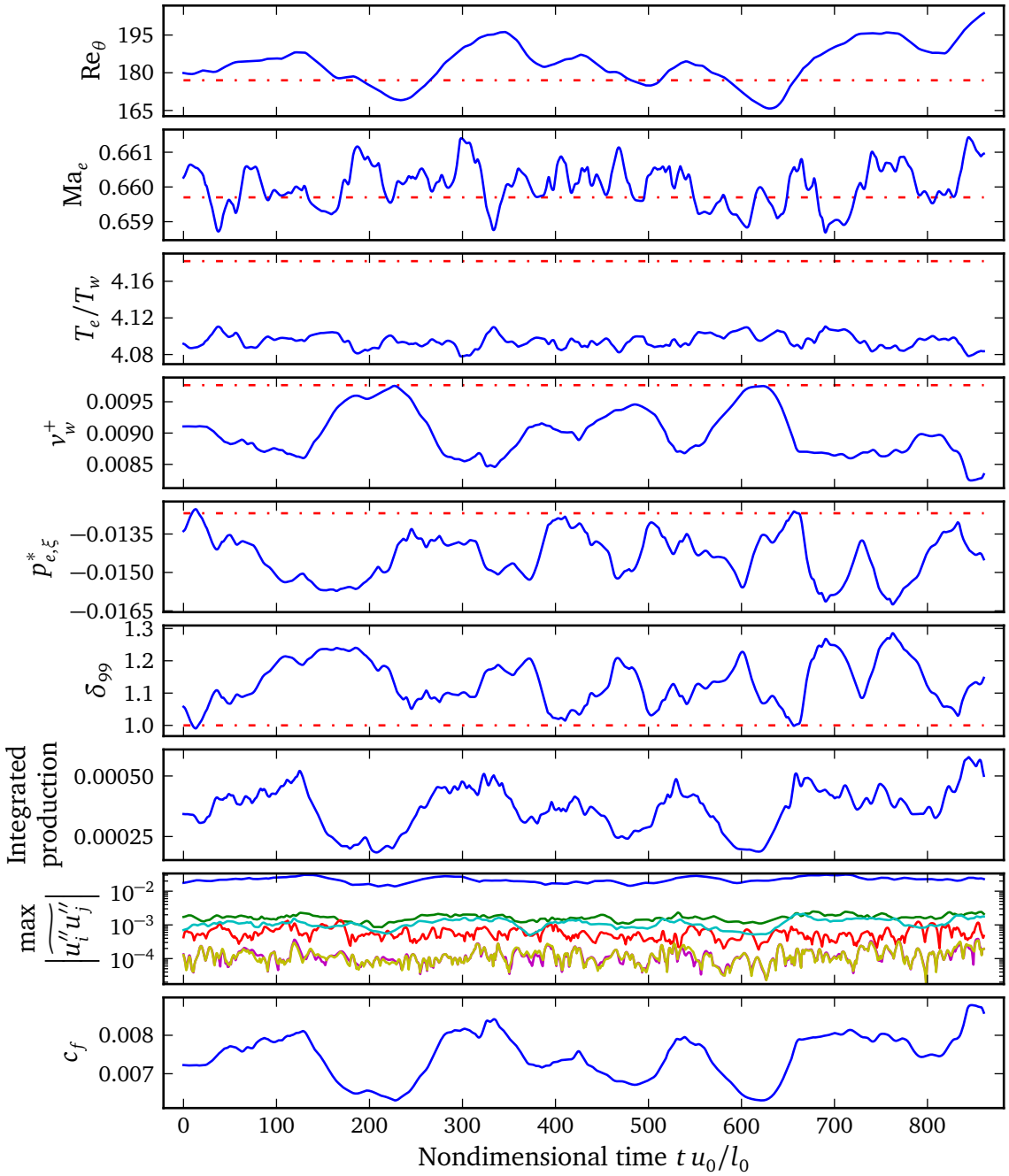

Figure 7.3: Refinement of exploratory simulation for location 2.299 m.

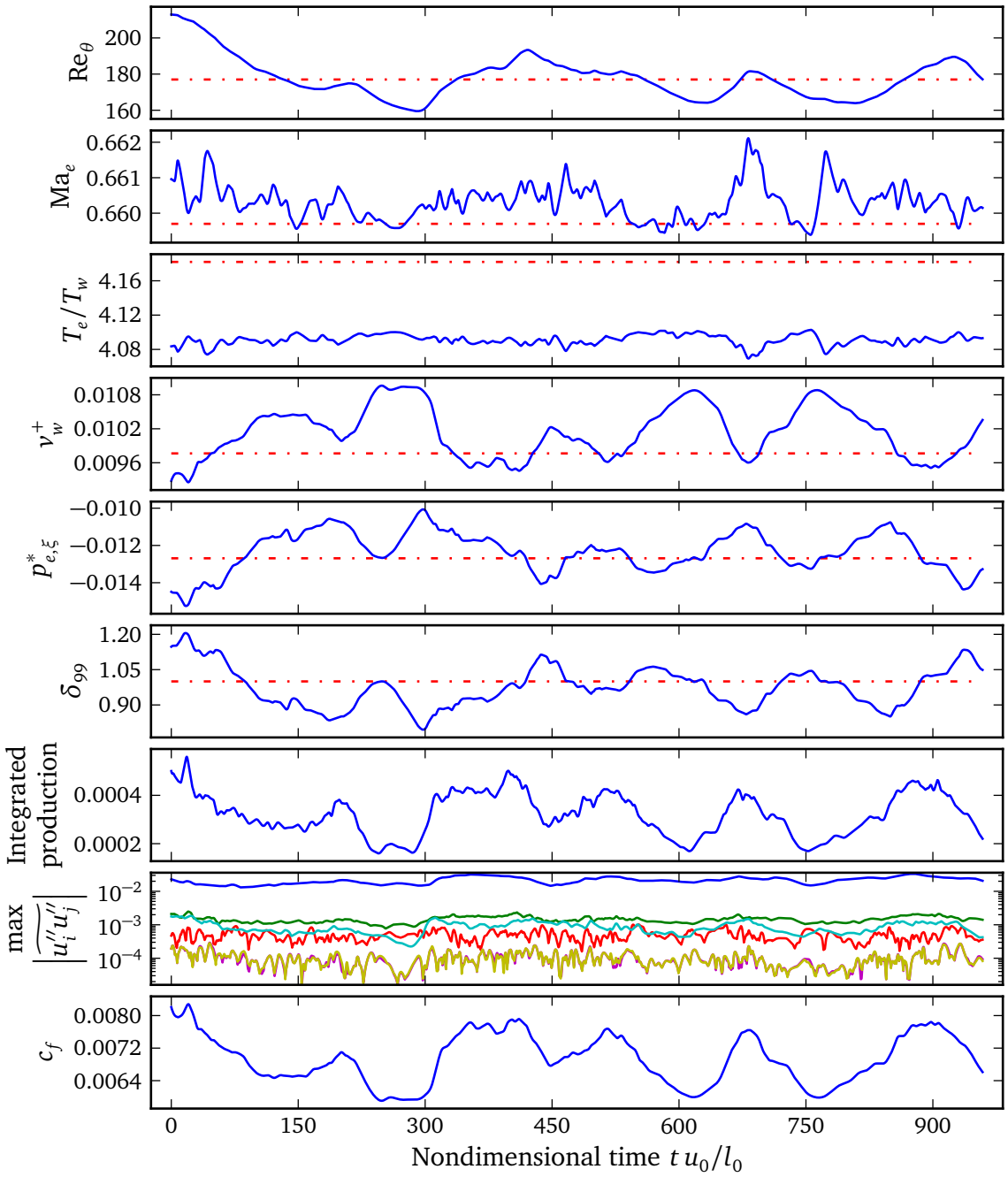

Figure 7.4: Continuation of refinement study for location 2.299 m. Input parameters adjusted to Re = 1150, $\mathrm{gr}_{t_0}(\Delta) = 0.01125$, and $\nu_w/\nu_0 = 2.915\mathrm{e}{-4}$ to better achieve target conditions.

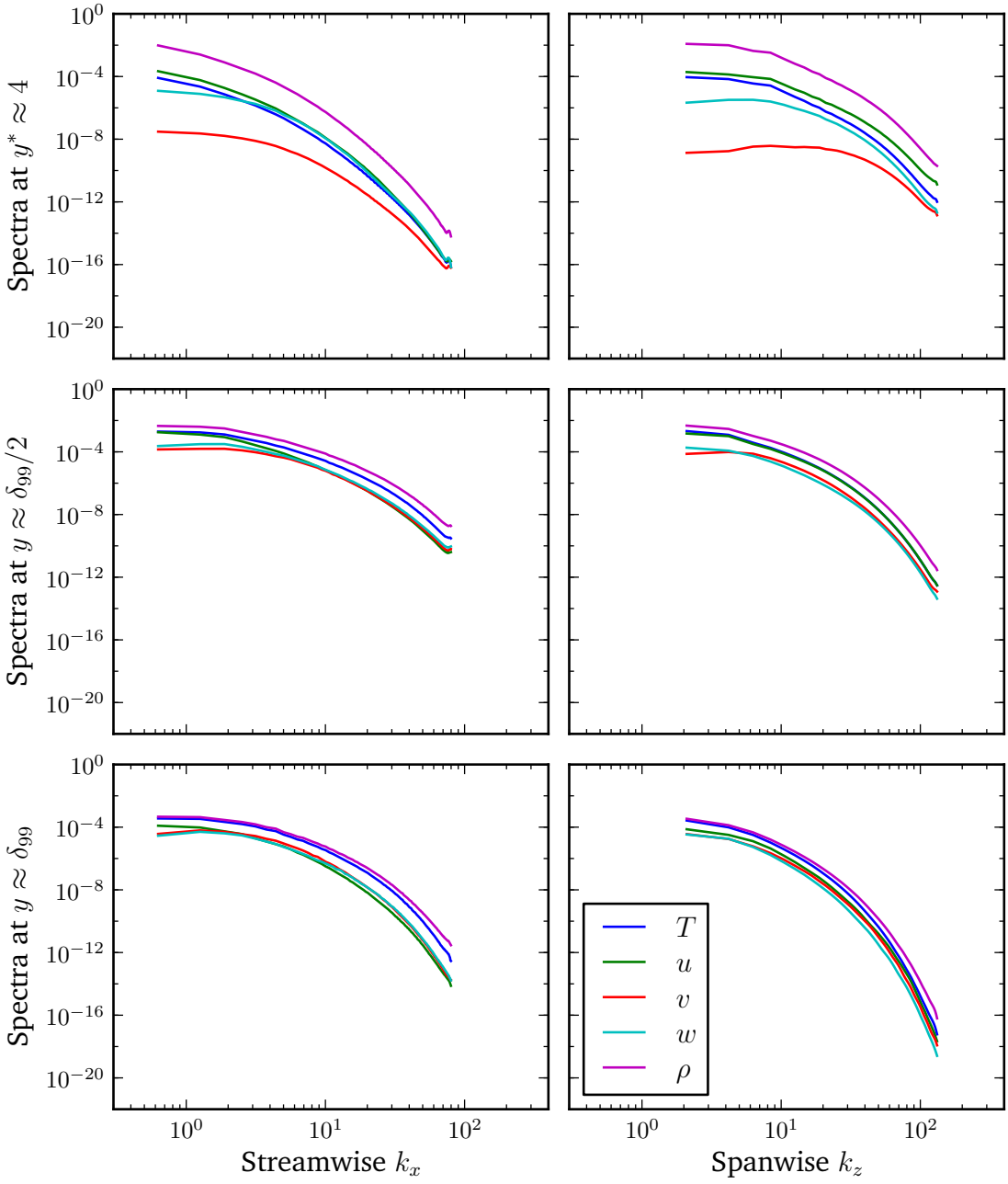

Figure 7.5: One-dimensional, unnormalized Fourier energy spectra from an ensemble over the location 2.299 m data appearing in Figure 7.4.

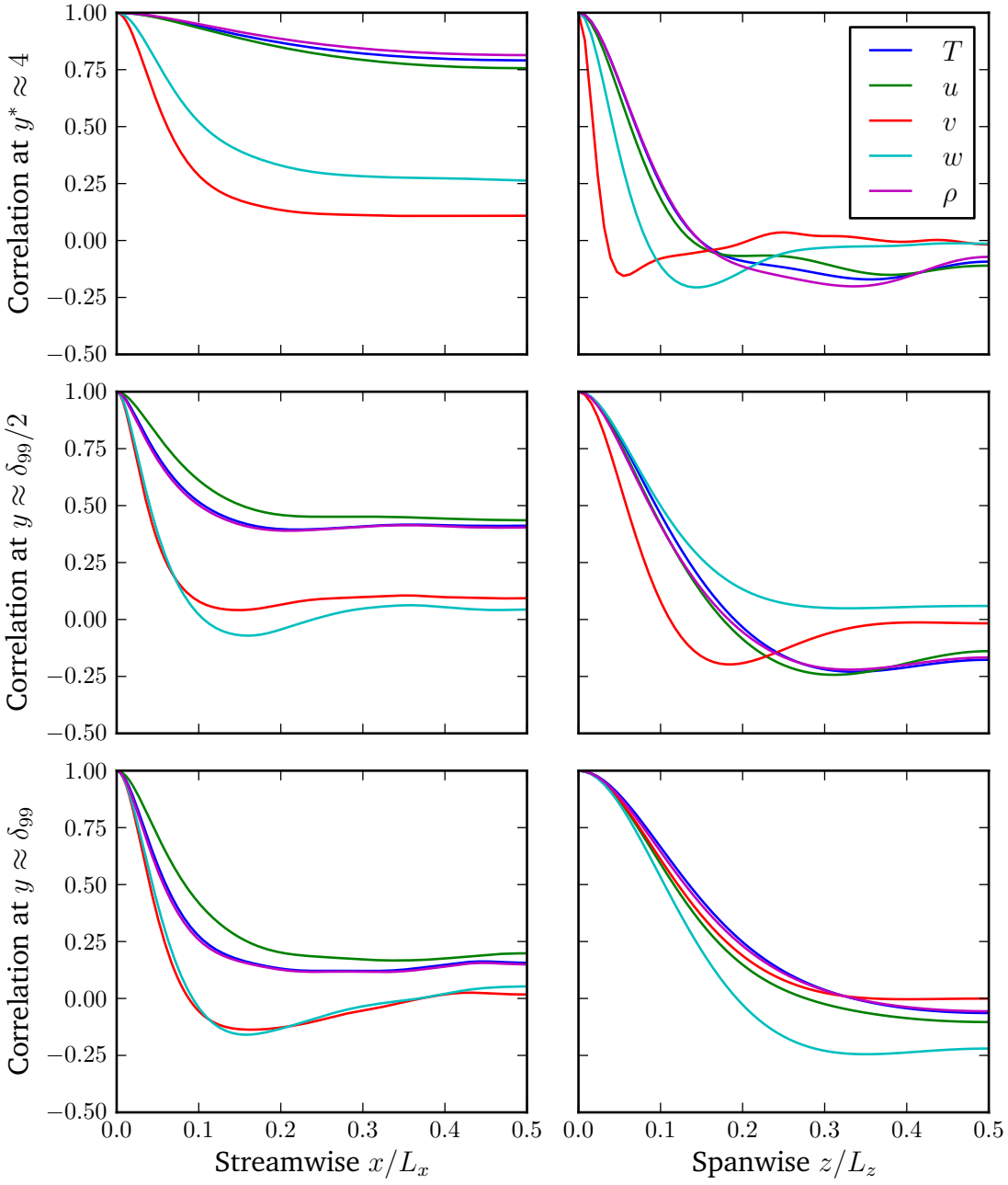

Figure 7.6: Two-point correlations from an ensemble over the location 2.299 m data appearing in Figure 7.4.

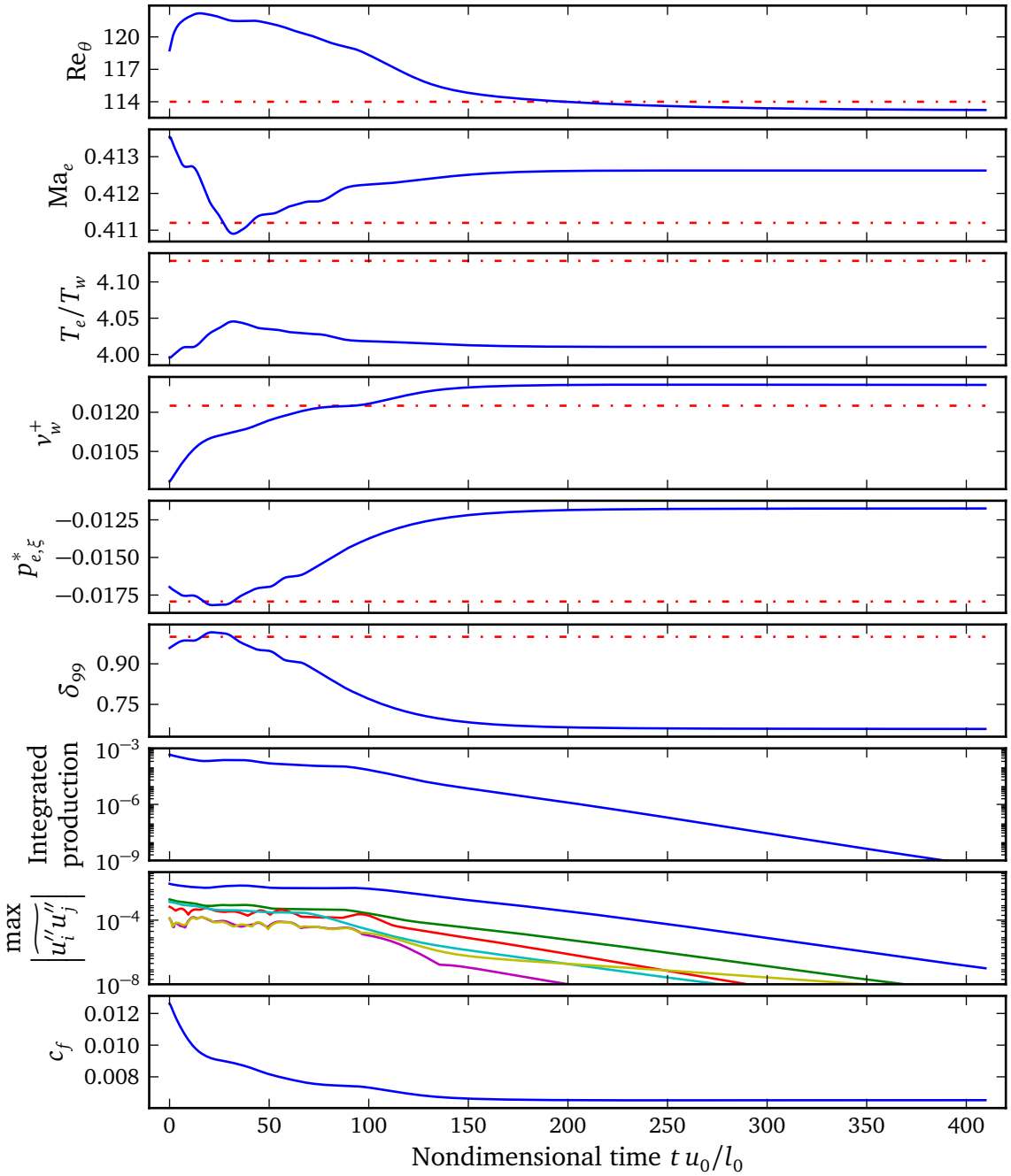

Figure 7.7: Refinement of exploratory simulation for location 1.389 m.

7.2.2 Results from Fully Turbulent Initial Conditions

Not one of the post-refinement cases from the prior section used an initial field known to demonstrate salient turbulent boundary layer features. They are, nonetheless, informative. In particular, Figures 7.1 and 7.2 suggest that conditions 4.134 m and 3.199 m both will relaminarize starting from a proper initial field.

Figures 7.8 and 7.9 on pages 183 and 184 investigate those two locations using stationary turbulent fields from simulations t4.134 and t3.199, documented in Chapter 6, as initial conditions. Local conditions from Table 7.2 were achieved by setting the necessary code inputs for initial fully turbulent fields with resolution $512 \times 256 \times 256$. Because the initial grids, designed for $\mathrm{Re}_\theta = 380$ and 531 flows, are excessive for $\mathrm{Re}_\theta \approx 225$ they were coarsened as the simulations proceeded. The 4.134 m case resolution was gradually brought down past $384 \times 256 \times 192$, past $384 \times 192 \times 192$, and finally to $256 \times 192 \times 128$ at $t \approx 34$ where $\Delta x^+ \approx 17.2$ and $\Delta z^+ \approx 10.3$. This case relaminarized after 10.4 turnovers in contrast to 6 observed in Figure 7.1. The 3.199 m case was handled similarly but was reduced only as far as $384 \times 192 \times 192$ at $t \approx 20$ where $\Delta x^+ \approx 13.2$ and $\Delta z^+ \approx 7.9$. This case relaminarized after 13.2 turnovers in contrast to the 36.3 observed in Figure 7.2. Both simulations used resolutions similar to those in Table 6.1, which were found adequate. Qualitatively both cases show the same features as the earlier refinement study did at these locations. Namely, the supersonic case at 4.134 m smoothly dissipated away while the subsonic case at 3.199 m had a longer dwell time before a relatively quick collapse.

For the studied parametrization of Bauman's fully laminar Orion MPCV solution, locations 4.134 m and 3.199 m represent the boundary layer conditions on the

thermal protection system *a priori* expected most likely to sustain turbulence. They possess Re_θ within 4.6% of peak 236 (found at 3.762 m), among the highest Ma, T_e/T_w within 0.8% of peak 4.321 (found at 3.983 m), and among the lowest ν_w^+. Given that expectation, having observed 4.134 m and 3.199 m relaminarize from fully turbulent initial conditions, and having discovered a field able to sustain nontrivial fluctuations at 2.299 m, the study was halted.

Despite comments made at the end of Section 7.1, a subsequent confirmation of the relaminarizations seen in Figures 7.8 and 7.9 at higher resolutions and for larger box sizes was not performed. Those comments pertained to the need to assess the sensitivity of the hypothetical edge of the turbulence sustaining region to changes in discretization. Having observed no such edge, that particular sensitivity became irrelevant.

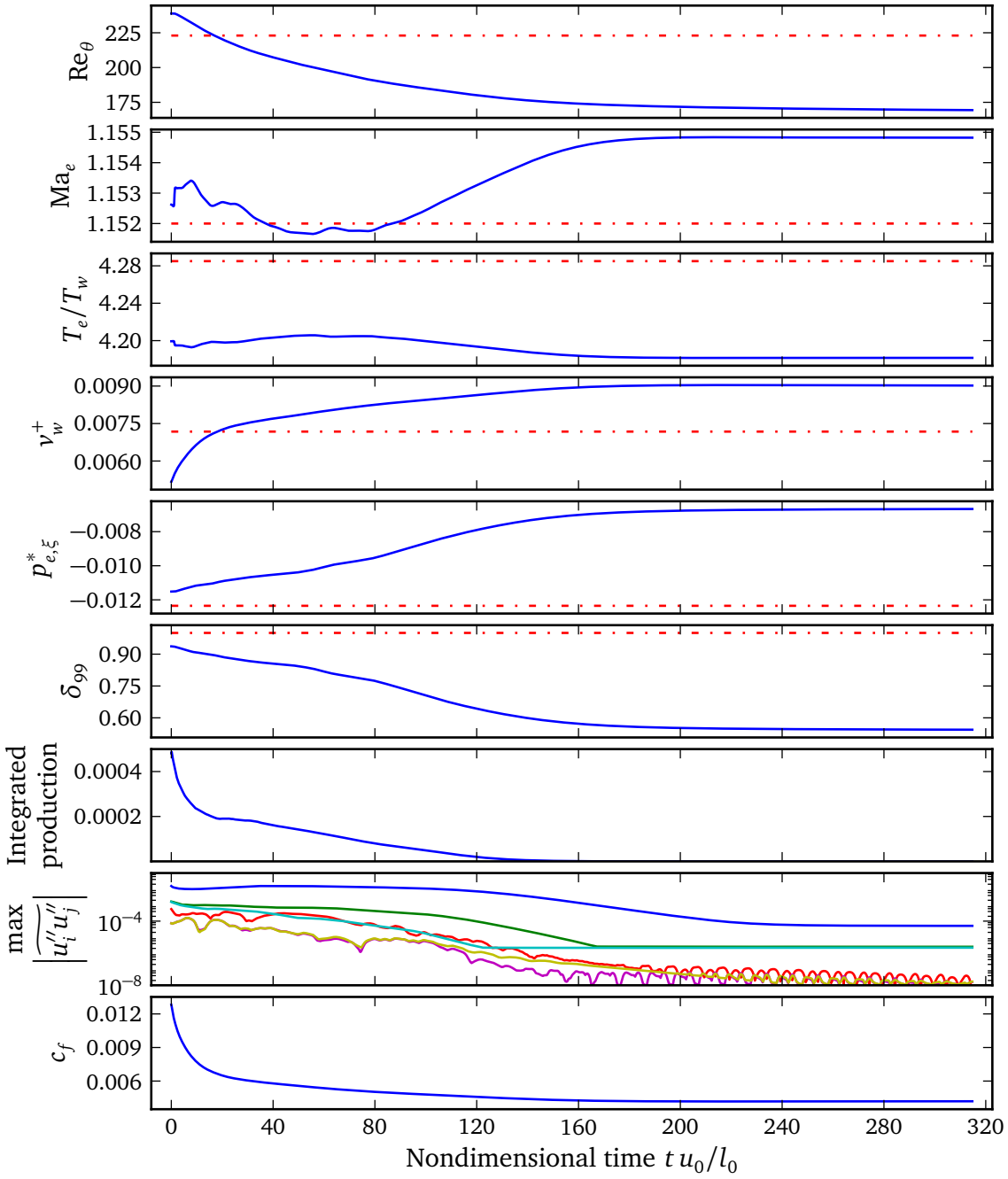

Figure 7.8: Fully turbulent initial condition study for location 4.314 m.

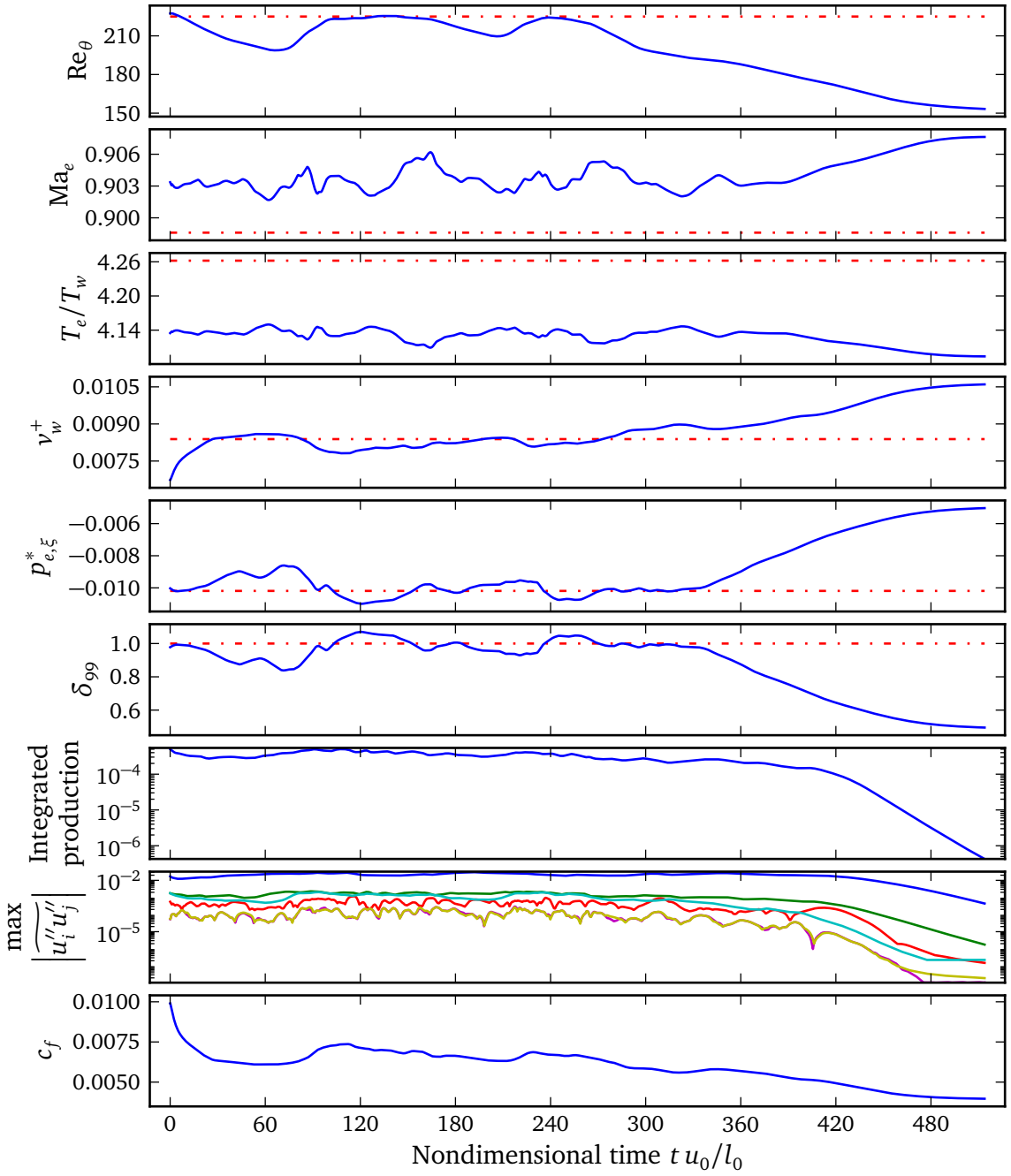

Figure 7.9: Fully turbulent initial condition study for location 3.199 m.

7.3 Discussion

Given the Orion MPCV boundary layer characterization in Figures 2.7 and 2.8, that local conditions at 4.134 m and 3.199 m relaminarized from fully turbulent initial conditions, as shown in Figures 7.8 and 7.9, suggests no turbulence sustaining region exists on this particular thermal protection system surface in this particular reentry scenario according to the present modeling applied per the chosen methodology. Those two locations possess among the highest Re_θ found in the Orion MPCV International Space Station return scenario combined with weak v_w^+ and $p_{e,\xi}^*$ and were *a priori* anticipated to sustain turbulence if any portion of the boundary layer could.

How robust is accepting the possible conclusion that the Orion MPCV is fully laminar in this scenario with respect to using that information to predict aerothermodynamic heating? By using turbulent initial conditions in a periodic domain as a surrogate for a fluctuation-rich flight environment, our methodology attempted to capture that the reentry vehicle is awash in perturbations from the freestream, from aerothermochemistry, from ablator outgassing, and from surface roughness. Setting aside concerns regarding the verisimilitude of the homogenized governing equations, the robustness of a fully laminar conclusion depends to a large extent on whether or not the turbulent initial condition surrogate was adequate.

Drawing on the nonlinear stability theory discussed in Section 2.7, turbulent initial conditions were adopted for the relaminarization study because they are physically relevant but moreso because they represent large, potentially self-sustaining disturbances relative to laminar flows. The discovery of the field able to sustain nontrivial fluctuations at 2.299 m, pictured in Figure 7.4, demonstrates that turbulent initial con-

ditions were not the most conservative possible way to emulate a fluctuation-rich flight environment for the purposes of determining where local conditions can sustain turbulence. Heightened conservatism is appropriate because in-flight perturbations cannot be characterized well-enough to apply transition models as discussed in Section 2.6.

Consequently, despite relaminarization from turbulent initial conditions at 4.134 m and 3.199 m, the existence of a long-lived, fluctuating field at 2.299 m forces us to conservatively conclude that the turbulence-sustaining region on the Orion MPCV extends from the edge of the thermal protection system to at least 2.299 m leeward of the stagnation point. Having observed location 1.389 m relaminarize from initial conditions like those that generated the fluctuation-sustaining 2.299 m field, we conclude that the turbulence sustaining region does not extend to within 1.389 m leeward of the stagnation point. That conclusion is predicated on the homogenized governing equations providing accurate predictions regarding the turbulence-sustaining behavior of spatially evolving boundary layers which has not been validated in the present work.

Where between locations 1.389 m and 2.299 m is the edge of the turbulence sustaining region? We suspect it lies closer to 2.299 m but we do not know conclusively. Investigating that interval will require a more sophisticated way than crude auxiliary simulations to determine the code inputs necessary to incrementally bring the fluctuation-sustaining 2.299 m field inward towards the stagnation point. Two suggestions were already made in Section 7.1. Calibrating a turbulence model equipped with spatiotemporal homogenization terms to reproduce statistics from the fluctuation-sustaining 2.299 m field appears to be a necessary first step towards either suggestion.

One factor contributing to the difficulty of obtaining code parameters to match

such local conditions was the implicit dependence of v_w^+ on all code inputs. The present study targeted a constant v_w^+ based on conditions found in Bauman's fully laminar Orion MPCV simulation. The metric was selected because it approximated outgassing from a steady ablative heat shield. As can be seen from the results, the normalized wall blowing became stronger as simulations relaminarized. A better approach for future work may be to control v_w/u_0 to match the local nondimensional heat flux B_q [16] from MPCV data. Matching the heat flux approximates an ablator able to react to flow conditions. Care is required, however, to not have the controller mechanism introduce undesirable time scales into the simulation.

It would be interesting to repeat the Bauman et al. [8] heat shield simulations with turbulence tripped at 1.389 m and to compare the result with both Figure 2.4 and Table 2.2. That prediction could be contrasted with heating data gathered during the upcoming NASA Exploration Flight Test-1 [118] in the hope that the simulation matches evidence of where on the heat shield turbulence-enhanced energy transport is present. However, a comparison may not be straightforward as that flight test will use a different reentry trajectory than the peak heating regime studied here.

Finally, if one wanted to limit a relaminarization study to only fully turbulent initial conditions and possibly find a turbulence-sustaining edge, the higher speed Exploration Flight Test-1 trajectory may be ideal. Studying a faster trajectory with the suggested methodology improvements may allow interrogating the physics at the cusp where turbulence can only barely be sustained.

Chapter 8

Conclusions

8.1 Summary of the Present Work

Turbulent boundary layers approximating those found on the NASA Orion Multi-Purpose Crew Vehicle (MPCV) thermal protection system during atmospheric reentry from the International Space Station have been studied by direct numerical simulation, with the ultimate goal of reducing aerothermodynamic heating prediction uncertainty. Simulations were performed using a new, well-verified, openly available Fourier/B-spline pseudospectral code called Suzerain equipped with a recent, "slow growth" spatiotemporal homogenization approximation developed by Topalian et al. [165]. A first study aimed to reduce turbulence-driven heating prediction uncertainty by providing high-quality data suitable for calibrating Reynolds-averaged Navier–Stokes turbulence models to address the atypical boundary layer characteristics found in such reentry problems. The unique boundary layer data includes strong favorable pressure gradients, cold isothermal wall conditions, and wall transpiration effects and has well-quantified uncertainties so that it may best inform turbulence models. A second study aimed to reduce transition-driven uncertainty by determining where on the thermal protection system surface the boundary layer could sustain turbulence. This study informs where fully laminar and where fully turbulent assumptions are appropriate in the reentry scenario without incurring the uncertainties associated

with transition modeling.

In the first study, the two data sets generated and investigated were a Ma $\approx$ 0.9 and a Ma $\approx$ 1.15 spatiotemporally homogenized boundary layer with $\mathrm{Re}_\theta \approx 382$ and $\mathrm{Re}_\theta \approx 531$, respectively. Boundary layer edge-to-wall temperature ratios were approximately 4.15 and wall blowing velocities, measured in plus units, were in the neighborhood of 8e−3. The favorable pressure gradients, achieved by supplying a stationary inviscid flow profile to the homogenization approximation, had acceleration parameters [86] of about 4e−6 and Pohlhausen parameters between 25 and 42. Skin frictions coefficients around 6e−3 and Nusselt numbers under 22 were observed. Due to the considerable thermodynamic property gradients, the subsonic simulation had an unexpectedly small displacement thickness while the supersonic simulation exhibited negative displacement effects. As a consequence, the Clauser parameter [26] was found misleading for characterizing these pressure gradients. Objective uncertainty estimates [114] for the data found coefficients of variation of less than 8e−3 for density, velocity, temperature, and viscosity inside the boundary layer edge and of roughly 10% for the specific turbulent kinetic energy for statistical ensembles gathered for 6.4–6.9 eddy turnover times. Semi-local scaling [67] collapsed all profiles investigated. The near-wall vorticity fluctuations show qualitatively different profiles than those from the incompressible [150] or compressible literature [60]. The turbulent Prandtl number was above 0.8 inside the boundary layer edge. Root-mean-squared property fluctuations matched expectations for isothermal wall conditions [27] but the supersonic results show evidence of minor problems in the numerical formulation related to the spatiotemporal homogenization when Ma > 1. Favre-averaged equation budgets were

reported and show the regions in which the homogenization approximation directly impacts the mean flow. In particular, the direct slow growth influence on the total energy and turbulent kinetic energy equations is small enough that such homogenized flows can serve as convenient model problems for calibration of models to be used in spatially evolving boundary layers.

In the second study, local boundary layer conditions were extracted from a laminar flow solution over the Orion MPCV thermal protection system during peak reentry heating which included shock effects, aerothermochemistry, curvature, and ablation. That information, as a function of leeward distance from the stagnation point along the MPCV symmetry plane, was approximated by Re_θ, Ma_e, $p^*_{e,\xi} = \frac{\delta}{\rho_e u_e^2}\frac{\partial p_e}{\partial \xi}$, $v_w^+ = v_w/u_\tau$, and T_e/T_w along with perfect gas assumptions. Homogenized turbulent boundary layers were initialized at those local conditions and evolved until either stationarity, implying the conditions could sustain turbulence, or relaminarization, implying the conditions could not. A computationally convenient periodic domain, which fluctuations cannot exit, served as a surrogate for a perturbation-rich flight environment. Fully turbulent fields relaminarized subject to conditions 4.134 m and 3.199 m leeward of the stagnation point. At those two locations, $\mathrm{Re}_\theta \approx 225$, $\mathrm{Ma}_e > 0.9$, and $T_e/T_w \approx 4.1$ all approach maxima over the heat shield while $p^*_{e,\xi}$ and v_w^+ become small (see Figures 2.7 and 2.8). These results suggest that nowhere on the MPCV thermal protection system can sustain turbulence in this reentry scenario. However, different and somewhat pathological initial conditions unexpectedly produced a long-lived, fluctuating field at leeward position 2.299 m. No evidence of turbulence-sustaining behavior appeared at leeward position 1.389 m. Accordingly, it was predicted that locations more than 1.389 m leeward of

the stagnation point can sustain turbulence in this scenario. Relaminarization for the Topalian et al. [165] homogenized boundary layers showed similar early and late time behavior as that described by Cal and Castillo [22] for spatially evolving flows.

8.2 Recommendations for Future Work

Regarding the first study, more investigation into the basic character of the spatiotemporally homogenized boundary layers produced by the Topalian et al. [165] technique is warranted. With a better understanding of the behavior of the approach on simpler cases, it would be possible to disentangle the combined influence of homogenization, strong favorable pressure gradients, cold walls, and wall transpiration. Future simulations might begin from the $\mathrm{Re}_\theta \approx 382$ simulation presented here and incrementally eliminate complicating features to produce a sequence of problems approaching more canonical, better understood flows. Several symptoms of minor problems with the present numerical formulation of the homogenization for $\mathrm{Ma} > 1$ were raised, including in one dimension for laminar solutions, suggesting that additional analysis of the homogenization is worthwhile. Though found usable here, it may be the case that either straightforward Giles-like nonreflecting boundary conditions [56, 57] or the chosen isothermal wall enforcement scheme or both are inappropriate. These symptoms may also indicate a malady in the model itself. Applying the homogenization approach to either the low Mach number, variable density or incompressible limits of the Navier–Stokes equations would be worthwhile. Doing so also may provide insight regarding the issues observed from the present numerical formulation.

Regarding the second study, it would be interesting to recompute the Orion

MPCV thermal protection system flow for peak heating during International Space Station reentry using our estimate of the edge of the turbulence-sustaining region. From this mixed laminar/turbulent solution the energy flux to the ablator could be compared against the fully laminar or fully turbulent results. That computation would also provide a prediction against which flight data from the upcoming NASA Exploration Flight Test-1 [118] might be compared. Obtaining a more precise location for the edge of the turbulence-sustaining region will require methodology improvements. In particular, a turbulence-model-based procedure to find the code inputs yielding the desired δ_{99}, Re_θ, Ma_e, $p^*_{e,\xi}$, v^+_w, and T_e/T_w would permit continuing the present relaminarization study based on the fluctuation-sustaining conditions found at 2.299 m. The present ad hoc approach for discovering input parameters, though it produced interesting and useful results, was operationally unsatisfying and its effective application below 2.299 m would be difficult. The constant wall blowing v^+_w designed to emulate steady-state outgassing from the ablator in future studies might better be replaced by a controller-based mechanism to adjust the wall blowing velocity to achieve nondimensional heat fluxes B_q [16] extracted from the original laminar flow solution for the reentry scenario. With such improvements in place, investigating higher-speed reentry trajectories for the Orion MPCV might simplify characterizing the edge of a turbulence-sustaining region given fully turbulent initial conditions and also be more fruitful from the perspective of improving basic understanding of the physics in these scenarios. Finally, the validity of the present methodology for detecting turbulence-sustaining regions might be investigated by comparing its predictions against experimental transition data gathered from a wind tunnel facility that has been configured to be exceptionally noisy.

Appendices

Appendix A

Derivation of the Mathematical Models

Here the mathematical models summarized in Chapter 3 are derived. While the first two sections containing the Navier–Stokes and Favre-averaged Navier–Stokes equations are classical and straightforward, the derivations are provided to document the few peculiar constitutive choices as well as to unambiguously fix nomenclature. The third section documents a new spatiotemporal homogenization approximation by Topalian et al. [165]. Dimensional equations are employed throughout this appendix. The final dimensional summary in each of the following subsections is nondimensionalized to arrive at the formulations used in the main body of the dissertation.

A.1 The Governing Equations

A.1.1 Conservation Laws

Consider a time-varying control volume Ω with surface $\partial\Omega$ and unit outward normal $\hat{n}$. For any scalar, vector, or tensor field quantity T, Leibniz' theorem states

$$\frac{d}{dt}\int_{\Omega(t)} T(x,t)\,dV = \int_{\Omega}\frac{\partial}{\partial t}T\,dV + \int_{\partial\Omega}\hat{n}\cdot wT\,dA = \int_{\Omega}\frac{\partial}{\partial t}T + \nabla\cdot wT\,dV \qquad \text{(A.1)}$$

where w is the velocity of $\partial\Omega$. When Ω follows a fixed set of fluid particles, w becomes the fluid velocity u.

Since mass $M = \int_\Omega \rho \, dV$ and mass conservation requires $\frac{d}{dt}M = 0$,

$$0 = \frac{d}{dt}M = \frac{d}{dt}\int_\Omega \rho \, dV = \int_\Omega \frac{\partial}{\partial t}\rho + \nabla \cdot u\rho \, dV. \tag{A.2}$$

Because the result holds for any control volume, locally it must be true that

$$\frac{\partial}{\partial t}\rho + \nabla \cdot \rho u = 0. \tag{A.3}$$

Separating total force into surface forces and body forces,

$$\sum F = \int_{\partial\Omega} f_s \, dA + \int_\Omega f \, dV = \int_{\partial\Omega} \sigma \hat{n} \, dA + \int_\Omega f \, dV = \int_\Omega \nabla \cdot \sigma + f \, dV \tag{A.4}$$

where σ is the Cauchy stress tensor. From linear momentum $I = \int_\Omega \rho u \, dV$ and its conservation $\frac{d}{dt}I = \sum F$,

$$\int_\Omega \frac{\partial}{\partial t}\rho u + \nabla \cdot (u \otimes \rho u) \, dV = \int_\Omega \nabla \cdot \sigma + f \, dV. \tag{A.5}$$

As the control volume may be arbitrary,

$$\frac{\partial}{\partial t}\rho u + \nabla \cdot (u \otimes \rho u) = \nabla \cdot \sigma + f. \tag{A.6}$$

Lastly, separating the pressure p and viscous contributions τ to the Cauchy stress tensor so that $\sigma = -pI + \tau$,

$$\frac{\partial}{\partial t}\rho u + \nabla \cdot (u \otimes \rho u) = -\nabla p + \nabla \cdot \tau + f. \tag{A.7}$$

The conservation of angular momentum implies $\sigma = \sigma^\mathsf{T}$ and therefore $\tau = \tau^\mathsf{T}$ too.

Combining internal and kinetic energy into an intrinsic density E, energy $\mathscr{E}$ is

$$\mathscr{E} = \int_\Omega \rho E \, dV. \tag{A.8}$$

Treating heat input Q as both a surface phenomenon described by an outward heat flux q_s and as a volumetric phenomenon governed by a body heating q_b,

$$Q = \int_\Omega \rho q_b \, dV - \int_{\partial\Omega} \hat{n} \cdot q_s \, dA = \int_\Omega q_b - \nabla \cdot q_s \, dV. \tag{A.9}$$

Power input $P = F \cdot v$ accounts for surface stress work and body force work to give

$$P = \int_{\partial\Omega} \sigma \hat{n} \cdot u \, dA + \int_\Omega f \cdot u \, dV = \int_\Omega \nabla \cdot \sigma u + f \cdot u \, dV. \tag{A.10}$$

Demanding energy conservation $\frac{d}{dt}\mathscr{E} = Q + P$,

$$\int_\Omega \frac{\partial}{\partial t} \rho E + \nabla \cdot u \rho E \, dV = \int_\Omega q_b - \nabla \cdot q_s \, dV + \int_\Omega \nabla \cdot \sigma u + f \cdot u \, dV. \tag{A.11}$$

Again, since the control volume was arbitrary,

$$\frac{\partial}{\partial t} \rho E + \nabla \cdot \rho E u = -\nabla \cdot q_s + \nabla \cdot \sigma u + f \cdot u + q_b. \tag{A.12}$$

Splitting σ's pressure and viscous stress contributions into separate terms,

$$\frac{\partial}{\partial t} \rho E + \nabla \cdot \rho E u = -\nabla \cdot q_s - \nabla \cdot p u + \nabla \cdot \tau u + f \cdot u + q_b. \tag{A.13}$$

A.1.2 Constitutive Assumptions

Assume the fluid is a thermally and calorically perfect gas governed by

$$p = \rho R T \tag{A.14}$$

where R is the gas constant. The constant volume C_v specific heat, constant pressure specific heat C_p, and acoustic velocity a relationships follow:

$$\gamma = \frac{C_p}{C_v} \qquad C_v = \frac{R}{\gamma - 1} \qquad C_p = \frac{\gamma R}{\gamma - 1} \qquad R = C_p - C_v \qquad a^2 = \gamma R T. \tag{A.15}$$

Also assume C_v and C_p and, therefore, γ are constant. The total (internal and kinetic) energy density is

$$E = C_v T + \frac{1}{2}u^2 = \frac{RT}{\gamma - 1} + \frac{1}{2}u^2 \tag{A.16}$$

where the notation $u^2 = u \cdot u$ is employed. The total enthalpy density H and (internal) enthalpy density h are

$$H = E + \frac{p}{\rho} = C_p T + \frac{1}{2}u^2 = \frac{\gamma RT}{\gamma - 1} + \frac{1}{2}u^2, \tag{A.17}$$

$$h = H - \frac{1}{2}u^2 = C_p T = \frac{\gamma RT}{\gamma - 1}. \tag{A.18}$$

See a gas dynamics reference, for example Liepmann and Roshko [94], for more details.

If one seeks a constitutive law for the viscous stress tensor τ using only velocity information, the principle of material frame indifference implies that uniform translation (given by velocity u) and solid-body rotation (given by the skew-symmetric rotation tensor $\omega = \frac{1}{2}\left(\nabla u - \nabla u^{\mathsf{T}}\right)$) may not influence τ. Considering contributions only up to the gradient of velocity, extensional strain (dilatation) and shear strain effects may depend on only the symmetric strain rate tensor $\varepsilon = \frac{1}{2}\left(\nabla u + \nabla u^{\mathsf{T}}\right)$ and its principal invariants.

Assuming τ is isotropic and depends linearly upon only ε, express it as

$$\begin{aligned}
\tau_{ij} &= c_{ijmn}\varepsilon_{mn} \\
&= \left(A\delta_{ij}\delta_{mn} + B\delta_{im}\delta_{jn} + C\delta_{in}\delta_{jm}\right)\varepsilon_{mn} \qquad \text{for some } A, B, C \in \mathbb{R} \\
&= A\delta_{ij}\varepsilon_{mm} + B\varepsilon_{ij} + C\varepsilon_{ji} \\
&= A\delta_{ij}\varepsilon_{mm} + (B + C)\,\varepsilon_{ji} \\
&= 2\mu\varepsilon_{ij} + \lambda\delta_{ij}\nabla \cdot u
\end{aligned} \tag{A.19}$$

where $\mu = \frac{1}{2}(B + C)$ is the dynamic coefficient of viscosity (shear) and $\lambda = A$ is the second coefficient of viscosity (dilatational). Reverting to direct notation,

$$\tau = 2\mu\varepsilon + \lambda(\nabla \cdot u) I = \mu\left(\nabla u + \nabla u^{\mathsf{T}}\right) + \lambda(\nabla \cdot u) I. \tag{A.20}$$

The bulk viscosity $\mu_B = \lambda + \frac{2}{3}\mu$ and the deviatoric part of the strain rate tensor,

$$S = \varepsilon - \frac{1}{3}\operatorname{tr}(\varepsilon) I = \frac{1}{2}\left(\nabla u + \nabla u^{\mathsf{T}}\right) - \frac{1}{3}(\nabla \cdot u) I, \tag{A.21}$$

may be used to write

$$\tau = 2\mu S + \mu_B(\nabla \cdot u) I. \tag{A.22}$$

The kinematic viscosity and bulk kinematic viscosity

$$\nu = \frac{\mu}{\rho} \qquad\qquad \nu_B = \frac{\mu_B}{\rho} \tag{A.23}$$

are often used to simplify notation.

Set the bulk viscosity μ_B to be a fixed multiple of the dynamic viscosity μ. This relationship may be written as either

$$\mu_B = \alpha\mu \qquad \text{or} \qquad \lambda = \left(\alpha - \frac{2}{3}\right)\mu \tag{A.24}$$

where a dimensionless proportionality constant α has been introduced. Stokes' hypothesis that bulk viscosity is negligible may be recovered by selecting $\alpha = 0$. Though Stokes' hypothesis is valid for most circumstances [41], we choose to separately track μ and λ terms in the model.

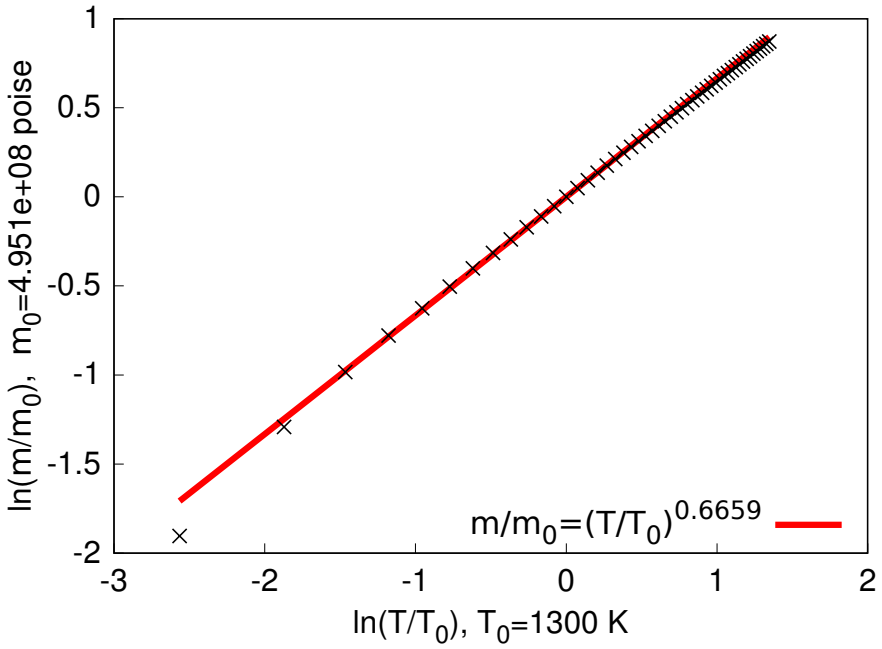

Figure A.1: Power law fit for air viscosity versus temperature over 100 to 5000 K using data from Svehla [157]. The least squares fit over this wide range is relatively insensitive to the chosen references μ_0 and T_0. For example, selecting $T_0 = 300K$ or $4000K$ causes exponents 0.6639 or 0.6673 to be optimal, respectively. Truncating the data to eliminate larger T generally produces larger exponents.

Assume that viscosity varies only with temperature according to

$$\frac{\mu}{\mu_0} = \left(\frac{T}{T_0}\right)^{\beta} \tag{A.25}$$

where μ_0 and T_0 are suitable reference values. This relationship models air well for temperatures up to several thousand degrees Kelvin [157] as shown in Figure A.1. Sutherland's law [156], often recommended for its greater accuracy [149, p. 46], was avoided because of the greater complexity its use would entail in expressions like (4.30).

Neglecting the transport of energy by molecular diffusion and radiative heat transfer, a linear relation is sought between the surface heat flux q_s and the temperature T. The principle of frame indifference implies only the temperature gradient is relevant so that

$$q_s = \underline{\kappa} \cdot \nabla T \tag{A.26}$$

where $\underline{\kappa}$ is a thermal conductivity tensor. Consistent with the assumption that τ is isotropic, assume $\underline{\kappa}$ is isotropic to obtain

$$q_s = -\kappa \nabla T \tag{A.27}$$

where κ is the scalar thermal conductivity. The negative sign has been introduced so that heat flows from hot to cold when $\kappa > 0$.

Assume the Prandtl number $\mathrm{Pr} = \mu C_p/\kappa$ is constant. Because C_p is constant the ratio μ/κ must be constant. The viscosity and thermal conductivity must either grow at identical rates or they must grow according to an inverse relationship. The latter is not observed in practice for this class of fluids, and so further assume

$$\frac{\mu}{\mu_0} = \frac{\kappa}{\kappa_0}. \tag{A.28}$$

A.1.3 Dimensional Summary

Combining the conservation laws with the above constitutive relations and assumptions, one arrives at the dimensional equations

$$\frac{\partial}{\partial t}\rho = -\nabla\cdot\rho u + \mathscr{S}_\rho \tag{A.29a}$$

$$\frac{\partial}{\partial t}\rho u = -\nabla\cdot(u\otimes\rho u) - \nabla p + \nabla\cdot\tau + f + \mathscr{S}_{\rho u} \tag{A.29b}$$

$$\frac{\partial}{\partial t}\rho E = -\nabla\cdot\rho E u + \nabla\cdot\frac{\kappa_0}{\mu_0}\mu\nabla T - \nabla\cdot pu + \nabla\cdot\tau u + f\cdot u + q_b + \mathscr{S}_{\rho E} \tag{A.29c}$$

where the right hand sides make use of

$$p = (\gamma-1)\left(\rho E - \frac{1}{2}\rho u^2\right) \tag{A.29d}$$

$$T = \frac{p}{\rho R} \tag{A.29e}$$

$$\mu = \mu_0\left(\frac{T}{T_0}\right)^\beta \tag{A.29f}$$

$$\lambda = \left(\alpha - \frac{2}{3}\right)\mu \tag{A.29g}$$

$$\tau = \mu\left(\nabla u + \nabla u^{\mathsf{T}}\right) + \lambda(\nabla\cdot u)I. \tag{A.29h}$$

Additional, equation-specific terms $\mathscr{S}_\rho$, $\mathscr{S}_{\rho u}$, and $\mathscr{S}_{\rho E}$ have been added to permit applying forcing arising from homogenization. Appropriately nondimensionalized, these equations are nothing but the model given in Section 3.1.

A.2 The Favre-Averaged Navier–Stokes Equations

The material in this section borrows from Oliver [111]. It departs from that particular document in that it employs the preceding constitutive relationships, avoids

introducing customary assumptions about the relative importance of unclosed terms, and accounts for arbitrary slow growth forcing.

A.2.1 Reynolds- and Favre-Averaging Techniques

The Reynolds average is the usual mean of a random variable. Consider a generic flow variable q. The value, $q(x, y, z, t)$, of this variable at a particular point in space, (x, y, z), and time, t, is a random variable. Assuming that the probability density function for $q(x, y, z, t)$ is given by $\pi_q(V; x, y, z, t)$, the Reynolds average is defined by

$$\bar{q}(x, y, z, t) \equiv \int V \pi_q(V; x, y, z, t)\, \mathrm{d}V. \tag{A.30}$$

The Favre average is defined as the density-weighted average. Thus, denoting the fluid density by $\rho(x, y, z, t)$, the Favre average of $q(x, y, z, t)$ is

$$\tilde{q}(x, y, z, t) \equiv \frac{\overline{\rho q}(x, y, z, t)}{\bar{\rho}(x, y, z, t)}. \tag{A.31}$$

It is assumed that both the Reynolds and Favre averages are well-defined for any required flow variable, q. That is, the integral on the right-hand side of (A.30) exists whenever required, and the Reynolds-averaged density, $\bar{\rho}$, is positive everywhere.

In the following, the flow variables will be decomposed into mean and fluctuating parts. Specifically, the fluctuations about the mean—denoted by $(\cdot)'$ and $(\cdot)''$ for the Reynolds and Favre averages, respectively—are defined by the following relationships:

$$q' \equiv q - \bar{q}, \tag{A.32}$$

$$q'' \equiv q - \tilde{q}. \tag{A.33}$$

Using the linearity of the Reynolds average and the fact that $\bar{q}$ and $\tilde{q}$ are deterministic,

$$\overline{q'} = \overline{q - \bar{q}} = \bar{q} - \bar{q} = 0, \tag{A.34}$$

$$\widetilde{q''} = \widetilde{q - \tilde{q}} = \tilde{q} - \tilde{q} = 0. \tag{A.35}$$

Furthermore,

$$\overline{\rho q''} = \bar{\rho}\widetilde{q''} = 0. \tag{A.36}$$

However, in general,

$$\overline{q''} = \overline{q - \tilde{q}} = \bar{q} - \tilde{q} \neq 0 \tag{A.37}$$

which proves that the Reynolds and Favre averages differ by exactly $\overline{q''}$.

Wherever necessary, realizations of random fields of flow quantities are assumed to be differentiable in both time and space so that Reynolds averaging and differentiation commute. For example,

$$\overline{\nabla u} = \nabla \bar{u}. \tag{A.38}$$

This commutativity is used to develop the FANS equations. In contrast, Favre averaging and differentiation do not, in general, commute:

$$\begin{aligned}
\rho \nabla q &= \rho \nabla q \\
\rho \widetilde{\nabla q} + \rho \left(\nabla q\right)'' &= \rho \nabla \tilde{q} + \rho \nabla q'' \\
\bar{\rho} \widetilde{\nabla q} &= \bar{\rho} \nabla \tilde{q} + \overline{\rho \nabla q''} \\
&= \bar{\rho} \nabla \tilde{q} - \overline{q'' \nabla \rho}.
\end{aligned}$$

Here the common convention that taking Favre fluctuations, $(\cdot)''$, has higher precedence than differentiation, $\nabla(\cdot)$, has been adopted. Rearranging to better examine the

difference between $\widetilde{\nabla q}$ and $\nabla\tilde{q}$ in terms of mean quantities,

$$\widetilde{\nabla q} - \nabla\tilde{q} = \widetilde{\nabla q''} = -\frac{\overline{q''\nabla\rho}}{\bar{\rho}} = \frac{\tilde{q}\nabla\bar{\rho}}{\bar{\rho}} - \frac{\overline{q\nabla\rho}}{\bar{\rho}}. \tag{A.39}$$

This lack of commutativity is not problematic as it is not required to derive the FANS equations. It does, however, slightly complicate the mean constitutive relationships. The fluctuating gradient and the gradient of the fluctuations differ according to

$$(\nabla q)'' - \nabla q'' = -\widetilde{\nabla q''}. \tag{A.40}$$

In some circumstances, the difference between quantities written using a fluctuating gradient and the gradient of the fluctuations can vanish. One useful example is

$$\widetilde{f''(\nabla g)''} = \frac{\overline{\rho f''(\nabla g)''}}{\bar{\rho}} = \frac{\overline{\rho f''\left(\nabla g'' - \widetilde{\nabla g''}\right)}}{\bar{\rho}} = \frac{\overline{\rho f''\nabla g''} - \overline{\rho f''}\widetilde{\nabla g''}}{\bar{\rho}} = \widetilde{f''\nabla g''}. \tag{A.41}$$

A.2.2 Derivation of the Favre-Averaged Equations

From (A.29) a lengthy algebraic procedure [111, §2] produces exact equations governing the evolution of mean conserved quantities $\bar{\rho}$, $\overline{\rho u} = \bar{\rho}\tilde{u}$, and $\overline{\rho E} = \bar{\rho}\tilde{E}$:

$$\frac{\partial}{\partial t}\bar{\rho} = -\nabla\cdot\bar{\rho}\tilde{u} + \overline{\mathscr{S}_\rho} \tag{A.42a}$$

$$\frac{\partial}{\partial t}\bar{\rho}\tilde{u} = -\nabla\cdot(\tilde{u}\otimes\bar{\rho}\tilde{u}) - \nabla\bar{p} + \nabla\cdot\left(\bar{\tau} - \bar{\rho}\widetilde{u''\otimes u''}\right) + \bar{f} + \overline{\mathscr{S}_{\rho u}} \tag{A.42b}$$

$$\begin{aligned}\frac{\partial}{\partial t}\bar{\rho}\tilde{E} = &-\nabla\cdot\bar{\rho}\tilde{H}\tilde{u} + \nabla\cdot\left(\left(\bar{\tau} - \bar{\rho}\widetilde{u''\otimes u''}\right)\tilde{u} - \frac{1}{2}\bar{\rho}\widetilde{u''^2u''} + \overline{\tau u''}\right)\\ &-\nabla\cdot\left(\bar{q}_s + \bar{\rho}\widetilde{h''u''}\right) + \bar{f}\cdot\tilde{u} + \overline{f\cdot u''} + \bar{q}_b + \overline{\mathscr{S}_{\rho E}}.\end{aligned} \tag{A.42c}$$

Several correlations impact the evolution of mean quantities: the Reynolds stress $-\bar{\rho}\widetilde{u''\otimes u''}$, the Reynolds heat flux $\bar{\rho}\widetilde{h''u''}$, turbulent transport $-\frac{1}{2}\bar{\rho}\widetilde{u''^2u''}$, turbulent

work $\overline{\tau u''}$, and the forcing-velocity correlation $\overline{f \cdot u''}$. The Reynolds stress and heat flux augment the viscous stress and heat flux, respectively. The turbulent transport and work terms represent transport of the turbulent kinetic energy density k, defined below, and viscous stress work due to turbulent velocity fluctuations, respectively.

We now turn to perfect gas relations from Section A.1.2. The Reynolds average of (A.14) gives

$$\bar{p} = R\overline{\rho T} = \bar{\rho} R \tilde{T} \tag{A.43}$$

while the Favre average of (A.17) finds both

$$\tilde{H} = \tilde{E} + R\tilde{T}, \qquad \tilde{h} = \frac{\gamma R \tilde{T}}{\gamma - 1}. \tag{A.44}$$

The turbulent kinetic energy density,

$$k = \frac{1}{2}\widetilde{u''^2}, \tag{A.45}$$

arises from averaging the total energy given by (A.16):

$$\begin{aligned}
\rho E &= \frac{R}{\gamma - 1}\rho T + \frac{1}{2}\rho u^2 \\
&= \frac{R}{\gamma - 1}\rho\left(\tilde{T} + T''\right) + \frac{1}{2}\rho\left(\tilde{u} + u''\right)^2 && \text{(A.46)} \\
\overline{\rho E} &= \frac{R}{\gamma - 1}\bar{\rho}\tilde{T} + \frac{1}{2}\bar{\rho}\tilde{u}^2 + \frac{1}{2}\overline{\rho u''^2} && \text{(A.47)} \\
\tilde{E} &= \frac{R}{\gamma - 1}\tilde{T} + \frac{1}{2}\tilde{u}^2 + k. && \text{(A.48)}
\end{aligned}$$

An exact equation may be derived for the evolution of k [111, §5]

$$\begin{aligned}
\frac{\partial}{\partial t}\bar{\rho}k = &-\nabla\cdot\bar{\rho}k\tilde{u} - \bar{\rho}\widetilde{u''\otimes u''} : \nabla\tilde{u} - \bar{\rho}\epsilon + \nabla\cdot\left(-\frac{1}{2}\bar{\rho}\widetilde{u''^2 u''} + \overline{\tau u''}\right) \\
&-\overline{u''}\cdot\nabla\bar{p} - \nabla\cdot\overline{p'u''} + \overline{p'\nabla\cdot u''} + \overline{f\cdot u''} + \overline{\mathscr{S}_{\rho u}\cdot u''}
\end{aligned} \tag{A.49}$$

where $A:B$ denotes $\mathrm{tr}\left(A^{\mathsf{T}}B\right)$, and the contribution of the slow growth terms has been tallied. The dissipation rate density ϵ, which governs the conversion rate from k to mean internal energy, is defined by

$$\bar{\rho}\epsilon = \overline{\tau : \nabla u''}. \tag{A.50}$$

Many authors, for example Guarini et al. [60], work with (A.49). However, a different form the turbulent kinetic energy equation is preferred here. As Lele [91, page 216] suggests, expanding $\rho H u$ using $\rho H = \rho E + p$, decomposing the non-density contributions into their mean and fluctuating contributions, averaging, and then subtracting $\left(\bar{\rho}\tilde{H} = \bar{\rho}\tilde{E} + \bar{p}\right)\tilde{u}$ proves the general identity

$$\bar{\rho}\widetilde{H''u''} = \bar{\rho}\widetilde{E''u''} + \bar{p}\overline{u''} + \overline{p'u''}. \tag{A.51}$$

Collecting $(H-E)''$, introducing perfect gas constitutive relations, and simplifying,

$$\overline{u''} = \frac{\widetilde{T''u''}}{\tilde{T}} - \frac{\overline{p'u''}}{\bar{p}}. \tag{A.52}$$

Substituting h'' everywhere for T'', noting $\bar{p}/\tilde{h} = \frac{\gamma-1}{\gamma}\bar{\rho}$, and differentiating,

$$\overline{p'u''} = \frac{\gamma-1}{\gamma}\bar{\rho}\widetilde{h''u''} - \bar{p}\overline{u''} \tag{A.53}$$

$$\nabla\cdot\overline{p'u''} = \frac{\gamma-1}{\gamma}\nabla\cdot\bar{\rho}\widetilde{h''u''} - \bar{p}\nabla\cdot\overline{u''} - \overline{u''}\cdot\nabla\bar{p}. \tag{A.54}$$

Rearranging the above result to mimic terms within (A.49)

$$-\overline{u''}\cdot\nabla\bar{p} - \nabla\cdot\overline{p'u''} = \bar{p}\nabla\cdot\overline{u''} - \frac{\gamma-1}{\gamma}\nabla\cdot\bar{\rho}\widetilde{h''u''} \tag{A.55}$$

allows trading an occurrence of $\overline{p'u''}$ for the Reynolds heat flux in the k equation:

$$\frac{\partial}{\partial t}\bar{\rho}k = -\nabla\cdot\bar{\rho}k\tilde{u} - \bar{\rho}\widetilde{u''\otimes u''} : \nabla\tilde{u} - \bar{\rho}\epsilon + \nabla\cdot\left(-\frac{1}{2}\bar{\rho}\widetilde{u''^2u''} + \overline{\tau u''}\right) + \bar{p}\nabla\cdot\overline{u''} - \frac{\gamma-1}{\gamma}\nabla\cdot\bar{\rho}\widetilde{h''u''} + \overline{p'\nabla\cdot u''} + \overline{f\cdot u''} + \overline{\mathscr{S}_{\rho u}\cdot u''}. \tag{A.56}$$

The trade reduces by one the number of correlations appearing in the k equation which do not appear in the mean continuity, momentum, or energy equations. It also encourages thermodynamic consistency when working with pressure correlation information.

Returning to the constitutive relations, combining (A.22) and (A.24),

$$\tau = 2\mu S + \alpha\mu(\nabla\cdot u)I. \tag{A.57}$$

Using the kinematic viscosity and averaging,

$$\tilde{S} = \frac{1}{2}\left(\widetilde{\nabla u} + \widetilde{\nabla u}^{\mathsf{T}}\right) - \frac{1}{3}\left(\widetilde{\nabla\cdot u}\right)I \tag{A.58}$$

$$\bar{\tau} = 2\bar{\mu}\tilde{S} + 2\bar{\rho}\,\widetilde{\nu''S''} + \alpha\bar{\mu}\widetilde{\nabla\cdot u}I + \alpha\bar{\rho}\,\widetilde{\nu''(\nabla\cdot u)''}I. \tag{A.59}$$

By (A.41), $\widetilde{\nu''(\nabla\cdot u)''}$ may also be written $\widetilde{\nu''\nabla\cdot u''}$ while $\widetilde{\nu''S''}$ is equivalent to a version using the deviatoric part of the strain rate of the fluctuating velocity field. Many FANS closure approximations neglect correlations between the kinematic viscosity and velocity derivatives. Many assume $\alpha = 0$. Accepting those approximations would eliminate the second through fourth terms in $\bar{\tau}$. Making the ubiquitous closure approximations $\widetilde{\nabla u} + \widetilde{\nabla u}^{\mathsf{T}} \approx \nabla\tilde{u} + \nabla\tilde{u}^{\mathsf{T}}$ and $\widetilde{\nabla\cdot u} \approx \nabla\cdot\tilde{u}$ are equivalent to neglecting $\widetilde{\nabla u''} + \widetilde{\nabla u''}^{\mathsf{T}}$ and $\widetilde{\nabla\cdot u''}$ per (A.39).

To find $\bar{q}_s$, combine (A.27) and the assumption of a constant Prandtl number

$$q_s = -\kappa\nabla T = -\frac{\kappa}{C_p}\nabla h = -\frac{\mu}{\mathrm{Pr}}\nabla h \tag{A.60}$$

and again employ the kinematic viscosity when averaging to obtain

$$\bar{q}_s = -\frac{1}{\mathrm{Pr}}\left(\bar{\mu}\widetilde{\nabla h} + \bar{\rho}\,\widetilde{\nu''(\nabla h)''}\right). \tag{A.61}$$

Again, by (A.41), $\widetilde{\nu''(\nabla h)''}$ may also be written $\widetilde{\nu''\nabla h''}$. Again, making the ubiquitous closure assumption $\widetilde{\nabla h} \approx \nabla\tilde{h}$ is equivalent to neglecting $\widetilde{\nabla h''}$ per (A.39). Straightforward averaging applied to (A.25) produces

$$\bar{\rho}\,\tilde{\nu} = \bar{\mu} = \mu_0\overline{\left(\frac{T}{T_0}\right)^{\beta}} \tag{A.62}$$

which is not computable given only Favre-averaged state. One commonly accepted simplification, not employed in the present work, is taking $\overline{\mu(T)} \approx \mu\left(\tilde{T}\right)$.

A.2.3 Dimensional Summary

The dimensional Favre-averaged Navier–Stokes equations of interest are:

$$\frac{\partial}{\partial t}\bar{\rho} = -\nabla\cdot\bar{\rho}\tilde{u} + \overline{\mathscr{S}_\rho} \tag{A.63a}$$

$$\frac{\partial}{\partial t}\bar{\rho}\tilde{u} = -\nabla\cdot(\tilde{u}\otimes\bar{\rho}\tilde{u}) - \nabla\bar{p} + \nabla\cdot\left(\bar{\tau} - \bar{\rho}\widetilde{u''\otimes u''}\right) + \bar{f} + \overline{\mathscr{S}_{\rho u}} \tag{A.63b}$$

$$\begin{aligned}\frac{\partial}{\partial t}\bar{\rho}\tilde{E} = &-\nabla\cdot\bar{\rho}\tilde{H}\tilde{u} + \nabla\cdot\left(\left(\bar{\tau} - \bar{\rho}\widetilde{u''\otimes u''}\right)\tilde{u} - \frac{1}{2}\bar{\rho}\widetilde{u''^2u''} + \overline{\tau u''}\right)\\ &-\nabla\cdot\left(\bar{q}_s + \bar{\rho}\widetilde{h''u''}\right) + \bar{f}\cdot\tilde{u} + \overline{f\cdot u''} + \bar{q}_b + \overline{\mathscr{S}_{\rho E}}\end{aligned} \tag{A.63c}$$

$$\begin{aligned}\frac{\partial}{\partial t}\bar{\rho}k = &-\nabla\cdot\bar{\rho}k\tilde{u} - \bar{\rho}\widetilde{u''\otimes u''} : \nabla\tilde{u} - \bar{\rho}\epsilon + \nabla\cdot\left(-\frac{1}{2}\bar{\rho}\widetilde{u''^2u''} + \overline{\tau u''}\right)\\ &+\bar{p}\nabla\cdot\overline{u''} - \frac{\gamma-1}{\gamma}\nabla\cdot\bar{\rho}\widetilde{h''u''} + \overline{p'\nabla\cdot u''} + \overline{f\cdot u''} + \overline{\mathscr{S}_{\rho u}\cdot u''}.\end{aligned} \tag{A.63d}$$

The equations are augmented by the following relationships:

$$\bar{p} = \bar{\rho}R\tilde{T} \qquad \bar{\rho}\,\tilde{\nu} = \bar{\mu} = \mu_0\overline{\left(\frac{T}{T_0}\right)^{\beta}} \qquad k = \frac{1}{2}\widetilde{u''^2} \qquad \bar{\rho}\epsilon = \overline{\tau : \nabla u''} \tag{A.63e}$$

$$\tilde{E} = \frac{R}{\gamma - 1}\tilde{T} + \frac{1}{2}\tilde{u}^2 + k \qquad \tilde{H} = \tilde{E} + R\tilde{T} \qquad \tilde{h} = \frac{\gamma R \tilde{T}}{\gamma - 1} \tag{A.63f}$$

$$\bar{q}_s = -\frac{1}{\mathrm{Pr}}\left(\bar{\mu}\widetilde{\nabla h} + \bar{\rho}\,\widetilde{v''(\nabla h)''}\right) \tag{A.63g}$$

$$\tilde{S} = \frac{1}{2}\left(\widetilde{\nabla u} + \widetilde{\nabla u}^{\mathsf{T}}\right) - \frac{1}{3}\left(\widetilde{\nabla \cdot u}\right) I \tag{A.63h}$$

$$\bar{\tau} = 2\bar{\mu}\tilde{S} + 2\bar{\rho}\,\widetilde{v''S''} + \alpha\bar{\mu}\widetilde{\nabla \cdot u} I + \alpha\bar{\rho}\,\widetilde{v''(\nabla \cdot u)''} I. \tag{A.63i}$$

Appropriately nondimensionalized, this system of equations produces the formulation shown in Section 3.2.

A.3 The Spatiotemporal Homogenization Approximation

For completeness, this section documents the as yet unpublished spatiotemporal homogenization approximation for the compressible Navier–Stokes equations created by Topalian et al. [165]. It appears here to preserve the state of the slow growth formulation as used by this dissertation. The homogenization approach communicated below may differ from the form ultimately published.

A.3.1 Requirements for a Tensor-Consistent Formulation

We derive the form that the slow growth sources can take that allows exact computation of the sources within the slow growth Reynolds-averaged Navier–Stokes (RANS) mean flow and mean turbulent kinetic energy equations, and that preserves the tensor-consistent property of the velocity field and, by extension, of the Reynolds stresses. The first two requirements ensure that uncertainty quantification studies from the data will not be hampered by modeling the slow growth sources to close the RANS

equations, and the last one maintains an important property of the turbulent velocity field.

We start by recognizing that for any conserved flow variable ρq the slow growth equations that describe its time evolution may take the form

$$\frac{\partial}{\partial t_f}\rho q + \mathscr{N}_{\rho q} = \mathscr{S}_{\rho q} \tag{A.64}$$

where $\frac{\partial}{\partial t_f}\rho q$ is the "fast" time derivative, $\mathscr{N}_{\rho q}$ is the spatial operator from Navier–Stokes, and $\mathscr{S}_{\rho q}$ is the slow growth source.

Assume that the slow growth evolution for any primitive variable has a similar form. In particular, for density and for any variable q

$$\frac{\partial \rho}{\partial t_f} + \mathscr{N}_\rho = \mathscr{S}_\rho, \tag{A.65}$$

$$\frac{\partial q}{\partial t_f} + \mathscr{N}_q = \mathscr{S}_q. \tag{A.66}$$

From the equations above we can obtain an evolution equation for conserved variables ρq as

$$\underbrace{q\frac{\partial \rho}{\partial t_f} + \rho\frac{\partial q}{\partial t_f}}_{\frac{\partial}{\partial t_f}\rho q} + \underbrace{q\mathscr{N}_\rho + \rho\mathscr{N}_q}_{\mathscr{N}_{\rho q}} = \underbrace{q\mathscr{S}_\rho + \rho\mathscr{S}_q}_{\mathscr{S}_{\rho q}}. \tag{A.67}$$

The flow variables on the RANS equations are closed exactly if we obtain closed expression for the mean of the slow growth sources. As is shown below, this condition is satisfied by having sources of the form

$$\mathscr{S}_\rho = \rho f_\rho, \tag{A.68}$$

$$\mathscr{S}_q = g_q + q'' h_q \tag{A.69}$$

where f, g, and h are functions of the Favre averages of conserved variables, and hence are computable during solution of the RANS slow growth. By taking the mean of the slow growth sources for the conserved flow variables we obtain

$$\overline{\mathscr{S}_\rho} = \overline{\rho} f_\rho,$$
$$\overline{\mathscr{S}_{\rho q}} = \overline{q\mathscr{S}_\rho} + \overline{\rho\mathscr{S}_q} = \overline{\rho q} f_\rho + \overline{\rho} g_q + \underbrace{\overline{\rho q''}}_{0} h_q,$$

which are computable during the solution of the RANS problem.

Note that the source form of $\mathscr{S}_q$ suggests a decomposition in terms on Favre mean and fluctuations of the primitive variables.

The requirement of tensor consistency of the velocity field is met if the velocity sources are the components of a vector. For (A.69), this condition is satisfied if the two terms on the rhs are vectors as well, which implies that g_{u_i} has to be a vector, and that h_{u_i} has to be a scalar since it is multiplied by the Favre fluctuation of the velocity component that corresponds to $\mathscr{S}_{u_i}$. Therefore, we consider from now on h_{u_i}=h_u. We will ensure during the modeling of these quantities that indeed these conditions are satisfied.

To analyze the requirement of closure of the k equations for RANS, we begin by deriving the slow growth equation of any Reynolds stress components. Any such component can be computed symbolically as

$$\begin{aligned} \underbrace{u_i'' u_j'' \frac{\partial}{\partial t_f}\rho + \rho u_i'' \frac{\partial}{\partial t_f} u_j'' + \rho u_j'' \frac{\partial}{\partial t_f} u_i''}_{\frac{\partial}{\partial t_f}\rho u_i'' u_j''} + \underbrace{u_i'' u_j'' \mathscr{N}_\rho + \rho u_i'' \mathscr{N}_{u_j} + \rho u_j'' \mathscr{N}_{u_i}}_{\mathscr{N}_{\rho u_i'' u_j''}} \\ = \underbrace{u_i'' u_j'' \mathscr{S}_\rho + \rho u_i'' \mathscr{S}_{u_j} + \rho u_j'' \mathscr{S}_{u_i}}_{\mathscr{S}_{\rho u_i'' u_j''}}. \end{aligned} \tag{A.70}$$

where it was considered that the fast time derivative of the Favre mean of the velocity components is zero, and hence, $\frac{\partial u_j}{\partial t_f}=\frac{\partial u_j''}{\partial t_f}$. The Reynolds average of the slow growth sources is given in this case by

$$\begin{aligned}\overline{\mathscr{S}_{\rho u_i'' u_j''}} &= \overline{u_i'' u_j'' \mathscr{S}_\rho} + \overline{\rho u_i'' \mathscr{S}_{u_j''}} + \overline{\rho u_j'' \mathscr{S}_{u_i''}} \\ &= \overline{u_i'' u_j'' \rho f_\rho} + \overline{\rho u_i'' g_{u_j}} + \overline{\rho u_i'' u_j'' h_{u_j}} + \overline{\rho u_j'' g_{u_i}} + \overline{\rho u_i'' u_j'' h_{u_i}} \\ &= \overline{\rho u_i'' u_j''} f_\rho + \overline{\rho u_i'' u_j''} h_{u_j} + \overline{\rho u_i'' u_j''} h_{u_i} \end{aligned} \tag{A.71}$$

The slow growth turbulent kinetic energy equation can be computed from the Reynolds stress equations, by considering that $\rho k=\frac{1}{2}\rho u_k'' u_k''$. Then,

$$\underbrace{\frac{1}{2}\frac{\partial}{\partial t}\rho u_i'' u_i''}_{\frac{\partial}{\partial t}\rho k} + \underbrace{\frac{1}{2}\mathscr{N}_{\rho u_i'' u_i''}}_{\mathscr{N}_{\rho k}} = \underbrace{\frac{1}{2}\mathscr{S}_{\rho u_i'' u_i''}}_{\mathscr{S}_{\rho k}}. \tag{A.72}$$

Hence, the slow growth RANS source results in

$$\begin{aligned}\overline{\mathscr{S}_{\rho k}} &= \frac{1}{2}\overline{\rho u_i'' u_i''} f_\rho + \frac{1}{2} 2 \overline{\rho u_i'' u_i''} h_u, \\ &= \overline{\rho} k f_\rho + 2\overline{\rho} k h_u, \end{aligned} \tag{A.73}$$

which is computable during a RANS solution if an equation for k is available in the RANS model.

A.3.2 Multiscale Expansion

For the homogenization of the time variable, consider the decomposition of any flow variable $q \in \{u_i, E\}$ into Favre mean and fluctuation components

$$q(x,y,z,t) = \widetilde{q}(y,t_s) + \underbrace{A_q(y,t_s)\, q_p''\big(x,y,z,t_f\big)}_{q''\left(x,y,z,t_f,t_s\right)}, \tag{A.74}$$

where $\widetilde{q}$ is the Favre mean, q'' is the Favre fluctuation, A_q is a normalization function and q_p'' are normalized Favre turbulent fluctuations. We assume that the mean and normalization functions depend on the slow time variable $t_s = \epsilon t$, where ϵ is a small parameter ($\epsilon \ll 1$), while the normalized turbulent fluctuations are a function of the fast time variable $t_f = t$. For density, we consider an analogous decomposition into Reynolds mean and fluctuations as

$$\rho(x,y,z,t) = \overline{\rho}(y,t_s) + \underbrace{A_\rho(y,t_s)\,\rho_p'\big(x,y,z,t_f\big)}_{\rho'\left(x,y,z,t_f,t_s\right)}. \tag{A.75}$$

Using the chain rule to decompose the time derivative into slow and fast terms, and considering the decomposition into mean and fluctuations components (A.74), the time derivative of any q can be expressed as

$$\begin{aligned} \frac{\partial q}{\partial t} &= \frac{\partial q}{\partial t_f} + \epsilon\left(\frac{\partial \widetilde{q}}{\partial t_s} + \frac{\partial q''}{\partial t_s}\right), \\ &= \frac{\partial q}{\partial t_f} + \epsilon\left(\frac{\partial \widetilde{q}}{\partial t_s} + \frac{q''}{A_q}\frac{\partial A_q}{\partial t_s}\right). \end{aligned} \tag{A.76}$$

If we specialize the terms in slow time derivative for a specific value of slow time, the equations describe the evolution of the flow in the fast time scale only, that is, the normalized turbulent fluctuations. This also implies that the mean and the RMS profiles remain unchanged (since they are only dependent on the slow time scale and the wall-normal direction). Therefore, this set of equations can be used to characterize the turbulent flow at a specific stage in its slow time evolution, and this can be done with the aid of direct numerical simulations (DNS). The challenge now is to model the slow derivatives of the flow variables at the chosen slow time.

A.3.3 Modeling the Slow Time Derivatives

For modeling the slow derivatives, we initially express the mean field of any flow variable q as the sum of an inviscid (I) and a defect (D) field components,

$$\widetilde{q}(t_s, y) = q_I(t_s, y) + \widetilde{q}_D(t_s, y), \tag{A.77}$$

with slow derivative

$$\frac{\partial \widetilde{q}}{\partial t_s} = \frac{\partial q_I}{\partial t_s} + \frac{\partial \widetilde{q}_D}{\partial t_s}, \tag{A.78}$$

We assume that the inviscid part is known, it satisfies the Euler equations, and it corresponds to the inviscid flow field found above the boundary layer.

We consider the transformation (t_s, y) to $(t_{s'}, \eta)$ with $t_{s'}{=}t_s$, and $\eta{=}\frac{y}{\Delta(t_s)}$, where Δ is a characteristic length in the boundary layer. The Jacobian of this transformation is

$$\begin{pmatrix} \left(\frac{\partial}{\partial t_s}\right)_y \\ \left(\frac{\partial}{\partial y}\right)_{t_s} \end{pmatrix} = \begin{pmatrix} 1 & -\frac{y}{\Delta^2}\frac{\partial \Delta}{\partial t_s} \\ 0 & \frac{1}{\Delta} \end{pmatrix} \begin{pmatrix} \left(\frac{\partial}{\partial t_{s'}}\right)_\eta \\ \left(\frac{\partial}{\partial \eta}\right)_{t_{s'}} \end{pmatrix} \tag{A.79}$$

To model the slow time derivatives, we assume that the mean defect profile and the normalization function evolve self-similarly in time so that any flow variable q can be written as

$$\widetilde{q}_D(t_s, y) = \widetilde{q}_D^A(t_{s'})\, F_q(\eta), \tag{A.80}$$

$$A_q(t_s, y) = A_q^A(t_{s'})\, G_q(\eta), \tag{A.81}$$

where the superindex A refers to the function amplitude. The function amplitudes $\widetilde{q}_D^A$ and A_q^A are dependent on slow time. We considered the self-similar variable η to be

given by,

$$\eta = \frac{y}{\Delta(t_s)}, \tag{A.82}$$

with Δ a characteristic length related with the boundary layer. Using the chain rule the derivatives with respect to t_s and y can now be computed as

$$\frac{\partial}{\partial t_s} = \frac{\partial}{\partial t_{s'}}\frac{\partial t_{s'}}{\partial t_s} + \frac{\partial}{\partial \eta}\frac{\partial \eta}{\partial t_s} = \frac{\partial}{\partial t_{s'}} - \left(\frac{y}{\Delta^2}\frac{\partial \Delta}{\partial t_s}\right)\frac{\partial}{\partial \eta}, \tag{A.83}$$

$$\frac{\partial}{\partial y} = \frac{\partial}{\partial t_{s'}}\frac{\partial t_{s'}}{\partial y} + \frac{\partial}{\partial \eta}\frac{\partial \eta}{\partial y} = \left(\frac{1}{\Delta}\right)\frac{\partial}{\partial \eta}. \tag{A.84}$$

Applying the expression for the slow time derivative (A.83) to the self similar mean (A.80) we get

$$\frac{\partial \widetilde{q}_D}{\partial t_s} = \frac{\partial \widetilde{q}_D^A}{\partial t_{s'}} F_q - \left(\frac{y}{\Delta^2}\frac{\partial \Delta}{\partial t_s}\right)\frac{\partial \widetilde{q}_D}{\partial \eta}. \tag{A.85}$$

Substituting (A.80) and (A.84) in the first and second term of the right hand side respectively, we get an expression of the slow growth derivative in terms of (t_s, y),

$$\frac{\partial \widetilde{q}_D}{\partial t_s} = \frac{\widetilde{q}_D}{\widetilde{q}_D^A}\frac{\partial \widetilde{q}_D^A}{\partial t_s} - \left(\frac{y}{\Delta}\frac{\partial \Delta}{\partial t_s}\right)\frac{\partial \widetilde{q}_D}{\partial y}. \tag{A.86}$$

Therefore,

$$-\epsilon\frac{\partial \widetilde{q}_D}{\partial t_s} = -\widetilde{q}_D\left(\frac{\epsilon}{\widetilde{q}_D^A}\frac{\partial \widetilde{q}_D^A}{\partial t_s}\right) + y\left(\frac{\epsilon}{\Delta}\frac{\partial \Delta}{\partial t_s}\right)\left(\frac{\partial \widetilde{q}_D}{\partial y}\right) \tag{A.87}$$

where now the defect mean is expressed in terms of the boundary layer mean and the inviscid mean.

Finally, the slow derivative of $\widetilde{q}$ becomes

$$\begin{aligned} -\epsilon\frac{\partial \widetilde{q}}{\partial t_s} &= -\epsilon\frac{\partial q_I}{\partial t_s} - \epsilon\frac{\partial \widetilde{q}_D}{\partial t_s} \\ &= -\frac{\partial q_I}{\partial t} - \widetilde{q}_D\left(\frac{\epsilon}{\widetilde{q}_D^A}\frac{\partial \widetilde{q}_D^A}{\partial t_s}\right) + y\left(\frac{\epsilon}{\Delta}\frac{\partial \Delta}{\partial t_s}\right)\left(\frac{\partial \widetilde{q}_D}{\partial y}\right) \end{aligned} \tag{A.88}$$

Similarly, for the Favre fluctuations, the slow derivative term becomes

$$-\epsilon\frac{\partial q''}{\partial t_s} = -q''\left(\frac{\epsilon}{A_q^A}\frac{\partial A_q^A}{\partial t_s}\right) + q'' y\left(\frac{\epsilon}{\Delta}\frac{\partial \Delta}{\partial t_s}\right)\frac{1}{A_q}\frac{\partial A_q}{\partial y} \tag{A.89}$$

We obtain the slow growth source for q by specializing the slow time derivative terms at a specific instant in slow time, $t_s{=}t_0$. In particular, the factor in parenthesis in these equations represents the logarithmic growth rate in slow time of any quantity f,

$$\mathrm{gr}_{t_0}(f) = \left(\frac{\epsilon}{f}\frac{\partial f}{\partial t_s}\right)_{t_s=t_0}. \tag{A.90}$$

Furthermore, the derivatives with respect to the slow time scale can be expressed with respect to the original time variable considering that $\frac{\partial}{\partial t_s}{=}\frac{1}{\epsilon}\frac{\partial}{\partial t}$ for functions that depend only on slow time. Therefore, the equation for slow growth source for q takes the form

$$\begin{aligned}\mathscr{S}_q = (q)_{t_0} = &\underbrace{-\frac{\partial q_I}{\partial t} - \widetilde{q}_D\,\mathrm{gr}_{t_0}\left(\widetilde{q}_D^A\right) + y\,\mathrm{gr}_{t_0}(\Delta)\,\frac{\partial \widetilde{q}_D}{\partial y}}_{g_q} \\ &+ q''\underbrace{\left(-\mathrm{gr}_{t_0}\left(A_q^A\right) + y\,\mathrm{gr}_{t_0}(\Delta)\,\frac{1}{A_q}\frac{\partial A_q}{\partial y}\right)}_{h_q}.\end{aligned} \tag{A.91}$$

where we introduced the notation $()_{t_0}{=}\left(-\epsilon\frac{\partial}{\partial t_s}\right)_{t_s=t_0}$, and where it is seen that the source complies with the form outlined in (A.69). This source expression applies to the velocity components u_i, and to the specific total energy E. We model next the normalization function A_q for each of these variables. For velocity, on one hand, the A_{u_i} is related to the RMS of the fluctuations of u_i. On the other hand, for the consistent formulation, it is required that the bracket h_u to be computable during a RANS simulation, since it may need to be used for slow growth source of the turbulent kinetic energy (A.73).

Furthermore, it has to be such that the slow growth formulation retains the tensor consistency property of the Reynold stresses. These requirements can be met if we model $A_u = \sqrt{2k} = \sqrt{\widetilde{u_k'' u_k''}}$. The normalization function for specific total energy can be modeled analogously as $A_E = \sqrt{\widetilde{E'' E''}}$.

For density, starting from (A.75), we can follow similar steps to reach

$$
\begin{aligned}
(\rho)_{t_0} &= (\overline{\rho})_{t_0} + (\rho')_{t_0} \\
&= -\frac{\partial \rho_I}{\partial t} - (\overline{\rho} - \rho_I)\ \mathrm{gr}_{t_0}\left(\overline{\rho}_D^A\right) + y\ \mathrm{gr}_{t_0}(\Delta)\left[\frac{\partial(\overline{\rho} - \rho_I)}{\partial y}\right] \\
&\quad - \rho'\ \mathrm{gr}_{t_0}\left(A_\rho^A\right) + \rho' y\ \mathrm{gr}_{t_0}(\Delta)\left[\frac{1}{A_\rho}\frac{\partial A_\rho}{\partial y}\right] \\
&= -\frac{\partial \rho_I}{\partial t} + \rho_I\ \mathrm{gr}_{t_0}\left(\overline{\rho}_D^A\right) - y\ \mathrm{gr}_{t_0}(\Delta)\frac{\partial \rho_I}{\partial y} \\
&\quad - \overline{\rho}\ \mathrm{gr}_{t_0}\left(\overline{\rho}_D^A\right) - \rho'\ \mathrm{gr}_{t_0}\left(A_\rho^A\right) + y\ \mathrm{gr}_{t_0}(\Delta)\left[\frac{\partial \overline{\rho}}{\partial y} + \frac{\rho'}{A_\rho}\frac{\partial A_\rho}{\partial y}\right].
\end{aligned}
$$

It is seen that this model for the slow growth source of density does not have the form required by (A.68). To satisfy this requirement, we modify this expression and make some parameter choices as follows. First we scale the first three terms, that involve quantities of the base flow field, by $\frac{\rho}{\overline{\rho}}$. This is equivalent to including additional source terms that scale with the density fluctuations, ρ'. Second, we require the amplitude growth rate parameters to be equal, this is, $\mathrm{gr}_{t_0}\left(\overline{\rho}_D^A\right) = \mathrm{gr}_{t_0}\left(A_\rho^A\right)$. And third, we choose $A_\rho = \overline{\rho}$. With these modifications, the slow growth source becomes

$$
\begin{aligned}
\mathscr{S}_\rho = (\rho)_{t_0} &= \frac{\rho}{\overline{\rho}}\left(-\frac{\partial \rho_I}{\partial t} + \rho_I\ \mathrm{gr}_{t_0}\left(\overline{\rho}_D^A\right) - y\ \mathrm{gr}_{t_0}(\Delta)\frac{\partial \rho_I}{\partial y}\right) \\
&\quad - \rho\ \mathrm{gr}_{t_0}\left(\overline{\rho}_D^A\right) + y\ \mathrm{gr}_{t_0}(\Delta)\frac{\rho}{\overline{\rho}}\frac{\partial \overline{\rho}}{\partial y} \\
&= \rho\ \underbrace{\frac{1}{\overline{\rho}}\left(-\frac{\partial \rho_I}{\partial t} - \overline{\rho}_D\ \mathrm{gr}_{t_0}\left(\overline{\rho}_D^A\right) + y\ \mathrm{gr}_{t_0}(\Delta)\frac{\partial \overline{\rho}_D}{\partial y}\right)}_{f_\rho},
\end{aligned}
\tag{A.92}
$$

and hence it reduces to the source form in (A.68).

A.3.4 A Spatiotemporal Model

In favorable pressure gradient scenarios, the temporal model produces boundary layer profiles that differ qualitatively from those of the spatial slow growth formulation, even for laminar flows. The main challenge is to construct a temporal model with volumetric sources, where the final solution resembles the one obtained from a spatially evolving flow. A way to overcome this shortcoming, while still maintaining a temporal formulation for the slow growth fluctuations, is to choose volumetric source terms that not only balance the inviscid temporal equation, maintaining the flow profiles at the chosen station, but also makes the mean profiles resemble the ones obtained from spatial slow growth. This is accomplished by setting:

$$(\dot{\overline{\rho}}) = \mathscr{S}_{\overline{\rho},x} - \mathscr{S}_{\overline{\rho},t}, \tag{A.93}$$

$$(\dot{\overline{\rho u_i}}) = \mathscr{S}_{\overline{\rho u_i},x} - \mathscr{S}_{\overline{\rho u_i},t}, \tag{A.94}$$

$$(\dot{\overline{\rho E}}) = \mathscr{S}_{\overline{\rho E},x} - \mathscr{S}_{\overline{\rho E},t}, \tag{A.95}$$

where $(\dot{f})$ is a volumetric source field added to the flow equation for f, and $\mathscr{S}_{,t}$ and $\mathscr{S}_{,x}$ are the slow growth sources for the temporal and spatial formulations, respectively.

To construct the spatiotemporal formulation, we include volumetric sources in the temporal formulation, such that the mean flow behaves as a homogenized spatially evolving flow. This property makes the formulation very convenient to characterize scenarios with various pressure gradients. To maintain the properties of tensor consistency and closure for RANS, we need for the volumetric sources to comply as well

with the requirements of equations (A.68–A.69).

The volumetric sources are modeled for the Navier–Stokes equations in terms of primitive variables. The time and streamwise varying Favre averaged terms are

$$\frac{\partial \overline{\rho}}{\partial t} + \widetilde{u}_i \frac{\partial \overline{\rho}}{\partial x_i} + \overline{\rho} \frac{\partial \widetilde{u}_i}{\partial x_i} = 0, \tag{A.96}$$

$$\frac{\partial \widetilde{u}_i}{\partial t} + \widetilde{u}_j \frac{\partial \widetilde{u}_i}{\partial x_j} + \frac{1}{\overline{\rho}} \frac{\partial \overline{p}}{\partial x_i} = \mathrm{Visc}_{u_i} + \mathrm{Turb}_{u_i}, \tag{A.97}$$

$$\frac{\partial \widetilde{E}}{\partial t} + \widetilde{u}_j \frac{\partial \widetilde{E}}{\partial x_j} + \frac{\overline{p}}{\overline{\rho}} \frac{\partial \widetilde{u}_j}{\partial x_j} + \frac{\widetilde{u}_j}{\overline{\rho}} \frac{\partial \overline{p}}{\partial x_j} = \mathrm{Visc}_E + \mathrm{Turb}_E. \tag{A.98}$$

For a statistically steady, spatially evolving boundary layer, the time derivative terms are zero. A slow growth homogenization of the equations above would produce, for the mean part of the solution, sources of the form

$$\mathscr{S}_{\overline{\rho},x} = \widetilde{u} \left(\overline{\rho}\right)_{x_0} + \overline{\rho} \left(\widetilde{u}\right)_{x_0}, \tag{A.99}$$

$$\mathscr{S}_{\widetilde{u}_i,x} = \widetilde{u} \left(\widetilde{u}_i\right)_{x_0} + \frac{1}{\overline{\rho}} \left(\overline{p}\right)_{x_0} \delta_{ix}, \tag{A.100}$$

$$\mathscr{S}_{\widetilde{E},x} = \widetilde{u} \left(\widetilde{E}\right)_{x_0} + \frac{\overline{p}}{\overline{\rho}} \left(\widetilde{u}\right)_{x_0} + \frac{\widetilde{u}}{\overline{\rho}} \left(\overline{p}\right)_{x_0} \tag{A.101}$$

where we introduced the notation $()_{x_0} = \left(-\epsilon \frac{\partial}{\partial x_s}\right)_{x_s = x_0}$, analogous to $()_{t_0} = \left(-\epsilon \frac{\partial}{\partial t_s}\right)_{t_s = t_0}$ defined earlier.

We propose that the slow growth sources of primitive variables for the spatiotemporal formulation be defined by

$$\mathscr{S}_{\rho,xt} = \underbrace{\left(\dot{\rho}\right)}_{\mathscr{S}_{\overline{\rho},x} - \mathscr{S}_{\overline{\rho},t}} + \underbrace{\mathscr{S}_{\rho,t}}_{\mathscr{S}_{\overline{\rho},t} + \mathscr{S}_{\rho',t}} = \mathscr{S}_{\overline{\rho},x} + \mathscr{S}_{\rho',t}, \tag{A.102}$$

$$\mathscr{S}_{q,xt} = \underbrace{\left(\dot{q}\right)}_{\mathscr{S}_{q,x} - \mathscr{S}_{q,t}} + \underbrace{\mathscr{S}_{q,t}}_{\mathscr{S}_{q,t} + \mathscr{S}_{q'',t}} = \mathscr{S}_{q,x} + \mathscr{S}_{q'',t} \tag{A.103}$$

with $\mathscr{S}_{,xt}$ the sources for the spatiotemporal model.

Density: The slow spatial derivative of mean density is given by

$$(\overline{\rho})_{x_0} = \left(-\frac{\partial \rho_I}{\partial x} - \overline{\rho}_D \, \mathrm{gr}_{x_0}\left(\overline{\rho}_D^A\right) + y \, \mathrm{gr}_{x_0}(\Delta) \frac{\partial \overline{\rho}_D}{\partial y} \right), \tag{A.104}$$

whereas the time derivative of the fluctuations part of the temporal model was given by

$$(\rho')_{t_0} = \frac{\rho'}{\overline{\rho}} \left(-\frac{\partial \rho_I}{\partial t} - \overline{\rho}_D \, \mathrm{gr}_{t_0}\left(\overline{\rho}_D^A\right) + y \, \mathrm{gr}_{t_0}(\Delta) \frac{\partial \overline{\rho}_D}{\partial y} \right). \tag{A.105}$$

Note that the addition of these two equations does not reduce to a source for ρ of the form $\mathscr{S}_{\rho,xt}{=}\rho f_\rho$, as proposed in (A.68). To overcome this issue, we note that the desired source form can be obtained if we adopt a slow growth source of the form

$$\mathscr{S}_{\rho,xt} \equiv \mathscr{S}_{\rho,x} = \mathscr{S}_{\rho,t} + (\dot{\rho}) = \widetilde{u}\,(\rho)_{x_0} + \rho\,(\widetilde{u})_{x_0}\,, \tag{A.106}$$

with $(\rho)_{x_0}$ given by

$$(\rho)_{x_0} = \rho \underbrace{\frac{1}{\overline{\rho}} \left(-\frac{\partial \rho_I}{\partial x} - \overline{\rho}_D \, \mathrm{gr}_{x_0}\left(\overline{\rho}_D^A\right) + y \, \mathrm{gr}_{x_0}(\Delta) \frac{\partial \overline{\rho}_D}{\partial y} \right)}_{f_{\rho,x}}, \tag{A.107}$$

with the spatial growth rate of Δ defined as $\mathrm{gr}_{x_0}(\Delta){=}\frac{\mathrm{gr}_{t_0}(\Delta)}{u_{I,\mathrm{w}}}$, and with the w subindex indicating a wall quantity. The slow growth plus volumetric source of the spatiotemporal formulation for density can be written as

$$\begin{aligned} \mathscr{S}_{\rho,xt} &= \widetilde{u}\,(\rho)_{x_0} + \rho\,(\widetilde{u})_{x_0}\,, \\ &= \rho \underbrace{\left(\widetilde{u} f_{\rho,x} + (\widetilde{u})_{x_0}\right)}_{f_{\rho,xt}} \end{aligned} \tag{A.108}$$

Velocity: The spatial slow derivative of the Favre averaged velocity is modeled as

$$(\widetilde{u}_i)_{x_0} = -\frac{\partial u_{i,I}}{\partial x} - \widetilde{u}_{i,D} \, \mathrm{gr}_{x_0}\left(\widetilde{u}_{i,D}^A\right) + y \, \mathrm{gr}_{x_0}(\Delta) \frac{\partial \widetilde{u}_{i,D}}{\partial y}, \tag{A.109}$$

and for mean pressure,

$$(\overline{p})_{x_0} = -\frac{\partial p_I}{\partial x} - \overline{p}_D \, \mathrm{gr}_{x_0}\left(\overline{p}_D^A\right) + y \, \mathrm{gr}_{x_0}(\Delta) \frac{\partial \overline{p}_D}{\partial y}. \tag{A.110}$$

The slow growth plus volumetric source for velocity then becomes,

$$\mathscr{S}_{u_i,xt} = \mathscr{S}_{\widetilde{u}_i,x} + \mathscr{S}_{u_i'',t} \tag{A.111}$$

$$= \underbrace{\widetilde{u}\,(\widetilde{u}_i)_{x_0} + \frac{1}{\overline{\rho}}(\overline{p})_{x_0}\,\delta_{ix}}_{g_{u_i,xt}} + u_i'' \underbrace{\left(-\mathrm{gr}_{t_0}\left(A_u^A\right) + y \, \mathrm{gr}_{t_0}(\Delta) \frac{1}{A_u}\frac{\partial A_u}{\partial y}\right)}_{h_{u_i,xt}}. \tag{A.112}$$

Energy: The spatial slow derivative of the Favre averaged velocity is modeled as

$$\left(\widetilde{E}\right)_{x_0} = -\frac{\partial E_I}{\partial x} - \widetilde{E}_D \, \mathrm{gr}_{x_0}\left(\widetilde{E}_D^A\right) + y \, \mathrm{gr}_{x_0}(\Delta) \frac{\partial \widetilde{E}_D}{\partial y}. \tag{A.113}$$

The slow growth plus volumetric source for energy then becomes,

$$\mathscr{S}_{E,xt} = \mathscr{S}_{\widetilde{E},x} + \mathscr{S}_{E'',t} \tag{A.114}$$

$$= \underbrace{\widetilde{u}\left(\widetilde{E}\right)_{x_0} + \frac{\overline{p}}{\overline{\rho}}(\widetilde{u})_{x_0} + \frac{\widetilde{u}}{\overline{\rho}}(\overline{p})_{x_0}}_{g_{E,xt}} + E'' \underbrace{\left(-\mathrm{gr}_{t_0}\left(A_E^A\right) + y \, \mathrm{gr}_{t_0}(\Delta) \frac{1}{A_E}\frac{\partial A_E}{\partial y}\right)}_{h_{E,xt}}. \tag{A.115}$$

A.3.5 Dimensional Summary

In summary, the slow growth sources are modeled as

$$\mathscr{S}_{\rho,xt} = \widetilde{u}\,(\rho)_{x_0} + \rho\,(\widetilde{u})_{x_0}, \tag{A.116a}$$

$$\mathscr{S}_{u_i,xt} = \widetilde{u}\,(\widetilde{u}_i)_{x_0} + \frac{1}{\overline{\rho}}(\overline{p})_{x_0}\,\delta_{ix} + \left(u_i''\right)_{t_0}, \tag{A.116b}$$

$$\mathscr{S}_{E,xt} = \widetilde{u}\left(\widetilde{E}\right)_{x_0} + \frac{\overline{p}}{\overline{\rho}}(\widetilde{u})_{x_0} + \frac{\widetilde{u}}{\overline{\rho}}(\overline{p})_{x_0} + (E'')_{t_0}. \tag{A.116c}$$

with the slow spatial and temporal evolution factors modeled by

$$(\rho)_{x_0} = \frac{\rho}{\overline{\rho}}\left(-\frac{\partial \rho_I}{\partial x} - \overline{\rho}_D \,\mathrm{gr}_{x_0}\left(\overline{\rho}_D^A\right) + y\,\mathrm{gr}_{x_0}(\Delta)\frac{\partial \overline{\rho}_D}{\partial y}\right) \tag{A.117a}$$

$$(\widetilde{u}_i)_{x_0} = -\frac{\partial u_{i,I}}{\partial x} - \widetilde{u}_{i,D}\,\mathrm{gr}_{x_0}\left(\widetilde{u}_{i,D}^A\right) + y\,\mathrm{gr}_{x_0}(\Delta)\frac{\partial \widetilde{u}_{i,D}}{\partial y} \tag{A.117b}$$

$$(\overline{p})_{x_0} = -\frac{\partial p_I}{\partial x} - \overline{p}_D\,\mathrm{gr}_{x_0}\left(\overline{p}_D^A\right) + y\,\mathrm{gr}_{x_0}(\Delta)\frac{\partial \overline{p}_D}{\partial y} \tag{A.117c}$$

$$\left(\widetilde{E}\right)_{x_0} = -\frac{\partial E_I}{\partial x} - \widetilde{E}_D\,\mathrm{gr}_{x_0}\left(\widetilde{E}_D^A\right) + y\,\mathrm{gr}_{x_0}(\Delta)\frac{\partial \widetilde{E}_D}{\partial y} \tag{A.117d}$$

$$\left(u_i''\right)_{t_0} = u_i''\left(-\mathrm{gr}_{t_0}\left(A_u^A\right) + y\,\mathrm{gr}_{t_0}(\Delta)\frac{1}{A_u}\frac{\partial A_u}{\partial y}\right) \tag{A.117e}$$

$$\left(E''\right)_{t_0} = E''\left(-\mathrm{gr}_{t_0}\left(A_E^A\right) + y\,\mathrm{gr}_{t_0}(\Delta)\frac{1}{A_E}\frac{\partial A_E}{\partial y}\right) \tag{A.117f}$$

based on a steady base flow solution to the Euler equations. That is, primitive data

$$\rho_I \qquad\qquad u_{i,I} \qquad\qquad E_I \qquad\qquad p_I$$

defines instantaneous viscous flow defects

$$\overline{\rho}_D = \overline{\rho} - \rho_I \qquad \widetilde{u}_{i,D} = \widetilde{u}_i - u_{i,I} \qquad \widetilde{E}_D = \widetilde{E} - E_I \qquad \overline{p}_D = \overline{p} - p_I \tag{A.118}$$

as well as the spatial growth rate $\mathrm{gr}_{x_0}(\Delta) = \frac{\mathrm{gr}_{t_0}(\Delta)}{u_{I,\mathrm{w}}}$. Here, $u_{I,\mathrm{w}}$ is the inviscid base flow streamwise velocity at the wall. The normalization functions are modeled as

$$A_u = \sqrt{\widetilde{u_k'' u_k''}} \qquad\qquad A_E = \sqrt{\widetilde{E''E''}} \tag{A.119}$$

Appropriately nondimensionalized, these equations produce the form summarized in Section 3.3. With appropriate modeling of the amplitude growth rate parameters, also discussed there, these expressions constitute a closed system of equations that allows us to perform DNS using the spatiotemporal slow growth formulation.

Appendix B

A Manufactured Solution for the Governing Equations

A time-varying manufactured solution is presented for the nondimensional governing equations summarized in Section 3.1. That is, forcing terms Q_ρ, $\vec{Q}_{\rho u}$, and $Q_{\rho E}$ are added to the mass, momentum, total energy equations so that their solution matches a prescribed form. This particular manufactured solution is the nondimensional analogue of that presented in Ulerich et al. [170]. The solution was used to verify the software described in Chapter 5. Additional background on manufactured solutions can be found in Malaya et al. [99].

For $\phi \in \{\rho, u, v, w, T\}$ analytical solutions are selected with the form

$$
\begin{aligned}
\phi(x,y,z,t) = {} & a_{\phi 0} && \cos\left(f_{\phi 0}\ t + g_{\phi 0}\right) \\
& + a_{\phi x}\ \cos\left(b_{\phi x}\ 2\pi x L_x^{-1} + c_{\phi x}\right) && \cos\left(f_{\phi x}\ t + g_{\phi x}\right) \\
& + a_{\phi xy} \cos\left(b_{\phi xy} 2\pi x L_x^{-1} + c_{\phi xy}\right) \cos\left(d_{\phi xy} 2\pi y L_y^{-1} + e_{\phi xy}\right) && \cos\left(f_{\phi xy} t + g_{\phi xy}\right) \\
& + a_{\phi xz} \cos\left(b_{\phi xz} 2\pi x L_x^{-1} + c_{\phi xz}\right) \cos\left(d_{\phi xz} 2\pi z L_z^{-1} + e_{\phi xz}\right) && \cos\left(f_{\phi xz} t + g_{\phi xz}\right) \\
& + a_{\phi y}\ \cos\left(b_{\phi y}\ 2\pi y L_y^{-1} + c_{\phi y}\right) && \cos\left(f_{\phi y}\ t + g_{\phi y}\right) \\
& + a_{\phi yz} \cos\left(b_{\phi yz} 2\pi y L_y^{-1} + c_{\phi yz}\right) \cos\left(d_{\phi yz} 2\pi z L_z^{-1} + e_{\phi yz}\right) && \cos\left(f_{\phi yz} t + g_{\phi yz}\right) \\
& + a_{\phi z}\ \cos\left(b_{\phi z}\ 2\pi z L_z^{-1} + c_{\phi z}\right) && \cos\left(f_{\phi z}\ t + g_{\phi z}\right)
\end{aligned}
$$

where a, b, c, d, e, f, and g are constant coefficient collections indexed by ϕ and one

or more directions. To aid in providing reusable, physically realizable coefficients for Cartesian domains of arbitrary size, domain extents L_x, L_y, L_z have been introduced. Partial derivatives ϕ_t, ϕ_x, ϕ_y, ϕ_z, ϕ_{xx}, ϕ_{xy}, ϕ_{xz}, ϕ_{yy}, ϕ_{yz}, and ϕ_{zz} may be computed directly from the chosen solutions.

The above solutions are plugged into the model from Section 3.1 and solved for the forcing terms Q_ρ, $\vec{Q}_{\rho u}$, and $Q_{\rho E}$. However, solving for these complete terms entirely within the context of a computer algebra system causes an explosion of terms. As the fully expanded forcing terms are too large to be usable in any meaningful way, they are not shown. Instead, starting from the solution and its the analytic derivatives, basic calculus followed by algebraic operations performed in floating point are used to obtain the necessary forcing *at runtime*. Computing the forcing terms looks as follows:

```
# Assuming that we are given
#   rho rho_t rho_x rho_xx rho_xy rho_xz rho_y rho_yy rho_yz rho_z rho_zz
#   u   u_t   u_x   u_xx   u_xy   u_xz   u_y   u_yy   u_yz   u_z   u_zz
#   v   v_t   v_x   v_xx   v_xy   v_xz   v_y   v_yy   v_yz   v_z   v_zz
#   w   w_t   w_x   w_xx   w_xy   w_xz   w_y   w_yy   w_yz   w_z   w_zz
#   T   T_t   T_x   T_xx   T_xy   T_xz   T_y   T_yy   T_yz   T_z   T_zz
# and the coefficients
#   alpha beta gamma Ma Pr Re
# compute the source terms
#   Q_rho Q_rhou Q_rhov Q_rhow Q_rhoe
# necessary to force the solution rho, u, v, w, and T.

# Computations stemming from the constitutive relationships
e       = T   / gamma / (gamma - 1) + Ma * Ma * (u*u   + v*v   + w*w  ) / 2
e_x     = T_x / gamma / (gamma - 1) + Ma * Ma * (u*u_x + v*v_x + w*w_x)
e_y     = T_y / gamma / (gamma - 1) + Ma * Ma * (u*u_y + v*v_y + w*w_y)
e_z     = T_z / gamma / (gamma - 1) + Ma * Ma * (u*u_z + v*v_z + w*w_z)
e_t     = T_t / gamma / (gamma - 1) + Ma * Ma * (u*u_t + v*v_t + w*w_t)
p       = (rho   * T           ) / gamma
p_x     = (rho_x * T + rho * T_x) / gamma
p_y     = (rho_y * T + rho * T_y) / gamma
p_z     = (rho_z * T + rho * T_z) / gamma
mu      = pow(T, beta)
```

```
mu_x     = beta * pow(T, beta - 1) * T_x
mu_y     = beta * pow(T, beta - 1) * T_y
mu_z     = beta * pow(T, beta - 1) * T_z
lambda_  = (3 * alpha - 2) * mu    / 3 # "lambda" is a Python keyword
lambda_x = (3 * alpha - 2) * mu_x  / 3 # Strange order of operations allows...
lambda_y = (3 * alpha - 2) * mu_y  / 3 # ...arbitrary precision library to...
lambda_z = (3 * alpha - 2) * mu_z  / 3 # ...handle (alpha-2/3) factor correctly
qx       = - 1 / Re / Pr / (gamma - 1) *  mu   * T_x
qy       = - 1 / Re / Pr / (gamma - 1) *  mu   * T_y
qz       = - 1 / Re / Pr / (gamma - 1) *  mu   * T_z
qx_x     = - 1 / Re / Pr / (gamma - 1) * (mu_x * T_x + mu * T_xx)
qy_y     = - 1 / Re / Pr / (gamma - 1) * (mu_y * T_y + mu * T_yy)
qz_z     = - 1 / Re / Pr / (gamma - 1) * (mu_z * T_z + mu * T_zz)

# Computations stemming from the compressible, Newtonian fluid model
rhou     = rho * u
rhov     = rho * v
rhow     = rho * w
rhoe     = rho * e
rhou_x   = rho_x * u + rho * u_x
rhov_y   = rho_y * v + rho * v_y
rhow_z   = rho_z * w + rho * w_z
rhou_t   = rho_t * u + rho * u_t
rhov_t   = rho_t * v + rho * v_t
rhow_t   = rho_t * w + rho * w_t
rhoe_t   = rho_t * e + rho * e_t

rhouu_x = (rho_x * u * u) + (rho * u_x * u) + (rho * u * u_x)
rhouv_y = (rho_y * u * v) + (rho * u_y * v) + (rho * u * v_y)
rhouw_z = (rho_z * u * w) + (rho * u_z * w) + (rho * u * w_z)
rhouv_x = (rho_x * u * v) + (rho * u_x * v) + (rho * u * v_x)
rhovv_y = (rho_y * v * v) + (rho * v_y * v) + (rho * v * v_y)
rhovw_z = (rho_z * v * w) + (rho * v_z * w) + (rho * v * w_z)
rhouw_x = (rho_x * u * w) + (rho * u_x * w) + (rho * u * w_x)
rhovw_y = (rho_y * v * w) + (rho * v_y * w) + (rho * v * w_y)
rhoww_z = (rho_z * w * w) + (rho * w_z * w) + (rho * w * w_z)
rhoue_x = (rho_x * u * e) + (rho * u_x * e) + (rho * u * e_x)
rhove_y = (rho_y * v * e) + (rho * v_y * e) + (rho * v * e_y)
rhowe_z = (rho_z * w * e) + (rho * w_z * e) + (rho * w * e_z)

tauxx = mu * (u_x + u_x) + lambda_ * (u_x + v_y + w_z)
tauyy = mu * (v_y + v_y) + lambda_ * (u_x + v_y + w_z)
tauzz = mu * (w_z + w_z) + lambda_ * (u_x + v_y + w_z)
tauxy = mu * (u_y + v_x)
tauxz = mu * (u_z + w_x)
```

```
tauyz = mu * (v_z + w_y)

tauxx_x = (   mu_x * (u_x  + u_x ) + lambda_x * (u_x  + v_y  + w_z )
            + mu   * (u_xx + u_xx) + lambda_  * (u_xx + v_xy + w_xz) )
tauyy_y = (   mu_y * (v_y  + v_y ) + lambda_y * (u_x  + v_y  + w_z )
            + mu   * (v_yy + v_yy) + lambda_  * (u_xy + v_yy + w_yz) )
tauzz_z = (   mu_z * (w_z  + w_z ) + lambda_z * (u_x  + v_y  + w_z )
            + mu   * (w_zz + w_zz) + lambda_  * (u_xz + v_yz + w_zz) )

tauxy_x = mu_x * (u_y + v_x) + mu * (u_xy + v_xx)
tauxy_y = mu_y * (u_y + v_x) + mu * (u_yy + v_xy)
tauxz_x = mu_x * (u_z + w_x) + mu * (u_xz + w_xx)
tauxz_z = mu_z * (u_z + w_x) + mu * (u_zz + w_xz)
tauyz_y = mu_y * (v_z + w_y) + mu * (v_yz + w_yy)
tauyz_z = mu_z * (v_z + w_y) + mu * (v_zz + w_yz)

pu_x = p_x * u + p * u_x
pv_y = p_y * v + p * v_y
pw_z = p_z * w + p * w_z
utauxx_x = u_x * tauxx + u * tauxx_x
vtauxy_x = v_x * tauxy + v * tauxy_x
wtauxz_x = w_x * tauxz + w * tauxz_x
utauxy_y = u_y * tauxy + u * tauxy_y
vtauyy_y = v_y * tauyy + v * tauyy_y
wtauyz_y = w_y * tauyz + w * tauyz_y
utauxz_z = u_z * tauxz + u * tauxz_z
vtauyz_z = v_z * tauyz + v * tauyz_z
wtauzz_z = w_z * tauzz + w * tauzz_z

Q_rho  = rho_t + rhou_x + rhov_y + rhow_z
Q_rhou = ( rhou_t + rhouu_x + rhouv_y + rhouw_z
                  + p_x / (Ma * Ma)
                  - (1 / Re) * (tauxx_x + tauxy_y + tauxz_z) )
Q_rhov = ( rhov_t + rhouv_x + rhovv_y + rhovw_z
                  + p_y / (Ma * Ma)
                  - (1 / Re) * (tauxy_x + tauyy_y + tauyz_z) )
Q_rhow = ( rhow_t + rhouw_x + rhovw_y + rhoww_z
                  + p_z / (Ma * Ma)
                  - (1 / Re) * (tauxz_x + tauyz_y + tauzz_z) )
Q_rhoe = ( rhoe_t + rhoue_x + rhove_y + rhowe_z
                  + pu_x + pv_y + pw_z + qx_x + qy_y + qz_z
                  - (Ma * Ma / Re) * (  utauxx_x + vtauxy_x + wtauxz_x
                                      + utauxy_y + vtauyy_y + wtauyz_y
                                      + utauxz_z + vtauyz_z + wtauzz_z) )
```

The errors arising in this process behave like standard floating point truncation issues. Refer to Ulerich et al. [170] for a more extended discussion of this approach.

Employing the manufactured solution requires fixing the more than two hundred coefficients appearing in the model and chosen solution forms. Selecting usable values is not difficult but it is time consuming. Reasonable coefficient choices for testing channel and flat plate codes are therefore presented.

In both geometries the streamwise, wall-normal, and spanwise directions are labeled x, y, and z respectively. Both x and z are periodic while $y \in \left\{0, L_y\right\}$ is not. Transient tests should likely take place within the duration $0 \leq t \leq 1/10$ nondimensional time units as the time phase offsets (for example, g_{Tyz}) have been chosen for appreciable transients to occur throughout this time window.

For isothermal channel flow code verification we recommend testing using

$$b_{\rho y} = b_{uy} = b_{vy} = b_{wy} = b_{Ty} = \frac{1}{2}$$

and the coefficients given in Table B.1. With these choices the manufactured solution satisfies isothermal, no-slip conditions at $y = 0, L_y$. For isothermal flat plate code verification we recommend testing using

$$b_{\rho y} = b_{uy} = b_{vy} = b_{wy} = b_{Ty} = \frac{1}{4}$$

and the coefficients given in Table B.1. With these choices the manufactured solution satisfies an isothermal, no-slip condition at $y = 0$.

Table B.1: Manufactured solution coefficient recommendations. Unlisted coefficients should be set to zero.

$\alpha = 0$
$\beta = 2/3$
$\gamma = 1.4$
$\mathrm{Ma} = 1.15$
$\mathrm{Pr} = 0.7$
$\mathrm{Re} = 100$
$L_x = 4\pi$
$L_y = 2$
$L_z = 4\pi/3$

$a_{\rho 0} = 1$
$a_{\rho xy} = 1/11$
$b_{\rho xy} = 3$
$d_{\rho xy} = 3$
$f_{\rho xy} = 3$
$g_{\rho xy} = \pi/4$
$a_{\rho y} = 1/7$
$b_{\rho y} = \textit{See §B}$
$f_{\rho y} = 1$
$g_{\rho y} = \pi/4 - 1/20$
$a_{\rho yz} = 1/31$
$b_{\rho yz} = 2$
$d_{\rho yz} = 2$
$f_{\rho yz} = 2$
$g_{\rho yz} = \pi/4 + 1/20$

$a_{uxy} = 37/251$
$b_{uxy} = 3$
$c_{uxy} = -\pi/2$
$d_{uxy} = 3$
$e_{uxy} = -\pi/2$
$f_{uxy} = 3$
$g_{uxy} = \pi/4$
$a_{uy} = 1$
$b_{uy} = \textit{See §B}$
$c_{uy} = -\pi/2$
$f_{uy} = 1$
$g_{uy} = \pi/4 - 1/20$
$a_{uyz} = 41/257$
$b_{uyz} = 2$
$c_{uyz} = -\pi/2$
$d_{uyz} = 2$
$e_{uyz} = -\pi/2$
$f_{uyz} = 2$
$g_{uyz} = \pi/4 + 1/20$

$a_{vxy} = 3/337$
$b_{vxy} = 3$
$c_{vxy} = -\pi/2$
$d_{vxy} = 3$
$e_{vxy} = -\pi/2$
$f_{vxy} = 3$
$g_{vxy} = \pi/4$
$a_{vy} = 2/127$
$b_{vy} = \textit{See §B}$
$c_{vy} = -\pi/2$
$f_{vy} = 1$
$g_{vy} = \pi/4 - 1/20$
$a_{vyz} = 5/347$
$b_{vyz} = 2$
$c_{vyz} = -\pi/2$
$d_{vyz} = 2$
$e_{vyz} = -\pi/2$
$f_{vyz} = 2$
$g_{vyz} = \pi/4 + 1/20$

$a_{wxy} = 11/409$
$b_{wxy} = 3$
$c_{wxy} = -\pi/2$
$d_{wxy} = 3$
$e_{wxy} = -\pi/2$
$f_{wxy} = 3$
$g_{wxy} = \pi/4$
$a_{wy} = 7/373$
$b_{wy} = \textit{See §B}$
$c_{wy} = -\pi/2$
$f_{wy} = 1$
$g_{wy} = \pi/4 - 1/20$
$a_{wyz} = 13/389$
$b_{wyz} = 2$
$c_{wyz} = -\pi/2$
$d_{wyz} = 2$
$e_{wyz} = -\pi/2$
$f_{wyz} = 2$
$g_{wyz} = \pi/4 + 1/20$

$a_{T0} = 1$
$a_{Txy} = 1/17$
$b_{Txy} = 3$
$c_{Txy} = -\pi/2$
$d_{Txy} = 3$
$e_{Txy} = -\pi/2$
$f_{Txy} = 3$
$g_{Txy} = \pi/4$
$a_{Ty} = 1/13$
$b_{Ty} = \textit{See §B}$
$c_{Ty} = -\pi/2$
$f_{Ty} = 1$
$g_{Ty} = \pi/4 - 1/20$
$a_{Tyz} = 1/37$
$b_{Tyz} = 2$
$c_{Tyz} = -\pi/2$
$d_{Tyz} = 2$
$e_{Tyz} = -\pi/2$
$f_{Tyz} = 2$
$g_{Tyz} = \pi/4 + 1/20$

Appendix C

Designing Inviscid Base Flows with Prescribed Pressure Gradients and Edge Mach Conditions

A procedure is derived for obtaining inviscid, perfect gas flow fields with either favorable or adverse pressure gradients and varying Mach numbers for use in homogenized boundary layer simulations. First, a compressible potential flow problem is formulated for an isenthalpic, radially symmetric source or sink flow. The resulting one-dimensional problem is cast into a form ordinary differential equation (ODE) integrators can solve to obtain primitive state as a function of radius. The solution is then mapped from (r, θ) into (x, y) coordinates and a base flow profile extracted from some constant x line segment. Finally, the segment chosen, as well as the radial problem boundary conditions used, are taken to match some edge state of interest based on simple algebraic relationships. A reference implementation is developed during the discussion to aid reproducibility.

C.1 The Isenthalpic Potential Flow Equations

A succinct, coordinate-independent derivation of the velocity-potential formulation of the compressible potential flow equations appears in Saad et al. [133, §II.A]. Their presentation is recounted here but velocity potential notation is suppressed.

Wherever necessary, sufficient smoothness is assumed.

Consider a perfect gas in which pressure p, density ρ, and sound speed a are related by a constant ratio of specific heats γ according to

$$\gamma p = \rho a^2. \tag{C.1}$$

The relative changes in these three quantities clearly obey

$$\rho \nabla a^2 = \gamma \nabla p - a^2 \nabla \rho. \tag{C.2}$$

In such a fluid, the total specific enthalpy H additionally relates the kinetic energy

$$H = \frac{a^2}{\gamma - 1} + \frac{1}{2}\vec{u}^2. \tag{C.3}$$

By assuming an isenthalpic flow with H everywhere constant,

$$\nabla a^2 = -\frac{\gamma - 1}{2} \nabla \vec{u}^2 \tag{C.4}$$

implying

$$\gamma \nabla p - a^2 \nabla \rho = -\frac{\gamma - 1}{2} \rho \nabla \vec{u}^2. \tag{C.5}$$

If the flow is steady, inviscid, and irrotational, the unforced momentum equation yields

$$\vec{\nabla} p = -\rho \vec{u} \cdot \vec{\nabla} \vec{u} = -\rho \left(\frac{1}{2} \vec{\nabla} (\vec{u} \cdot \vec{u}) - \vec{u} \times \vec{\nabla} \times \vec{u} \right) = -\frac{1}{2} \rho \vec{\nabla} \vec{u}^2. \tag{C.6}$$

The irrotational velocity may be replaced by the gradient of a scalar potential, *viz.*

$$\vec{u} = \vec{\nabla} \phi + \vec{\nabla} \times \vec{A} = \vec{\nabla} \phi. \tag{C.7}$$

Though commonly employed, $\vec{\nabla}\phi$ plays little role here. Substituting (C.6) into (C.5) and simplifying,

$$a^2 \nabla \rho = \nabla p, \tag{C.8}$$

shows isentropy holds since, by definition, $\left(\frac{\partial p}{\partial \rho}\right)_s = a^2$. Rearranging (C.8) and invoking (C.6),

$$\vec{\nabla}\rho = \frac{1}{a^2}\vec{\nabla}p = -\frac{\rho}{2a^2}\vec{\nabla}\vec{u}^2. \tag{C.9}$$

Examining the steady continuity equation and applying (C.9),

$$0 = \vec{\nabla}\cdot\rho\vec{u} = \rho\vec{\nabla}\cdot\vec{u} + \vec{u}\cdot\vec{\nabla}\rho = \rho\vec{\nabla}\cdot\vec{u} - \frac{\rho\vec{u}}{2a^2}\cdot\vec{\nabla}\vec{u}^2. \tag{C.10}$$

Because $\rho > 0$ and $a > 0$, the above equation may only be nontrivially satisfied when

$$\frac{1}{2}\vec{u}\cdot\vec{\nabla}\vec{u}^2 = a^2\vec{\nabla}\cdot\vec{u}. \tag{C.11}$$

As suggested by Saad et al., the constant specific total enthalpy assumption, $H = H_0$, is used to connect a and u with a reference specific enthalpy $h_0 = \frac{a_0^2}{\gamma-1}$ and a reference velocity u_0,

$$\frac{a^2}{\gamma-1} + \frac{1}{2}\vec{u}^2 = \frac{a_0^2}{\gamma-1} + \frac{1}{2}u_0^2 \tag{C.12}$$

everywhere. As specific total energy E must be strictly positive, from $H = E + p/\rho$ it follows

$$\frac{p}{\rho} < \frac{a_0^2}{\gamma-1} + \frac{1}{2}u_0^2 \tag{C.13}$$

is necessary for realizability. After rearranging, the constant stagnation enthalpy condition (C.12),

$$a^2 = a_0^2 + \frac{\gamma - 1}{2}\left(u_0^2 - \vec{u}^2\right), \tag{C.14}$$

may be used within (C.11) to find the useful dimensional result,

$$\vec{u} \cdot \vec{\nabla}\vec{u}^2 = \left[2a_0^2 + (\gamma - 1)\left(u_0^2 - \vec{u}^2\right)\right] \vec{\nabla} \cdot \vec{u}. \tag{C.15}$$

C.2 Nondimensionalization of the Equations

To nondimensionalize, choose some reference length l_0 and declare

$$x = x^* l_0 \qquad a = a^* a_0 \qquad u = u^* u_0 = u^* \mathrm{Ma}_0 a_0 \qquad \rho = \rho^* \rho_0 \qquad p = p^* \rho_0 a_0^2 \tag{C.16}$$

where the starred quantities are dimensionless. Inserting the definitions into (C.15),

$$\begin{aligned} \frac{{\mathrm{Ma}_0}^3 a_0^3}{l_0} \vec{u}^* \cdot \vec{\nabla}^* \vec{u}^{*2} &= \left[2a_0^2 + {\mathrm{Ma}_0}^2 a_0^2 (\gamma - 1)\left(1 - \vec{u}^{*2}\right)\right] \frac{\mathrm{Ma}_0 a_0}{l_0} \vec{\nabla}^* \cdot \vec{u}^* \\ &= \frac{{\mathrm{Ma}_0}^3 a_0^3}{l_0} \left[\frac{2}{{\mathrm{Ma}_0}^2} + (\gamma - 1)\left(1 - \vec{u}^{*2}\right)\right] \vec{\nabla}^* \cdot \vec{u}^*. \end{aligned} \tag{C.17}$$

Rescaling and dropping the star notation, one arrives at

$$\vec{u} \cdot \vec{\nabla}\vec{u}^2 = \left[2{\mathrm{Ma}_0}^{-2} + (\gamma - 1)\left(1 - \vec{u}^2\right)\right] \vec{\nabla} \cdot \vec{u}. \tag{C.18}$$

With some $\vec{u} = \vec{\nabla}\phi$ satisfying (C.18) in hand, computing local ρ and p is of interest. Nondimensionalizing (C.14) permits direct computation of a from

$$a^2 = 1 + \mathrm{Ma}_0^2 \frac{\gamma - 1}{2}\left(1 - \vec{u}^2\right) \tag{C.19}$$

where clearly a realizable $a^2 > 0$ requires

$$u^2_{\text{valid}} < \frac{2}{\text{Ma}_0^2(\gamma-1)} + 1. \tag{C.20}$$

By squaring the sonic condition $\frac{uu_0}{aa_0} = 1$ and solving, one obtains

$$u^2_{\text{sonic}} = (\gamma+1)^{-1}\left(2\text{Ma}_0^{-2} + \gamma - 1\right) < u^2_{\text{valid}}. \tag{C.21}$$

Condition (C.13) restricts the relative magnitudes of nondimensional p and ρ,

$$\frac{p}{\rho} < \frac{1}{\gamma-1} + \frac{1}{2}\text{Ma}_0^2, \tag{C.22}$$

as well as, using (C.1), the maximum attainable nondimensional sound speed,

$$a^2 = \frac{\gamma p}{\rho} < \frac{\gamma}{\gamma-1} + \frac{\gamma}{2}\text{Ma}_0^2. \tag{C.23}$$

Employing (C.9), nondimensionalizing, multiplying by l_0, and simplifying,

$$\frac{\vec{\nabla}\rho}{\rho} = \vec{\nabla}\log\rho = -\frac{\text{Ma}_0^2}{2}\frac{\vec{\nabla}\vec{u}^2}{a^2}. \tag{C.24}$$

Nondimensionalizing (C.6) and scaling by $\frac{l_0}{\rho_0 a_0^2}$,

$$\vec{\nabla}p = -\frac{1}{2}\text{Ma}_0^2\rho\vec{\nabla}\vec{u}^2. \tag{C.25}$$

Both of the previous two local statements can be made global by integrating over some domain Ω and applying a corollary of Gauss' theorem:

$$\int_{\partial\Omega}\log\rho\,\mathrm{d}S = -\frac{\text{Ma}_0^2}{2}\int_\Omega \frac{\vec{\nabla}\vec{u}^2}{a^2}\,\mathrm{d}x \tag{C.26}$$

$$\int_{\partial\Omega} p\,\mathrm{d}S = -\frac{\text{Ma}_0^2}{2}\int_\Omega \rho\vec{\nabla}\vec{u}^2\,\mathrm{d}x. \tag{C.27}$$

C.3 Reduction to the Radially Symmetric Geometry

Suppose a two-dimensional domain possessing radial symmetry for which $\vec{u} = u(r)\,\hat{r}$. Then the velocity potential $\vec{\nabla}\phi$ is superfluous because (C.18) is nothing but the scalar equation

$$2u^2(r)\,u'(r) = \left[2\mathrm{Ma}_0{}^{-2} + (\gamma-1)\left(1-u^2(r)\right)\right]\left(r^{-1}u(r) + u'(r)\right). \tag{C.28}$$

Suppressing the dependence of u on r and collecting u' terms,

$$\left(2u^2 - \left[2\mathrm{Ma}_0{}^{-2} + (\gamma-1)\left(1-u^2\right)\right]\right)u' = \left[2\mathrm{Ma}_0{}^{-2} + (\gamma-1)\left(1-u^2\right)\right]r^{-1}u. \tag{C.29}$$

Solving for u',

$$u' = \frac{u}{r}\,\frac{\left[2\mathrm{Ma}_0{}^{-2} + (\gamma-1)\left(1-u^2\right)\right]}{2u^2 - [2\mathrm{Ma}_0{}^{-2} + (\gamma-1)(1-u^2)]}, \tag{C.30}$$

permits integrating u across $R \in [R_1, R_2]$ given a boundary condition at either radius R_1 or R_2.

Given some u, we now turn to computing local thermodynamic state. Equation (C.19) fixes a. The $u = u(r)$ assumption reduces (C.26) to

$$\begin{aligned}\rho(R_2) &= \exp\left[-\frac{\mathrm{Ma}_0^2}{2}\int_{R_1}^{R_2}\frac{\left(u^2\right)'}{a^2}\,r\,\mathrm{d}r + \log\rho(R_1)\right] \\ &= \rho(R_1)\exp\left[-\mathrm{Ma}_0^2\int_{R_1}^{R_2}\frac{uu'}{a^2}\,r\,\mathrm{d}r\right].\end{aligned} \tag{C.31}$$

Likewise (C.27) becomes

$$\begin{aligned}p(R_2) &= -\frac{\mathrm{Ma}_0^2}{2}\int_{R_1}^{R_2}\rho\left(u'\right)^2\,r\,\mathrm{d}r + p(R_1) \\ &= -\mathrm{Ma}_0^2\int_{R_1}^{R_2}\rho uu'\,r\,\mathrm{d}r + p(R_1).\end{aligned} \tag{C.32}$$

Notice (C.30) easily supplies pointwise u' for the computation of both ρ and p.

C.4 The Sub- and Supersonic Radial Nozzle Problems

Equations (C.19), (C.30), (C.31) and (C.32) may be used to find nondimensional solutions to idealized sub- and supersonic radial nozzle and diffuser problems. Many texts, for example White [175, §9.4] and Landau and Lifshitz [83, §97], discuss the situation when the nozzle area changes slowly. In contrast, the preceding treatment permits geometries violating that assumption.

A subsonic nozzle may be posed on $[R_1, R_2]$ by employing (C.21) to set either

$$-|u_{\text{sonic}}| < u(R_2) < 0, \qquad \text{(subsonic nozzle inflow)} \tag{C.33}$$

$$-|u_{\text{sonic}}| < u(R_1) < 0. \qquad \text{(subsonic nozzle outflow)} \tag{C.34}$$

These conditions cause $-u$ to increase and p to decrease when traversing the domain from R_2 to R_1. However, the problem becomes stiff as the flow accelerates towards the sonic condition. Caveat numerical errors, specifying the outflow problem with a carefully chosen R_1 produces an equivalent nozzle as the physics are frictionless.

A supersonic nozzle may be posed on $[R_1, R_2]$ by additionally making use of (C.20) to set either

$$|u_{\text{sonic}}| < u(R_1) < u_{\text{valid}}, \qquad \text{(supersonic nozzle inflow)} \tag{C.35}$$

$$|u_{\text{sonic}}| < u(R_2) < u_{\text{valid}}. \qquad \text{(supersonic nozzle outflow)} \tag{C.36}$$

These conditions cause u to increase and p to decrease when traversing the domain from R_1 to R_2.

Working with these conditions in conjunction with (C.30) presents initial value problems amenable to solution by ordinary differential equation (ODE) integrators. For

example, Octave [37] with the `odepkg` package can solve such problems. One possible implementation appears in Listing C.1 along with verification tests. Its demo logic produces the solutions depicted in Figure C.1. Though only scalar $u'(r)$ needs to be integrated, this implementation integrates the state vector $[u, \rho, p]^{\mathrm{T}}$ so that `odepkg`'s automated solution tolerance controls apply equally to all three scalar quantities.

Listing C.1: `radialflow.m`: A nondimensional radial flow solver implementation

```
% Solve radialflow IVP for [u; rho; p] given [Ma gam R1 R2 u1 rho1 p1]
% via a "coupled" ODE-based approach.  Plot results when no values requested.
function [r u rho p a2 up rhop pp] = radialflow(Ma, gam, R1, R2, u1, rho1, p1,
                                                tol=sqrt(eps))

  [Ma2 gam1] = deal(Ma.^2, gam-1);
  assert(u1.^2 < 2 / Ma2 / gam1 + 1,
         'Ma=%g, gam=%g, u1=%g imply a.^2 <= 0', Ma, gam, u1);

  vopt  = odeset('RelTol',  tol, 'InitialStep', 0.01*abs(R1-R2),
                 'AbsTol',  eps, 'MaxStep',     0.10*abs(R1-R2));
  [r x] = ode45(@radialflow_rhs, [R1 R2], [u1 rho1 p1], vopt, Ma2, gam1);
  [u  rho  p    ] = deal(x(:,1), x(:,2), x(:,3));
  [up rhop pp a2] = radialflow_details(r, u, rho, p, Ma2, gam1);

  if 0 == nargout
    figure();
    plot(r, u, 'o-', r, rho, '+-', r, p, 'x-', r, Ma*abs(u)./sqrt(a2), '*-');
    legend('Velocity', 'Density', 'Pressure', 'Local Mach', ...
           'location', 'westoutside', 'orientation', 'vertical');
    xlabel('Radius');
    box('off');
  end
end

% ODEs [u; rho; p]' given r, x=[u; rho; p], Ma2=Ma.^2, gam1=gam-1
function f = radialflow_rhs(r, x, Ma2, gam1)
  [up, rhop, pp] = radialflow_details(r, x(1), x(2), x(3), Ma2, gam1);
  f              = [up; rhop; pp];
end

% Find pointwise derivatives and sound speed given state, Ma2=Ma.^2, gam1=gam-1
```

```
function [up, rhop, pp, a2] = radialflow_details(r, u, rho, p, Ma2, gam1)
  u2   = u.^2;
  C    = (2./Ma2 + gam1.*(1 - u2));
  up   = (u.*C) ./ (r.*(2*u2 - C));
  pp   = -Ma2.*rho.*u.*up;
  a2   = 1 + 0.5*Ma2.*gam1.*(1 - u2);
  rhop = pp ./ a2;
end

%!test
%! % Does a solution satisfy steady governing equations in radial setting?
%! % A verification test, including derivatives, against governing equations.
%! % Pressure p1 computed from ideal gas equation of state.
%! pkg load odepkg; Ma=1.5; gam=1.4; Rin=10; Rout=Rin+1/2; u1=-2/7; rho1=9/10;
%! p1 = rho1/gam *(1+(gam-1)/2*Ma.^2*(1-u1.^2));
%! [r u rho p a2 up rhop pp] = radialflow(Ma, gam, Rin, Rout, u1, rho1, p1);
%! assert(zeros(size(r))', (u.*rho./r+rho.*up+u.*rhop)', 10*eps);  # Mass
%! assert(pp', (-Ma.^2.*rho.*u.*up)', 10*eps);                    # Momentum
%! assert(a2', (1 + Ma.^2.*(gam-1)./2.*(1-u.^2))', 10*eps);       # Energy
%! assert((rho.*a2)', (gam.*p)', 10*eps);                         # Ideal EOS

%!demo % Solve subsonic nozzle (specifying outflow) and plot to file
%! pkg load odepkg; Ma=2; gam=1.4; Rin=1; Rout=Rin+1;
%! u_sonic = sqrt((2/Ma.^2 + gam - 1) / (gam + 1));
%! radialflow(Ma, gam, Rout, Rin, -u_sonic/5, 1, 1/2);
%! print('nozzle_subsonic.eps', '-depsc2', '-S640,480', '-F:9');
%! close();

%!demo % Solve supersonic nozzle (specifying inflow) and plot to file
%! pkg load odepkg; Ma=1; gam=1.4; Rin=1; Rout=Rin+1;
%! u_sonic = sqrt((2/Ma.^2 + gam - 1) / (gam + 1));
%! radialflow(Ma, gam, Rin, Rout, 1.5*u_sonic, 1/2, 1);
%! print('nozzle_supersonic.eps', '-depsc2', '-S640,480', '-F:9');
%! close();
```

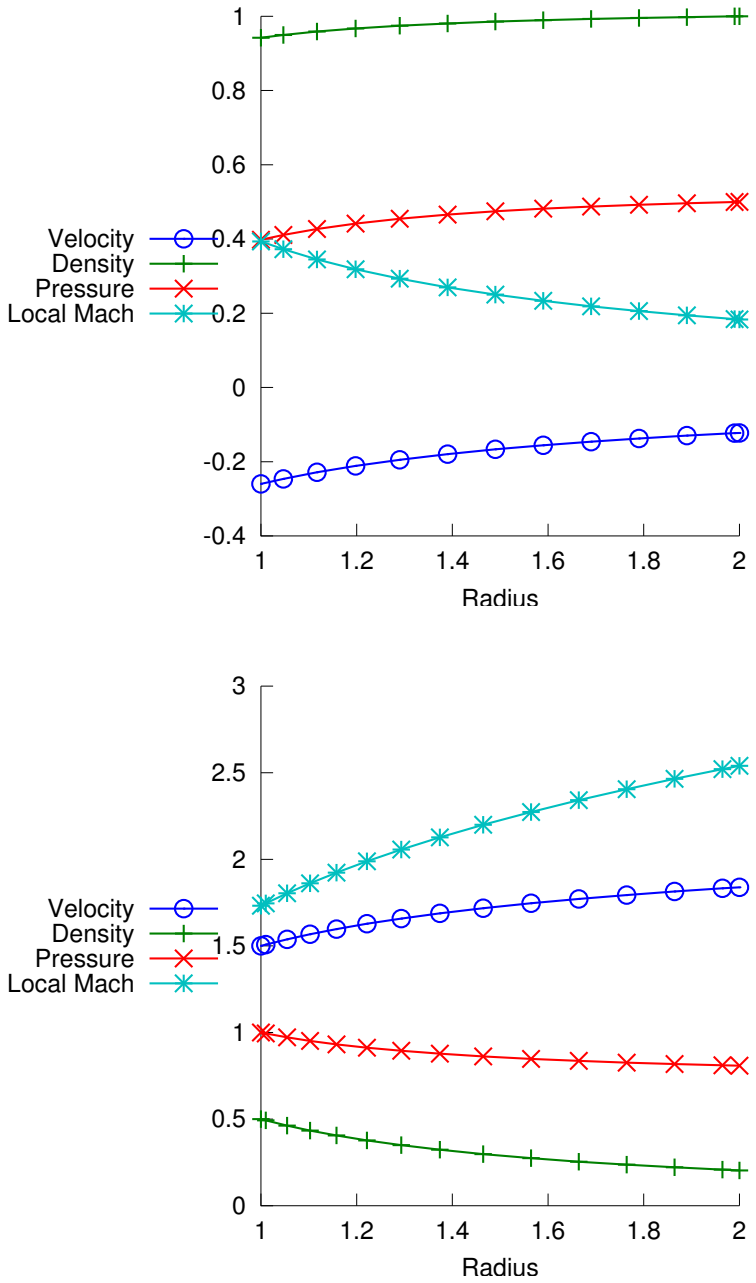

Figure C.1: Sample solutions saved by the `radialflow.m` demo logic in Listing C.1. The subsonic case (above) flows from right-to-left while the supersonic case (below) flows from left-to-right.

C.5 Quantities of Interest for a Cartesian Base Flow

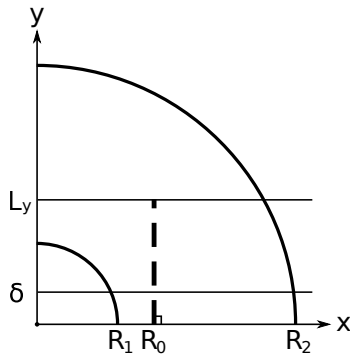

Figure C.2: A Cartesian setting overlaid on the radially symmetric domain

Suppose a Cartesian flow profile of height L_y is desired from a constant x line segment within a radially varying solution. Referring to Figure C.2, assume a solution $u(R)$ with accompanying $\rho(R)$, $p(R)$, and $a(R)$ is valid for any $R \in [R_1, R_2]$. Then for some (x,y) and corresponding $R = \sqrt{x^2+y^2}$ one may compute:

$$
\begin{array}{lll}
\rho(x,y) = \rho(R) & \partial_x \rho = \dfrac{x}{R}\rho'(R) & \partial_y \rho = \dfrac{y}{R}\rho'(R) \\
u_x(x,y) = u(R)\dfrac{x}{R} & \partial_x u_x = \dfrac{1}{R^2}\left[x^2 u'(R) + \dfrac{y^2}{R}u(R)\right] & \partial_y u_x = \dfrac{xy}{R^2}\left[u'(R) - \dfrac{1}{R}u(R)\right] \\
u_y(x,y) = u(R)\dfrac{y}{R} & \partial_x u_y = \dfrac{xy}{R^2}\left[u'(R) - \dfrac{1}{R}u(R)\right] & \partial_y u_y = \dfrac{1}{R^2}\left[y^2 u'(R) + \dfrac{x^2}{R}u(R)\right] \\
p(x,y;\mathrm{Ma}) = \dfrac{\mathrm{Ma}^2}{{\mathrm{Ma}_0}^2}p(R) & \partial_x p = \dfrac{\mathrm{Ma}^2}{{\mathrm{Ma}_0}^2}\dfrac{x}{R}p'(R) & \partial_y p = \dfrac{\mathrm{Ma}^2}{{\mathrm{Ma}_0}^2}\dfrac{y}{R}p'(R) \\
a(x,y;\mathrm{Ma}) = \dfrac{\mathrm{Ma}}{\mathrm{Ma}_0}a(R) & \partial_x a = \dfrac{1-\gamma}{2}\dfrac{x}{R}\dfrac{\mathrm{Ma}\mathrm{Ma}_0\,u(R)}{a(R)}u'(R) & \partial_y a = \dfrac{1-\gamma}{2}\dfrac{y}{R}\dfrac{\mathrm{Ma}\mathrm{Ma}_0\,u(R)}{a(R)}u'(R).
\end{array}
$$

The Ma and Ma_0 factors on p and a rescale them for use in a nondimensionalization possessing a potentially different Mach number, Ma, assuming $p_0 = \rho_0 a_0^2$, ρ_0, and u_0 still hold in the target setting. This is exactly the nondimensional setting of Chapter 3. Such a translation permits using radial solutions for the steady, nondimensional,

primitive Euler equations written in Cartesian coordinates:

$$\begin{bmatrix}0\\0\\0\\0\end{bmatrix} = \begin{bmatrix}u_x & \rho & 0 & 0\\ 0 & u_x & 0 & \rho^{-1}\mathrm{Ma}^{-2}\\ 0 & 0 & u_x & 0\\ 0 & \rho a^2 & 0 & u_x\end{bmatrix} \partial_x \begin{bmatrix}\rho\\u_x\\u_y\\p\end{bmatrix} + \begin{bmatrix}u_y & 0 & \rho & 0\\ 0 & u_y & 0 & 0\\ 0 & 0 & u_y & \rho^{-1}\mathrm{Ma}^{-2}\\ 0 & 0 & \rho a^2 & u_y\end{bmatrix} \partial_y \begin{bmatrix}\rho\\u_x\\u_y\\p\end{bmatrix}. \tag{C.37}$$

More concretely, take the profile from the line segment $(R_0, 0)$ to $\left(R_0, L_y\right)$. Clearly, selecting

$$R_1 = R_0 \qquad\qquad R_2 = \sqrt{R_0^2 + L_y^2} \tag{C.38}$$

produces the smallest radial domain possessing a solution along this segment. When working with both sub- and supersonic profiles, it is convenient to abstract away the change in sign of u_x. Let ξ denote the x direction possibly reflected so that streamwise velocity is always positive. That is,

$$\xi = \begin{cases} x & \text{if } u(R_1) \geq 0 \\ -x & \text{otherwise} \end{cases} \tag{C.39}$$

so that

$$\frac{\partial}{\partial \xi} = \operatorname{sgn}(u)\frac{\partial}{\partial x} = \frac{x \operatorname{sgn}(u)}{R}\frac{\partial}{\partial R}. \tag{C.40}$$

Practically, whenever $u(R_1) < 0$ instead of evaluating u_x, $\partial_x u_x$, etc. at (x, y) one evaluates u_x, $\partial_x u_x$, etc. at $(-x, y)$ to take advantage of the solution's symmetry about the y axis.

Listing C.2: `radialflow_qoi.m`: A kernel computing Cartesian base flow quantities

```
% Solve radial flow for Ma_e and p_exi at Cartesian point (R1, delta).
function [Ma_e p_exi] = radialflow_qoi(delta, gam, Ma, R1, u1, rho1, p1)
  try
    [r u rho p a2 up rhop pp] = radialflow(Ma, gam, R1,
                                           sqrt(R1.^2+delta.^2), u1, rho1, p1);
    Ma_e  = Ma * r(1) * abs(u(end)) ...
          / (r(end) * realsqrt(a2(end)));
    p_exi = sign(u(end)) * r(end) * delta * pp(end) ...
          / (Ma.^2 * r(1) * rho(end) * u(end).^2);
  catch
    warning('radialflow_qoi(%g, %g, %g, %g, %g, %g, %g) fails: %s',
            delta, gam, Ma, R1, u1, rho1, p1, lasterror.message);
    Ma_e = p_exi = NaN;
  end
end
```

At some location of interest with such a profile, say an edge distance δ from the x-axis, one may also compute the edge Mach number and a nondimensional pressure gradient parameter

$$\begin{aligned} \mathrm{Ma}_e &\equiv \left.\frac{u_0 u_\xi}{a_0 a}\right|_{(R_0,\delta)} & p_{e,\xi} &\equiv \left.\frac{l_0\delta}{\rho_0\rho\, u_0^2 u^2}\frac{\partial(p_0 p)}{\partial(l_0\xi)}\right|_{(R_0,\delta)} \\ &= \left.\frac{\mathrm{Ma}_0 R_0}{R}\frac{|u(R)|}{a(R)}\right|_{R=\sqrt{R_0^2+\delta^2}} & &= \left.\frac{\mathrm{sgn}(u)\,\delta}{\mathrm{Ma}_0^2\rho u^2}\frac{\partial p}{\partial x}\right|_{(R_0,\delta)} \\ & & &= \left.\frac{\mathrm{sgn}(u) R\,\delta\, p'(R)}{\mathrm{Ma}_0^2 R_0\,\rho(R)\,u^2(R)}\right|_{R=\sqrt{R_0^2+\delta^2}} \\ & & &= -\left.\frac{R\,\delta\,u'(R)}{R_0\,|u(R)|}\right|_{R=\sqrt{R_0^2+\delta^2}} \end{aligned} \tag{C.41}$$

to interrogate the solution's nature at (R_0, δ).

A kernel building atop Listing C.1 that computes these quantities appears in Listing C.2. By solving to boundary $R_2 = \sqrt{R_0^2 + \delta^2}$, the kernel solves the smallest possible problem. More importantly, it causes the ODE integrator to automatically

produce full-order accurate results at (R_0, δ) without requiring the integrator to possess dense output capabilities.

C.6 Producing a Flow Matching Given Edge Conditions

We wish to produce Cartesian base flows satisfying (C.37) possessing some prescribed edge Mach number Ma_e, some prescribed edge pressure gradient $p_{e,\xi}$, a unit magnitude edge streamwise velocity u_ξ, and a unit edge density ρ. The final two conditions are mandated for operational convenience in Chapters 6 and 7 rather than from some physical concern.

Considering first the edge velocity magnitude, by (C.40)

$$1 = u_\xi(R_0, \delta) = |u_x(R_0, \delta)| = \left| u\left(R \equiv \sqrt{R_0^2 + \delta^2}\right) \frac{R_0}{R} \right| \implies |u(R)| = \frac{R}{R_0}. \tag{C.42}$$

Folding that implication into the edge Mach number definition (C.41),

$$\mathrm{Ma}_e = \frac{\mathrm{Ma}_0 R_0}{R} \frac{|u(R)|}{a(R)} = \frac{\mathrm{Ma}_0 R_0}{R} \frac{R}{R_0 a(R)} \implies a(R) = \frac{\mathrm{Ma}_0}{\mathrm{Ma}_e}. \tag{C.43}$$

Linking these two conditions through the equation of state (C.19),

$$\begin{aligned} a^2(R) = \frac{\mathrm{Ma}_0^2}{\mathrm{Ma}_e^2} &= 1 + \mathrm{Ma}_0^2 \frac{\gamma - 1}{2} \left(1 - u^2(R)\right) \\ &= 1 + \mathrm{Ma}_0^2 \frac{\gamma - 1}{2} \left(1 - \frac{R^2}{R_0^2}\right) \\ &= 1 - \mathrm{Ma}_0^2 \frac{\gamma - 1}{2} \frac{\delta^2}{R_0^2} \end{aligned} \tag{C.44}$$

forces

$$\mathrm{Ma}_0 = \left(\frac{1}{\mathrm{Ma}_e^2} + \frac{\gamma - 1}{2} \frac{\delta^2}{R_0^2} \right)^{-1/2}. \tag{C.45}$$

Satisfying (C.23) in conjunction with the required behavior of $a(R)$ shows

$$1 = \rho(R) \implies p(R) = \frac{\mathrm{Ma}_0^2}{\gamma \mathrm{Ma}_e^2}. \tag{C.46}$$

Turning now to the pressure gradient definition (C.41),

$$\begin{aligned}
p_{e,\xi} &= -\frac{R\,\delta\,u'(R)}{R_0\,|u(R)|} \\
&= -\delta\,u'(R) \\
&= -\delta \frac{u(R)}{R} \frac{\left[2\mathrm{Ma}_0{}^{-2} + (\gamma-1)\left(1-u^2(R)\right)\right]}{2u^2(R) - \left[2\mathrm{Ma}_0{}^{-2} + (\gamma-1)\left(1-u^2(R)\right)\right]} \\
&= -\delta \frac{|u(R)|}{R\,\operatorname{sgn} u(R)} \frac{\mathrm{Ma}_e{}^{-2}}{\frac{R^2}{R_0^2} - \mathrm{Ma}_e{}^{-2}} \\
&= -\frac{\delta}{R_0\,\operatorname{sgn} u(R)} \frac{R_0^2}{\mathrm{Ma}_e^2 R^2 - R_0^2} \\
&= -\frac{\delta}{\operatorname{sgn} u(R)} \frac{R_0}{R_0^2\left(\mathrm{Ma}_e^2 - 1\right) + \mathrm{Ma}_e^2 \delta^2}
\end{aligned} \tag{C.47}$$

implies one should solve

$$0 = R_0^2\left(\mathrm{Ma}_e^2 - 1\right) p_{e,\xi} \operatorname{sgn} u(R) + R_0 \delta + \mathrm{Ma}_e^2 \delta^2 p_{e,\xi} \operatorname{sgn} u(R) \tag{C.48}$$

for a strictly positive root to obtain a suitable R_0. If two such roots exist, the larger is taken as it will produce solutions with desirably smaller derivatives in the y direction.

The term $\operatorname{sgn} u(R)$ appearing above may be set per $\operatorname{sgn} p_{e,\xi}$ and $\operatorname{sgn}\left(\mathrm{Ma}_e^2 - 1\right)$ to achieve the requested pressure gradient regardless of sub- versus supersonic conditions. Thus R_0 is ultimately an implicit function of only Ma_e, $p_{e,\xi}$, and δ. To obtain a favorable pressure gradient, select

$$\operatorname{sgn} u(R) = \operatorname{sgn}\left(\mathrm{Ma}_e^2 - 1\right), \qquad p_{e,\xi} < 0 \tag{C.49}$$

thus modeling a sub- or supersonic nozzle. In this case R_0 is found from solving

$$\begin{aligned} 0 &= R_0^2 \left(\mathrm{Ma}_e^2 - 1\right) p_{e,\xi} \operatorname{sgn}\left(\mathrm{Ma}_e^2 - 1\right) + R_0 \delta + \mathrm{Ma}_e^2 \delta^2 p_{e,\xi} \operatorname{sgn}\left(\mathrm{Ma}_e^2 - 1\right) \\ &= R_0^2 \left|\mathrm{Ma}_e^2 - 1\right| p_{e,\xi} + R_0 \delta + \mathrm{Ma}_e^2 \delta^2 p_{e,\xi} \operatorname{sgn}\left(\mathrm{Ma}_e^2 - 1\right), \qquad p_{e,\xi} < 0. \end{aligned} \tag{C.50}$$

To obtain an adverse pressure gradient, select

$$\operatorname{sgn} u(R) = -\operatorname{sgn}\left(\mathrm{Ma}_e^2 - 1\right), \qquad p_{e,\xi} > 0 \tag{C.51}$$

thus modeling a sub- or supersonic diffuser. In this case R_0 is obtained from solving

$$\begin{aligned} 0 &= -R_0^2 \left(\mathrm{Ma}_e^2 - 1\right) p_{e,\xi} \operatorname{sgn}\left(\mathrm{Ma}_e^2 - 1\right) + R_0 \delta - \mathrm{Ma}_e^2 \delta^2 p_{e,\xi} \operatorname{sgn}\left(\mathrm{Ma}_e^2 - 1\right) \\ &= -R_0^2 \left|\mathrm{Ma}_e^2 - 1\right| p_{e,\xi} + R_0 \delta - \mathrm{Ma}_e^2 \delta^2 p_{e,\xi} \operatorname{sgn}\left(\mathrm{Ma}_e^2 - 1\right), \qquad p_{e,\xi} > 0. \end{aligned} \tag{C.52}$$

Evidently the preceding two cases may be merged to yield the general result

$$0 = -R_0^2 \left|\mathrm{Ma}_e^2 - 1\right| \left|p_{e,\xi}\right| + R_0 \delta - \mathrm{Ma}_e^2 \delta^2 \left|p_{e,\xi}\right| \operatorname{sgn}\left(\mathrm{Ma}_e^2 - 1\right) \tag{C.53}$$

with the edge velocity sign always taken according to

$$\operatorname{sgn} u(R) = -\operatorname{sgn}\left[p_{e,\xi}\left(\mathrm{Ma}_e^2 - 1\right)\right]. \tag{C.54}$$

In summary, given some δ, γ, Ma_e, and $p_{e,\xi}$ a matching base flow may be produced as follows:

1. Solve the quadratic equation (C.53) for for all real, strictly positive roots R_0.

2. Compute Ma_0 from (C.45).

3. Compute $R = \sqrt{R_0^2 + \delta^2}$.

4. Set $u(R) = \pm R/R_0$ per (C.42) with the sign governed by (C.54).

5. Set $\rho(R) = 1$ and compute $p(R)$ from (C.46).

6. Choose the largest R_0 satisfying realizability condition (C.22).

Logic performing these steps appears in Listing C.3. The resulting parameters and initial conditions may be integrated from R to R_0 (or any other radius) using Listing C.1. That the flow profile on segment $(R_0, 0)$ to (R_0, δ) has the desired properties may be verified with Listings C.1 and C.2 as shown in the unit tests.

Listing C.3: `radialflow_match.m`: Match specified boundary layer edge quantities

```
% Produce a radial flow matching the given boundary layer edge conditions.
function [Ma R0 R uR rhoR pR] = radialflow_match(delta, gam, Ma_e, p_exi)
  % Track candidates from zero, one, or two positive real roots for R0
  R0  = roots([ -abs(Ma_e.^2 - 1)*abs(p_exi),
                delta,
              -Ma_e.^2 * delta.^2 * abs(p_exi) * sign(Ma_e.^2 - 1) ]);
  R0  = sort(R0(arrayfun(@isreal,R0) & real(R0) > 0), 'descend');
  Ma  = 1 ./ realsqrt(1/Ma_e.^2 + (gam - 1)*delta.^2./R0.^2/2);
  R   = realsqrt(R0.^2 + delta.^2);
  uR  = -R ./ R0 * sign(p_exi.*(Ma_e.^2 - 1));
  rhoR = ones(size(R0));
  pR  = rhoR .* Ma.^2 ./ gam ./ Ma_e.^2;

  % Thin candidates down to realizable solution with largest R0
  [ok iok] = max((pR ./ rhoR) < (1 ./ (gam - 1) + Ma.^2 / 2));
  if ok
    R0 = R0(iok); Ma  = Ma (iok); R  = R (iok);
    uR = uR(iok); rhoR = rhoR(iok); pR = pR(iok);
  else
    warning('radialflow_match(%g, %g, %g, %g) has no realizable solution',
            delta, gam, Ma_e, p_exi);
    Ma = R0 = R = uR = rhoR = pR = NaN;
  end
end
```

```
%!test % Round trip: Supersonic nozzle
%! delta=1; gam=1.4087;
%! [Ma R0 R uR rhoR pR] = radialflow_match(delta, gam, 1.1906, -0.025439);
%! [r u rho p]          = radialflow(Ma, gam, R, R0, uR, rhoR, pR);          %-->R0
%! [R1 u1 rho1 p1]      = deal(r(end), u(end), rho(end), p(end));            %&R0
%! [Ma_e p_exi]         = radialflow_qoi(delta, gam, Ma, R1, u1, rho1, p1); %-->R
%! assert([Ma_e p_exi], [1.1906, -0.025439], -sqrt(eps));

%!test % Round trip: Subsonic nozzle
%! delta=1; gam=1.4088;
%! [Ma R0 R uR rhoR pR] = radialflow_match(delta, gam, 0.54927, -0.014755);
%! [r u rho p]          = radialflow(Ma, gam, R, R0, uR, rhoR, pR);          %-->R0
%! [R1 u1 rho1 p1]      = deal(r(end), u(end), rho(end), p(end));            %&R0
%! [Ma_e p_exi]         = radialflow_qoi(delta, gam, Ma, R1, u1, rho1, p1); %-->R
%! assert([Ma_e p_exi], [0.54927, -0.014755], -sqrt(eps));

%!test % Round trip: Supersonic diffuser with non-unit delta
%! delta=0.5; gam=1.4;
%! [Ma R0 R uR rhoR pR] = radialflow_match(delta, gam, 1.5, +0.02);
%! [r u rho p]          = radialflow(Ma, gam, R, R0, uR, rhoR, pR);          %-->R0
%! [R1 u1 rho1 p1]      = deal(r(end), u(end), rho(end), p(end));            %&R0
%! [Ma_e p_exi]         = radialflow_qoi(delta, gam, Ma, R1, u1, rho1, p1); %-->R
%! assert([Ma_e p_exi], [1.5, +0.02], -sqrt(eps));

%!test % Round trip: Subsonic diffuser
%! delta=1; gam=1.4;
%! [Ma R0 R uR rhoR pR] = radialflow_match(delta, gam, 0.5, +0.015);
%! [r u rho p]          = radialflow(Ma, gam, R, R0, uR, rhoR, pR);          %>R0
%! [R1 u1 rho1 p1]      = deal(r(end), u(end), rho(end), p(end));            %&R0
%! [Ma_e p_exi]         = radialflow_qoi(delta, gam, Ma, R1, u1, rho1, p1); %-->R
%! assert([Ma_e p_exi], [0.5, +0.015], -sqrt(eps));
```

Appendix D

Archived Simulations

Two general types of data have been captured from each completed simulation and archived on the Corral[1] and Ranch[2] resources at the Texas Advanced Computing Center[3] (TACC). These complete archives will be made available on request. Reduced data, as described towards the end of this appendix, will be made available online[4] for general consumption.

The first type of data archived describes the software environment used for the simulations. From each production batch job the information shown in Table D.1 was preserved. In addition to providing an execution record and raw data for performance variability investigations, these details permit determining what, if any, portions of the software stack may have changed between any two given batch jobs.

The second type of data archived contains instantaneous physics. This data consists of complete instantaneous field snapshots taken periodically during each simulation run along with a variety of scenario parameters and descriptive grid statistics. This data is stored in HDF5 [161] files via the ESIO library [120]. These snapshots

[1] `lonestar:/corral-tacc/utexas/pecos/turbulence/thesis-rhys-chapter{5,6,7}/`
[2] `rhys@ranch:{cevisslam,channels}/`
[3] `http://www.tacc.utexas.edu/`
[4] `http://turbulence.ices.utexas.edu/`

Table D.1: Software and hardware execution details captured from every production batch job as human-readable text files. Files named like `*.dat` provide time measured relative to a wall clock, the simulation physics, and time step number.

Filename	Contents
`bc.dat`	Trace of conserved state behavior at boundaries
`binary`	Absolute path to the compiled Suzerain binary
`cpuinfo`	`/proc/cpuinfo` from MPI rank zero
`dependencies`	Runtime-resolved shared library dependencies
`environment`	Environment variables in effect at runtime
`kernel`	`/proc/kernel` from MPI rank zero
`log.dat`	Complete execution log according to Suzerain
`meminfo`	`/proc/meminfo` from MPI rank zero
`output`	Complete execution log according to the batch system
`qoi.dat`	Trace of scalar quantities of interest like Re_θ
`state.dat`	Trace of mean and fluctuating conserved state
`version`	Suzerain version information from the compiled binary

are Suzerain restart files. Table D.2 describes a subset of the data captured. An effort was made to preserve the discrete operator details so that others might post-process the fields using consistent numerics but without needing access to a B-spline package. While fields are stored as Fourier and B-spline expansion coefficients for efficiency and operational flexibility, Suzerain can convert this data to physical space if necessary.

During simulation execution, *in situ* instantaneous mean samples of various quantities as a function of wall-normal position are taken more frequently than full restart checkpoints. The samples are stored in separate HDF5 files sharing much with Suzerain's restart files. The quantities thus sampled are a superset of information necessary to compute the instantaneous Favre-averaged Navier–Stokes residuals per Section 3.2.

After a simulation completes, all such samples and associated instantaneous

Table D.2: A small subset of the details comprising a Suzerain restart file. HDF5 comments in the file provide operational context. For example, information on field storage ordering is provided in the comments of `/rho`, `/rho_E`, etc.

HDF5 Dataset	Contents
`alpha`	Ratio of bulk to dynamic viscosity
`beta`	Temperature power law exponent
`breakpoints_y`	Breakpoint locations used for wall-normal B-spline basis
`collocation_points_x`	Collocation points for the dealiased, streamwise X direction
`collocation_points_y`	Collocation points for wall-normal discrete operators
`collocation_points_z`	Collocation points for the dealiased, spanwise Z direction
`DAFx`	Dealiasing factor in streamwise X direction
`DAFz`	Dealiasing factor in spanwise Z direction
`Dy0T`	Transpose of banded, wall-normal Y collocation mass matrix
`Dy1T`	Transpose of banded, wall-normal Y first derivative
`Dy2T`	Transpose of banded, wall-normal Y second derivative
`evmagfactor`	Safety factor in $(0, 1]$ used to adjust time step aggressiveness
`gamma`	Ratio of specific heats
`htdelta`	Wall-normal breakpoint hyperbolic tangent stretching
`knots`	Knots used to build B-spline basis
`k`	Wall-normal B-spline order (4 indicates piecewise cubic)
`kx`	Wavenumbers in streamwise X direction
`kz`	Wavenumbers in spanwise Z direction
`Lx`	Nondimensional grid length in streamwise X direction
`Ly`	Nondimensional grid length in wall normal Y direction
`Lz`	Nondimensional grid length in spanwise Z direction
`Ma`	Mach number
`Nx`	Global logical extents in streamwise X direction
`Ny`	Global logical extents in wall-normal Y direction
`Nz`	Global logical extents in spanwise Z direction
`Pr`	Prandtl number
`Re`	Reynolds number
`rho`	Nondimensional density
`rho_E`	Nondimensional total energy
`rho_u`	Nondimensional streamwise momentum
`rho_v`	Nondimensional wall-normal momentum
`rho_w`	Nondimensional spanwise momentum
`t`	Simulation physical time

residuals are aggregated into a single “reduced data” HDF5 file. This reduced data permits third parties to easily access many first and second order turbulence statistics without requiring them to post-process many gigabytes of raw field data on a dedicated cluster environment. In addition, the autoregressive uncertainty estimates described in Section 4.3 are included for each Reynolds-averaged scalar. This reduced data is easily downloadable and may be imported into common software like GNU Octave, MATLAB®, *Mathematica*®, or Python in a single command.

Bibliography

[1] NASA's exploration systems architecture study, final report. Technical Report NASA TM 214062, November 2005. (page 31).

[2] AIAA Computational Fluid Dynamics Committee on Standards. AIAA guide for verification and validation of computational fluid dynamics simulations. AIAA, 1998. G-077-1998. (page 14).

[3] Stephen A. Arnette, Mo Samimy, and Gregory S. Elliott. The effects of expansion on the turbulence structure of compressible boundary layers. *Journal of Fluid Mechanics*, 367:67–105, 1998. doi: 10.1017/S0022112098001475. (pages 13, 21).

[4] ASME Committee V&V 10. Standard for verification and validation in computational solid mechanics. ASME, 2006. (page 14).

[5] ASME Committee V&V 20. Standard for verification and validation in computational fluid dynamics and heat transfer. ASME, 2009. (page 14).

[6] Satish Balay, William D. Gropp, Lois Curfman McInnes, and Barry F. Smith. Efficient management of parallelism in object oriented numerical software libraries. In E. Arge, A. M. Bruaset, and H. P. Langtangen, editors, *Modern Software Tools in Scientific Computing*, pages 163–202. Birkhäuser Press, 1997. (page 106).

[7] M. Baum, T. Poinsot, and D. Thévenin. Accurate boundary conditions for multicomponent reactive flows. *Journal of Computational Physics*, 116(2):247–261, February 1995. doi: 10.1006/jcph.1995.1024. (page 82).

[8] Paul T. Bauman, Roy Stogner, Graham F. Carey, Karl W. Schulz, Rochan Upadhyay, and Andre Maurente. Loose-coupling algorithm for simulating hypersonic flows with radiation and ablation. *Journal of Spacecraft and Rockets*, 48(1):72–80, January 2011. doi: 10.2514/1.50588. (pages 1, 3, 9, 15, 33, 34, 127, 162, 163, 187).

[9] Ron F. Blackwelder and Leslie S. G. Kovasznay. Large-scale motion of a turbulent boundary layer during relaminarization. *Journal of Fluid Mechanics*, 53:61–83, April 1972. doi: 10.1017/S0022112072000047. (page 24).

[10] Olivier Botella and Karim Shariff. B-spline methods in fluid dynamics. *International Journal of Computational Fluid Dynamics*, 17(2):133–149, March 2003. doi: 10.1080/1061856031000104879. (page 57).

[11] C. Bourassa and F. O. Thomas. An experimental investigation of a highly accelerated turbulent boundary layer. *Journal of Fluid Mechanics*, 634:359–404, August 2009. doi: 10.1017/S0022112009007289. (page 24).

[12] Rodney D. W. Bowersox. Combined laser doppler velocimetry and cross-wire anemometry analysis for supersonic turbulent flow. *AIAA Journal*, 34(11):2269–2275, November 1996. doi: 10.2514/3.13390. (page 13).

[13] Rodney D. W. Bowersox and Thomas A. Buter. Turbulence measurements in a mach 2.9 boundary layer including mild pressure gradients. *AIAA Journal*, 34 (12):2479–2483, December 1996. doi: 10.2514/3.13427. (pages 13, 31, 139).

[14] George E. P. Box, Gwilym M. Jenkins, and Gregory C. Reinsel. *Time Series Analysis: Forecasting and Control*. John Wiley, fourth edition, June 2008. ISBN 978-0470272848. (page 98).

[15] John P. Boyd. *Chebyshev and Fourier Spectral Methods*. Dover, 2001. ISBN 978-0486411835. (page 53).

[16] P. Bradshaw. Compressible turbulent shear layers. *Annual Review of Fluid Mechanics*, 9(1):33–52, 1977. doi: 10.1146/annurev.fl.09.010177.000341. (pages 112, 129, 187, 192).

[17] Piet M. T. Broersen. Finite sample criteria for autoregressive order selection. *IEEE Transactions on Signal Processing*, 48(12):3550–3558, December 2000. doi: 10.1109/78.887047. (page 98).

[18] Piet M. T. Broersen. Automatic spectral analysis with time series models. *IEEE Transactions on Instrumentation and Measurement*, 51(2):211–216, April 2002. doi: 10.1109/19.997814.

[19] Piet M. T. Broersen. *Automatic autocorrelation and spectral analysis*. Springer–Verlag, 2006. doi: 10.1007/1-84628-329-9. (page 98).

[20] W. Byron Brown and John N. B. Livingood. Solutions of laminar-boundary-layer equations which result in specific-weight-flow profiles locally exceeding free-stream values. Technical Report 2800, Lewis Flight Propulsion Laboratory, 1952. (page 139).

[21] J. C. Buell. Direct simulations of compressible wall-bounded turbulence. *CTR Annual Research Briefs*, pages 347–356, 1990. (pages 53, 71, 114).

[22] Raúl B. Cal and Luciano Castillo. Similarity analysis of favorable pressure gradient turbulent boundary layers with eventual quasilaminarization. *Physics of Fluids*, 20(10):105106+, 2008. doi: 10.1063/1.2991433. (pages 24, 30, 35, 168, 170, 191).

[23] C. Canuto, M. Y. Hussaini, A. Quarteroni, and T. A. Zang. *Spectral Methods: Fundamentals in Single Domains*. Scientific Computation. Springer-Verlag, 2006. ISBN 3540307257. (page 53).

[24] P. Chassaing, R. A. Antonia, L. Joly Anselmet, and S. Sarker. *Variable Density Fluid Turbulence*. Kluwer Academic Publishers, 2010. ISBN 978-9048160402. (pages 9, 143).

[25] S. H. Cheung, T. A. Oliver, E. E. Prudencio, S. Prudhomme, and R. D. Moser. Bayesian uncertainty analysis with applications to turbulence modeling. *Reliability Engineering & System Safety*, 96:1137–1149, 2011. doi: 10.1016/j.ress.2010.09.013. (page 10).

[26] Francis H. Clauser. Turbulent boundary layers in adverse pressure gradients. *Journal of the Aeronautical Sciences*, 21(2):91–108, February 1954. doi: 10.2514/8.2938. (pages 33, 35, 137, 189).

[27] G. N. Coleman, J. Kim, and R. D. Moser. A numerical study of turbulent supersonic isothermal-wall channel flow. *Journal of Fluid Mechanics*, 305:159–183, 1995. doi: 10.1017/S0022112095004587. (pages 103, 110, 112, 113, 114, 116, 129, 134, 145, 189).

[28] Gary N. Coleman and Richard D. Sandberg. A primer on direct numerical simulation of turbulence - methods, procedures and guidelines. Technical Report AFM 09/01a, March 2010. URL `http://eprints.soton.ac.uk/66182/`. (page 119).

[29] Hugh W. Coleman and W. Glenn Steele. *Experimentation, Validation, and Uncertainty Analysis for Engineers*. John Wiley & Sons, third edition, 2009. ISBN 978-0470168882. (page 99).

[30] Stephen H Davis and Christian Kerczek. A reformulation of energy stability theory. *Archive for Rational Mechanics and Analysis*, 52(2), 1973. doi: 10.1007/BF00282321. (page 27).

[31] Juan C. Del Álamo and Javier Jiménez. Spectra of the very large anisotropic scales in turbulent channels. *Physics of Fluids*, 15(6):L41–L44, June 2003. doi: 10.1063/1.1570830. (page 112).

[32] Juan C. Del Álamo, Javier Jiménez, Paulo Zandonade, and Robert D. Moser. Scaling of the energy spectra of turbulent channels. *Journal of Fluid Mechanics*, 500:135–144, February 2004. doi: 10.1017/S002211200300733X. (page 112).

[33] Fred L. Drake and Guido Rossum. *The Python Language Reference Manual*. Network theory Ltd., 2011. ISBN 978-1906966140. (page 99).

[34] Joseph J. Dudis and Stephen H. Davis. Energy stability of the buoyancy boundary layer. *Journal of Fluid Mechanics*, 47:381–403, April 1971. doi: 10.1017/S0022112071001113. (page 27).

[35] Joseph J. Dudis and Stephen H. Davis. Energy stability of the Ekman boundary layer. *Journal of Fluid Mechanics*, 47(02):405–413, April 1971. doi: 10.1017/S0022112071001125. (page 27).

[36] Paul A. Durbin and Bjorn A. Pettersson Reif. *Statistical Theory and Modeling for Turbulent Flows*. Wiley, 2011. ISBN 978-0470689318. (page 9).

[37] John W. Eaton, David Bateman, and Søren Hauberg. *GNU Octave Manual Version 3*. Network Theory Limited, 2008. URL `http://www.octave.org`. (pages 99, 105, 236).

[38] Isaac Ekoto, Rodney Bowersox, and Larry Goss. Planar measurements of supersonic boundary layers with curvature driven pressure gradients. In *45th AIAA Aerospace Sciences Meeting and Exhibit*, January 2007. doi: 10.2514/6.2007-1137. (page 13).

[39] Isaac W. Ekoto, Rodney D. W. Bowersox, Thomas Beutner, and Larry Goss. Response of supersonic turbulent boundary layers to local and global mechanical distortions. *Journal of Fluid Mechanics*, 630:225–265, 2009. doi: 10.1017/S0022112009006752.

[40] I.W. Ekoto, R.D.W. Bowersox, T. Beutner, and L. Goss. Supersonic boundary layers with periodic surface roughness. *AIAA Journal*, 46(2):486–497, 2008. doi: 10.2514/1.31729. (page 13).

[41] Mohamed Gad el Hak. Questions in fluid mechanics: Stokes' hypothesis for a Newtonian, isotropic fluid. *Journal of Fluids Engineering*, 117(1):3–5, 1995. doi: 10.1115/1.2816816. (page 198).

[42] Bjorn Engquist and Andrew Majda. Absorbing boundary conditions for the numerical simulation of waves. *Mathematics of Computation*, 31(139):629, September 1977. ISSN 0025-5718. doi: 10.1090/S0025-5718-1977-0436612-4. (pages 81, 84, 85).

[43] Alexander Fedorov. Transition and stability of high-speed boundary layers. *Annual Review of Fluid Mechanics*, 43(1):79–95, 2011. doi: 10.1146/annurev-fluid-122109-160750. (pages 2, 21).

[44] Stephen Fergason and Brian Argrow. Simulations of nonclassical dense gas dynamics. In *35th AIAA Thermophysics Conference*. American Institute of Aeronautics and Astronautics, June 2001. doi: 10.2514/6.2001-2752. (page 139).

[45] H. H. Fernholz and P. J. Finley. A critical compilation of compressible turbulent boundary layer data. Technical Report AGARDograph 223, June 1977. (pages 11, 13).

[46] H. H. Fernholz and P. J. Finley. A critical commentary on mean flow data for two-dimensional compressible turbulent boundary layers. Technical Report AGARDograph 253, May 1980. (page 11).

[47] H. H. Fernholz, P. J. Finley, and V. Mikulla. A further compilation of compressible boundary layer data with a survey of turbulence data. Technical Report AGARDograph 263, November 1981. (page 11).

[48] Antonino Ferrante and Said Elghobashi. Reynolds number effect on drag reduction in a microbubble-laden spatially developing turbulent boundary layer. *Journal of Fluid Mechanics*, 543:93–106, October 2005. doi: 10.1017/S0022112005006440. (page 15).

[49] R. Friedrich. Compressible turbulent flows: Aspects of prediction and analysis. *ZAMM Journal of Applied Mathematics and Mechanics*, 87(3):189–211, March 2007. doi: 10.1002/zamm.200610312. (page 112).

[50] R. Friedrich, H. Foysi, and S. Sarkar. Turbulence scalings in supersonic channel flow. *Journal of Fluid Mechanics*, 509:207–216, June 2004. doi: 10.1017/S0022112004009371. (page 112).

[51] G. P. Galdi and S. Rionero. Local estimates and stability of viscous flows in an exterior domain. *Archive for Rational Mechanics and Analysis*, 81(4):333–347, 1983. doi: 10.1007/BF00250859. (page 27).

[52] G. P. Galdi and B. Straughan. A nonlinear analysis of the stabilizing effect of rotation in the Benard problem. *Proceedings of the Royal Society of London. A. Mathematical and Physical Sciences*, 402(1823):257–283, December 1985. doi: 10.1098/rspa.1985.0118. (page 28).

[53] Giovanni P. Galdi and Mariarosaria Padula. A new approach to energy theory in the stability of fluid motion. *Archive for Rational Mechanics and Analysis*, 110 (3):187–286, 1990. doi: 10.1007/BF00375129. (page 28).

[54] B. Ganapathisubramani, N. T. Clemens, and D. S. Dolling. Large-scale motions in a supersonic turbulent boundary layer. *Journal of Fluid Mechanics*, 556:271–282, 2006. doi: 10.1017/S0022112006009244. (page 13).

[55] S. Garg and G. S. Settles. Measurements of a supersonic turbulent boundary layer by focusing schlieren deflectometry. *Experiments in Fluids*, 25(3):254–264, 1998. doi: 10.1007/s003480050228. (page 13).

[56] M. Giles. Non-reflecting boundary conditions for the Euler equations. Technical Report TR-88-1, MIT CFD Laboratory, Department of Aeronautics and Astronautics, 1988. (pages 81, 84, 85, 88, 191).

[57] Michael B. Giles. Nonreflecting boundary conditions for Euler equation calculations. *AIAA Journal*, 28(12):2050–2058, 1990. doi: 10.2514/3.10521. (pages 81, 191).

[58] R. L. Gran, J. E. Lewis, and T. Kubota. The effect of wall cooling on a compressible turbulent boundary layer. *Journal of Fluid Mechanics*, 66(03):507–528, 1974. doi: 10.1017/S0022112074000334. (page 13).

[59] Stephen E. Guarini. *Direct numerical simulation of supersonic turbulent boundary layers*. PhD thesis, Stanford University, 1998. (pages 17, 20, 60, 61, 62, 63, 65, 77, 82, 88, 97).

[60] Stephen E. Guarini, Robert D. Moser, Karim Shariff, and Alan Wray. Direct numerical simulation of a supersonic turbulent boundary layer at Mach 2.5. *Journal of Fluid Mechanics*, 414:1–33, 2000. doi: 10.1017/S0022112000008466. (pages viii, 51, 118, 129, 134, 142, 145, 148, 150, 189, 206).

[61] Gaël Guennebaud, Benoît Jacob, et al. Eigen v3. http://eigen.tuxfamily.org, 2010–2014. (page 105).

[62] Michael A. Heroux, Roscoe A. Bartlett, Vicki E. Howle, Robert J. Hoekstra, Jonathan J. Hu, Tamara G. Kolda, Richard B. Lehoucq, Kevin R. Long, Roger P. Pawlowski, Eric T. Phipps, Andrew G. Salinger, Heidi K. Thornquist, Ray S. Tuminaro, James M. Willenbring, Alan Williams, and Kendall S. Stanley. An overview of the Trilinos project. *ACM Transactions on Mathematical Software*, 31(3):397–423, 2005. doi: 10.1145/1089014.1089021. (page 106).

[63] Brian Hollis, Karen Berger, Thomas Horvath, Joseph Coblish, Joseph Norris, Randolph Lillard, and Benjamin Kirk. Aeroheating testing and predictions for project orion CEV at turbulent conditions. In *46th AIAA Aerospace Sciences Meeting and Exhibit*. American Institute of Aeronautics and Astronautics, January 2008. doi: 10.2514/6.2008-1226. (pages 21, 22, 23).

[64] A. Honkan and Y. Andreopoulos. Vorticity, strain-rate and dissipation characteristics in the near-wall region of turbulent boundary layers. *Journal of Fluid Mechanics*, 350(1), 1997. doi: 10.1017/S0022112097006770. (page 17).

[65] Sergio Hoyas and Javier Jiménez. Scaling of the velocity fluctuations in turbulent channels up to $\mathrm{Re}_\tau = 2003$. *Physics of Fluids*, 18(1):011702, January 2006. doi: 10.1063/1.2162185. (pages 51, 112).

[66] Sergio Hoyas and Javier Jiménez. Reynolds number effects on the Reynolds-stress budgets in turbulent channels. *Physics of Fluids*, 20(10):101511, 2008. doi: 10.1063/1.3005862. (page 112).

[67] P. G. Huang, G. N. Coleman, and P. Bradshaw. Compressible turbulent channel flows: DNS results and modelling. *Journal of Fluid Mechanics*, 305:185–218, 1995. doi: 10.1017/S0022112095004599. (pages 103, 110, 112, 115, 118, 119, 134, 144, 189).

[68] Masashi Ichimiya, Ikuo Nakamura, and Shintaro Yamashita. Properties of a relaminarizing turbulent boundary layer under a favorable pressure gradient. *Experimental Thermal and Fluid Science*, 17(1-2):37–48, May 1998. doi: 10.1016/S0894-1777(97)10047-4. (page 24).

[69] O. Iida and Y. Nagano. The relaminarization mechanisms of turbulent channel flow at low reynolds numbers. *Flow, Turbulence and Combustion*, 60(2):193–213, June 1998. doi: 10.1023/A:1009999606355. (page 24).

[70] R. Johnson. Higher order B-spline collocation at the Greville abscissae. *Applied Numerical Mathematics*, 52(1):63–75, January 2005. doi: 10.1016/j.apnum.2004.04.002. (page 57).

[71] Daniel D. Joseph. On the stability of the Boussinesq equations. 20(1):59–71, 1965. doi: 10.1007/BF00250190. (page 27).

[72] Daniel D. Joseph. Nonlinear stability of the Boussinesq equations by the method of energy. 22(3):163–184, 1966. doi: 10.1007/BF00266474. (page 27).

[73] Imelda B. Joson and Edwin L. Aguirre. Heat shield for NASA's new Orion spacecraft set for 2014 test flight. SPACE.com, July 2013. URL `http://www.space.com/22046-nasa-orion-spacecraft-heat-shield.html`. (page 31).

[74] G. Khujadze and M. Oberlack. DNS and scaling laws from new symmetry groups of ZPG turbulent boundary layer flow. *Theoretical and Computational Fluid Dynamics*, 18(5):391–411, November 2004. doi: 10.1007/s00162-004-0149-x. (page 15).

[75] G. Khujadze and M. Oberlack. New scaling laws in ZPG turbulent boundary layer flow. *Proceedings of 5th International Symposium on Turbulence and Shear Flow Phenomena*, pages 443–448, 2007. (page 15).

[76] John Kim, Parviz Moin, and Robert Moser. Turbulence statistics in fully developed channel flow at low reynolds number. *Journal of Fluid Mechanics*, 177: 133–166, 1987. doi: 10.1017/S0022112087000892. (pages 112, 113, 122, 123).

[77] Benjamin S. Kirk, Roy H. Stogner, Paul T. Bauman, and Todd A. Oliver. Modeling hypersonic entry with the fully-implicit Navier-Stokes (FIN-S) stabilized finite element flow solver. *Computers & Fluids*, 92:281–292, March 2014. doi: 10.1016/j.compfluid.2013.10.003. (pages 29, 33, 163).

[78] Jukka Komminaho and Martin Skote. Reynolds stress budgets in Couette and boundary layer flows. 68(2):167–192, 2002. doi: 10.1023/A:1020404706293. (page 15).

[79] H. H. Ku. Notes on the use of propagation of error formulas. *Journal of Research of the National Bureau of Standards. Section C: Engineering and Instrumentation*, 70C(4):263–273, October 1966. ISSN 0022-4316. (page 99).

[80] Pijush K. Kundu, Ira M. Cohen, and David R. Dowling. *Fluid Mechanics*. 2012. ISBN 9780123821003. (page 137).

[81] Wai Y. Kwok. *Growth suppression in simulated compressible turbulent mixing layers*. PhD thesis, University of Illinois at Urbana-Champaign, 2002. (pages 60, 61, 62, 63, 65).

[82] Wai Y. Kwok, Robert D. Moser, and Javier Jiménez. A critical evaluation of the resolution properties of B-spline and compact finite difference methods. *Journal of Computational Physics*, 174(2):510–551, December 2001. doi: 10.1006/jcph.2001.6919. (pages 51, 57, 58).

[83] L. D. Landau and E. M. Lifshitz. *Fluid Mechanics*. Course of Theoretical Physics, Vol. 6. Butterworth–Heinemann, 2nd edition, 2004. ISBN 0750627670. (page 235).

[84] Julie Langou, Julien Langou, Piotr Luszczek, Jakub Kurzak, Alfredo Buttari, and Jack Dongarra. Exploiting the performance of 32 bit floating point arithmetic in obtaining 64 bit accuracy (revisiting iterative refinement for linear systems). In *Proceedings of the 2006 ACM/IEEE conference on Supercomputing*, SC '06. ACM, 2006. doi: 10.1145/1188455.1188573. (page 105).

[85] R. M. Latin and R. D. W. Bowersox. Flow properties of a supersonic turbulent boundary layer with wall roughness. *AIAA Journal*, 38(10):1804–1821, 2000. doi: 10.2514/2.862. (page 13).

[86] B. E. Launder. Laminarization of the turbulent boundary layer in a severe acceleration. *Journal of Applied Mechanics*, 31(4):707+, 1964. doi: 10.1115/1.3629738. (pages 24, 35, 128, 189).

[87] R. Lechner, J. Sesterhenn, and R. Friedrich. Turbulent supersonic channel flow. *J. Turbulence*, 2(1):1–25, 2001. doi: 10.1088/1468-5248/2/1/001. (page 112).

[88] Myoungkyu Lee and Robert D. Moser. Direct numerical simulation of turbulent channel flow up to Re_τ=5200. *In preparation*. (page 103).

[89] Myoungkyu Lee, Nicholas Malaya, and Robert D. Moser. Petascale direct numerical simulation of turbulent channel flow on up to 786K cores. In *Proceedings of SC13: International Conference for High Performance Computing, Networking, Storage and Analysis*, SC '13, New York, NY, USA, 2013. ACM. doi: 10.1145/2503210.2503298. (pages 103, 105, 121, 124).

[90] Myoungkyu Lee, Rhys Ulerich, Nicholas Malaya, and Robert Moser. Experiences from leadership computing in simulations of turbulent fluid flows. *Computing in Science and Engineering*, 99:1, 2014. doi: 10.1109/MCSE.2014.51. (pages 103, 121).

[91] Sanjiva K. Lele. Compressibility effects on turbulence. *Annual Review of Fluid Mechanics*, 26(1):211–254, 1994. doi: 10.1146/annurev.fl.26.010194.001235. (pages 44, 206).

[92] J. E. Lewis, R. L. Gran, and T. Kubota. An experiment on the adiabatic compressible turbulent boundary layer in adverse and favourable pressure gradients. *Journal of Fluid Mechanics*, 51:657–672, January 1972. doi: 10.1017/S0022112072001296. (page 13).

[93] X. Li, Y. Ma, and D. Fu. DNS and scaling law analysis of compressible turbulent channel flow. *Science in China Series A: Mathematics*, 44(5):645–654, 2001. doi: 10.1007/BF02876712. (page 112).

[94] H. W. Liepmann and A Roshko. *Elements of Gasdynamics*. Dover, New York, 2002. ISBN 0486419630. (pages 140, 197).

[95] Joel J. Luker, Chad S. Hale, and Rodney D. W. Bowersox. Experimental analysis of the turbulent shear stresses for distorted supersonic boundary layers. *Journal of Propulsion and Power*, 14(1):110–118, January 1998. doi: 10.2514/2.5256. (page 13).

[96] Joel J. Luker, Rodney D. W. Bowersox, and Thomas A. Buter. Influence of curvature-driven favorable pressure gradient on supersonic turbulent boundary layer. *AIAA Journal*, 38(8):1351–1359, August 2000. doi: 10.2514/2.1134. (pages 13, 21, 33, 139).

[97] Thomas S. Lund, Xiaohua Wu, and Kyle D. Squires. Generation of turbulent inflow data for spatially-developing boundary layer simulations. *Journal of Computational Physics*, 140(2), March 1998. doi: 10.1006/jcph.1998.5882. (page 15).

[98] L. M. Mack. Boundary layer linear stability theory. Technical Report 709, AGARD, 1984. (page 25).

[99] Nicholas Malaya, Kemelli C. Estacio-Hiroms, Roy H. Stogner, Karl W. Schulz, Paul T. Bauman, and Graham F. Carey. MASA: a library for verification using manufactured and analytical solutions. *Engineering with Computers*, pages 1–10, 2012. doi: 10.1007/s00366-012-0267-9. (pages 108, 223).

[100] Nicholas Malaya, Todd A. Oliver, Rhys Ulerich, and Robert D. Moser. Estimating uncertainties in statistics computed from DNS. In *65th Annual Meeting of the APS Division of Fluid Dynamics*, San Diego, CA, November 2012. (page 103).

[101] P. Maremonti. Asymptotic stability theorems for viscous fluid motions in exterior domains. *Rendiconti del Seminario Matematico della Università di Padova*, 71: 35–72, 1984. URL http://www.numdam.org/item?id=RSMUP_1984__71__35_0. (page 27).

[102] Shivaji Medida. Curvilinear extension to the Giles non-reflecting boundary conditions for wall-bounded flows. Master's thesis, University of Toledo, University of Toledo, 2007. (pages 82, 85).

[103] Youhei Morinishi and Shinji Tamano. Study on differences in turbulence statistics between compressible and incompressible low-Reynolds number turbulent channel flows using semi-local scaling. *JSME International Journal Series B*, 48 (4):743–749, 2005. doi: 10.1299/jsmeb.48.743. (pages 112, 134).

[104] Robert D. Moser, Gabriel Terejanu, Todd A. Oliver, and Christopher S. Simmons. Validating the prediction of unobserved quantities. ICES Report 12-32, August 2012. URL http://www.ices.utexas.edu/media/reports/2012/1232.pdf. (pages 11, 14).

[105] R. Mukund, P. R. Viswanath, R. Narasimha, A. Prabhu, and J. D. Crouch. Relaminarization in highly favourable pressure gradients on a convex surface. *Journal of Fluid Mechanics*, 566:97–115, October 2006. doi: 10.1017/S0022112006002473. (pages 24, 168).

[106] R. Narasimha and K. R. Sreenivasan. Relaminarization in highly accelerated turbulent boundary layers. *Journal of Fluid Mechanics*, 61:417–447, October 1973. doi: 10.1017/S0022112073000790.

[107] R. Narasimha and K. R. Sreenivasan. *Relaminarization of Fluid Flows*, volume 19, pages 221–309. Elsevier, 1979. doi: 10.1016/S0065-2156(08)70311-9. (pages 24, 35, 128, 168).

[108] Ioannis Nompelis, Travis Drayna, and Graham Candler. A parallel unstructured implicit solver for hypersonic reacting flow simulation. In *17th AIAA Computational Fluid Dynamics Conference*, Fluid Dynamics and Co-located Conferences. American Institute of Aeronautics and Astronautics, June 2005. doi: 10.2514/6.2005-4867. (page 29).

[109] Tinsley Oden, Robert Moser, and Omar Ghattas. Computer predictions with quantified uncertainty, part I. *SIAM News*, 43(9), November 2010. URL http://www.siam.org/news/news.php?id=1842. (page 11).

[110] Tinsley Oden, Robert Moser, and Omar Ghattas. Computer predictions with quantified uncertainty, part II. *SIAM News*, 43(10), November 2010. URL http://www.siam.org/news/news.php?id=1857. (page 11).

[111] Todd A. Oliver. Favre-averaged Navier–Stokes and turbulence model equation documentation. Technical report, Predictive Engineering and Computational Sciences, University of Texas at Austin, October 2011. (pages 201, 204, 205).

[112] Todd A. Oliver and Robert D. Moser. Bayesian uncertainty quantification applied to RANS turbulence models. *Journal of Physics: Conference Series*, 318(4): 042032, 2011. doi: 10.1088/1742-6596/318/4/042032. (page 10).

[113] Todd A. Oliver and Robert D. Moser. Accounting for uncertainty in the analysis of overlap layer mean velocity models. *Physics of Fluids*, 24(7):075108+, 2012. doi: 10.1063/1.4733455. (page 10).

[114] Todd A. Oliver, Nicholas Malaya, Rhys Ulerich, and Robert D. Moser. Estimating uncertainties in statistics computed from direct numerical simulation. *Physics of Fluids*, 26(3):035101+, March 2014. doi: 10.1063/1.4866813. (pages 98, 99, 103, 114, 116, 117, 189).

[115] Mariarosaria Padula. On the stability of a steady state of a viscous compressible fluid. *Chapman and Hall CRC Monographs and Surveys in Pure and Applied Mathematics*, pages 317–326, 2000. (page 28).

[116] Mariarosaria Padula. *Asymptotic Stability of Steady Compressible Fluids*. Springer Verlag, 2011. ISBN 978-3642211362. (page 28).

[117] Grant Palmer. Uncertainty analysis of CEV LEO and lunar return entries. In *39th AIAA Thermophysics Conference*. American Institute of Aeronautics and Astronautics, June 2007. doi: 10.2514/6.2007-4253. (page 7).

[118] Robert Z. Pearlman. NASA slips first test flight of Orion space capsule to December. SPACE.com, March 2014. URL http://www.space.com/

25086-nasa-orion-space-capsule-test-flight.html. (pages 31, 162, 187, 192).

[119] PECOS Development Team. The groovy toolkit: GRVY. https://red.ices.utexas.edu/projects/software/wiki/ESIO, 2010. (page 105).

[120] PECOS Development Team. ESIO: A parallel I/O library for scientific applications. https://red.ices.utexas.edu/projects/software/wiki/ESIO, 2011. (pages 106, 247).

[121] Dmitry Pekurovsky. P3DFFT user guide. http://code.google.com/p/p3dfft/, 2008. (page 103).

[122] K. Pohlhausen. Zur näherungsweisen integration der differentialgleichung der iaminaren grenzschicht. *ZAMM - Journal of Applied Mathematics and Mechanics / Zeitschrift für Angewandte Mathematik und Mechanik*, 1(4):252–290, 1921. doi: 10.1002/zamm.19210010402. (page 35).

[123] T. Poinsot and S. Lele. Boundary conditions for direct simulations of compressible viscous flows. *Journal of Computational Physics*, 101(1):104–129, July 1992. doi: 10.1016/0021-9991(92)90046-2. (pages 80, 81, 97).

[124] Stephen B. Pope. *Turbulent Flows*. Cambridge University Press, October 2000. ISBN 0521598869. (page 9).

[125] M. B. Priestley. *Spectral Analysis and Time Series: Univariate Series.*, volume 1. J.W. Arrowsmith, 1981. ISBN 0125649010. (page 98).

[126] M. B. Priestley. *Spectral Analysis and Time Series: Multivariate Series, Prediction and Control*, volume 2. Academic Press, 1981. ISBN 0125649029. (page 98).

[127] H. L. Reed, W. S. Saric, and D. Arnal. Linear stability theory applied to boundary layers. *Annual Review of Fluid Mechanics*, 28(1):389–428, 1996. doi: 10.1146/annurev.fl.28.010196.002133. (page 25).

[128] Patrick J. Roache. *Verification and Validation in Computational Science and Engineering*. Hermosa Publishers, 1998. ISBN 0913478083. (page 108).

[129] Patrick J Roache and Stanly Steinberg. Symbolic manipulation and computational fluid dynamics. *AIAA Journal*, 22(10):1390–1394, 1984. doi: 10.1016/0021-9991(85)90045-2. (page 108).

[130] Clarence W. Rowley and Tim Colonius. Discretely nonreflecting boundary conditions for linear hyperbolic systems. *Journal of Computational Physics*, 157(2): 500–538, January 2000. doi: 10.1006/jcph.1999.6383. (pages 81, 85, 96).

[131] Christopher J. Roy. Review of code and solution verification procedures for computational simulation. *Journal of Computational Physics*, 205(1):131–156, May 2005. doi: 10.1016/j.jcp.2004.10.036. (page 108).

[132] Christopher J. Roy and Frederick G. Blottner. Review and assessment of turbulence models for hypersonic flows. *Progress in Aerospace Sciences*, 42(7-8): 469–530, 2006. doi: 10.1016/j.paerosci.2006.12.002. (pages 7, 14).

[133] Tony Saad, Brian Maicke, and Joseph Majdalani. Coordinate independent forms of the compressible potential flow equations. In *47th AIAA/ASME/SAE/ASEE Joint Propulsion Conference & Exhibit*. American Institute of Aeronautics and Astronautics, 2011. doi: 10.2514/6.2011-5862. (pages 229, 231).

[134] Andre Saxer and M. B. Giles. Quasi-three-dimensional nonreflecting boundary conditions for Euler equations calculations. *Journal of Propulsion and Power*, 9 (2):263–271, April 1993. doi: 10.2514/3.23618. (page 82).

[135] P. Schlatter, Q. Li, G. Brethouwer, A. V. Johansson, and D. S. Henningson. High-Reynolds number turbulent boundary layers studied by numerical simulation. *Bulletin of the American Physical Society*, 54, 2009. URL `http://meetings.aps.org/link/BAPS.2009.DFD.BA.1`. (page 15).

[136] P. Schlatter, R. Örlü, Q. Li, G. Brethouwer, J. H. M. Fransson, A. V. Johansson, P. H. Alfredsson, and D. S. Henningson. Turbulent boundary layers up to $\mathrm{Re}_\theta = 2500$ studied through simulation and experiment. *Physics of Fluids*, 21(5): 051702, 2009. doi: 10.1063/1.3139294. (pages 15, 155).

[137] Philipp Schlatter and Ramis Örlü. Assessment of direct numerical simulation data of turbulent boundary layers. *Journal of Fluid Mechanics*, 659:116–126, 2010. doi: 10.1017/S0022112010003113. (page 15).

[138] Hermann Schlichting and Klaus Gersten. *Boundary Layer Theory*. Springer, eighth edition, 2000. ISBN 3540662707. (pages 137, 140).

[139] F.A. Schraub and S.J. Kline. A study of the structure of the turbulent boundary layer with and without longitudinal pressure gradients. Technical Report MD-12, Thermosciences Division, Stanford University, 1965. (page 24).

[140] Karl W. Schulz, Rhys Ulerich, Nicholas Malaya, Paul T. Bauman, Roy Stogner, and Chris Simmons. Early experiences porting scientific applications to the Many Integrated Core (MIC) platform. In *TACC-Intel Highly Parallel Computing Symposium*, Austin, Texas, April 2012. URL `http://www.tacc.utexas.edu/documents/13601/aa8e98bc-3544-4136-81aa-3920ae882a65`. (page 79).

[141] L. W. Schwartz. A perturbation solution for compressible viscous channel flows. *Journal of Engineering Mathematics*, 21(1):69–86, March 1987. doi: 10.1007/BF00127695. (page 112).

[142] James Serrin. On the stability of viscous fluid motions. *Archive for Rational Mechanics and Analysis*, 3-3(1):1–13, 1959. doi: 10.1007/BF00284160. (pages 25, 27).

[143] Gary S. Settles and Lori J. Dodson. Hypersonic shock/boundary-layer interaction database. Technical Report NASA CR 177577, 1991. (pages vi, 10, 12, 127).

[144] Gary S. Settles and Lori J. Dodson. Hypersonic turbulent boundary-layer and free sheer database. Technical Report NASA CR 177610, 1993. (pages 11, 12, 13, 16, 17).

[145] Gary S. Settles and Lori J. Dodson. Hypersonic shock/boundary-layer interaction database: New and corrected data. Technical Report NASA CR 177638, 1994. (page 12).

[146] Gary S. Settles and Lori J. Dodson. Supersonic and hypersonic shock/boundary-layer interaction database. *AIAA Journal*, 32(7):1377–1383, July 1994. doi: 10.2514/3.12205. (page 12).

[147] Mark P. Simens, Javier Jiménez, Sergio Hoyas, and Yoshinori Mizuno. A high-resolution code for turbulent boundary layers. *Journal of Computational Physics*, 228(11):4218–4231, June 2009. doi: 10.1016/j.jcp.2009.02.031. (pages 15, 112).

[148] Douglas R. Smith and Alexander J. Smits. The effects of steamline curvature and pressure gradient on the behavior of turbulent boundary layers in supersonic flow. In *25th AIAA Fluid Dynamics Conference*, June 1994. doi: 10.2514/6.1994-2227. (pages 33, 139).

[149] Alexander J. Smits and Jean-Paul Dussauge. *Turbulent Shear Layers in Supersonic Flow*. Springer Verlag, 2005. ISBN 978-0387261409. (pages 136, 140, 142, 199).

[150] Philippe R. Spalart. Direct simulation of a turbulent boundary layer up to $\mathrm{Re}_\theta = 1410$. *Journal of Fluid Mechanics*, 187:61–98, 1988. doi: 10.1017/S0022112088000345. (pages 15, 17, 18, 20, 35, 129, 148, 166, 168, 189).

[151] Philippe R. Spalart, Robert D. Moser, and Michael M. Rogers. Spectral methods for the Navier–Stokes equations with one infinite and two periodic directions. *Journal of Computational Physics*, 96(2):297–324, 1991. doi: 10.1016/0021-9991(91)90238-G. (pages 51, 54, 60).

[152] Katepalli R. Sreenivasan. Laminarescent, relaminarizing and retransitional flows. *Acta Mechanica*, 44(1):1–48, March 1982. doi: 10.1007/BF01190916. (pages 24, 30, 163, 168).

[153] Stanly Steinberg and Patrick J Roache. Symbolic manipulation and computational fluid dynamics. *Journal of Computational Physics*, 57(2):251–284, 1985. doi: 10.1016/0021-9991(85)90045-2. (page 108).

[154] Roy Stogner, Paul T. Bauman, Karl W. Schulz, Rochan Upadhyay, and Andre Maurente. Uncertainty and parameter sensitivity in multiphysics reentry flows. In *49th AIAA Aerospace Sciences Meeting including the New Horizons Forum and Aerospace Exposition*, January 2011. doi: 10.2514/6.2011-764. (pages 1, 8, 9, 127).

[155] Yasushi Sumitani and Nobuhide Kasagi. Direct numerical simulation of turbulent transport with uniform wall injection and suction. *AIAA Journal*, 33(7): 1220–1228, July 1995. doi: 10.2514/3.12363. (pages 136, 145, 149, 155).

[156] William Sutherland. The viscosity of gases and molecular force. *The London, Edinburgh, and Dublin Philosophical Magazine and Journal of Science*, 36(223): 507–531, 1893. (page 199).

[157] Roger A. Svehla. Estimated viscosities and thermal conductivities of gases at high temperatures. Technical Report R-132, Glenn Research Center, January 1962. (page 199).

[158] SymPy Development Team. *SymPy: Python library for symbolic mathematics*, 2009. URL `http://www.sympy.org`. (page 101).

[159] Alessandro Talamelli, Nicola Fornaciari, Westin, and P. Henrik Alfredsson. Experimental investigation of streaky structures in a relaminarizing boundary layer. *Journal of Turbulence*, 3, 2002. doi: 10.1088/1468-5248/3/1/018. (page 24).

[160] The Apache Project. Apache log4cxx. `http://logging.apache.org/log4cxx/`, 2010. (page 105).

[161] The HDF Group. Hierarchical data format version 5. `http://www.hdfgroup.org/HDF5`, 2000–2014. (pages 105, 247).

[162] H. Thomann. Effect of streamwise wall curvature on heat transfer in a turbulent boundary layer. *Journal of Fluid Mechanics*, 33:283–292, July 1968. doi: 10.1017/S0022112068001308. (page 21).

[163] Victor Topalian, Onkar Sahni, Todd A. Oliver, and Robert D. Moser. Slow growth formulation for DNS of temporally evolving boundary layers. In *64th Annual Meeting of the APS Division of Fluid Dynamics*, November 2011. (pages 2, 17, 20, 46).

[164] Victor Topalian, Todd A. Oliver, Rhys Ulerich, and Robert D. Moser. Direct numerical simulation of a compressible reacting boundary layer using a temporal slow growth homogenization. In *66th Annual Meeting of the APS Division of Fluid Dynamics*, Pittsburg, PA, November 2013. (pages 102, 103).

[165] Victor Topalian, Todd A. Oliver, Rhys Ulerich, and Robert D. Moser. A consistent spatiotemporal slow growth formulation for the calibration and uncertainty quantification of RANS turbulence models. *In preparation*, 2014. (pages 2, 20, 29, 39, 45, 102, 126, 153, 155, 168, 188, 191, 194, 209).

[166] Victor Topalian, Todd A. Oliver, Rhys Ulerich, and Robert D. Moser. A new temporal slow growth formulation for DNS of wall–bounded turbulence. *In preparation*, 2014. (pages 2, 18, 19, 37, 102, 143, 149).

[167] Lloyd N. Trefethen and Laurence Halpern. Well-posedness of one-way wave equations and absorbing boundary conditions. *Mathematics of Computation*, 47 (176):421, 1986. doi: 10.1090/S0025-5718-1986-0856695-2. (page 85).

[168] Kevin E. Trenberth. Some effects of finite sample size and persistence on meteorological statistics. Part I: Autocorrelations. *Monthly Weather Review*, 112, 1984. doi: 10.1175/1520-0493(1984)112%3C2359:SEOFSS%3E2.0.CO;2. (page 98).

[169] Rhys Ulerich and Robert D. Moser. Turbulence statistics with quantified uncertainty in cold-wall supersonic channel flow. In *65th Annual Meeting of the APS Division of Fluid Dynamics*, San Diego, CA, November 2012. (page 110).

[170] Rhys Ulerich, Kemelli C. Estacio-Hiroms, Nicholas Malaya, and Robert D. Moser. A transient manufactured solution for the compressible Navier–Stokes equations with a power law viscosity. In *10th World Congress on Computational Mechanics*, São Paulo, Brazil, July 2012. doi: 10.5151/meceng-wccm2012-16661. (pages 108, 223, 227).

[171] Prem Venugopal. *Direct numerical simulation of turbulence in a model solid rocket motor*. PhD thesis, University of Illinois at Urbana-Champaign, 2003. (pages 60, 61, 62, 63, 65).

[172] Marcel Vinokur. On one-dimensional stretching functions for finite-difference calculations. *Journal of Computational Physics*, 50(2):215–234, May 1983. doi: 10.1016/0021-9991(83)90065-7. (page 58).

[173] Hans von Storch and Francis W. Zwiers. *Statistical Analysis in Climate Research*. Cambridge University Press, March 2001. ISBN 0521012309. (page 98).

[174] Brian Warner, Dustin J. Mitchell, et al. Buildbot: The continuous integration framework. http://buildbot.net/, 2003–2014. (page 107).

[175] Frank M. White. *Fluid Mechanics*. McGraw–Hill, 4th edition, 1999. ISBN 978-0070697164. (page 235).

[176] David C. Wilcox. *Turbulence Modeling for CFD*. DCW Industries, third edition, 2006. ISBN 978-1928729082. (pages 7, 9).

[177] Michael J. Wright, Graham V. Candler, and Marco Prampolini. Data-parallel lower-upper relaxation method for the Navier-Stokes equations. *AIAA Journal*, 34(7):1371–1377, July 1996. doi: 10.2514/3.13242. (page 29).

[178] Michael J. Wright, Deepak Bose, and Y. K. Chen. Probabilistic modeling of aerothermal and thermal protection material response uncertainties. *AIAA Journal*, 45(2):399–410, February 2007. doi: 10.2514/1.26018. (page 7).

[179] Xiaohua Wu and Parviz Moin. Direct numerical simulation of turbulence in a nominally zero-pressure-gradient flat-plate boundary layer. *Journal of Fluid Mechanics*, 630:5–41, 2009. doi: 10.1017/S0022112009006624. (pages 15, 17).

[180] Xiaohua Wu, Robert G. Jacobs, Julian C. R. Hunt, and Paul A. Durbin. Simulation of boundary layer transition induced by periodically passing wakes. *Journal of Fluid Mechanics*, 398(1):109–153, 1999. doi: 10.1017/S0022112099006205. (page 15).

[181] Shan Yang. *A shape Hessian based analysis of roughness effects on fluid flows*. PhD thesis, The University of Texas at Austin, 2011. (page 54).

Vita

To add.

Permanent address: 1310 Newning Ave. #C
Austin, Texas 78704

This dissertation was typeset with LaTeX[†] by the author.

[†]LaTeX is a document preparation system developed by Leslie Lamport as a special version of Donald Knuth's TeX Program.